ARYL AND SUPER ARYL-EXTENDED CALIX[4]PYRROLES: SYNTHESIS AND APPLICATIONS

Qingqing Sun

UNIVERSITAT ROVIRA i VIRGILI

Aryl and Super Aryl-Extended Calix[4]pyrroles: Synthesis and Applications

QINGQING SUN

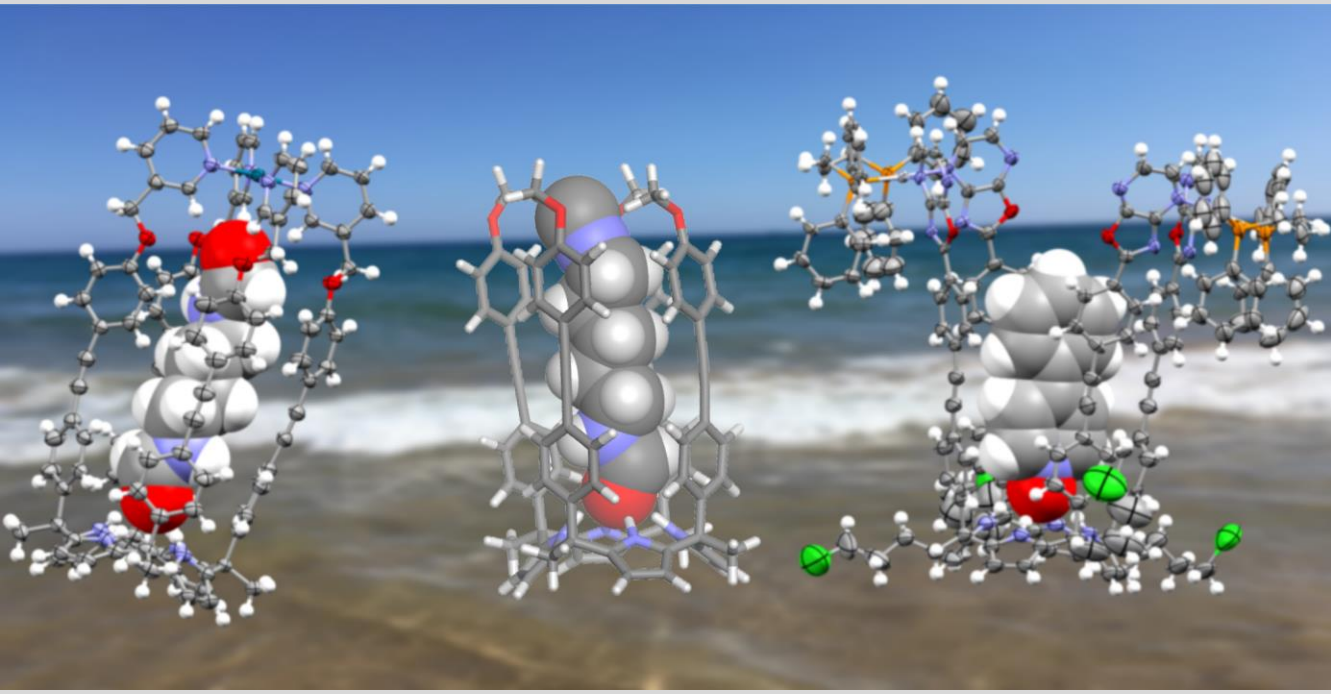

DOCTORAL THESIS
2021

UNIVERSITAT ROVIRA I VIRGILI
ARYL AND SUPER ARYL-EXTENDED CALIX[4]PYRROLES: SYNTHESIS AND APPLICATIONS
Qingqing Sun

UNIVERSITAT ROVIRA I VIRGILI
ARYL AND SUPER ARYL-EXTENDED CALIX[4]PYRROLES: SYNTHESIS AND APPLICATIONS
Qingqing Sun

DOCTORAL THESIS

Qingqing Sun

Aryl and Super Aryl-Extended Calix[4]pyrroles: Synthesis and Applications

Supervised by Prof. Pablo Ballester Balaguer

UNIVERSITAT
ROVIRA i VIRGILI

Tarragona

2021

UNIVERSITAT ROVIRA I VIRGILI
ARYL AND SUPER ARYL-EXTENDED CALIX[4]PYRROLES: SYNTHESIS AND APPLICATIONS
Qingqing Sun

ICIQ
Institut Català d'Investigació Química

Av. Països Catalans, 16
43007 Tarragona, Spain
Tel. (+34) 977 920 200
email: iciq@iciq.es

UNIVERSITAT ROVIRA i VIRGILI
Dept. de Química Analítica i Química Orgànica

Carrer de Marcel·lí Domingo, 1
43007 Tarragona, Spain
Tel. (+34) 977 55 97 69
email: sdn4@urv.cat

I STATE that the present study, entitled "Aryl and Super Aryl-Extended Calix[4]pyrroles: Synthesis and Applications", presented by Qingqing Sun for the award of the degree of Doctor, has been carried out under my supervision at the Institute of Chemical Research of Catalonia (ICIQ).

Tarragona, June 2021

Doctoral Thesis Supervisor

Prof. Pablo Ballester Balaguer

UNIVERSITAT ROVIRA I VIRGILI
ARYL AND SUPER ARYL-EXTENDED CALIX[4]PYRROLES: SYNTHESIS AND APPLICATIONS
Qingqing Sun

Acknowledgements

I would like to thank all the people who made critical contributions to the work consist on my PhD thesis. Their support and encouragement allowed me to achieve this degree and made my study and life in Tarragona a wonderful time.

My first sincere appreciation must go to my supervisor, **Prof. Pablo Ballester**, for offering me the opportunity to join his research group and allowing me to grow as a researcher over the last four years at ICIQ. His patience, inspiration, immense knowledge and plentiful experience have made great influence on my personal and academic advances. He has always been enthusiastically supportive of me and every group members, and always willing to give invaluable advice and guidance to me regardless of how busy he was. It has been one the greatest honors of my life to work for him and alongside him.

Apart from my supervisor, I would like to thank two postdoctoral researchers, **Gemma Aragay** and **Lluís Martínez**, for their kind help and guidance in the lab techniques and research projects. **Gemma** has a good experience for the laboratory management and she has always attempted to fix the issues both on the academic and intrumental aspects in times of need.

I would like to express my special acknowledgement to two former lab colleagues when I join in the group, **Luis Escobar** and **Ricardo Molina**. **Luis** has always been energetic to the academic work and ready to help me during the difficult conceptual development stage. Thanks for his continuous support and suggestions, which enriched my professional knowledge and put important endeavor to my achievements. As a fumehood mate, **Ricardo** has always been kind to me and provide me his most patientce and tolerance to my constantly mixtakes. Without his assistance and support, I would not easily adapt to this new environment and start my research work.

I would like to thank my former and current group members, **Giulia Moncelsi**, **Guillem Peñuelas**, **Andrés Felipe**, **Dragoş Dăbuleanu**, **Pedro Ferreira**, **Chiara Mirabella, Andrea Rivoli, Yifan Li, Quentin Bouvier and Alba Medina** for their encouragement, feedback, friendship and the beautiful moment we shared together.

I really appreciate **Beatriz Martin** for her kindness and support to me and our group. We were fortunate to have you amongst us.

I would like to thank all the visiting researchers who shared me with a short period of time. Thanks to **Diana Vargas**, **Kaisa Helttunen**, **Giacomo Berton**, **Jia Liang Sun**, **David Villarón**, **Jorn de Jong, Inmaculada Sempere, Sebastian Novosedlik, Stefania Gambaro** and **Cristina Vega**.

I would also like to thank **Prof. Laura Rodríguez**, **Prof. Christopher A Hunter**, **Andrea Pinto** and **Gloria Tobajas** for the productive collaborations.

Many thanks to the ICIQ Research Support Units that have been participated in my research during these years. Specifically, I would like to thank **Kerman Gómez, Israel Macho** and **Gabriel González**, for their help in the NMR measurements. I also thank **Simona Curreli**, **Marta Serrano, Meritxell Díaz**, **Noemí Cabello** and **Vanessa Martínez** for their help in the analysis of complex samples with large molecular weight. Thanks to **Eduardo C. Escudero-Adán** and **Jordi Benet** for his dedication and grateful discussions about X-ray crystallography.

Finally, I would like to express my gratitude to my parents for their tremendous understanding and timely encouragement. Thanks my brother for helping me to take care of my parents. I would also like to express my special appreciation with love to my husband, **Yanchao Lyu**. He has been my best friend and great companion, encouraged and helped me get through difficult times in the most positive way. Without his unparalleled love and support, it would be impossible for me to complete my study.

The work contained in this Thesis has been made possible thanks to the financial support of Ministerio de Ciencia, Innovación y Universidades (MCIU), Fondo Europeo de Desarrollo Regional (FEDER), Generalitat de Catalunya, ICIQ Foundation and China Scholarship Council (CSC).

my parents,

UNIVERSITAT ROVIRA I VIRGILI
ARYL AND SUPER ARYL-EXTENDED CALIX[4]PYRROLES: SYNTHESIS AND APPLICATIONS
Qingqing Sun

Table of Contents

UNIVERSITAT ROVIRA I VIRGILI
ARYL AND SUPER ARYL-EXTENDED CALIX[4]PYRROLES: SYNTHESIS AND APPLICATIONS
Qingqing Sun

Chapter 1

Introduction: Aryl and Super Aryl-Extended Calix[4]pyrroles: Synthesis and Applications

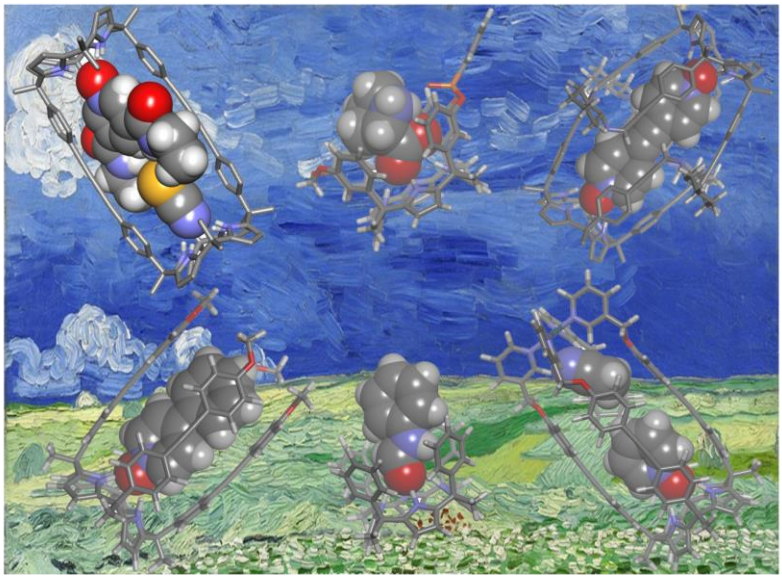

UNIVERSITAT ROVIRA I VIRGILI
ARYL AND SUPER ARYL-EXTENDED CALIX[4]PYRROLES: SYNTHESIS AND APPLICATIONS
Qingqing Sun

1.1 Introduction

Molecular recognition using synthetic receptors has attracted ever-increasing interest in the area of supramolecular chemistry.[1,2] The incorporation of aromatic panels to the receptor's scaffold allows further elaboration of its aromatic cavity. Receptors with large aromatic cavities surrounding most of the surface of the bound guests are known as molecular vessels. The inclusion of guests in molecular containers enables controlling their molecular properties, reactivities and on-demand catch and release behavior.[3,4,5] However, most of the developed molecular vessels feature non-polar cavities. This characteristic dramatically limits their use in molecular recognition processes based only on size and shape complementary. The inclusion of polar substrates in molecular vessels requires the placement of convergent functional groups in their aromatic cavities. For this reason, considerable synthetic efforts were devoted to the development of molecular vessels featuring polar cavities.[6,7] One of the aims of this endeavor is to mimic the binding performance of proteins, that is, achieving selective and high affinity binding of biologically relevant polar molecules in water solution.[8,9] The interest in designing molecular vessels with polar cavities is driven not only by their potential applications in selective molecular recognition but also in other areas such as molecular self-assembly, chemical sensing and supramolecular catalysis.[10] In recent years, our group focused on the use of the tetra-*alpha* isomers of aryl and super-aryl extended calix[4]pyrroles as molecular vessels for the selective binding of polar guests. The cone conformation of the tetra-*alpha* isomers of aryl and super-aryl extended calix[4]pyrroles defines an aromatic cavity closed at one end by a polar binding site and opened at the opposite end. In this section, we illustrate our recent advances in the synthesis of aryl and super aryl-extended calix[4]pyrroles. In addition, we highlight their applications as molecular containers, molecular carriers and supramolecular chemosensors.

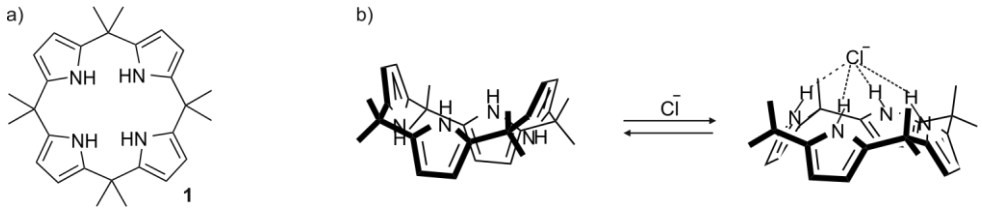

Figure 1.1. a) Line drawing structure of octa-methyl calix[4]pyrrole **1**; b) binding equilibrium between the 1,3-alternate conformational isomer of calix[4]pyrrole **1** and the corresponding 1:1 complex with Cl^- in cone conformation.

Calix[4]pyrroles are macrocyclic compounds containing four pyrrole units linked together by four fully substituted sp^3 hybridized *meso* carbon atoms.[11,12] Calix[4]pyrroles are conformationally flexible and adopt different conformations in solution characterized by the relative orientation of their pyrrole units.[10] Specifically, in non-polar solvents, such as chloroform and dichloromethane, calix[4]pyrroles adopt an 1,2- or 1,3-alternate conformation. In contrast, calix[4]pyrroles display a cone or partial-cone conformation in polar solvents, such as acetonitrile and acetone. The

substitution of the *meso* carbons with phenyl groups produced aryl-extended calix[4]pyrroles. Aryl-extended calix[4]pyrroles exist as several configurational isomers. The cone conformation of the all-*alpha* isomer of aryl-extended calix[4]pyrroles features a polar aromatic cavity. In this conformation, the pyrrole NHs can establish four convergent hydrogen-bonding interactions with the hydrogen bonding acceptor atoms of the included guests. (Figure 1.1b).[2] In the past two decades, octa-methyl calix[4]pyrrole **1** and its derivatives have been extensively investigated as receptors towards anions and neutral polar molecules in organic solvents.[13] Aryl-extended calix[4]pyrroles can be further elaborated into the super-aryl extended counterparts. The simultaneous incorporation of *meso*-alkyl chains at the lower rim improved the solubility of aryl and super aryl-extended calix[4]pyrroles in organic solvents. It also allowed gaining water-solubility of the receptors by including suitable charged terminal groups without perturbing their binding site.[14] The conversion of aryl and super-aryl extended calix[4]pyrroles into cavitand derivatives leads to the enhancement of binding selectivity and affinity.[15] Calix[4]pyrrole receptors featuring deep and polar aromatic cavities have been exploited to modulate chemical reactivity, facilitate the transport of anions and amino acids across liposomal membranes [16] and self-assembly of mono metallic-cages.[17,18]

1.2 "Two-wall" aryl-extended calix[4]pyrroles

As mentioned above, aiming at increasing the binding selectivity and affinity of octa-methyl calix[4]pyrrole **1**, different aromatic substituents were introduced at its *meso*-positions. The incorporation of two aryl groups into opposite *meso*-carbons of the calix[4]pyrrole core yields the so-called "two-wall"[19,20] aryl-extended calix[4]pyrroles.

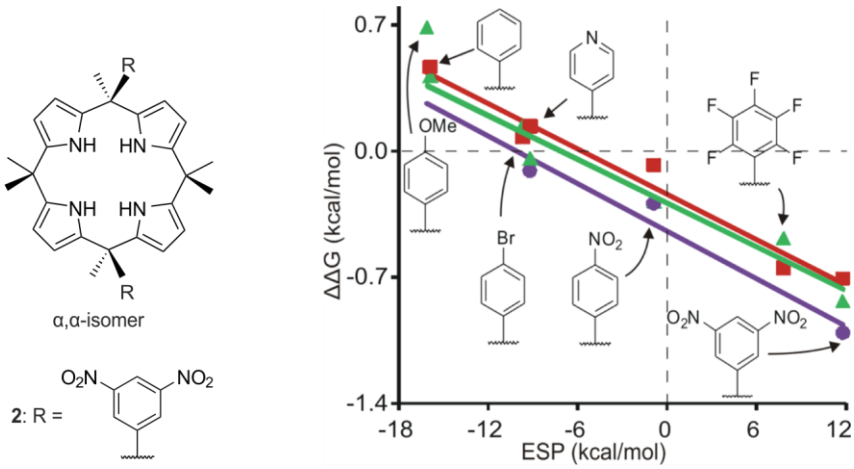

Figure 1.2. left) Line-drawing structure of *α,α*-isomer of "two-wall" aryl-extended calix[4]pyrrole receptors and **2**. right) Plot of the experimental values of the anion-π interaction derived from the binding of chloride (green), bromide (red), or iodide (purple) with receptors correlate with the ESP values calculated at the centroid of the aromatic walls. Reproduced with permission from ref. 19. Copyright 2014, American Chemical Society.

The “two-wall” aryl-extended calix[4]pyrroles exist as two configurational isomers, *αα* and *αß*. In the cone conformation, the α,α-isomer displays a deep aromatic cleft suitable for the inclusion of mono- and polyatomic anions, as well as neutral polar molecules. The bound anions are sandwiched between the two aromatic walls of the *α,α*-“two-wall” aryl-extended calix[4]pyrrole isomer. This characteristic rendered these receptors as suitable model systems to evaluate the strength of anion-π interactions in solution.

In 2014, our group reported the synthesis of a series of *α,α*-isomer of “two-wall” aryl-extended calix[4]pyrroles bearing electronically different aromatic panels. The 1:1 anionic complexes formed by the calix[4]pyrrole series and tetraalkylammonium salts of halides and nitrate were thermodynamically characterized in organic solution.[19] The differences between the free binding energies determined for the anionic complexes of “two-wall” *α,α*-receptors and those of the “no-wall” calix[4]pyrrole **1**, used as reference, allowed a rough quantification of the strength of the various anion-π interactions. The existence of a clear linear relationship between the electronic nature of the aromatic walls and the thermodynamic stabilities of the anionic complexes was evidenced (Figure 1.2). Moreover, the nitro-substituted “two-wall” aryl-extended calix[4]pyrrole **2** displayed excellent selectivity for the transport of nitrate anions through lipid-based lamellar membranes *vs* halides.[20]

The synthesis of macrocyclic receptors is one of the central topics in the area of host-guest chemistry. The structure of the macrocyclic compounds is rather rigid and presents well-defined recognition pockets, which greatly enhanced preorganization and substrate complementarity.[21] Relying on these characteristics, our group reported the first synthesis of a *bis*-calix[4]pyrrole oligo-macrocycle. The oligo-macrocycle **3** was synthesized by the Hay coupling reaction of two *bis*-aryl-ethynyl substituted “two-wall” aryl-extended calix[4]pyrroles. Although initial experiments suggested that the use of a ditopic templating guest was beneficial for the synthesis of the macrocycle in high yields, further studies evidenced that in the absence of the template good yields of **3** were also obtained.[22] The homo-ditopic calix[4]pyrrole macrocycle **3** was capable of simultaneously binding in solution one 3,5-pyridinecarboxamide-*N*-oxide, one cyanate anion and the corresponding tetrabutylammonium (TBA^+) counter-anion. This led to the quantitative formation of an unprecedented ion-paired 4-particles complex featuring pseudo-rotaxane topology (Figure 1.3).

The group also explored the allosteric cooperativity exhibited by the *bis*-calix[4]pyrrole macrocycle **3** in the complexation of ion-pair dimers and quartets in chloroform solution.[23] Remarkably, macrocycle **3** was found to function as a heteroditopic receptor in the binding of two cyanate or chloride TBA ion pairs by means of a highly cooperative process. Wherein, the two anions were bound to the distal calix[4]pyrrole binding sites of **3**, one TBA^+ cation was sandwiched between the two NCO^- or Cl^- anions displaying a close-contact cascade binding geometry. The other TBA^+

cation was bound in the shallow cavity of one calix[4]pyrrole unit displaying a receptor-separated binding mode.

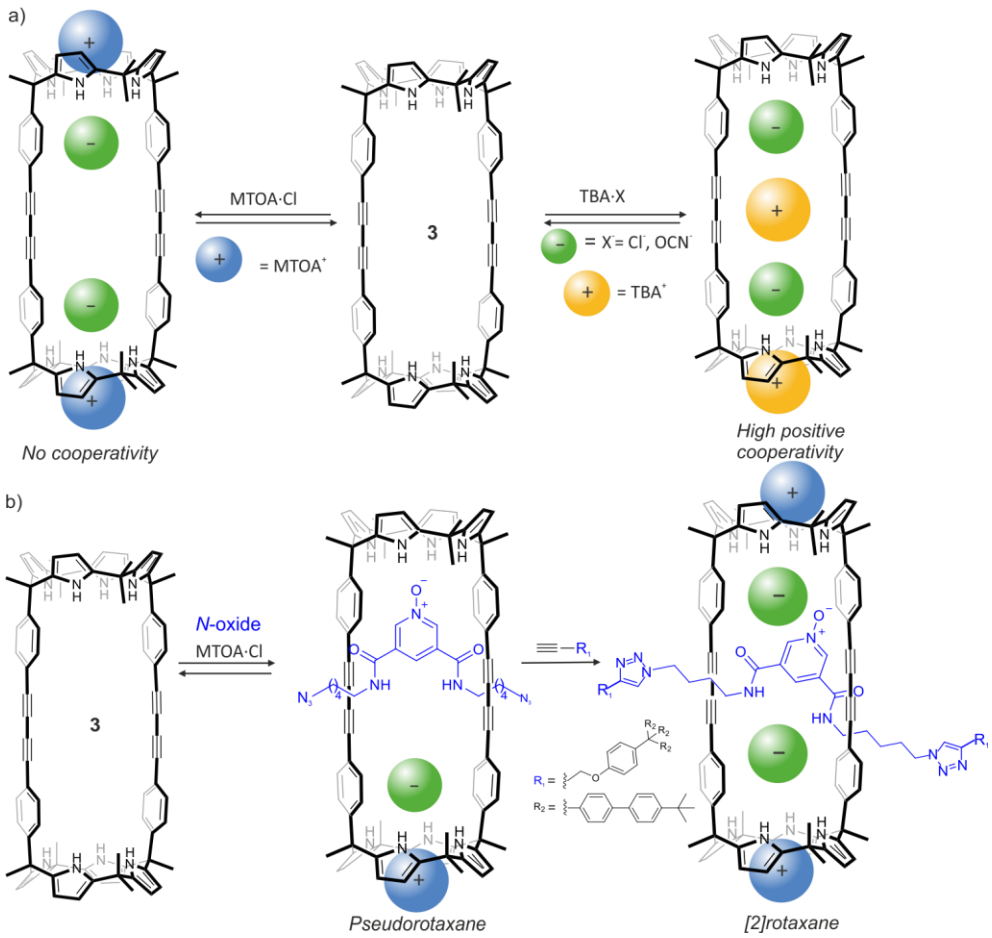

Figure 1.3. Schematic representation of the different equilibria involved in the assembly of Ballester's *bis*-calix[4]pyrrole symmetric macrocycle **3** with a) ion-paired 2:1 complexes; b) pseudorotaxane and [2]rotaxane architectures.

In contrast, the binding cooperativity diminished in the complexation of two copies of methyl trioctylammonium chloride (MTOACl). The final five-particles assembly showed the two bound ion-pairs in a receptor-separated binding mode (Figure 1.3).This difference was derived from the superior fit of the methyl group of the methyl trioctylammonium ($MTOA^+$) cation in the electron-rich aromatic cavities opposed to the bound anions. Subsequently, we synthesized a neutral [2]rotaxane using macrocycle **3** as a cyclic component. We explored the ion-pair recognition properties of the [2]rotaxane (Figure 1.3) and reported their behavior as an efficient heteroditopic receptor for various tetraalkylammonium chloride/cyanate salts in organic solvents.[24]

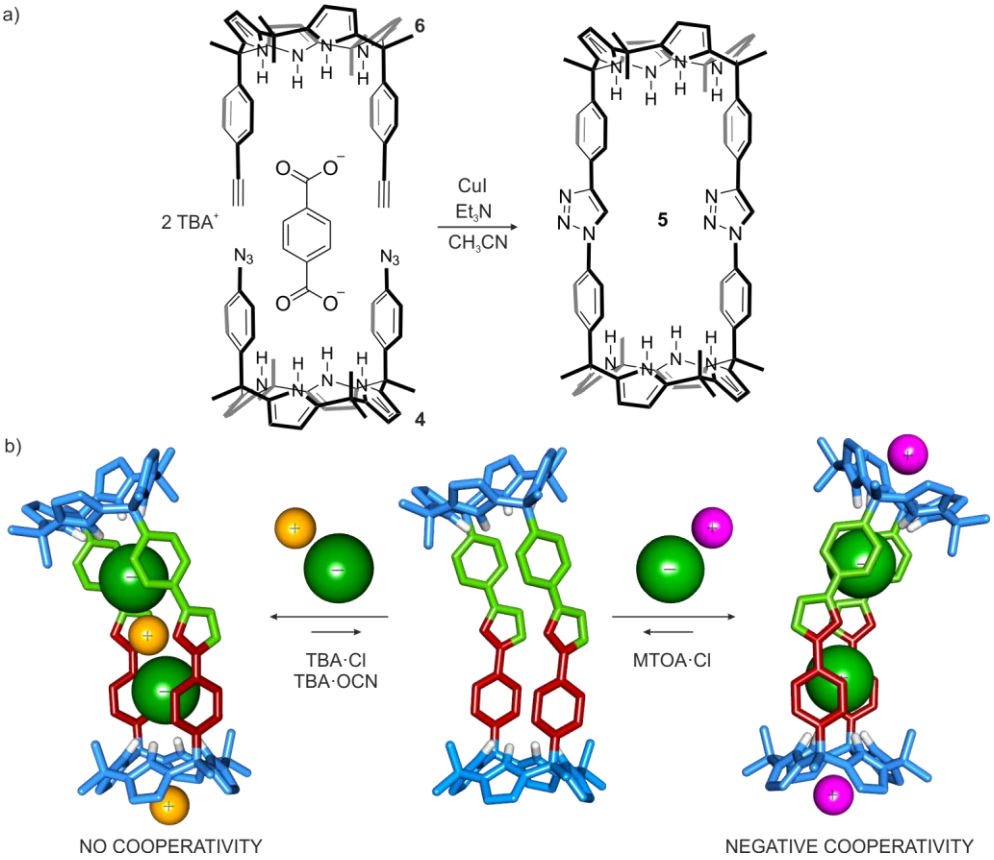

Figure 1.4. a) Synthesis of oligo-macrocyclic bis-calix[4]pyrrole receptor **5** and b) representations of chemical equilibria involved in the interactions of the receptor **5** with different ion pairs. Reproduced with permission from ref. 25. Copyright 2018, American Chemical Society.

We further reported the allosteric cooperativity in the binding of ion-pair dimers to the non-symmetrical oligo-macrocyclic bis-calix[4]pyrrole receptor **5**. We prepared bis-calix[4]pyrrole receptor **5** by a double copper-catalyzed alkyne-azide cycloaddition reactions of the bis-4-ethynyl-phenyl "two-wall" aryl-extended calix[4]pyrrole **6** with the bis-4-azidephenyl "two-wall" counterpart **4**. The oligo-macrocycle **5** contains two calix[4]pyrrole units linked by two triazole spacers (Figure 1.4)[25] We performed binding studies of receptor **5** with tetraalkylammonium chloride/cyanate salts, *i.e.* TBAOCN, TBACl and MTOACl in organic solvents. We used ^{1}H NMR titrations and ITC experiments for the thermodynamic characterization of the complexes. We found that the binding processes provided 2:1 ion paired complexes that were thermodynamically and kinetically stable. The formed 2:1 complexes featured different binding geometries and cooperativity depending on the nature of the ion-pair cation. That is, in the case of TBA salts, the assembled 2:1 complex displayed an included ion-triplet in close-contact binding geometry but did not display signs of allosteric binding cooperativity. In contrast, the use of MTOACl yielded a 2:1 complex with the two

ion pairs bound in receptor-separated binding geometry. The formation of the complex occurred through two steps binding process involving negative allosteric cooperativity. These results were ascribed from the better fit of the methyl group of the MTOA cation than the TBA cation in the shallow cavity defined by the four pyrrole rings.

1.3 "Four-wall" aryl-extended calix[4]pyrroles

"Four-wall" aryl-extended calix[4]pyrroles were obtained by Sessler *et al*. from the acid-catalyzed condensation of pyrrole and the corresponding methyl aryl-ketone at room temperature.[26] The reaction mixture consisted of the four possible configurational isomers, *αßαß*, *ααßß*, *αααß* and *αααα*, depending on the relative orientation of the *meso*-aryl substituents, larger macrocycles and other linear oligomers. Suitable purification of the reaction crude allowed the isolation of the targeted *αααα*-isomer in reduced yields. In the cone conformation, the tetra-α isomer of "four-wall" aryl-extended calix[4]pyrrole features a deep, polar aromatic cavity closed at one end by the four convergent pyrrole NHs and opened at the opposite end.[27] The dimension of the cavity makes it suitable for the inclusion of a variety of anions and electron-rich neutral guests that are size and shape complementary.

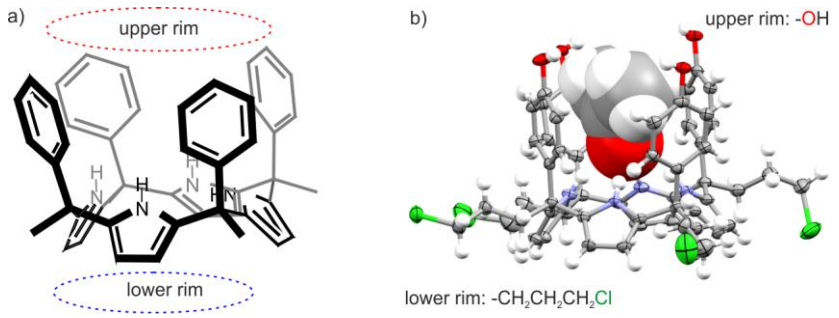

Figure 1.5. a) Molecular structure of the tetra-α isomer of "four-wall" aryl-extended calix[4]pyrrole in the cone conformation; b) Example of aryl-extended calix[4]pyrrole functionalized with hydroxyl group at its upper rim and alkyl chains with terminal chloro substituents at the lower rim

"Four-wall" aryl-extended calix[4]pyrroles possess an "upper rim" surrounding the open end of the aromatic cavity and a "lower rim" defined by the alkyl substituents at the *meso*-carbon. Proper functionalization of the "upper and lower rims" of "four-wall" aryl-extended calix[4]pyrroles allows the construction of more elaborated molecular containers, cavitands and capsular architectures, which would increase the potential applications of these molecular scaffolds both in organic solvents and water solution (Figure 1.5).

In 2008, our group prepared a series of tetra-α "four-wall" aryl-extended calix[4]pyrrole receptors by introducing different substituents in the *para*-position of the *meso*-phenyl groups defining the "upper rim". A different *para*-substituent of the aromatic walls was used to modulate the electronic

nature of the *meso*-phenyl groups. We used the developed series of "four-wall" aryl-extended calix[4]pyrroles as model systems to quantify anion-π interactions in solution.[28,29] The binding process of the "four-wall" calix[4]pyrrole receptors with chloride anion produced the formation of 1:1 anionic complexes, which were mainly stabilized through hydrogen-bonding interactions between the four pyrrole NHs and the included chloride anion. These complexes adopt a binding geometry featuring the calix[4]pyrrole core in a cone conformation and the chloride deeply located in the aromatic cavity. The geometrical features displayed by the cone conformation of the tetra-α isomers of "four-wall" aryl-extended calix[4]pyrroles have been extensively exploited in several applications, such as the assembly of calix[4]pyrrole-based dimeric capsules,[30,31,32,33,34,35,36] transport of anions[37] and biologically relevant molecules across liposomal membranes[38] and the development of signaling molecular devices,[39,40] among others.

1.3.1 Self-assembly of dimeric calix[4]pyrrole capsules

Considering the ability of the urea groups to act as both hydrogen-bond donors and acceptors and their previous use in the self-assembly of dimeric capsules based on tetra-urea-calix[4]arenes,[41,42] our group described the synthesis of two tetra-α isomers of "four-wall" aryl-extended calix[4]pyrroles, equipped with four urea moieties at their upper rims. The ^{1}H NMR spectra of the tetra-urea calix[4]pyrrole **7**[32] and the chiral counterpart **8** in CD_2Cl_2 solution at millimolar concentration showed broad and ill-defined protons signals. This observation was indicative of the involvement of the tetra-urea calix[4]pyrroles in the formation of oligomeric aggregates stabilized by the formation of intermolecular hydrogen bonds. Interestingly, the addition of 0.5 equiv. of 4,4'-bipyridine-1,1'-dioxide **9** to the above-mentioned CD_2Cl_2 solution of **7** produced sharp and well-resolved signals for all protons. This behavior was indicative of the formation of discrete species in solution. However, we did not observe two separate aromatic doublets for the proton signals, H^a and H^b, *ortho* to the urea groups of **7**, which was characteristic of the dimerization process for the structurally related calix[4]arene tetra-ureas. In an attempt to evidence the formation of the assembled dimeric tetra-urea calix[4]pyrrole capsule **9**⊂**7**$_2$, we cooled down the solution to 200 K. This led to the observation of the expected two aromatic doublets for the H^a and H^b protons in the ^{1}H NMR spectrum. In the case of the **9**⊂**7**$_2$ capsule, the chemical exchange process between the two doublets of the *ortho* protons was not controlled by the energy barrier required for the change in the sense of the unidirectional orientation of the urea groups but by that of the rotation of the *meso*-phenyl substituents. The bis-pyridine bis *N*-oxide **9** was able to bind simultaneously the two calix[4]pyrrole components of the dimer locking them in the cone conformation. In this conformation, the eight urea groups of the two distinct calix[4]pyrrole components were ready to interdigitate and form an endohedrally functionalized dimeric capsule stabilized by a hydrogen bonded belt of 16 hydrogen bonds. The large and polar aromatic cavity of the capsule was defined by the two calix[4]pyrrole scaffolds (Figure 1.6).

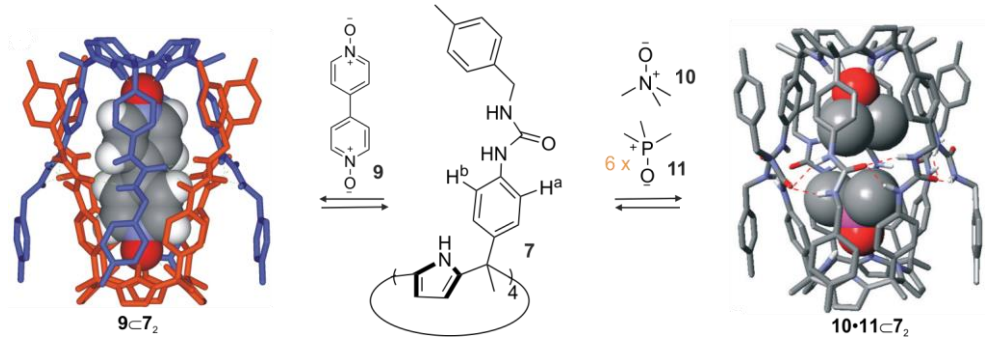

Figure 1.6. Self-assembled dimeric capsules: left) **9**⊂**7**$_2$ and right) **10**•**11**⊂**7**$_2$ from the tetra-urea calix[4]pyrrole **7** in the presence of guests **9**, **10** and **11**, respectively. Encapsulated guests are shown as CPK models and tetra-urea calix[4]pyrrole **7** is displayed in stick representation. Reproduced with permission from ref. 36. Copyright 2012, Royal Society of Chemistry.

To further analyze the templating effect of the encapsulated guests, monotopic polar guests, such as trimethylamine *N*-oxide **10** and trimethylphosphine *N*-oxide **11** were investigated. It was found that the homocapsules, **10**$_2$⊂**7**$_2$ or **11**$_2$⊂**7**$_2$ were also successfully assembled through the co-encapsulation of two guests, each hemisphere of the capsule included one guest. The resulting dimeric capsules templated by the encapsulation of monotopic guests were thermodynamically less stable than those prepared through the inclusion of the ditopic bis *N*-oxide **9**. Surprisingly, the addition of 0.5 equiv. of *N*-oxide **10** and 6 equiv. of phosphine oxide **11** to a CD_2Cl_2 solution of tetra-urea calix[4]pyrrole **7** induced the predominant formation of the heterocapsule **10**•**11**⊂**7**$_2$. The homocapsules, **10**$_2$⊂**7**$_2$ and **11**$_2$⊂**7**$_2$ were also present in solution but to a much reduced extent (Figure 1.6). The self-assembled heterocapsule resembles a biomolecular reaction vessel, which was able to efficiently encapsulate two different guests in its cavity.

In analogy to the tetra-urea calix[4]pyrrole **7**, its enantiopure counterpart **8**, bearing methyl substituents at the benzylic carbon atoms, dimerized into the **10**$_2$⊂(*SM*•*SP*)-**8**$_2$ capsule in the presence of equimolar amounts of trimethyl *N*-oxide **10**.[43] This four-particle assembly contained two cyclo-diastereomeric hemispheres (*M* and *P*). The two tetraurea calix[4]pyrrole hemispheres display the same absolute configuration at all their benzylic carbon atoms (e.g. *S*). However, the formation of the urea belt of the capsule requires the orientation of the urea groups of the two hemispheres in an unidirectional manner. In turn, this provoked that the two hemispheres of the capsule became cyclo-chiral diastereoisomers (*S,M*:*P,S*). Motivated by the unique properties of point chirality and cyclochirality present in the tetra-urea components of the dimeric capsule, we explored the self-sorting ability of the chiral tetra-urea with non-chiral counterparts.

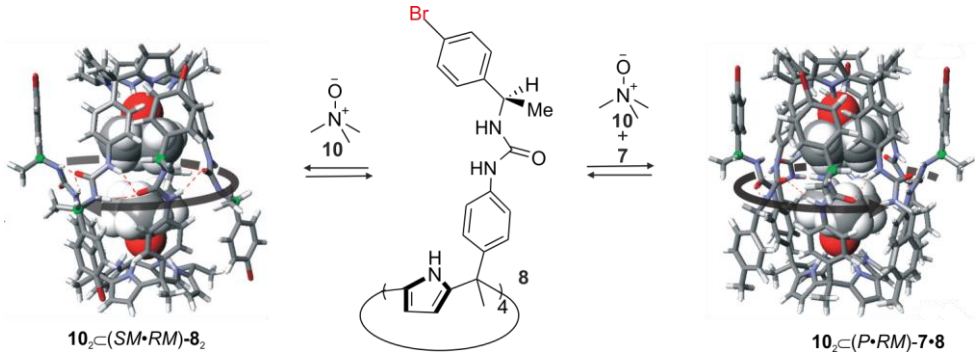

Figure 1.7. Self-assembly a) homodimeric capsule $\mathbf{10}_2\subset(SM\bullet SP)$-$\mathbf{8}_2$ and b) heterodimeric capsule $\mathbf{10}_2\subset(P\bullet RM)$-**7•8** using the enantiopure tetra-urea calix[4]pyrrole **8** and achiral **7** in the presence of *N*-oxide **10**. Encapsulated guests are shown as CPK models and tetra-urea calix[4]pyrroles **8** and **7** are displayed in stick representation. Reproduced with permission from ref. 43. Copyright 20110, American Chemical Society.

An equimolar mixture of *N*-oxide **10**, non-chiral tetra-urea calix[4]pyrrole **7** and chiral tetra-urea calix[4]pyrrole **8** in CD_2Cl_2 solution quantitatively assembled to form the exclusive heterodimeric capsule $\mathbf{10}_2\subset(P\bullet RM)$-**7•8**. This result suggested the existence of an efficient transfer of chiral information from the periphery of the capsule (point chirality of the stereogenic carbon) to the asymmetry offered by the unidirectional sense of rotation of the urea groups involved in the hydrogen-bonding belt stabilizing the dimeric assembly (Figure 1.7).

The self-assembly of molecular capsules relying on dynamic covalent bonds is a valuable synthetic strategy. This strategy merges the strength of covalent bonds with the reversibility and selectivity of non-covalent interactions. In 2014, Rebek *et al* reported the cylindrical dynamic capsules assembled from a resorcin[4]arene tetra-acetal scaffold and aromatic diamines exploiting the formation of dynamic covalent imine bonds.[44] Intrinsically, the lack of polar functionality in the capsule's aromatic cavity restricted its selectivity for guest encapsulation to size and shape complementary and disfavored the binding of polar substrates. These findings inspired us to develop related supramolecular capsules containing a polar aromatic cavity. In first instance, we aimed to achieve the binding of polar substrates with high affinity. A more demanding goal involved mimicking enzyme mediated reactions or even enzymatic catalysis. Recently, our group disclosed two dissymmetric octa-amine capsular containers, **13** and **14**, featuring large aromatic polar interiors. These dynamic covalent capsules were self-assembled from tetra-aldehyde calix[4]pyrrole **12** and 1,2-substituted aliphatic diamines, **15** and **16**. The emergence of the capsular assemblies required the encapsulation of the ditopic bis-pyridine bis *N*-oxide guest, **17** (Figure 1.8). As stated above, the bis *N*-oxide brings together the two tetra-aldehyde calix[4]pyrrole components through the establishment of hydrogen bonding, CH-π and π-π interactions forming a 2:1 complex. Moreover, the inclusion of the *N*-oxide locks the two tetra-aldehyde calix[4]pyrroles in the cone conformation.

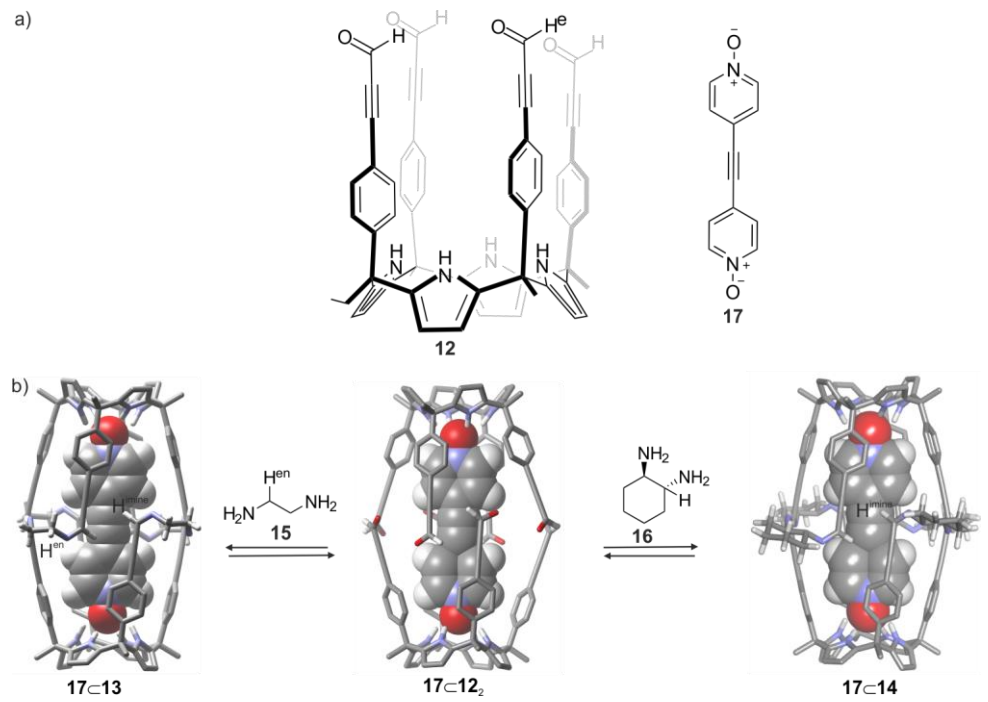

Figure 1.8. a) Line-drawing structures of tetra-aldehyde **12** and templating guest bis *N*-oxide **17**. b) Energy-minimized structures of the self-assembled homodimeric capsules of **17**⊂**13** and **17**⊂**14** from **17**⊂**12**$_2$ complex with different diamine linkers, **15** and **16**, respectively. Encapsulated guests are shown as CPK models and tetra-aldehyde **12** is displayed in stick representation. Reproduced with permission from ref. 44. Copyright 2017, Royal Society of Chemistry.

Upon addition of two equivalents of diamine **15** to the 2:1 complex, **17**⊂**12**$_2$, in $CDCl_3$ solution, the diagnostic proton signals for the quantitative assembly of the octa-imine dynamic covalent capsule **13** were observed in the ^{1}H NMR spectrum of the mixture. For example, the signal for the aldehyde proton (H^e) in the **17**⊂**12**$_2$ complex disappeared with the concomitant emergence of the signal for the proton in the imine bonds (H^{imine}) of the capsule. At the same time, the methylene protons of the diamine linker (H^{en}) resonated as one broad signal and moved downfield compared to those proton signals in the free diamine. Noteworthy, the capsular complex **17**⊂**13** is dissymmetric and existed as racemic mixture of *M* and *P* enantiomers. Likewise, the addition of two equivalents of enantiomerically pure diamine linker **16** to the $CDCl_3$ solution of **17**⊂**12**$_2$ solution produced the quantitative formation of the dynamic covalent dimeric capsule **17**⊂**14**. X-ray analysis of a single crystal of **17**⊂**14** revealed that the eight reversible imine bonds in the dissymmetrical capsule **14** feature *Z*-configuration in order to match the dimension requirements of the encapsulated guest. Remarkably, the asymmetry imposed by unidirectional sense of rotation of the bis-imine covalent connections of the two calix[4]pyrrole units, together with the stereogenic carbon chirality of the enantiopure diamine linker (*1R*,*2R*)-**15** lead to the exclusive observation of a single diastereomeric capsule *P*-(*1R*,*2R*)-**13**. This result evidenced the efficient chirality transfer

from the stereogenic carbon atoms of the diamine linker to the supramolecular chirality featured by the capsular container **14** (Figure 1.8).

1.3.2 Transport of anions and amino acid across liposomal membranes

The efficient transport of anions and amino acids across liposomal membranes plays an important role in a number of cellular functions, such as metabolism energetics, cell signaling, cellular pH, and regulation of cell volume.[45,46] Dysfunction of the ion channels and defective endogenous carriers responsible for this transport is correlated with a variety of human diseases, such as cystic fibrosis (Cl^- transport deficiency)[47] and primary inherited aminoacidurias (defects in the renal absorption of amino acids).[48] In this regard, the development of synthetic compounds, aka carriers, that are capable to facilitate the transport of biologically relevant molecules and ions across liposomal membranes constitutes an important application of supramolecular chemistry concepts.

Calix[4]pyrroles are known as effective anions and ion pairs receptors, as well as anion carriers through lipid bilayer membranes.[20, 49 , 50 , 51] Not long ago, our research group and others demonstrated that “two-wall” and “four-wall” aryl-extended calix[4]pyrrole derivatives are effective carriers for mono- and polyatomic anions through phospholipid membranes.[20,37] Notably, the two calix[4]pyrrole receptors, **18** and **19**, displayed different transport activities depending on the method used for their insertion into liposomal membranes (Figure 1.9).[37] That is, the pre-insertion methodology (carriers were incorporated into the membranes during the liposome’s formation to be used in the HPTS assay[52]) showed that the chloride transport activity of the tetra-α isomer of “four-wall” calix[4]pyrrole over-performed that of the “two-wall” analogue. However, opposite results were observed by applying the post-insertion method and the HPTS assay. Most likely, the reduced transport activity exhibited by the “four-wall” calix[4]pyrrole carrier using the post-insertion method was derived from its poor deliverability into the lipid bilayer in the DMSO solution.

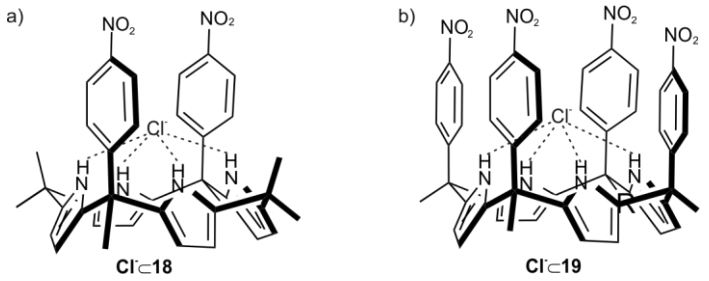

Figure 1.9. Molecular complexes of a) Cl^-⊂**18** and b) Cl^-⊂**19**.

Depending on the nature of the substituents present in the *meso*-aromatic panels (upper rim), “four-wall” aryl-extended calix[4]pyrroles and their cavitand derivatives displayed different affinity and selectivity in the binding of small polar molecules in aqueous and organic solvents. In this vein, we reported that the *mono*-phosphonate bridged calix[4]pyrrole cavitand **20** is an effective

and selective receptor for L-proline (**L-Pro**) binding in CD_2Cl_2 solution.[38] The intracellular concentration level of L-proline is usually taken as indicative of some cancers as well as hyperprolinemia type I and type II.[53]

We first described that cavitand **20** was able to extract 1 equiv. of L-proline, which has limited solubility in CD_2Cl_2, in solid-liquid experiments. The ^1H NMR spectroscopic analyses of the CD_2Cl_2 solution obtained after the extraction experiment evidenced the formation of a 1:1 complex between receptor **20** and L-proline for which we could estimate a binding constant value *K*a(**L-Pro⊂20**) larger than 10^6 M^{-1}. Additional support for the formation and binding geometry of the **L-Pro⊂20** inclusion complex was obtained from X-ray diffraction analysis of a single-crystal. In the solid state, the **L-Pro⊂20** complex showed that **L-Pro** was deeply included in the polar cavity of **20**. One oxygen atom of the carboxylate group of **L-Pro** was bound to **20** via the formation of four hydrogen-bonds with the pyrrole NH protons. An additional hydrogen bond was observed between the protonated amino group of **L-Pro** and the oxygen of the P=O group (Figure 1.10).

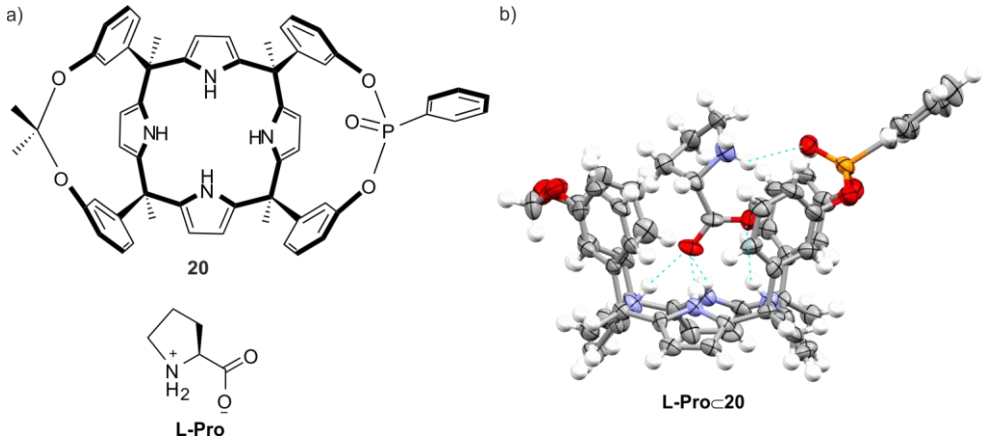

Figure 1.10. a) Line-drawing structures of receptor **20** and **L-Pro** (L-proline); b) X-ray structure of the complex **L-Pro⊂20.**

We investigated the pre-insertion of cavitand **20** in the membrane of egg yolk phosphatidylcholine (EYPC) vesicles to facilitate L-proline transport. Initially, we probed the facilitated transport efficiency of **20** using ^{13}C NMR spectroscopy and ^{13}C labeled amino acids. Liposomes containing ^{13}C unlabeled amino acids, L-proline or L-alanine (L-Ala) were suspended in a solution containing the corresponding ^{13}C labeled amino acids, at the same concentration, and a paramagnetic salt (1 mM $MnSO_4$) (Figure 1.11a and b). The extravesicular amino acids would have their ^{13}C resonances broadened due to the binding to the paramagnetic Mn^{2+} ion. In contrast, any labeled amino acids that had been transported to the interior of the vesicles should show sharp ^{13}C resonances because the paramagnetic ion cannot cross the liposomal membrane. We observed a significant enhancement of the ^{13}C signal assigned to intravesicular $^{13}C(1)$-**L-Pro** in the presence

of the embedded carrier (0.1% molar ratio). This result was indicative of the facilitated diffusion of **L-Pro** by carrier **20**. Conversely, the facilitated transport of a non-cyclic α-amino acid like L-Ala, which was not quantitively extracted by cavitand **20** in the solid-liquid extraction experiment, was effective only at high concentrations (1% carrier/EYPC molar ratio) of the carrier **20**. The larger efficiency and selectivity of carrier **20** in facilitating the transport of **L-Pro** correlates well with the formation of thermodynamically stable **L-Pro⊂20** complex.

The transport kinetics of the facilitated process were assessed using [^{3}H] radiolabeled amino acids. **L-Pro** and L-Ala were used in both influx and efflux transport experiments in which the radiolabeled amino acid is present either in the extravesicular or intravesicluar region at the beginning of the experiment. After 60 min of transport, the degree of influx or efflux could be measured by adhering the liposomes to nitrocellulose filters, washing them thoroughly and measuring the radioactivity level of the trapped liposomes. The obtained results showed a 30-fold increase in transport rate of **L-Pro** using carrier **20** at 0.2% **20**:EYPC molar ratio in comparison to the transport rate measured in the absence of the transporter (Figure 1.11c).

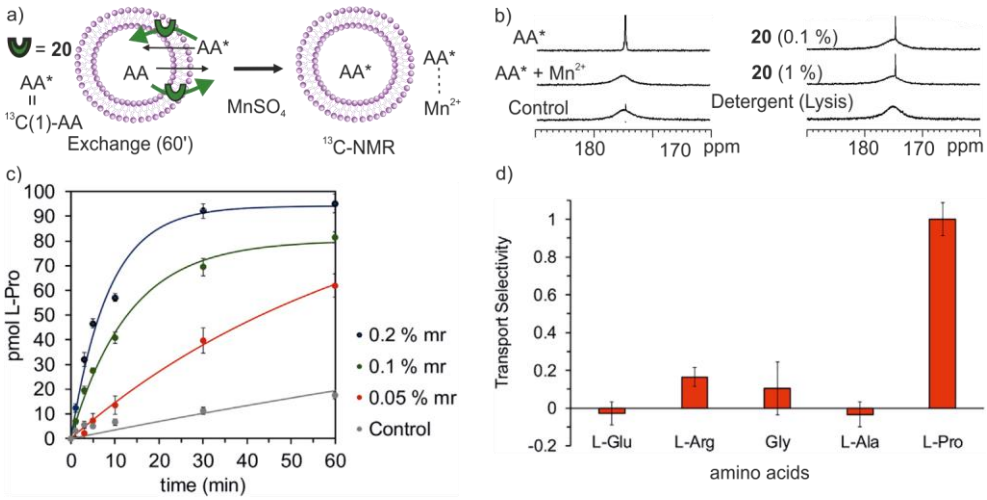

Figure 1.11. a) Schematic representation of the ^{13}C NMR assay used to monitor **L-Pro** transport; b) ^{13}C NMR spectra of ^{13}C(1)-**L-Pro** in the absence and in the presence of carrier **20**; c) Non-linear fits of the experimental data of **L-Pro** influx transport experiments (points) obtained at different carrier:lipid molar ratio to the theoretical kinetic model of a reversible first-order reaction; d) Determined transport selectivity values for **20** with different natural radioactive-labeled amino acids. Reproduced with permission from ref. 38. Copyright 2010, Cell Press.

In addition to **L-Pro**, the ability of **20** to transport other amino acids (L-Ala, L-Arg, Gly, L-Glu, L-Ile and L-Val) was also explored using the same radiometric method. The obtained results demonstrated that carrier **20** displayed a remarkable selectivity for the facilitated transport of **L-Pro** over the other studied amino acids (Figure 1.11d). The ability of cavitand **20** to facilitate transport of **L-Pro** across the membrane of human cells, for example, HeLa cells was also investigated. The

cells were pre-incubated with POPC (1-palmi-toyl-2-oleyl-sn-glycero-3-phosphocholine) liposomes containing **20** at 10% **20**:POPC molar ratio. These transport experiments were conducted using a choline chloride solution, to minimize endogenous **L-Pro** transport. We found a significant enhancement of the **L-Pro** concentration within the cells only at high concentrations of **L-Pro** in solution. The results obtained within cells are promising and augur well for the potential application of amino acids synthetic carriers as biological therapeutics.

1.3.3 Chemosensors for the recognition of creatinine

The same mono-phosphonate bridged calix[4]pyrrole cavitand **20** was exploited as carrier in an ion-selective electrode (ISE) for the recognition and sensing of creatinine in human bodily fluids.[39] Creatinine is a metabolic waste product, the concentration levels of which are widely taken as a clinical indicator of kidney performance and renal functions.[54,55]

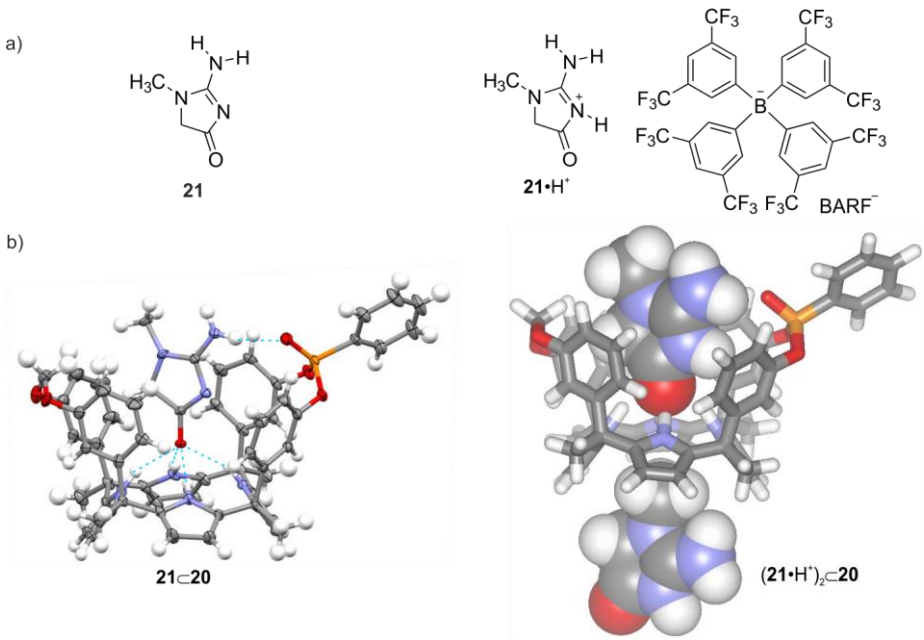

Figure 1.12. (a and b) Upper panel: line-drawing structures of creatinine **21** and creatininium cation (**21**•H^+) as the BARF salt. Lower panel: X-ray structure of the inclusion complex of **21**⊂**20** and energy-minimized structure of the putative 2:1 complex (**21**•H^+)$_2$⊂**20**. The bound guests are shown as CPK models and the receptor is displayed in stick representation. Reproduced with permission from ref. 39. Copyright 2016, Wiley-VCH.

Receptor **20** was able to extract neutral creatinine **21** from solid-liquid extractions into the dichloromethane phase. It also displayed high binding affinity for creatinine and its protonated form **21**•H^+. Single crystal X-ray diffraction studies revealed that the cavity dimensions of **20** are ideal for the inclusion of creatinine by surrounding most of its surface. The formed inclusion 1:1 complex

21⊂20 was stabilized by a combination of CH-π, π-π and five complementary hydrogen-bonding interactions (four with pyrrole NHs and one with the upper rim P=O group) (Figure 1.12).

Within the research program aiming at the development of fluorescent calix[4]pyrrole chemosensors for the recognition and quantification of creatinine in solution, we recently reported the design and synthesis of the novel fluorescent aryl-extended calix[4]pyrrole sensor **22**. This molecular sensor consists on the covalent attachment of a dansyl fluorophore to the basic scaffold of receptor **20**. In order to achieve the connection between the receptor and the sensing unit, we bridged two aromatic rings with an amino-phenyl linker. Owing to the lack of changes in fluorescence emission for the direct titrations of **22** with creatinine **21** and its lipophilic analogue hexylcreatinine **23**, we were forced to develop alternative competitive indicator displacement assays (IDAs) (Figure 1.13).[40,56,10]

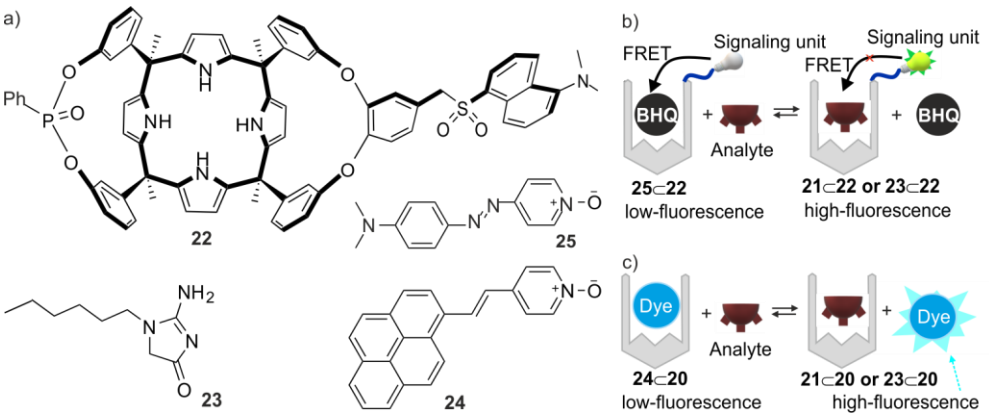

Figure 1.13. a) Line-drawing structures of receptor **22** and guests **23**-**25**. Schematic approaches to optical sensing of creatinine or hexylcreatinine (Analyte) using calix[4]pyrrole receptors **22** and **20**: b) displacement of a black-hole quencher (BHQ) **25** and deactivation of FRET quenching of a **22** appended fluorophore (signaling unit) and c) displacement of a fluorescent dye included in the receptor **20**. Reproduced with permission from ref. 40. Copyright 2020, American Chemical Society.

One of the developed IDAs consisted on the ensemble formed by the non-fluorescent receptor **20** and the fluorescent pyrene pyridine *N*-oxide indicator **24**. The fluorescence of the indicator **24** was significantly quenched upon formation of the host-guest complex **24⊂20**. In the presence of creatinine or hexylcreatinine, the indicator **24** was displaced from the complex leading to the restoration of the fluorescence emission intensity (turn-on). In another IDA, we used the fluorescent receptor **22** and the black-hole quencher (BHQ) **25**. The addition of the pyridyl *N*-oxide guest **25** to the solution of receptor **22** induced the fluorescence quenching of the dansyl group through Förster resonance energy transfer (FRET) upon formation of the **25⊂22** complex. The competitive displacement of the quencher by hexylcreatinine produced the **23⊂22** complex and induced a fluorescence turn-on. In short, the dissociation of the **25⊂22** complex inhibited the

FRET. The two photophysical strategies used for the IDAs are based on the key principle that creatinine and its derivatives are size, shape and function complementary to the cavities of the phosphonate-functionalized calix[4]pyrroles **20** and **22**. Both calix[4]pyrrole receptors were found to bind creatinine and hexylcreatinine with a 1:1 binding stoichiometry as inferred from the ^{1}H and ^{31}P NMR spectroscopy, isothermal titration calorimetry (ITC), together with UV-Vis absorption and fluorescence emission. Remarkably, the FRET-based IDA ensemble formed by the fluorescent calix[4]pyrrole **22** and the black-quencher *N*-oxide **25** displayed high selectivity and a limit of detection (LOD) of ~ 110 nM for creatinine in organic chlorinated solvents. The LOD is comparable to those of commercial diagnostic systems. This work represents unprecedented examples of synthetic fluorescent supramolecular sensors for the sensing and quantification of creatinine. We expect that our findings will inspire future work on the development of new molecular sensors and devices capable of clinical applications.

1.3.4 Molecular recognition using "four-wall" aryl-extended calix[4]pyrroles

Molecular recognition of polar substrates in water using macrocyclic synthetic receptors represents a challenging endeavor. The investigated model system and the results derived from them will provide invaluable knowledge to further understanding the remarkable properties exhibited by proteins and other biological polymers.[10,57] To gain access to water solubility, we appended ionizable or charged groups at either the upper or lower rims of tetra-α aryl-extended calix[4]pyrroles. In 2019, our group firstly reported two examples of water-soluble aryl-extended calix[4]pyrroles by covalently introducing four ionizable groups, carboxylic acids in the case of **26** and amino groups for **27**, respectively, in the *para* position of their upper rims. Binding studies revealed the formation of high affinity (*ca.* 2×10^4 M^{-1}) 1:1 host:guest complexes in pure water solution for both calix[4]pyrrole receptors with pyridine *N*-oxide **28**. These findings were taken as evidence that the different water-solubilizing groups did not affect the thermodynamic stabilities of the formed inclusion complexes. As inferred from both ^{1}H NMR titration studies and X-ray diffraction analyses, the oxygen atom of the bound pyridine *N*-oxide **28** established four simultaneous hydrogen bonds with the pyrrole NHs of the calix[4]pyrrole core in cone conformation. At the same time, the aromatic pyridyl unit of the bound guest interacts with the four aromatic walls of the receptor through π-π and CH-π interactions. However, for the 4-phenyl pyridine *N*-oxide **29**, the binding affinity with the tetra-carboxylate "four- wall" calix[4]pyrrole was reduced by one order of magnitude ($K_a \approx 2.0 \times 10^3$ M^{-1}). Most likely, the extra phenyl unit of **29** produced unfavorable solvation/desolvation interactions upon complex formation (Figure 1.14). Introducing water-solubilizing groups at the lower rim of aryl-extended calix[4]pyrroles is another strategy to endow these receptors with water solubility.

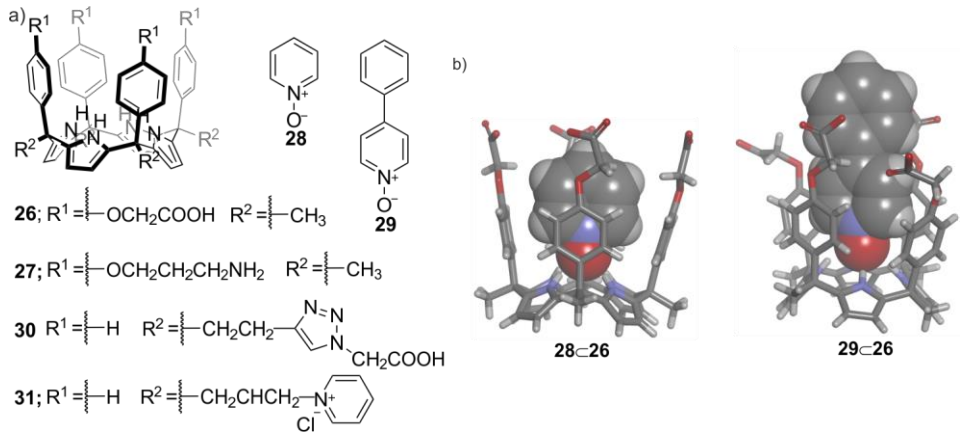

Figure 1.14. a) Line-drawing structures of water-soluble aryl-extended calix[4]pyrroles **26**, **27**, **30**, **31** and pyridine *N*-oxide guests **28** and **29**; b) energy-minimized structure (MM3) of the inclusion complexes **28**⊂**26** and **29**⊂**26**. The bound guests are shown as CPK models and receptor is displayed in stick representation.

The functionalization of the lower rim of "four-wall" aryl-extended calix[4]pyrrole with four carboxylic acid groups yielded receptor **30**. In this case, the terminal water-solubilizing groups were located far away from the binding pocket of the calix[4]pyrrole core. This feature might avoid any interference of the water-solubilizing groups with the binding process compared to the previous upper-rim substituted calix[4]pyrrole designs as **26**.[58] Although the water-solubilizing groups were located at different positions in aryl-extended calix[4]pyrrole receptors, **26** and **30**, they showed similar binding affinities for pyridine *N*-oxide **28**. This finding supported that the placement of the water-solubilizing groups at either the upper or lower rims of the aryl-extended calix[4]pyrroles produced a minimum influence on the thermodynamic stability of the formed host-guest complexes. Isothermal titration calorimetry (ITC) experiments performed in water solution demonstrated the binding of aryl-extended calix[4]pyrrole receptors with pyridine *N*-oxides was mainly driven by enthalpy. This thermodynamic signature could be translated into the "non-classical" hydrophobic effect, which emanates from the formation of complexes of synthetic receptors having a well-defined binding geometry (Figure 1.14).

We also prepared water-soluble tetra-pyridinium receptor **31**, equipped with four pyridinium cations at the lower rim of the aryl-extended calix[4]pyrrole.[59] This functionalization allowed receptor **31** to be soluble in neutral water at millimolar concentrations and different pHs. ^{1}H NMR spectroscopy studies revealed that receptor **31** was capable of selective binding the *cis*-isomers of *N*-phenyl acetamides and formamides in water with binding affinities larger than 10^{3} M^{-1}. Molecular modelling studies were used to investigate the structures of the formed complexes. Secondary and tertiary amides usually exist in solution as a mixture of *trans*- and *cis*-rotamers of the σ-bond connecting the carbonyl carbon with the nitrogen atom. Typically, the *trans*-rotamer is energetically more favorable than the *cis*-counterpart irrespectively of the amide's substituents and used

solvent. The *trans*-*cis* interconversion is slow on the NMR chemical shift time scale but fast on the human time scale, which leads to the observation of separate *trans* and *cis* proton signals in the ^{1}H NMR spectrum of the mixture. The inclusion of the *cis*-rotamer in the deep polar aromatic cavity of the water-soluble aryl-extended calix[4]pyrrole **31** was driven by a combination of hydrogen-bonding, CH-π and NH-π interactions and the hydrophobic effect. Interestingly, molecular modelling studies showed that the inclusion of *trans*-rotamer of *N*-phenyl formamide **32** was energetically less favorable due to steric clashes with the *meso*-aryl substituents. Thus, aryl-extended calix[4]pyrrole receptor **31** was able to acts as a minimal chaperone increasing the concentration of the *cis*-rotamer of formamides by means of its selective binding (Figure 1.15).

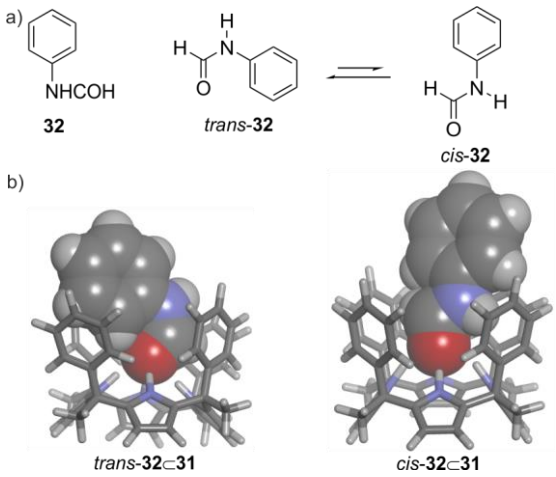

Figure 1.15. a) Line-drawing structure of **32** and the equilibrium between *trans*- and *cis*-rotamers of **32**; b) Energy-minimized structure (MM3) of the inclusion complex: *trans*-**32**⊂**31** and *cis*-**32**⊂**31.** The bound guests are shown as CPK models and receptor is displayed in stick representation. Water-solubilizing groups were pruned to methyl groups to simplify the calculation. Reproduced with permission from ref. 58. Copyright 2018, Royal Society of Chemistry.

To facilitate the applications of aryl-extended calix[4]pyrroles, a synthetic methodology involving the functionalization of both their upper and lower rims was developed by our group in 2017.[14] We used methyltributylammonium chloride as an additive to promote the formation of the tetra-*α* isomer of aryl-extended calix[4]pyrroles in a moderate yields. Using our synthetic methodology, we prepared the precursor of the water-soluble aryl-extended calix[4]pyrrole receptors, **33** and **34**, bearing two bridging phosphonate groups and two methylene bridges at their upper rims, respectively. These receptors were soluble in water owing to the attachment of four pyridinium groups at the lower rims.[60] Using ^{1}H NMR titration experiments, we demonstrated that the two calix[4]pyrrole receptors formed thermodynamically and kinetically stable 1:1 complex with the six-membered ring lactam **35** in water solution. We also estimated that the binding constant values of the complexes were larger than 10^4 M^{-1}. The bound lactam **35** was deeply included in the aromatic cavities of the receptors through the establishment of hydrogen bonding interactions between the

oxygen atom of the lactam and the pyrrole NHs of the calix[4]pyrrole unit. Multiple CH-π, NH-π interactions and the hydrophobic effect were also involved in the stabilization of the host-guest complexes (Figure 1.16).

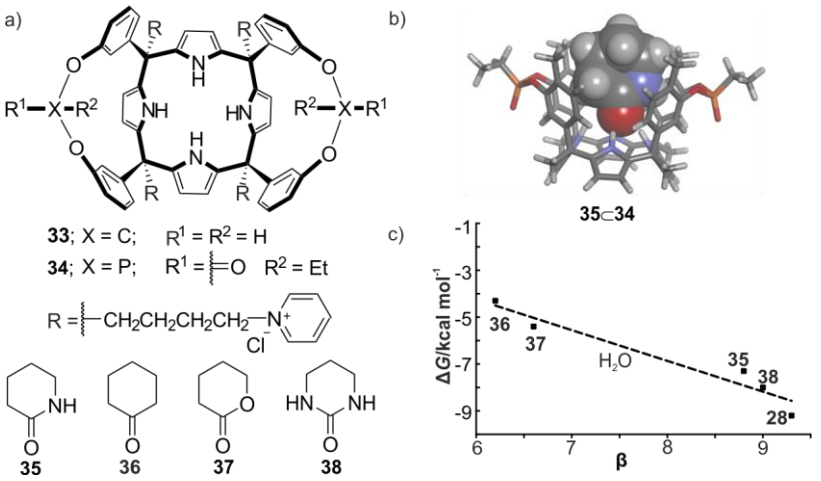

Figure 1.16. a) Line-drawing structures of aryl-extended calix[4]pyrrole receptors **33** and **34** and six-membered cyclic guests, **35**-**38**; b) energy-minimized structure (MM3) of the inclusion complex **35**⊂**34**; c) plot of Δ*G vs*. Hydrogen bonding acceptor capabilities (ß) for the inclusion complexes of the cyclic guest with receptor **34** in water. The bound guests are shown as CPK models and receptor is displayed in stick representation. Water-solubilizing groups were pruned to methyl groups to simplify the calculation.

We tried to assess the contributions of hydrogen-bonding and the hydrophobic effect to the binding process of aryl-extended calix[4]pyrrole receptors in water with a library of cyclic polar guests: lactam **35**, cyclic ketone **36**, lactone **37**, cyclic urea **38** and pyridine *N*-oxide **28**. All of the employed guests have a hydrogen-bonding accepting oxygen atom but different levels of hydrophobicity and hydrogen-bonding capability of their polar units (Figure 1.16). In striking contrast to our initial expectations, the experimental results, derived from ^{1}H NMR titration experiments, showed that aryl-extended calix[4]pyrrole receptors exhibited a higher binding affinity for the less hydrophobic guests. This finding suggested that hydrophobicity did not dominate the binding event. ITC experiments showed that the binding process of the cyclic guests was driven by enthalpy ("non-classical" hydrophobic effect). Moreover, we found the existence of a linear relationship between the binding free energies of the inclusion complexes and the hydrogen bonding accepting ability (β) of their carbonyl's oxygen atom. For instance, in water, the 1:1 complex of the calix[4]pyrrole with cyclic urea **38** featured a binding constant value that was two orders of magnitude larger than that of the less polar cyclic ketone **36** (Ka = 1.4 × 10^{3} M^{-1}). Taken together, these results suggested that the hydrogen bonding interactions had a significant contribution to the guest binding. Most likely, the aromatic cavity of the aryl-extended calix[4]pyrrole receptors precluded the solvation of the hydrogen-bonding groups (NH pyrrole) from

solvation with bulk water molecules. This shielding effect could be responsible for the observed binding enhancement assigned to the formation of hydrogen bonds in water solution.

1.4 Super aryl-extended calix[4]pyrroles

1.4.1 Molecular recognition in water using super aryl-extended calix[4]pyrroles

With the aim to further improve the binding affinity and selectivity of aryl-extended calix[4]pyrroles, *para*-ethynyl-aryl substituents were installed at their upper rims affording super aryl-extended calix[4]pyrroles. Super aryl-extended calix[4]pyrroles feature a much deeper aromatic cavity than the aryl-extended counterparts. The enlargement of the aromatic cavity was expected to deliver an enhancement of the hydrophobic effect. This was expected to be translated into a larger thermodynamic stabilization of the resulting encapsulation complexes, especially in aqueous solution.

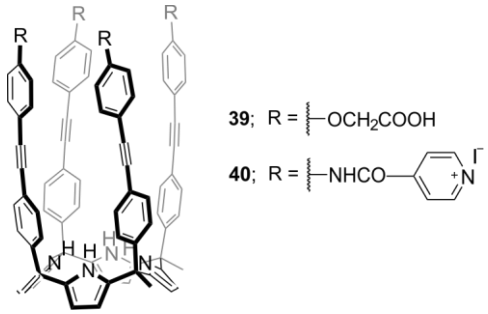

Figure 1.17. Line-drawing structures of super aryl-extended calix[4]pyrrole receptors **39** and **40**.

Initially, we attached four carboxylic acid and four pyridinium groups at the upper rim of super aryl-extended calix[4]pyrroles, **39** and **40**, respectively, in trying to gain water solubility (Figure 1.17).[57] Unfortunately, in both cases, the super aryl-extended calix[4]pyrrole derivatives formed suspensions in water at millimolar concentrations. This result indicated that bearing only four water-solubilizing groups was not enough to warrant water solubility to super aryl-extended calix[4]pyrroles.

In order to overcome this limitation, we recently disclosed the attachment of eight carboxylic acids, eight pyridinium and eight 1-methyl-1H-imidazolium ions at the periphery (upper and lower rims) of super-aryl extended calix[4]pyrrole scaffolds. In doing so, we obtained three water soluble aryl-extended calix[4]pyrrole receptors, **41**-**43**. The synthesized octa-acid super aryl-extended calix[4]pyrrole **41** was only soluble in basic water (pH ~ 10) at millimolar concentrations, owing to the ionization of the octa-acid **41** into the octa-carboxylate derivative, [**41**-8H]$^{8-}$. In contrast, the octa-pyridinium **42** and octa-imidazolium **43** super aryl-extended counterparts displayed water solubility independently of the pH of the solution. It is worth noting that the ^{1}H NMR spectra of the

two positively charged calix[4]pyrrole receptors at millimolar concentrations in D_2O at 298 K showed broad proton signals. This observation indicated the existence of aggregation processes and/or intermediate exchange dynamics on the chemical shift time scale between different conformational isomers (cone and alternate).

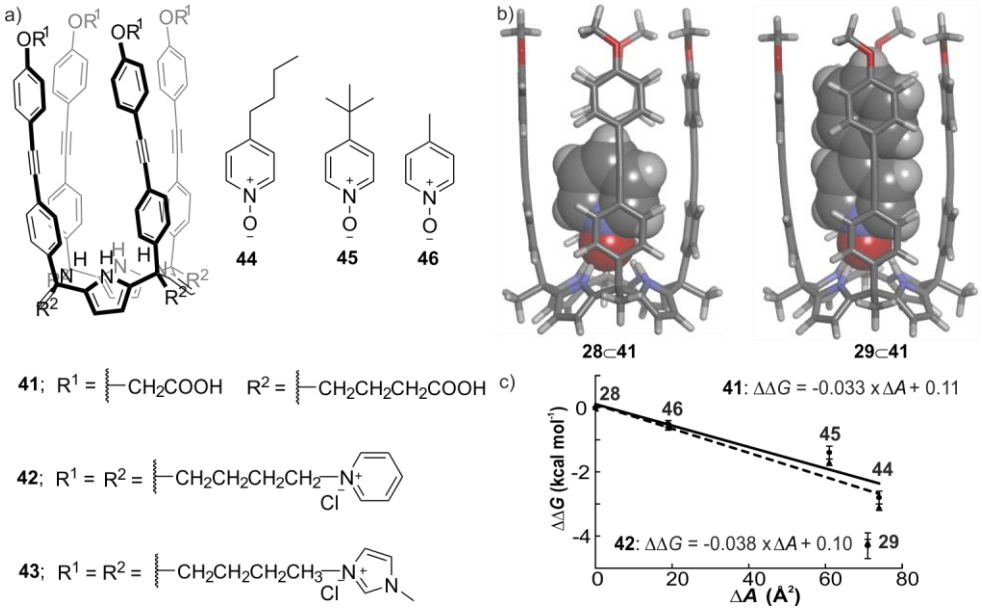

Figure 1.18. a) Line-drawing structures of water-soluble super aryl-extended calix[4]pyrrole receptors **41**-**43** and pyridine *N*-oxide guests **44**-**46**; b) energy-minimized structure (MM3) of the inclusion complexes **28**⊂**41** and **29**⊂**41**; c) difference in free energy (ΔΔ*G*) *vs*. surface area (Δ*A*) of the *para*-substituent for the complexes of the pyridyl *N*-oxide derivatives with receptors **41** and **42**. The data of the complexes of **41** and **42** are shown as circles and triangles, respectively.

Having these receptors at hand, we got interested in the quantification of hydrophobic effect using a series of pyridine *N*-oxide derivatives and both the negatively charged octa-acid **41** and the positively charged octa-pyridinium **42** super aryl-extended calix[4]pyrroles as model systems (Figure 1.18a).[15] The selected pyridine *N*-oxide guests featured different substitutions at its *para*-position: methyl, *tert*-butyl, *n*-butyl and phenyl (**29**). Not surprisingly, the two receptors formed thermodynamically and kinetically stable 1:1 complex with the *N*-oxide guest series, **44**-**46**. The binding processes were probed using ^{1}H NMR titrations and ITC experiments. Notably, a pair of complexes for a given *N*-oxide with two different calix[4]pyrrole receptors displayed similar binding constants. All binding constants were estimated to be larger than 10^5 M^{-1}. Taken together, these findings indicated that the nature of the appended water solubilizing groups in the super aryl-extended calix[4]pyrrole receptors and the pH of the solution did not have a significant effect on binding affinity. Rebek and co-workers reported similar results in the complexation of neutral guests with resorcin[4]arene cavitands.[61,62] As expected, the binding affinity of the two super aryl-

extended calix[4]pyrrole receptors for pyridine *N*-oxide increased in more than one order of magnitude with respect to those of the water-soluble aryl-extended counterparts. The enhancement in binding affinities was ascribed to the improved hydrophobic character of the deeper aromatic cavity of super aryl-extended receptors. The increase in the surface area of the *para*-substituent of the *N*-oxides was translated into a gain in free energy of binding. Most likely, the reinforced binding affinity came from the hydrophobic effect. This is related to a reduction in the water accessible surface area in the formed complex, as well as the concomitant increase in the non-polar contacts between the two binding components. The plot of the calculated free energies of binding *versus* the surface areas of the *para*-substituents of the *N*-oxides showed linear relationships (Figure 1.18c). The analyses of the plots allowed the quantification of the hydrophobic effect operating in the studied host-guest model systems. The determined energy values for the hydrophobic effect were compatible with those reported from site-directed mutagenesis of protein residues and phase transfer studies.[63,64,65] Interestingly, super aryl-extended calix[4]pyrrole receptors, **41** and **42**, displayed nanomolar dissociation constants for 4-phenyl pyridine *N*-oxide **29**, which derived from the binding of the polar *N*-oxide-pyridyl group, as well as the formation of a cluster of aromatic interactions between the non-polar *para*-phenyl residue of the guest and the aromatic groups at the upper section of the receptors' cavity.

1.4.2 Self-assembly of mono-metallic Pd(II)/Pt(II)-cages

Self-assembled supramolecular architectures constructed by synthetic ligands and metal coordination atoms have attracted growing interest as primitive mimics of enzyme able to perform functions such as molecular recognition,[13,66] catalysis,[67] sensing[68] and drug delivery.[69,70] As a subset of supramolecular coordination complexes, metal-organic cages featuring enclosed internal voids and well-defined coordination geometries have been reported in the literature. Coordination cage assemblies can accommodate size, shape and function complementary guests into their cavities. The functionalization of the organic ligands used for the assembly of the coordination cages plays an important role in the development of structurally and chemically diverse structures.

In 2019, our group reported the self-assembly of a mono-metallic cage using Pd(II) ions and the tetra-*α* isomer of super aryl-extended calix[4]pyrrole ligand, **47**, bearing four 3-pyridyl substituents at its upper rim in a 2:1 $CDCl_3/CD_3CN$ solution mixture.[17] The assembled [**47**•Pd]$^{2+}$ cage features two endohedral and converging polar binding sites that are defined by the pyrrole NHs of the calix[4]pyrrole unit and the inwardly-directed *α*-pyridyl protons, respectively. These latter protons acquired a noticeable hydrogen-bond acceptor character owing to the coordination of the pyridyl residues to the Pd(II)-metal. Single crystal X-ray diffraction data revealed that, in the solid state, ligand **47** adopted the cone conformation by binding one acetonitrile molecule through hydrogen-bonding interactions. The addition of 1 equiv. of Pd(II) to the 2:1 $CDCl_3/CD_3CN$ solution mixture containing ligand **47**, followed by thermal equilibration induced the almost quantitative assembly of [**47**•Pd]$^{2+}$ cage. Evidence for the cage formation was derived from the ^{1}H NMR spectroscopy and

X-ray analyses of a single crystal (Figure 1.19). The solid state structure of the [**47**•Pd]$^{2+}$ cage featured a cylindrical geometry. Two acetonitrile molecules were included in the aromatic cavity of the cage in opposite orientations. One acetonitrile molecule was stabilized by hydrogen bonds formation between the inner *α*-pyridyl protons and its nitrogen atom. The other was included in the calix[4]pyrrole core of the cage and formed hydrogen-bonds with the pyrrole NHs. This result demonstrated that the efficient assembly and stabilization of metallocage [**47**•Pd]$^{2+}$ required the functional complementation of the two opposite polar binding sites. Notably, when super aryl-extended ligand **47** was replaced by the aryl-extended calix[4]pyrrole ligand **48**, proton signals corresponding to ill-defined polymeric aggregates emerged in the ^{1}H NMR spectrum of the mixture with the Pd(II) salt instead of the expected diagnostic signals for the presence of the corresponding coordination cage (i.e. chemical shift changes of the *α*-pyridyl protons).

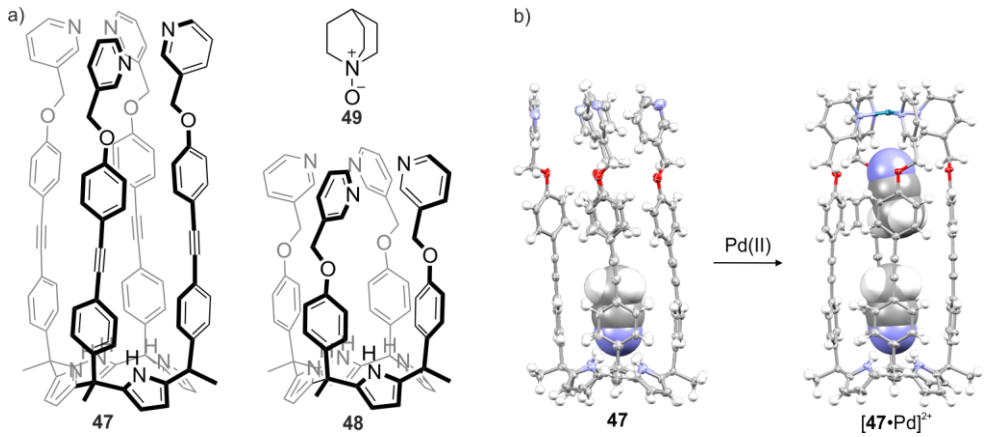

Figure 1.19. a) Line-drawing structures of aryl-extended calix[4]pyrrole receptors **47**, **48** and quinuclidine *N*-oxide **49**; b) scheme of self-assembly of [**47**•Pd]$^{2+}$ cage (X-ray structures are shown). Reproduced with permission from ref. 17. Copyright 2019, Royal Society Chemistry.

Based on the energy-minimized structures of putative complex of the coordination cage [**47**•Pd]$^{2+}$, we selected the mono- and ditopic pyridine *N*-oxide guests, **28**, **29** and **9**, to assess its assembly. Experimentally, we observed that the super aryl-extended ligand **47** and the pyridine *N*-oxide guests formed 1:1 inclusion complexes with binding constants larger than 10^4 M^{-1}. This result was consistent with previous findings in the binding of *N*-oxides with super-aryl extended calix[4]pyrroles.[57] The addition of Pd(II) salt precursor to the solution containing the 1:1 pyridine *N*-oxide **28** complex induced the almost quantitative and rapid formation of the cage **28**⊂[**47**•Pd]$^{2+}$. In this case, one acetonitrile molecule was expected to be co-encapsulated with the pyridine *N*-oxide. The acetonitrile molecule should occupy the binding site defined by the inwardly directed α-pyridyl protons of the cage, as observed in the $(CH_3CN)_2$•[**47**•Pd]$^{2+}$ complex. Indeed, the X-ray structure of a single crystal of the **28**⊂[**47**•Pd]$^{2+}$ complex confirmed the presence of the co-included acetonitrile in the cage's cavity. In contrast, 4-phenyl pyridine *N*-oxide **29** did not induce the assembly of the

metallocage to a significant extent despite the formation of stable 1:1 complex with ligand **47**. Most likely, the lack of space for the co-inclusion of acetonitrile solvent molecule into the cavity, together with reduced hydrogen-bonding complementarity offered by the 4-phenyl substituent of the *N*-oxide **29** were responsible for the unsuccessful cage assembly. Gratifyingly, the ditopic *bis*-pyridine *N*-oxide **9** was able to induced the assembly of the cage complex, **9**⊂[**47**•Pd]$^{2+}$, without the assistance of any solvent molecule. However, the reduced upfield shifted observed for the pyrrole NH protons, as well as the existence of significant disorders in the X-ray structure of **9**⊂[**47**•Pd]$(BF_4)_2$ in the cage's solution, indicated that the *bis*-pyridine *N*-oxide **9** was not capable of establishing a perfect ditopic interaction with the two distal polar binding sites of the [**47**•Pd]$^{2+}$ cage and shuttled between them (Figure 1.20a and b).

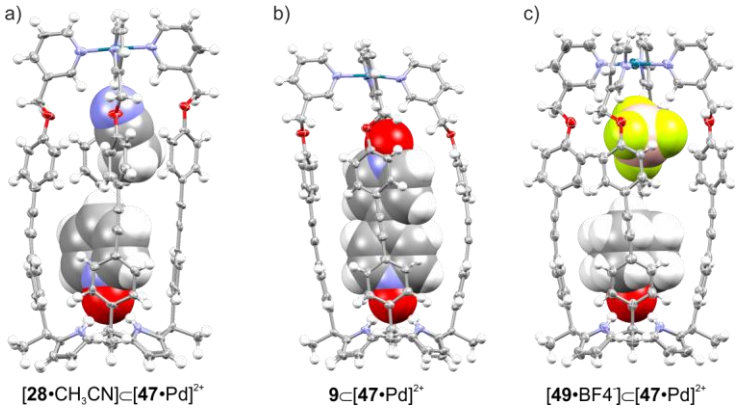

Figure 1.20. X-ray crystal structures of a) [**28**•CH_3CN]⊂[**47**•Pd]$^{2+}$; b) **9**⊂[**47**•Pd]$^{2+}$ and c) [**49**•$BF4^-$]⊂[**47**•Pd]$^{2+}$. Reproduced with permission from ref. 18. Copyright 2019, Wiley VCH.

Studies on the guest in/out exchange mechanisms operating in the assembled mono-metallic Pd(II) cages were performed by using a sterically more demanding guest, quinuclidine *N*-oxide **49** (Figure 1.19 and Figure 1.20c).[18] In contrast to the rapid and quantitative formation of the cage complexes observed for pyridine *N*-oxide **28** and bis-pyridine bis *N*-oxide **9**, the addition of 1 equiv. of quinuclidine *N*-oxide **49** to a solution of the $(CH_3CN)_2$•[**47**•Pd]$^{2+}$ cage complex produced the slow emergence of the **49**⊂[**47**•Pd]$^{2+}$ complex to a maximum of 70%, even after the equilibration of the mixture for several hours at r.t. Interestingly, guest displacement experiments performed using bis-pyridine bis *N*-oxide **9** as a competitive guest showed that the kinetics of the formation of the cage **9**⊂[**47**•Pd]$^{2+}$ complex were quite different if the pyridine-*N*-oxide complex, **28**⊂[**47**•Pd]$^{2+}$, or the quinuclidine-*N*-oxide counterpart, **49**⊂[**47**•Pd]$^{2+}$, were used as starting materials. Specifically, in the case of bound pyridine *N*-oxide **28** the formation of the competitive **9**⊂[**47**•Pd]$^{2+}$ cage complex was very quick (< 30 s). In contrast, we observed very slow kinetics in the exchange of the bis-*N*-oxide **9** for the encapsulated quinuclidine-*N*-oxide **49** in the initial cage complex. These results suggested that a "French doors" mechanism, involving the concerted rotation of the *meso*-aromatic walls of the Pd(II) cage, was operative for the entrance/exchange of the planar *N*-oxides

28 and **9**. In contrast, the exchange/entrance of the sterically more demanding quinuclidine *N*-oxide **49** may occurred through a different exchange mechanism (Figure 1.21).

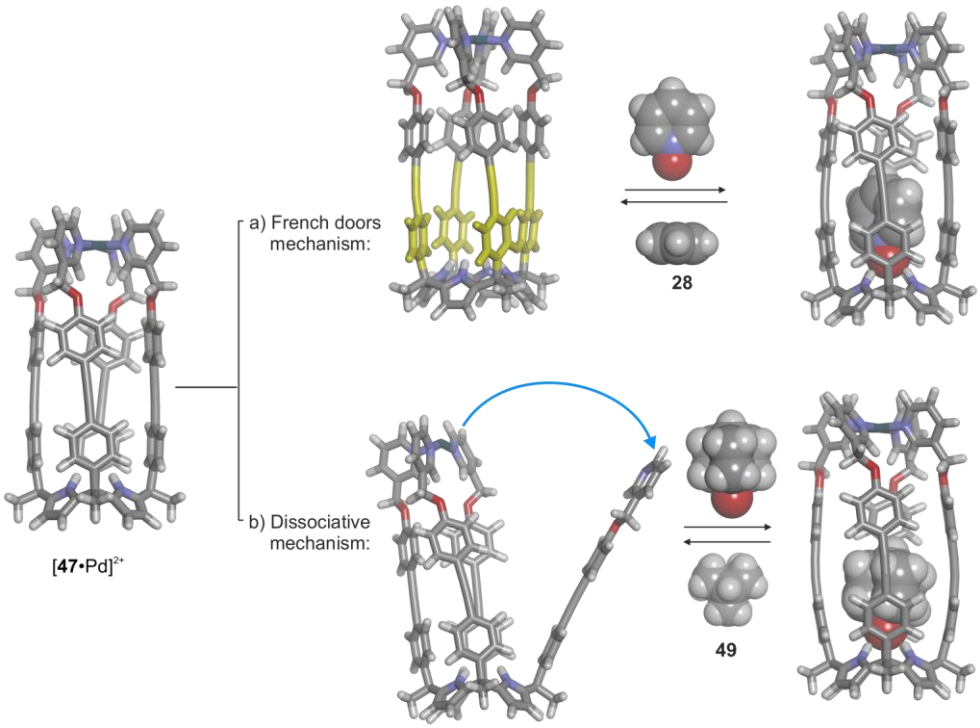

Figure 1.21. Proposed guest entrance/exchange mechanisms for the [**47**•Pd]$^{2+}$ cage: a) "French doors" and b) partial ligand-metal dissociation mechanisms. Encapsulated acetonitrile solvent molecules are omitted for clarify. The top and side views of the *N*-oxide guests **28** and **49** as CPK models are shown above and below the equilibria arrows. Reproduced with permission

To dissect the possible exchange mechanism of the quinuclidine *N*-oxide **49** in the metallocage [**47**•Pd]$^{2+}$, we assembled the structurally analogous platinum cage [**47**•Pt]$^{2+}$. At ambient conditions, the pyridyl *N*-Pt(II) bond is thermodynamically and kinetically more stable or inert than its pyridyl *N*-Pd(II) counterpart.[71,72] In short, the dissociation of a coordination bond was expected to be energetically more expensive for [**47**•Pt]$^{2+}$ cage. ^{1}H DOSY experiments and X-ray diffraction data revealed that the [**47**•Pt]$^{2+}$ cage featured the same dimension than the [**47**•Pd]$^{2+}$ counterpart. Two acetonitrile molecules were also encapsulated into the [**47**•Pt]$^{2+}$ cage's cavity to satisfy the requirement of its two opposite and polar binding sites. Notably, the addition of 1 equiv. of quinuclidine *N*-oxide **49** to the $(CH_3CN)_2$•[**47**•Pt]$^{2+}$ cage solution at millimolar concentration did not produce the characteristic signals of the **49**⊂[**47**•Pt]$^{2+}$ cage complex even after leaving the solution for 5 days at r.t. Please note that this finding contrasts with the rapid (in seconds) and quantitative formation of the corresponding pyridine *N*-oxides cage complexes, **28**⊂[**47**•Pt]$^{2+}$ and **9**⊂[**47**•Pt]$^{2+}$, under identical conditions. We attempted the assembly of the cage complex of quinuclidine-*N*-

oxide **49**⊂[**47**•Pt]$^{2+}$ starting from the parent 1:1 inclusion complex. This produced a 50:50 mixture of the targeted **49**⊂[**47**•Pt]$^{2+}$ cage complex and the $(CH_3CN)_2$•[**47**•Pt]$^{2+}$ counterpart. The subsequent competitive displacement experiment of bound **49** in the **49**⊂[**47**•Pt]$^{2+}$ cage complex, using the bis-pyridine bis *N*-oxide **9** and the previous mixture of the two cage complexes, did not induce the exclusive observation of the cage complex **9**⊂[**47**•Pt]$^{2+}$. Instead, we obtained a new mixture of cage complexes, **49**⊂[**47**•Pt]$^{2+}$ (Figure 1.20c) and **9**⊂[**47**•Pt]$^{2+}$, in an analogous 50:50 ratio. Taken together, these results indicated that the exchange of the guest in [**47**•Pt]$^{2+}$ cage operated exclusively via a "French doors" mechanism. This precluded the entrance and in/out exchange of the bulky quinuclidine *N*-oxide **49**. On the contrary, a partial metal-ligand coordination bond dissociation mechanism is operative for the [**47**•Pd]$^{2+}$cage allowing the entrance/release of the quinuclidine *N*-oxide **49**.

1.5 Conclusions

In the introduction section of this Thesis, we revised recent advances on the design and synthesis of aryl and super aryl-extended calix[4]pyrroles developed in Ballester's group. We also discussed potential applications of these scaffolds in different areas encompassing molecular recognition, sensing, self-assembly of dimeric capsules and metallocages, and also covering the facilitated transport of ions and amino acids across liposomal membranes. Aryl-extended calix[4]pyrroles feature two or four aryl groups at the *meso*-carbon positions, which are responsible for their upper rim substituents. Its *meso*-carbons can also be substituted with alkyl substituents having terminal functional groups defining the lower rim. The cone conformation of the tetra-alpha isomers of aryl-extended calix[4]pyrroles have a deep aromatic cavity closed at one end by the pyrrole NHs and opened at the opposite one. The unique structural characteristics displayed by the aryl-extended calix[4]pyrrole receptors translate into high binding affinities and superior selectivity in the binding of anions, ion pairs and biologically relevant polar guests both in organic solvents and in water.

We also reviewed examples of super aryl-extended calix[4]pyrroles bearing substituents at both their upper and lower rims. Compared to aryl-extended calix4]pyrroles, these receptors feature a much deeper aromatic cavity and increased binding affinity in water owing to the enhanced hydrophobic effect. The location of suitable substituents at the upper rims of super aryl-extended calix[4]pyrroles led to its use for the construction of self-assembled mono-metallic Pd(II)/Pt(II)-cages having two endohedral and convergent polar binding sites. The assembled metallocages are able to encapsulate polar guests and allow the reversible entrance/release of the bound guests through different exchange mechanisms depending on their steric demand. Prospective applications of aryl and super aryl-extended calix[4]pyrroles as supramolecular protecting groups, reaction vessels and drug delivery carriers are awaiting in further investigations of the properties of these interesting and unique compounds.

1.6 Aims of the thesis

The main objective of the research work of this thesis is the design and synthesis of organometallic receptors for ion-pairs, water-soluble supramolecular containers, self-assembled metallocages and metallocavitands. Most of the developed containers feature a large concave cavity with a polar interior. Our design focused on the use of aryl and super aryl-extended calix[4]pyrrole scaffolds, which are ideal candidates for the efficient selective recognition and encapsulation of polar guests in organic solvents and in water. We expected that the unique molecular recognition properties of calix[4]pyrrole derivatives could be exploited in the assembly of functionalized covalent and metal-mediated molecular containers, as well as to discover new applications in areas as diverse as catalysis, sensing and the transport of biologically relevant substrates through liposomal membranes.

Specifically, we pursued the following objectives:

O.1) **Synthesis of a "two wall" aryl-extended calix[4]pyrrole receptor bearing one gold(I) phosphine moiety at its upper rim and the study of its binding properties with tetraalkylammonium chloride salts.**

Previous reports described *α,α*-isomers of "two-wall" aryl-extended calix[4]pyrroles featuring two identical *meso*-aryl substituents at their upper rims displaying C_{2v} symmetry in organic solution. In cone conformation, these receptors feature a polar aromatic cleft suitable for the binding of tetraalkylammonium chloride salts featuring receptor-separated binding geometry. The bound Cl^- was sandwiched between the two opposing aromatic panels and established four simultaneous hydrogen bonds with the pyrrole NHs. At the same time, the cation counterpart was normally bound in the opposite shallow aromatic cavity defined by the four electron rich pyrrole rings. The introduction of substituents with different electronic nature at the upper rim would modulate the binding properties of the receptors. We envisaged that the attachment of a gold(I) phosphine moiety to one of the two *meso*-aryl substituents would affect its binding affinity towards the tetraalkylammonium chloride salts. Additionally, the intrinsic luminescence properties of the mono-gold(I) calix[4]pyrrole receptor could be used to monitor the binding process.

O.2) **Hydrolysis of difunctional symmetrical compounds in the presence of a polar super aryl-extended calix[4]pyrrole container.**

Super aryl-extended calix[4]pyrroles feature a deeper polar aromatic cavity compared to the aryl-extended analogues. Super aryl-extended calix[4]pyrroles are known to form thermodynamically and kinetically stable 1:1 complexes with a series of neutral mono- and difunctional aliphatic guests in water. Examples of synthetic molecular containers used to modulate the selectivity in desymmetrization reactions have been reported. However, reports on the use of molecular containers featuring polar cavities is scarce. In this regard, we envisaged that the water-soluble

super aryl-extended calix[4]pyrrole could serve as a sequestering and protecting group in the mono-functionalization of symmetric difunctional compounds featuring independent reacting groups. We aim at improving the selectivity and yield of the mono-reacted compounds in the hydrolysis reactions chaperoned by super aryl-extended calix[4]pyrrole containers.

O.3) **Self-assembly of water-soluble metallocages based on super aryl-extended calix[4]pyrrole scaffolds.**

We aim to prepare water-soluble coordination cages featuring functionalized polar binding sites. Our design is based on the use of super aryl-extended calix[4]pyrrole ligands bearing four pyridyl substituents at its upper rims. We envisaged that the efficient self-assembly of metallocages in water requires size and shape complementary polar guests to complement the binding requirements of assemblies' cavities. The selected guests should be included in the deep cavity of the super aryl-extended calix[4]pyrrole ligand and form stable inclusion complexes. The open end of the cavity in the pre-organized inclusion 1:1 complex will be sealed by forming multiple metal-pyridyl coordination bonds. This metal-ligands arrangement will define the second binding site of the polar interior.

O.4) **Self-assembly of metallocavitands based on super aryl-extended calix[4]pyrrole scaffolds.**

We sought to construct metallocavitands featuring molecular recognition abilities towards polar functional guests and potential properties to mediate chemical reactions and the stabilization of reactive species. Generally, depending on the nature of the ligands and metals, metal-ligand self-assembly processes yield concave and bowl-shaped metallocavitands with large aromatic cavities. In this respect, we envisaged that oxazolo[4,5-*b*]pyrazinyl substituted super aryl-extended calix[4]pyrrole could be a promising ligand for the assembly of polar metallocavitands. In analogy to the metallocage assembly, a polar guest is also required to fix the calix[4]pyrrole unit in the cone conformation and pre-organize the substituents at its upper rim for metal binding. The coordination of metal precursors to the tetra-oxazolo[4,5-*b*]pyrazinyl calix[4]pyrrole should reinforce its cone/vase conformation and provide potential applications in metal catalyzed reactions.

1.7 Outline of the thesis

The doctoral thesis is divided in five chapters: the present general introduction (chapter 1), four chapters containing a dedicated introduction, experimental results and discussion, and the corresponding experimental sections (chapters 2-5). We also include a final section summarizing the conclusions of this work.

In **Chapter 2**, we describe the synthesis of an unprecedented mono-gold(I) phosphine receptor based on a "two-wall" aryl-ethynyl extended calix[4]pyrrole. We compare the binding properties of

the parent *α,α*-bis-aryl-ethylnyl calix[4]pyrrole ligand and the prepared organometallic counterpart for the binding of the same tetraalkylammonium chloride salts in dichloromethane and acetone. ^{1}H NMR, UV-Vis titrations and ITC experiments performed in the two solvents indicated a noticeable decrease in the binding affinity of the mono-gold(I) phosphine calix[4]pyrrole for tetraalkylammonium salts compared to its parent ligand. The increase in the negative value of the electrostatic surface potential at the center of the aromatic ring of the gold(I) substituents was responsible to the observed results and the presence of chloride bound complexes.

In **Chapter 3**, we report the hydrolysis reaction of bis-isonitriles bearing different alkyl chains in the presence of a polar water-soluble super aryl-extended calix[4]pyrrole receptor. The receptor forms highly stable 1:1 complexes with the bis-isonitriles and mono-functionalized compounds, mono-isonitrile and mono-formamide. We assessed the binding constants of different complexes using ITC experiments. Based on these results we concluded that the hydrophobic effect is the main driving force. We show that the hydrolysis reaction produces mixtures of non-statistical composition and a significant decrease in the reaction rates in the presence of 1 equiv. of the receptor. The analyses of the kinetic data suggested that the observed modifications in reaction rates and selectivity are related to the efficient sequestration and protection of the reacting substrates that is exerted by the molecular containers.

In **Chapter 4**, we report the synthesis of a water-soluble tetra-α tetra-pyridyl super aryl-extended calix[4]pyrrole ligand. We describe the self-assembly of water-soluble metallocages using the tetra-pyridyl ligand and Pd(II) salts in the presence of mono- and di-topic templating guest. The ditopic guests complement the two endohedral binding sites, whereas monotopic guests only satisfy the binding characteristics of the calix[4]pyrrole unit of the metallocage. We surmised that the self-assembly of the latter cage complexes requires the co-inclusion of a water molecule to complement the distal and opposite binding site defined by the inwardly directed α-pyridyl protons. Finally, we disclose the entrance/exchange mechanism of the encapsulated guests that is operative in the complexes of the water-soluble mono-metallic Pd(II)-cages.

In **Chapter 5**, we describe the synthesis of a super aryl-extended calix[4]pyrrole receptor equipped with four oxazolo[4,5-*b*]pyrazinyl at its upper rim. We exploited this receptor as a ligand by studying the self-assembly of metallocavitand containers using mono-topic pyridyl *N*-oxides and formamide derivatives as guests. The tetra-oxazolo[4,5-*b*]pyrazinyl calix[4]pyrrole ligand can coordinate only 2 equiv. of Pd(II) metal in organic solution. The emergence of the assembled metallocavitands requires the presence of suitable guests in solution. The obtained metallocavitands feature large polar interiors and display high binding affinity and selectivity in the binding of polar guests. The obtained results augur well for the exploration of potential applications of the unprecedented metallocavitands in catalysis and molecular sensing.

1.8 References and Notes

[1] M. D. Pluth, R. G. Bergman, K. N. Raymond, *Science* **2007**, *316*, 85.

[2] D. S. Kim, J. L. Sessler, *Chem. Soc. Rev.* **2015**, *44*, 532-546.

[3] T. Iwasawa, P. Wash, C. Gibson, J. Rebek, *Tetrahedron* **2007**, *63*, 6506-6511.

[4] Y. Yu, J. Rebek, *Acc. Chem. Res.* **2018**, *51*, 3031-3040.

[5] A. B. Grommet, L. M. Lee, R. Klajn, *Acc. Chem. Res.* **2020**, *53*, 2600-2610.

[6] Y.-C. Horng, P.-S. Huang, C.-C. Hsieh, C.-H. Kuo, T.-S. Kuo, *Chem. Commun. (Cambridge, U. K.)* **2012**, *48*, 8844-8846.

[7] M. R. Kember, C. K. Williams, *J. Am. Chem. Soc.* **2012**, *134*, 15676-15679.

[8] S. Kubik, *Angew. Chem., Int. Ed.* **2009**, *48*, 1722-1725.

[9] A. P. Davis, *Chem. Soc. Rev.* **2020**, *49*, 2531-2545.

[10] L. Escobar, P. Ballester, *Chem. Rev. (Washington, DC, U. S.)* **2021**, *121*, 2445-2514.

[11] S. K. Kim, J. L. Sessler, *Acc. Chem. Res.* **2014**, *47*, 2525-2536.

[12] P. A. Gale, J. L. Sessler, V. Král, V. Lynch, *J. Am. Chem. Soc.* **1996**, *118*, 5140-5141.

[13] A. Galan, P. Ballester, *Chem. Soc. Rev.* **2016**, *45*, 1720-1737.

[14] A. Díaz-Moscoso, D. Hernández-Alonso, L. Escobar, F. A. Arroyave, P. Ballester, *Org. Lett.* **2017**, *19*, 226-229.

[15] L. Escobar, P. Ballester, *Org. Chem. Front.* **2019**, *6*, 1738-1748.

[16] Q. Sun, L. Escobar, P. Ballester, *Angew. Chem., Int. Ed.* **2021**, *60*, 10359-10365.

[17] L. Escobar, D. Villarón, E. C. Escudero-Adán, P. Ballester, *Chem. Commun. (Cambridge, U. K.)* **2019**, *55*, 604-607.

[18] L. Escobar, E. C. Escudero-Adán, P. Ballester, *Angew. Chem., Int. Ed.* **2019**, *58*, 16105-16109.

[19] L. Adriaenssens, G. Gil-Ramírez, A. Frontera, D. Quiñonero, E. C. Escudero-Adán, P. Ballester, *J. Am. Chem. Soc.* **2014**, *136*, 3208-3218.

[20] L. Adriaenssens, C. Estarellas, A. Vargas Jentzsch, M. Martinez Belmonte, S. Matile, P. Ballester, *J. Am. Chem. Soc.* **2013**, *135*, 8324-8330.

[21] Z. Lai, T. Zhao, J. L. Sessler, Q. He, *Coord. Chem. Rev.* **2020**, *425*, 213528.

[22] V. Valderrey, E. C. Escudero-Adán, P. Ballester, *J. Am. Chem. Soc.* **2012**, *134*, 10733-10736.

[23].V. Valderrey, E. C. Escudero-Adán, P. Ballester, *Angew. Chem., Int. Ed.* **2013**, *52*, 6898-6902.

[24] J. R. Romero, G. Aragay, P. Ballester, *Chem. Sci.* **2017**, *8*, 491-498.

[25] R. Molina-Muriel, G. Aragay, E. C. Escudero-Adán, P. Ballester, *J. Org. Chem.* **2018**, *83*, 13507-13514.

[26] P. Anzenbacher, K. Jursíková, V. M. Lynch, P. A. Gale, J. L. Sessler, *J. Am. Chem. Soc.* **1999**, *121*, 11020-11021.

[27] F. Biedermann, H.-J. Schneider, *Chem. Rev. (Washington, DC, U. S.)* **2016**, *116*, 5216-5300.

[28] G. Gil-Ramírez, E. C. Escudero-Adán, J. Benet-Buchholz, P. Ballester, *Angew. Chem., Int. Ed.* **2008**, *47*, 4114-4118.

[29] P. Ballester, *Acc. Chem. Res.* **2013**, *46*, 874-884.

[30] L. Adriaenssens, P. Ballester, *Chem. Soc. Rev.* **2013**, *42*, 3261-3277.

[31] P. Ballester, *Chem. Soc. Rev.* **2010**, *39*, 3810-3830.

[32] P. Ballester, G. Gil-Ramírez, *Proc. Natl. Acad. Sci. U. S. A.* **2009**, *106*, 10455.

[33] L. Osorio-Planes, M. Espelt, M. A. Pericàs, P. Ballester, *Chem. Sci.* **2014**, *5*, 4260-4264.

[34] A. Galán, V. Valderrey, P. Ballester, *Chem. Sci.* **2015**, *6*, 6325-6333.

[35] A. Galán, E. C. Escudero-Adán, P. Ballester, *Chem. Sci.* **2017**, *8*, 7746-7750.

[36] M. Chas, P. Ballester, *Chem. Sci.* **2012**, *3*, 186-191.

[37] L. Martínez-Crespo, J. L. Sun-Wang, P. Ferreira, C. F. M. Mirabella, G. Aragay, P. Ballester, *Chem.--Eur. J.* **2019**, *25*, 4775-4781.

[38] L. Martinez-Crespo, J. Liang Sun-Wang, A. Felipe Sierra, G. Aragay, E. Errasti-Murugarren, P. Bartoccioni, M. Palacin, P. Ballester, *Chem* **2020**, *6*, 3054-3070.

[39] T. Guinovart, D. Hernández-Alonso, L. Adriaenssens, P. Blondeau, M. Martínez-Belmonte, F. X. Rius, F. J. Andrade, P. Ballester, *Angew. Chem., Int. Ed.* **2016**, *55*, 2435-2440.

[40] A. F. Sierra, D. Hernández-Alonso, M. A. Romero, J. A. González-Delgado, U. Pischel, P. Ballester, *J. Am. Chem. Soc.* **2020**, *142*, 4276-4284.

[41] K. D. Shimizu, J. Rebek, *Proc. Natl. Acad. Sci. U. S. A.* **1995**, *92*, 12403.

[42] O. Mogck, V. Böhmer, W. Vogt, *Tetrahedron* **1996**, *52*, 8489-8496.

[43] M. Chas, G. Gil-Ramírez, E. C. Escudero-Adán, J. Benet-Buchholz, P. Ballester, *Org. Lett.* **2010**, *12*, 1740-1743.

[44] A. Asadi, D. Ajami, J. Rebek, *Chem. Commun. (Cambridge, U. K.)* **2014**, *50*, 533-535.

[45] D. C. Gadsby, *Nat. Rev. Mol. Cell Biol.* **2009**, *10*, 344-352.

[46] C. A. Hübner, T. J. Jentsch, *Hum. Mol. Genet.* **2002**, *11*, 2435-2445.

[47] M. P. Anderson, R. J. Gregory, S. Thompson, D. W. Souza, S. Paul, R. C. Mulligan, A. E. Smith, M. J. Welsh, *Science* **1991**, *253*, 202.

[48] D. Torrents, J. Mykkänen, M. Pineda, L. Feliubadaló, R. Estévez, R. d. Cid, P. Sanjurjo, A. Zorzano, V. Nunes, K. Huoponen, A. Reinikainen, O. Simell, M.-L. Savontaus, P. Aula, M. Palacín, *Nat. Genet.* **1999**, *21*, 293-296.

[49] C. C. Tong, R. Quesada, J. L. Sessler, P. A. Gale, *Chem. Commun. (Cambridge, U. K.)* **2008**, 6321-6323.

[50] M. G. Fisher, P. A. Gale, J. R. Hiscock, M. B. Hursthouse, M. E. Light, F. P. Schmidtchen, C. C. Tong, *Chem. Commun. (Cambridge, U. K.)* **2009**, 3017-3019.

[51] M. Yano, C. C. Tong, M. E. Light, F. P. Schmidtchen, P. A. Gale, *Org. Biomol. Chem.* **2010**, *8*, 4356-4363.

[52] The HPTS assay was used to measure the rate of pH-gradient dissipation and evaluate the anion-transport activity of synthetic carriers by monitoring the fluorescent changes of the entrapped pH-sensitive dye.

[53] N. Sahu, D. Dela Cruz, M. Gao, W. Sandoval, Peter M. Haverty, J. Liu, J.-P. Stephan, B. Haley, M. Classon, G. Hatzivassiliou, J. Settleman, *Cell Metab.* **2016**, *24*, 753-761.

[54] R. Cánovas, M. Cuartero, G. A. Crespo, *Biosens. Bioelectron.* **2019**, *130*, 110-124.

[55] S. Peng, Q. He, G. I. Vargas-Zúñiga, L. Qin, I. Hwang, S. K. Kim, N. J. Heo, C.-H. Lee, R. Dutta, J. L. Sessler, *Chem. Soc. Rev.* **2020**, *49*, 865-907.

[56] A. C. Sedgwick, J. T. Brewster, T. Wu, X. Feng, S. D. Bull, X. Qian, J. L. Sessler, T. D. James, E. V. Anslyn, X. Sun, *Chem. Soc. Rev.* **2021**, *50*, 9-38.

[57] L. Escobar, G. Aragay, P. Ballester, *Chem.--Eur. J.* **2016**, *22*, 13682-13689.

[58] D. Hernández-Alonso, S. Zankowski, L. Adriaenssens, P. Ballester, *Org. Biomol. Chem.* **2015**, *13*, 1022-1029.

[59] L. Escobar, A. Díaz-Moscoso, P. Ballester, *Chem. Sci.* **2018**, *9*, 7186-7192.

[60] G. Peñuelas-Haro, P. Ballester, *Chem. Sci.* **2019**, *10*, 2413-2423.

[61] C. H. Haas, S. M. Biros, J. J. Rebek, *Chem. Commun. (Cambridge, U. K.)* **2005**, 6044-6045.

[62] S. M. Biros, J. Rebek, *Chem. Soc. Rev.* **2007**, *36*, 93-104.

[63] K. N. Houk, A. G. Leach, S. P. Kim, X. Zhang, *Angew. Chem., Int. Ed.* **2003**, *42*, 4872-4897.

[64] Y. Nozaki, C. Tanford, *J. Biol. Chem.* **1971**, *246*, 2211-2217.

[65] S. Damodaran, K. B. Song, *J. Biol. Chem.* **1986**, *261*, 7220-7222.

[66] A. J. McConnell, C. S. Wood, P. P. Neelakandan, J. R. Nitschke, *Chem. Rev. (Washington, DC, U. S.)* **2015**, *115*, 7729-7793.

[67] C. J. Brown, F. D. Toste, R. G. Bergman, K. N. Raymond, *Chem. Rev. (Washington, DC, U. S.)* **2015**, *115*, 3012-3035.

[68] M. Han, D. M. Engelhard, G. H. Clever, *Chem. Soc. Rev.* **2014**, *43*, 1848-1860.

[69] T. R. Cook, P. J. Stang, *Chem. Rev. (Washington, DC, U. S.)* **2015**, *115*, 7001-7045.

[70] Y. Sun, C. Chen, J. Liu, P. J. Stang, *Chem. Soc. Rev.* **2020**, *49*, 3889-3919.

[71] M. Fujita, M. Tominaga, A. Hori, B. Therrien, *Acc. Chem. Res.* **2005**, *38*, 369-378.

[72] A. Baba, T. Kojima, S. Hiraoka, *J. Am. Chem. Soc.* **2015**, *137*, 7664-7667.

UNIVERSITAT ROVIRA I VIRGILI
ARYL AND SUPER ARYL-EXTENDED CALIX[4]PYRROLES: SYNTHESIS AND APPLICATIONS
Qingqing Sun

Chapter 2

Influence of the Attachment of a Gold(I) Phosphine Moiety at the Upper Rim of a Calix[4]pyrrole on the Binding of Tetraalkylammonium Chloride Salts

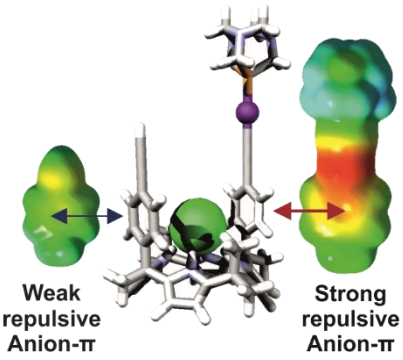

Part of this chapter has been published in:

Q. Sun, G. Aragay, A. Pinto, E. Aguiló, L. Rodríguez, P. Ballester, *Chem.--Eur. J.* **2020**, *26*, 3348-3357.

UNIVERSITAT ROVIRA I VIRGILI
ARYL AND SUPER ARYL-EXTENDED CALIX[4]PYRROLES: SYNTHESIS AND APPLICATIONS
Qingqing Sun

2.1 Introduction

Calix[4]pyrroles are macrocyclic compounds consisting of four pyrrole units linked through their 2 and 5 positions via four tetra-substituted sp^3 hybridized *meso* carbon atoms.[1,2] In non-polar solvents, calix[4]pyrroles exist in solution as alternate conformations. Remarkably, they are known to undergo a conformational change from alternate to cone conformation upon anion binding. However, in solid state, examples of bound calix[4]pyrroles with neutral polar substrates demonstrated that non-cone conformations are also possible.[3,4] The introduction of two aryl groups in opposed *meso*-carbons renders the so-called "two wall" calix[4]pyrrole as two possible constitutional isomers (Figure 2.1) [4,5,6,7,8] In cone conformation, the α,α-isomer displays a polar aromatic cleft ideal for the binding of mono-atomic spherical anions *i.e.* chloride. The anion establishes four simultaneous hydrogen bonds with the pyrrole NHs and it is sandwiched between the opposing *meso*-aryl substituents, which are oriented in a parallel arrangement. Calix[4]pyrroles are known to function as heteroditopic receptors for ion-pairs, especially in non-polar solvents like chloroform ($CHCl_3$) or dichloromethane (CH_2Cl_2).[9,10,11,12,13,14] Normally, the cation prefers to bind opposite to the anion. That is, it is partially included in the shallow and electron rich aromatic cavity defined by the four-pyrrole rings in the cone conformation that is opposite the bound anion. This type of binding geometry of the ion-paired complex is referred as a receptor-separated binding mode. Alternatively, the cation might be located on top of the anion resulting in an ion-paired complex with close-contact binding mode.[10] In more polar organic solvents, like acetone or acetonitrile,[15,16] the influence of the cation in the binding process is reduced owing to the partial dissociation of the salt ion-pair and the resulting ion-paired complexes.

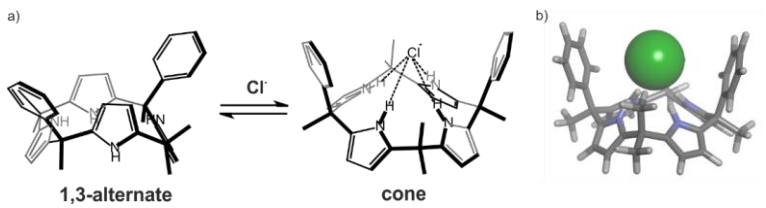

Figure 2.1. a) Binding equilibrium between the 1,3-alternate conformational isomer of a free "two-wall" aryl-extended calix[4]pyrrole and the corresponding 1:1 complex with Cl^- in cone conformation. b) Energy minimized (MM3) structure of the chloride complex. The receptor is shown in stick representation and the chloride as CPK model.

The introduction of electron withdrawing and electron donating groups on the *para* and *meta* positions of the *meso*-aryl substituents (upper rim) of "two wall" α,α-calix[4]pyrroles modulates their binding affinity towards anions.[5] Specifically, we described that anion binding with aryl-extended calix[4]pyrroles decreases with the increase in the number and electron-donating character of the aromatic substituents. This effect was attributed to an increase in the negative value of the electrostatic surface potential (ESP) at the centroid of the aryl substituent resulting in more repulsive anion-π interactions.[5]

To the best of our knowledge, all described "two wall" α,α-calix[4]pyrrole receptors display C_{2v} symmetry, that is, their two *meso*-aryl substituents are identical. Likewise, the introduction of organometallic moieties in the *meso*-aryl substituents of these receptors remains unexplored.

In particular, the introduction of gold(I) alkynyl substituents in the *meso*-aryl groups would provide intrinsic luminescence properties to the receptors and their complexes.[17] In this sense, calix[4]arene receptors modified with alkynyl gold derivatives showed changes in their optical properties upon cation binding.[18,19,20] In addition, this type of substituents endow the supramolecular receptors with the possibility to be involved in weak aurophilic interactions (Au···Au).[21,22]

Herein, we describe the synthesis of the "two-wall" α,α-isomer aryl-extended calix[4]pyrrole **1** (Scheme 2.1) bearing one gold(I) alkynyl substituent in the *para*-position of only one of the two *meso*-aryl substituents. We also describe the unusual binding properties of the mono-gold(I) alkynyl derivative **1** in DCM and acetone solutions towards tetraalkylammonium chloride salts. As could be expected, calix[4]pyrrole **1** acts as an excellent heteroditopic receptor in DCM solution, displaying an impressive selectivity for the binding of methyl-tri-octyl ammonium chloride (MTOACl) in comparison to tetra-butyl ammonium chloride (TBACl). It is noteworthy that previous reports of tetraalkylammonium ion-pairs binding with heteroditopic calix[4]pyrrole receptors already demonstrated a large increase in the binding affinity of the salts featuring at least one methyl substituent in the organic cation. This observation was attributed to the superior fit of the methyl group in the shallow aromatic cavity opposite to the bound anion.[12,23]

In acetone solution, owing to the partial dissociation of the ion-pairs the binding selectivity of **1** seems to level off. However, in both solvents, the resulting 1:1 fully ion-paired complex (DCM) or partially dissociated ion-paired complex (acetone) feature the bound-host in two different geometries/conformations as inferred by the observation of two sets of separate proton signals in their proton NMR spectra. Remarkably, the results of Isothermal Titration Calorimetry (ITC) experiments, performed in acetone solution for the two receptors and tetraalkylammonium salts, fit nicely to a simple 1:1 binding model not taking into account ion-pairing processes. The derived apparent binding constant values and the results of DFT calculations provide support for the existence of the stronger repulsive chloride-π interactions in the chloride complex of the organometallic receptor **1**, which might also explain its existence in solution as a mixture of two conformers. Noteworthy, our recent studies, after the publication, showed that the organometallic receptor **1** evolved over time in solution and produced multiple sets of signals. This findings demonstarted that our previous hypothesis was not fully considered.

2.2 Results and Discussion

2.2.1 Synthesis

The synthesis of the gold(I) phosphine calix[4]pyrrole receptor **1** was carried out starting from 10α,20α-bis(4-[ethynylphenyl])calix[4]pyrrole **2** as precursor ligand. Compound **2** was prepared following a reported literature procedure.[24,25] The bis-alkynyl calix[4]pyrrole **2** was deprotonated by suspending it in a KOH methanol solution. DCM was added to the above suspension in order to obtain a solution. Next, a DCM solution of the AuClPTA precursor complex **3** (PTA = 1,3,5-triaza-7-phosphaadamantane)[26] was added dropwise. After two hours of stirring, the reaction mixture was partially concentrated and hexane was added to induce the precipitation of a pale yellow solid. The mono-gold(I) aryl-ethynyl phosphine derivative **1** was isolated in moderate yield (60%) after precipitation of the solid from DCM/hexane mixture (Scheme 2.1). Compound **1** was fully characterized by a complete set of high-resolution spectra (Scheme 2.1).

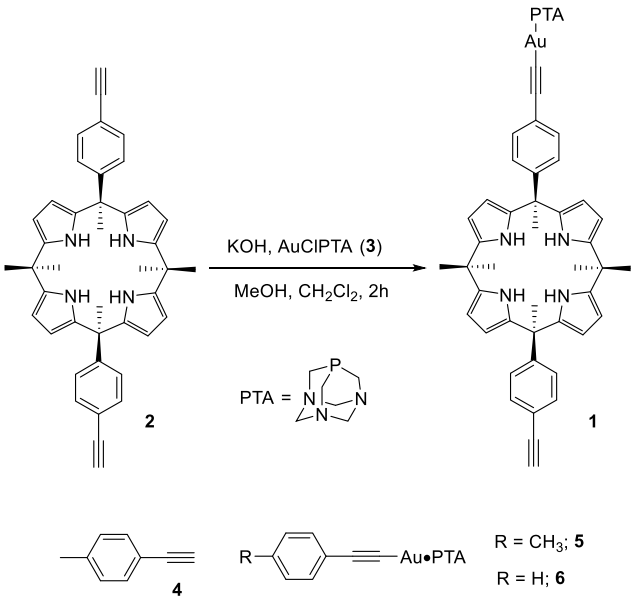

Scheme 2.1. Synthesis of the mono-gold(I) phosphine calix[4]pyrrole derivative **1**. The molecular structure of the parent compound **2**, the gold(I) salt precursor **3** and the model systems **4**, **5** and **6** are shown.

2.2.2 Photophysical characterizations

The absorption and emission (λ_{exc} = 300 nm) spectra of the mono-gold(I) phosphine calix[4]pyrrole **1** and the bis-aryl-ethynyl parent ligand **2** were recorded in DCM solution (10 μM) (Figure 2.2). The most relevant absorption and emission bands are detailed in Table 2.1.

Excitation at 300 nm of a DCM solution of **1** resulted in two weak emission bands with maxima at *ca.* 370 nm and 465 nm. The bands were assigned to fluorescence and phosphorescence ^{3}IL transitions, respectively. The increase of intensity of the lowest energy emission band upon oxygen removal supports the phosphorescence ^{3}IL emission assignment. On the other hand, no significant emission was detected for a solution of **2** in the same solvent neither at room temperature nor at 77 K.

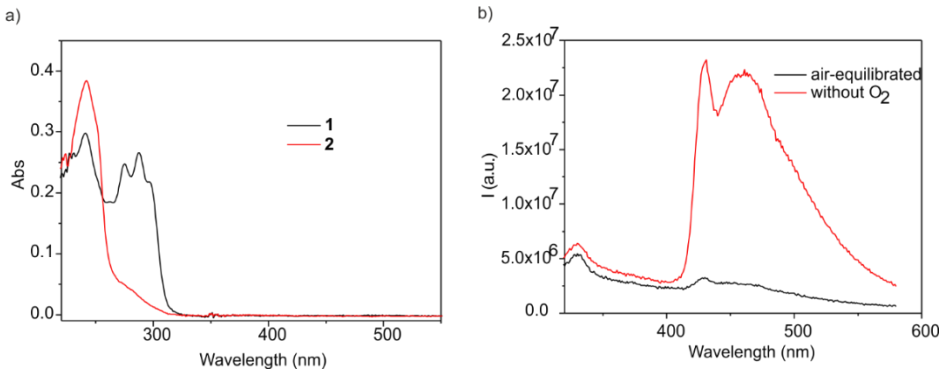

Figure 2.2. a) Absorption spectra of a 10 μM DCM solution of **1** and **2** in DCM; b) Emission (λ_{exc} = 300 nm) spectra of a 10 μM DCM solution of **1** in the presence (black line) and absence (red line) of O_2.

This result is a nice example on how heavy-atom-induced spin-orbital coupling effects can induce luminescence of non-emissive chromophores,[27,28] in particular, from metal-perturbed π-π* excited states localized on aryl-ethynyl ligands through fast population of the triplet state by intersystem crossing.[29,22]

Table 2.1. Absorption (λ_{max} (nm), (ε 10^{-3} (M^{-1} cm^{-1})) and emission (solution, λ_{max} (nm)) data of compounds **1** and **2** in 1·× 10^{-5} M dichloromethane solution at 298 K and 77 K (λ_{exc} = 300 nm). Fluo and Phos refer to fluorescence and phosphorescence emission bands, respectively.

Compound	Absorption	Emission	
		298 K	77 K
2	243 (38.1), 253sh (27.8), 280 (4.15)		
1	243 (29.11), 253sh (22.06), 274 (24.80), 288 (26.52), 299 (21.54)	339, 370 (Fluo) 430, 465 (Phos)	430, 470

2.2.3 Binding studies of receptor **2** with tetraalkylammonium chloride salts

^{1}H NMR binding studies in DCM solution

First, we probed the interaction of the parent bis-aryl-ethynyl calix[4]pyrrole receptor **2** with TBACl and MTOACl in DCM solution using ^{1}H NMR spectroscopy. The ^{1}H NMR spectrum of **2** in DCM (~ 1 mM) showed sharp and well-resolved proton signals in agreement with a C_{2v} symmetry. The incremental addition of TBACl (0.1-12 equiv) to the above solution induced chemical shift changes on some of the proton signals of **2** (Figure 2.3 left panel and Experimental Section). This observation indicated that the binding process with the ion-pair experienced fast exchange dynamics on the chemical shift time scale.

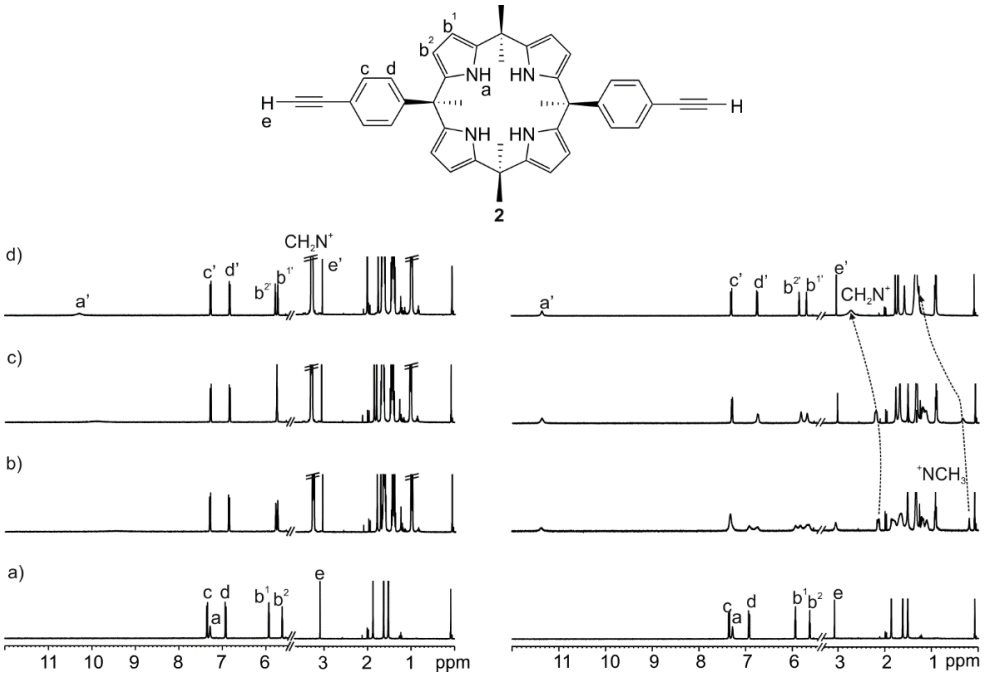

Figure 2.3. Left panel) ^{1}H NMR spectra acquired during the titration of **2** (1 mM) with incremental amounts of TBACl in DCM solution: a) 0; b) 3.0 c) 5.0 and d) 10 equiv. Right panel) ^{1}H NMR spectra acquired during the titration of **2** (1mM) with incremental amounts of MTOACl in DCM solution: a) 0; b) 0.5; c) 1.0 and d) 2.0 equiv. See top panel for proton assignment. Primed signals correspond to protons in bound **2**.

The NH proton signal of **2** moved downfield ($\Delta\delta$ ~ + 3.0 ppm) suggesting its involvement in hydrogen-bonding interactions with the chloride. The aromatic proton signals shifted slightly upfield ($\Delta\delta$ ~ - 0.1 ppm) in response to the chloride-π interactions established in the complex Cl⊂**2**•TBA. One of the *β*-pyrrole protons moved upfield and the other downfield. These chemical shift changes are diagnostic that chloride binding is concomitant with a change in receptor's conformation from alternate, in the free state, to cone, in the bound receptor (Figure 2.1). Finally, the methylene

proton alpha to the nitrogen atom of the TBA cation shifted downfield as its concentration was increased. This behavior supports the involvement of the TBA cation in the ion-paired complex formed in solution, Cl⊂**2**•TBA, featuring a receptor separated binding mode.

The TBA cation binds opposite to the anion in the electron-rich aromatic cavity defined by the pyrrole ring in the cone conformation. In this location, it experiences the shielding effect of the pyrrole rings and resonates slightly upfield ($\Delta\delta$ ~ - 0.12 ppm when 0.1 equiv are added) with respect to the chemical shift value of the TBA in the TBACl ion-pair (δ = 3.3 ppm). As the concentration of TBACl is increased, the amount of TBA in the free ion-pair, TBACl, also increases with respect to that bound in the ion-paired complex, Cl⊂**2**•TBA. This produces that the signal of the TBA methylene protons moves towards δ = 3.3 ppm owing to the fast chemical exchange regime that is operative for the equilibrium between the TBA cation in the salt ion-pair, TBACl, and ion-paired complex, Cl⊂**2**•TBA. The partial formation of the Cl⊂**2**•TBA complex in an equimolar mixture of the binding partners at a concentration suitable to acquire the ^{1}H NMR spectrum (~ 1 mM) allowed us to estimate that the binding constant of Cl⊂**2**•TBA complex considering a 1:1 stoichiometry must be lower than 10^4 M^{-1}. The fit of the chemical shift changes experienced by the β-pyrrole proton signals during the titration to a theoretical 1:1 binding model was good and afforded a more accurate value for the binding constant as K(Cl⊂**2**•TBA) = 2.7 × 10^2 M^{-1} (Figure 2.4).

The analogous ^{1}H NMR titration of receptor **2** with MTOACl provided significant different results (Figure 2.3, right panel). Thus, the addition of 0.5 equiv of MTOACl produced broadening of some signals of the receptor, as well as the observation of two sets of separate signals of equal intensity for others. One of the two sets corresponded to the free receptor, while the new one was assigned to the protons in bound **2**. In the presence of 1 equiv of MTOACl only the set of signals corresponding to bound **2** was detected. The addition of more than 1 equiv of the ion-pair salt induced the sharpening of the signals of the receptor but it did not produce any chemical shift changes. Taken together, these observations indicate that **2** and MTOACl formed a 1:1 ion-paired complex, Cl⊂**2**•MTOA, displaying slow/intermediate exchange dynamics on the chemical shift timescale between the free and bound receptor. We can also estimate that the binding constant value for the 1:1 complex K(Cl⊂**2**•MTOA) is larger than 10^4 M^{-1}, owing to its almost quantitative formation in an equimolar mixture of the binding partners at millimolar concentration. In analogy to the TBA cation, the MTOA cation must be also located in the electron- rich and shallow cavity defined by the pyrrole rings of bound **2**. The methyl group, *alpha* to the nitrogen atom of the MTOA cation, resonates highly upfield shifted (δ = 0.19 ppm) owing to its deeper inclusion in the aromatic cavity, where it experiences the strong shielding effect caused by the four aromatic pyrrole rings. The methylene groups *alpha* to the nitrogen atom of the MTOA cation are more exposed and affected to a lesser extent. We also assigned a separated receptor binding geometry to the Cl⊂**2**•MTOA complex. When more than 1 equiv of MTOACl is added, the signals of the methyl and

methylene protons *alpha* to the nitrogen start moving downfield. This dynamic behavior derives from fast chemical exchange process that exist between the MTOA cation in free and bound ion-pairs, MTOACl and Cl⊂**2**•MTOA, respectively.

The increase in affinity constant for the Cl⊂**2**•MTOA complex (estimated as > 10^4 M^{-1}) compared to that of the Cl⊂**2**•TBA counterpart (K(Cl⊂**2**•TBA) = 2.7 × 10^2 M^{-1}) supports that receptor **2** is acting as a heteroditopic receptor in DCM solution. The superior fit of the methyl group of the MTOA cation in the aromatic cavity opposed to the bound chloride is mainly responsible for the observed selectivity.

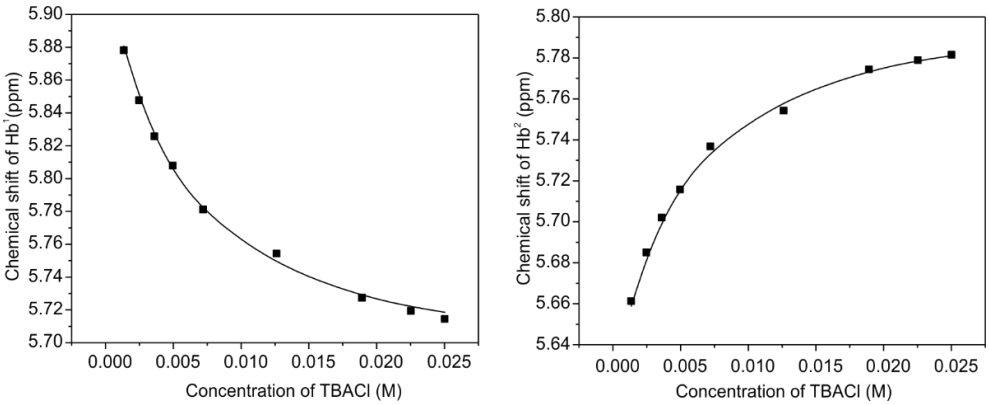

Figure 2.4. Chemical shift of proton signals Hb^1 (right panel) and Hb^2 (left panel) of **2**) upon incremental amounts of TBACl (circles) and fit of the titration data to a theoretical 1:1 binding model (solid line) using HypNMR software.

UV-Vis titrations in DCM solution

To determine an accurate value for the binding constant of the Cl⊂**2**•MTOA complex, we also probed the binding process using UV-Vis spectroscopy titrations ([**2**] = 20 μM). We observed a non-monotonic behavior for the absorbance changes at most wavelengths (Figure 2.5). For example, at the maximum of the band centered at 242 nm, the absorbance intensity decreased until the addition of 6.4 equiv and started to increase when more equivalents of the salt were added. This biphasic behavior suggested the co-existence in solution, at this lower concentration, of the anionic chloride complex [Cl⊂**2**]$^-$ and the ion-paired counterpart Cl⊂**2**•MTOA in significant extents. Flood and co-workers analyzed ^{1}H NMR titration data of a triazolophane receptor with TBACl in DCM solution, displaying fast chemical exchange on the chemical shift time scale, as well as the corresponding UV-Vis data using an elaborated binding model.[30]

We applied a closely related binding model, which considers the ion-pairing of the MTOACl salt (K_{ip}), the formation of the 1:1 chloride anionic complex, [Cl⊂**2**]$^-$, ($K_{1:1}$), and its subsequent ion-pairing to yield the ternary complex Cl⊂**2**•MTOA ($K_{1:1ip}$), to perform the mathematical analysis of the UV-Vis titration using the HypSpec software.[31] It is worth to note that the unrestricted factor

analysis in HypSpec of the UV-Vis titration data already revealed three mathematically significant light absorbing species. During the fit, we fixed the value of the ion-pairing of the MTOACl salt as K_{ip} = 3.0 × 10^4 M^{-1}.[30] We manually optimized the values of *K*([Cl⊂**2**]$^-$) and *K*(Cl⊂**2**•MTOA). The returned values for the best fit, which also provided sensible UV-Vis spectra for [Cl⊂**2**]$^-$ and Cl⊂**2**•MTOA, were *K*([Cl⊂**2**]$^-$) = 6.3 × 10^4 M^{-1} and *K*(Cl⊂**2**•MTOA) = 6.3 × 10^8 M^{-2}. Based on Fuoss's law,[32] as well as in previous results reported by Flood and co-workers, the equilibrium constant of complex ion-pairing constant *K*([Cl⊂**2**]$^-$ ‹-› Cl⊂**2**•MTOA) should be smaller than the K_{ip} of the MTOACl salt. Based on the values returned from the fit, we calculated *K*([Cl⊂**2**]$^-$ ‹-› Cl⊂**2**•MTOA) = 1.0 × 10^4 M^{-1}. The value is in agreement with our expectations, thus providing some indication of the quality and fit of the data analysis. If the Cl⊂**2**•MTOA complex is considered to have a 1:1 stoichiometry, its apparent average binding constant can be estimated as *K*(Cl⊂**2**•MTOA) = (6.3 × 10^8 M^{-2})$^{1/2}$ = 2.5 × 10^4 M^{-1}. In doing so, we can determine that the Cl⊂**2**•MTOA complex is two orders of magnitude more stable than the Cl⊂**2**•TBA analogue.

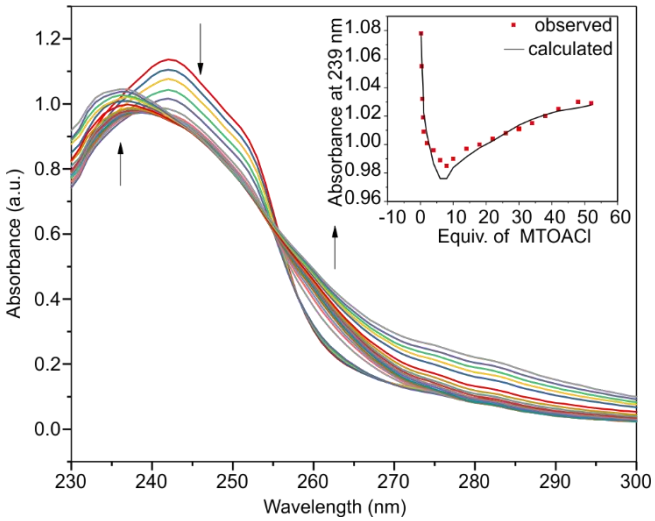

Figure 2.5. UV-Vis spectra acquired for the titration of **2** (20μM) with MTOACl (0-52 equiv) in DCM solution. Inset: Fit of the titration data to the extended binding model at 239 nm. The biphasic behaviour of the titration data is nicely reproduced by the extended binding model (see text for details).

The analogous titration of **2** with incremental amounts of TBACl lead to a steady diminution of absorbance. Even after the addition of 32 equiv of the salt, we did not reach the saturation point. We concluded that the observed spectral changes were not suitable for further mathematical analysis of the binding process. Most likely, at this concentration ([**2**] = 20 μM) the extent at which the complexes (anionic and ion-paired) are formed in solution is low and the absorbance changes might be mainly related to the increase of the dielectric constant of the media. Taken together, the results of the UV-Vis titrations support that at μM concentrations the anionic complex [Cl⊂**2**]$^-$ is present at very low concentrations and the ion-paired counterpart, independently of the cation, is

the almost exclusive complex formed in solution. This finding is a direct consequence of the fact that the values of the ion-pairing constant in DCM for the salt and complexes are larger than 10^4 M^{-1}.

ITC titration in DCM solution

The binding of MTOACl with receptor **2** in DCM was also investigated by isothermal titration calorimetry (ITC). Noteworthy, the resulting binding isotherm showed a single sigmoidal behavior that nicely fit to a simple 1:1 binding model (see Experimental Section). The determined apparent binding constant was K(Cl⊂**2**•MTOA) = 6.0±0.5 × 10^4 M^{-1}, which is in the same order of magnitude to the one estimated for the formation of the complex in a single step from the UV-Vis titration (*vide supra*). The binding of chloride to receptor **2** is enthalpically driven and highly exothermic, as might be expected for a binding process taking place in a non-polar solvent.

2.2.4 Binding studies of receptor **1** with tetraalkylammonium chloride salts

Having clarified the binding properties of the parent ligand **2** towards MTOACl and TBACl in DCM solution, we felt prepared to analyze those of the organometallic gold(I) derivative **1**.

General considerations

The substitution of the terminal alkynyl hydrogen atom of an aryl-ethynyl substituent by gold(I)•PTA residue should have a strong impact on the electronic properties of the phenyl group. We therefore performed DFT calculations in order to determine the modification of the electrostatic surface potential (ESP) at the center of the aromatic ring provoked by this substitution. We computed the ESPs of 1-ethynyl-4-methyl benzene **4** and [2-[4-(methyl)phenyl]ethynyl](1,3,5-triaza-7-phosphaadamantane-κP)Au(I) **5** (Scheme 2.1) as model systems of the two different aromatic walls present in the mono-gold(I) phosphine calix[4]pyrrole derivative **1**, at the BP86[33,34]-D3[35]/def2-SVP level of theory using GAUSSIAN version 09 (Figure 2.6).[36]

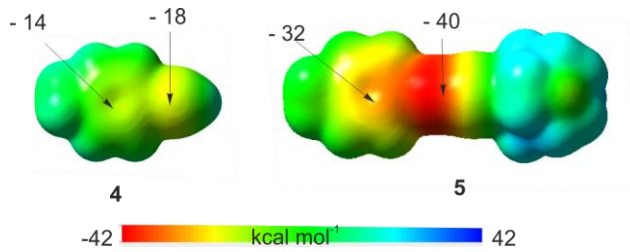

Figure 2.6. Calculated ESP values for the model systems **4** and **5** of the aromatic walls in **1**. ESP cubes mapped at electron density value of 0.0004 a.u.

As shown in Figure 2.6, the introduction of the gold(I)•PTA as terminal residue of the ethynyl substituent doubles the ESP value at the center of the aryl ring. This result indicates that the aryl

ring with the gold(I)•PTA unit becomes more electron rich and prone to be involved in a more repulsive anion-π interaction than an analogous compound with a simple ethynyl substituent.

We estimated that ESP values of the order of -12 kcal mol^{-1} at the center of the aromatic ring corresponded to a free energy value of the chloride-π interaction close to 0 kcal mol^{-1}.[5] We also demonstrated the existence of a linear-relationship between ESP and $\Delta\Delta G$ values for chloride-π interactions. By extrapolation of this linear-relationship, we assign a significant repulsive interaction, $\Delta\Delta G \sim 0.8$ kcal mol^{-1}, between the anion and the aryl of the gold(I)-ethynyl phosphine substituent (ESP = -32 kcal mol^{-1}).

^{1}H NMR titrations with **1** in DCM solution

We first probed the interaction of mono-gold(I) phosphine calix[4]pyrrole derivative **1** with MTOACl and TBACl using ^{1}H NMR spectroscopy. Calix[4]pyrrole **1** has a reduced solubility in DCM solution. Its ^{1}H NMR spectrum in DCM solution showed four aromatic proton signals in agreement with a C_s symmetry. The aromatic protons for the ethynyl substituted *meso*-phenyl group resonate as doublets at δ = 7.34 and 6.92 ppm. The latter signal corresponds to the aromatic protons *ortho* to the *meso*-carbon. In turn, the aromatic protons of the *meso*-phenyl bearing *p*-ethynyl gold(I)•PTA substituent appear slightly upfield shifted at δ = 7.19 and 6.81 ppm (Figure 2.7a - left panel). The difference observed in chemical shifts is in agreement with the *meso*-phenyl having the pristine ethynyl substituent being more electron-poor, as it is also derived from the DFT calculations. The protons of the PTA ligand appear as three separate signals. Two doublets corresponding to the axial and equatorial protons of the six-membered ring containing the three nitrogen atoms and one singlet for the methylene protons connecting the nitrogen atoms to the phosphorus. The four chemically non-equivalent *β*-pyrrole proton (Hb^1-Hb^4) produced only two separate signals. The addition of incremental amounts of each salt to separate DCM solutions of **1** produced changes in the registered ^{1}H NMR spectra that are identical to those described by the parent ligand **2** in the corresponding previous section.

The most relevant changes are the downfield shift of the pyrrole NH protons of the bound receptor indicating the involvement of these protons in hydrogen bonding interactions with the bound anion. In short, the mono-gold(I) phosphine **1** also acts as a heteroditopic receptor for ion-pairs in DCM solution.[37] The obtained results served to estimate that the binding constant *K*(Cl⊂**1**•MTOA) is still larger than 10^4 M^{-1}. On the other hand, the fit of the chemical shift changes experience by the protons of **1** in the titration with TBACl to a theoretical 1:1 binding model assigns the value of *K*(Cl⊂**1**•TBA) lower than 50 M^{-1} (Figure 2.7 - left panel and Experimental Section). The reduction in the magnitude of the binding constant for the Cl⊂**1**•TBA compared to that of Cl⊂**2**•TBA can be used to assign a value of 0.6 kcal mol^{-1} as a minimum estimate of the chloride-π interaction that putatively operates in the former. Gratifyingly, this value is in the same order of magnitude with our predictions using DFT calculations.

Noteworthy, we encountered a much-unexpected observation in the ^{1}H NMR titration experiments of **1** in DCM solution. That is, the appearance of second set of signals for the bound receptor **1**. These signals became visible when we added the salt over the equimolar point and remained as low intensity signals after further incremental addition. We surmised that the ion-paired chloride complex **1** could be present in solution as a mixture of two conformers of the bound receptor.[45]

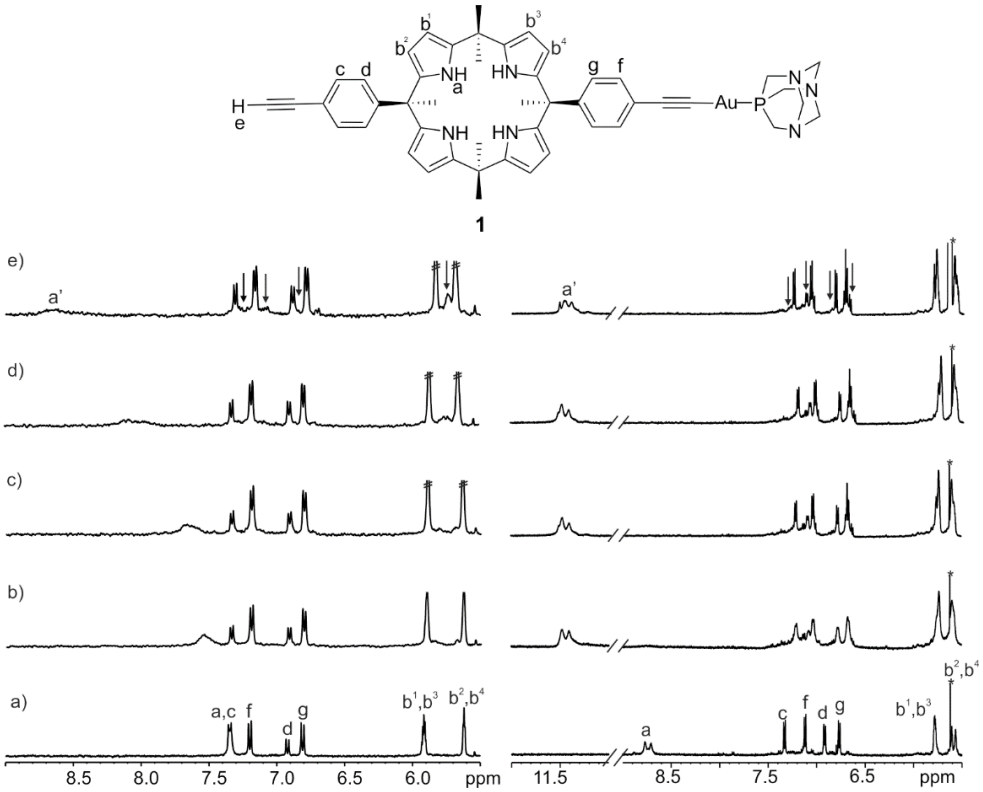

Figure 2.7. Left panel) Downfield region of the ^{1}H NMR spectra acquired during the titration of **1** (1 mM) with incremental amounts of TBACl in DCM solution: a) 0; b) 0.5; c) 1.0; d) 2.0 and e) 3.0 equiv. Right panel) Downfield region of the ^{1}H NMR spectra acquired during the titration of **1** (1mM) with incremental amounts of TBACl in acetone-d_6 solution: a) 0; b) 0.5; c) 1.0; d) 2.0 and e) 3.0 equiv. See top panel for proton assignment. Primed signals correspond to protons in bound **1**. Black arrows correspond to a new set of emerging proton signals for the bound **1**.

Attempts to perform UV-Vis titrations of **1** in DCM solution

We titrated a solution of **1** in DCM ([**1**] = 10 μM) with incremental amounts of MTOACl (0-75 equiv) maintaining the concentration of the receptor constant throughout the titration. We observed the steady decrease of the absorbance of all the bands in response to the addition of the salt.

Surprisingly to us, the change of absorbance did not reach saturation or showed signs of a biphasic behavior as observed for **2**. The UV-Vis titration of **1** in DCM solution using TBACl

displayed an identical behavior (see Figure 2.8a). We prepared the organometallic gold complex 2-phenyl-ethynyl-(1,3,5-triaza-7- phosphaadamantane-κ*P*)Au(I), **6**, as model system of the metallated aromatic wall of **1**, in order to examine the effect caused by the incremental addition of tetraalkylammonium chloride salts on its absorption spectrum.

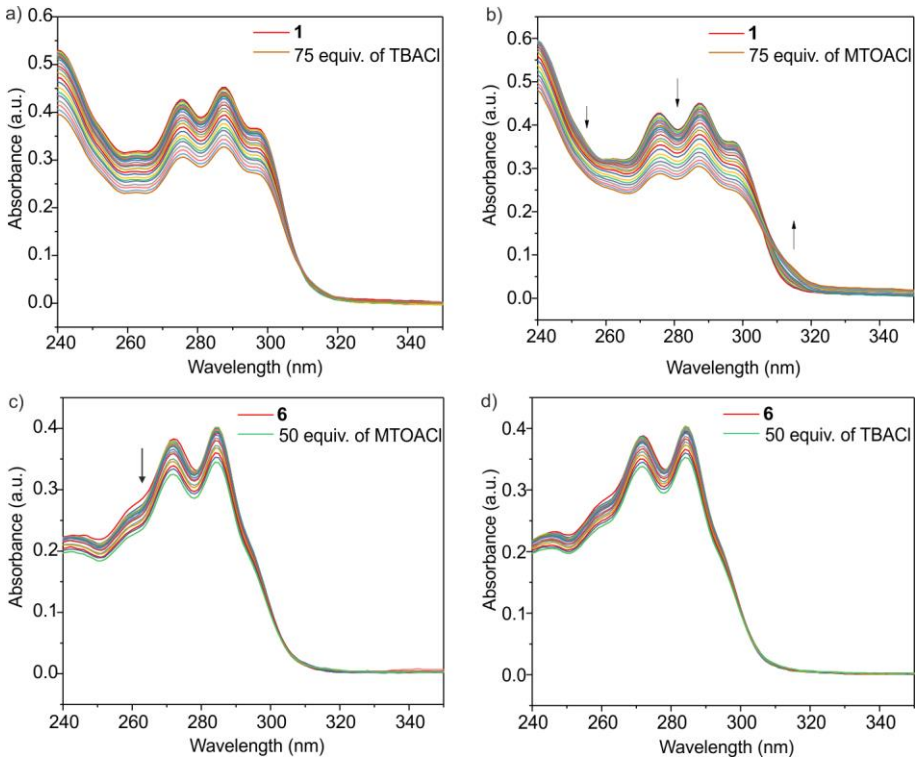

Figure 2.8. UV-Vis absorption spectra acquired during the titration of a 10 μM DCM solution of receptors **1** and **6** with increasing amounts of guests: a) receptor **1** with TBACl (up to 75 equiv.) and b) MTOACl (up to 75 equiv.); c) receptor **6** with MTOACl (up to 75 equiv.) and d) TBACl (up to 75 equiv.). The concentration of receptor was maintained constant throughout the titration.

We were surprised to discover that the absorbance of the UV-Vis spectrum of **6** in DCM solution decreased as the amount of the salts increased. Based on these results, we concluded that UV-Vis spectroscopy is not a suitable technique to study the binding of chloride to the mono-gold(I) alkynyl receptor **1**. The absorption spectrum of the chromophore is modified in response to a process that is not directly related to the chloride binding (Figure 2.8).

Additional ^{1}H NMR titrations of **1** in acetone solution

To gain further evidence of the presence of two chloride complexes of **2** in solution, possibly a mixture of conformers, we performed additional titration experiments of **1** with the two salts in acetone solution. In acetone solution, the ion-pairing is expected to be weaker and this might

facilitate the formation of the second chloride complex to a different extent. Moreover, the oxygen atom of acetone is a good hydrogen bond acceptor. The putative formation of hydrogen bonds between the solvent and dangling pyrrole NHs could favor the chloride bound receptor to adopt other conformation than the cone. In this respect, we observed in the solid state that "two-wall" calix[4]pyrroles adopt alternate conformation when bound to polar solvents like acetone or acetonitrile (see Figure 2.12 for X-ray of **2**).[4,38]

The gold(I) metallated calix[4]pyrrole **1** also features a very reduced solubility in acetone-d_6. We titrated 1 mM solutions of **1** with incremental amounts of both salts, TBACl and MTOACl, in separate NMR tubes. Contrary to the experiments carried out in DCM solution, but in agreement with our expectations, the results of the titrations with the two salts are quite similar. In short, the more polar environment provided by acetone minimizes ion-pairing and **1** behaves mainly as a monotopic anion receptor (Figure 2.7 – right panel).

In both titrations, the chloride binding saturates after the addition of 1 equiv. of salt. The addition of more than 1 equiv of the salt induces small changes in the protons of the bound receptors. All in all, these results are consistent with a binding affinity of **1** for chloride in acetone-d^6 solution, K[Cl⊂**1**]$^-$, larger than 10^4 M^{-1}. Unfortunately, at this point, the lack of accurate binding constant values for the [Cl⊂**1**]$^-$ and [Cl⊂**2**]$^-$ [39] anionic complexes in acetone-d^6 does not allow us to test our theoretical predictions in favor of the energetically more favorable [Cl⊂**2**]$^-$ complex, owing to the reduced repulsive chloride-π interactions (see Experimental section on ITC experiments in acetone to overcome this limitation).

Molecular modelling studies

The results above show that the [Cl⊂**2**]$^-$ anionic complex (acetone solution) and its ion-paired counterparts Cl⊂**2**•TBA/MTOA (DCM solutions) are present in solution as single conformers featuring a unique binding geometry in the latter case. In striking contrast, the complexes of the mono-gold(I) phosphine calix[4]pyrrole **1** exist in solution as mixture of two conformers and possibly with different binding geometries. We ascribed this difference to the existence of stronger repulsive chloride-π interactions in the case of the [Cl⊂**1**]$^-$ complex.[40,41] These energetic repulsions might induce the bound receptor to adopt a conformation different from the cone. The increase in repulsive chloride-π interactions derives from the more electron rich nature of the *meso*-phenyl ring equipped with the gold(I)•PTA ethynyl substituent that is present in **1**. For the same token, the alkynyl π-system covalently bound to the Au^I atom largely increases its electron density and may energetically favor the location of the tetraalkylammonium cation close to it instead of opposed to the bound chloride. This arrangement of the anion and the cation will result in the formation of ion-paired complex with close-contact binding geometry having an energy in par with the alternative receptor-separated binding mode even when the bound receptor adopts the

cone conformation. For ion-paired complexes in which the bound receptor is not in cone conformation, the close-contact binding geometry should be likely preferred.

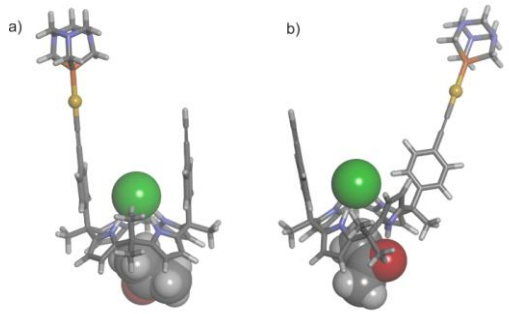

Figure 2.9. Energy minimized structures bp86-D3 def2-SVP of [Cl⊂**1**]⁻: a) receptor in cone conformation; b) receptor in half-cone conformation. The receptor is shown in ball and stick representation. The chloride and the implicit acetone as CPK models. The gold atom is displayed as scaled ball and stick representation. The calculation assigns an energy advantage of 2.2 kcal mol^{-1} to the complex with the receptor in cone conformation.

In order to assign relative energies and structures to the different binding modes hypothesized for the [Cl⊂**1**]⁻ complex, we performed DFT calculation at the BP86[33,34]-D3[35] def2-SVP level of theory and a continuum solvent model using GAUSSIAN 09.[36] Figure 2.9 depicts the energy-minimized structures of the [Cl⊂**1**]⁻ complex in which the receptor adopts cone and half-cone conformations. For a fairer comparison of energies, we introduced an implicit molecule of acetone in the structures. This molecule satisfies the hydrogen-bonding needs of the dangling NH pyrrole on the half-cone bound receptor conformation. The calculations assign an energetic advantage of 2.2 kcal mol^{-1} to the [Cl⊂**1**]⁻ complex with the receptor in cone conformation (Figure 2.9).

We postulate that the two sets of proton signals observed for bound **1** in the ^{1}H NMR titrations performed in DCM-d_2 and acetone-d_6 correspond to the two binding geometries of the [Cl⊂**1**]⁻ complex.[42,43] The one featuring receptor **1** in cone conformation is energetically favored and present in solution largely. We did not compute the structures for the receptor separated or close contact ion-paired complexes of Cl⊂**1**•TBA/MTOA because experimentally the cation exchange between the free and bound state is fast on the chemical shift timescale and also a putative chemical exchange between the two sites of the complex should also take place in the same dynamic regime. Consequently, cation exchange processes cannot be considered as responsible for the observation of two separate proton signals of the bound receptor.

Isothermal titration calorimetry (ITC) experiments in acetone

The assessment of accurate values for the binding constant of the anionic complexes formed in acetone was not possible using UV-Vis titrations. The absorbance of the solvent is in the range of

the absorbance of receptors **1** and **2**. Instead, we performed isothermal titration calorimetry (ITC) experiments (direct and reverse titrations) to characterize thermodynamically the binding processes of both tetraalkylammonium chloride salts, TBACl and MTOACl, with the two receptors **1** and **2**. In all cases, the resulting exothermic binding isotherms showed a single sigmoidal behavior with the inflexion point centered at a 1:1, receptor: salt, ratio. Consequently, we fit all isotherms using a simple 1:1 binding model and the thermodynamic parameters returned from the fit (Δ*H* and *K*a) are referred as apparent values owing to the simplification of the used model, which does not take into account the ion-pairing processes that might occur in the solvent. In other words, we consider that at the concentration used for the titration, both the salt and the complex are almost fully dissociated in this solvent. Table 2.2 summarizes the thermodynamic parameters determined from the ITC experiments.

We can draw several conclusions from the listed data. Firstly, for a given receptor the determined value of the binding constant for its anionic chloride complex should be identical, independently of the salt used as chloride precursor. This would be the expected result if anionic complexes and salts were completely dissociated. However, the obtained results show differences in the binding constant determined for the two salts with a single receptor. For example, the value of K_a[Cl⊂**1**]$^-$ is slightly larger (double) when MTOACl is used as chloride precursor instead of TBACl. This finding is also observed with receptor **2**. Most likely, these results derive from not fully dissociation of ion-pairs in acetone solution. Nevertheless, we consider that in acetone solution the effect of the cation (doubling the *K*a values) is markedly reduced compared to DCM solution (two orders of magnitude difference in *K*a values).

Table 2.2. Apparent binding constants (*K*a, M^{-1}), enthalpies (Δ*H*, Kcal mol^{-1}) and free energies (Δ*H*, Kcal mol^{-1}) of the binding equilibria of **1** and **2** with TAACl salts (TAA = TBA^+ or $MTOA^+$) in acetone at 298 K using direct ITC titrations.[44]

Receptor	**1**		**2**	
Salt	TBACl	MTOACl	TBACl	MTOACl
$K_a \times 10^{-4}$	1.0 ± 0.1[a]	2.4 ± 0.2[a]	4.8 ± 0.4[b]	7.1 ± 0.9[b]
Δ*H*	-3.6 ± 0.2[a]	-2.1 ± 0.4[a]	-3.0 ± 0.1[b]	-3.4 ± 0.1[b]
Δ*G*	-5.3 ± 0.1	-6.0 ± 0.1	-6.3 ± 0.1	-6.5 ± 0.1

[a] K_a and Δ*H* are the average values from two independent direct titrations (salt over receptor). Errors are reported as standard deviation. [b] K_a and Δ*H* are the average values from one direct titration (salt over receptor) and one reverse titration (receptor over salt). Errors are reported as standard deviation of the two measurements.

Secondly, we have now accurate values for the apparent binding constants of the two receptors with chloride, which although not being identical, they can be used to calculate the effect exerted by the putative chloride-π interaction operative in the complexes with receptor **1**. Thus by subtracting the free energies of binding of the two complexes produced by the two salt precursors,

we derived a value between 1.0 – 0.5 kcal mol^{-1} for the repulsive interaction. This estimate agrees nicely with the calculated one using DFT calculations (0.8 kcal mol^{-1}) on model systems (*vide supra*). Finally, the binding of chloride in both receptors is both enthalpy and entropy driven. The entropic term is an important component to binding. This observation indicates the importance of the solvation and desolvation process that take place in polar organic solvents *i.e.* acetone for the binding of chloride through hydrogen-bonding interactions in deep and polar aromatic clefts.

2.3 Conclusions

In summary, we report the synthesis of an unprecedented organometallic "two-wall" α,α-calix[4]pyrrole **1** featuring a gold(I) phosphine covalently attached to one of its two *para*-ethynyl groups in the *meso*-aryl substituents. In DCM solution, the parent ligand **2** and its mono-gold(I) derivative **1** act as heteroditopic receptors in the binding of tetraalkylammonium chloride salts producing 1:1 ion-paired complexes. The two receptors show high selectivity and affinity for the binding of methyltrioctyl ammonium chloride (MTOACl) compared to tetrabutyl ammonium chloride (TBACl) owing to the better fit of the methyl group of the MTOA cation in the shallow aromatic cavity opposed to the anion binding site. Moreover, we calculated that the Cl⊂**1**•TBA complex is energetically destabilized with respect to the Cl⊂**2**•TBA analogue by ~ 0.6 kcal mol^{-1} because of stronger repulsive chloride-π interactions. The experimentally determined value is in agreement with the one derived from DFT calculations using model systems **4** and **5**. The increase in the negative ESP value at the center of the phenyl ring displaying the *para*-gold(I) phosphine ethynyl substituent is responsible for this deleterious effect and possibly for the existence in solution of the Cl⊂**1**•TBA/MTOA complexes as a mixtures of two conformers.[45] In the chlorinated solvent, the binding constant values of Cl⊂**1**•MTOA and Cl⊂**2**•MTOA are too large (> 10^4 M^{-1}) to be measured accurately using ^{1}H NMR spectroscopy. At μM concentrations, UV-Vis titrations in DCM solution revealed the co-existence of the anionic chloride complex [Cl⊂**2**]$^-$ and its ion-paired Cl⊂**2**•MTOA counterpart. We assessed their stability constant using an elaborated binding model. Unfortunately, the results of the UV-Vis titrations of **1** in DCM were hampered by spectroscopic changes resulting from a non-specific interaction between the chloride and the gold(I) aryl-ethynyl residue. In acetone solution, compounds **1** and **2** mainly function as homotopic receptors for chloride. The stability constants of the anionic chloride complexes, [Cl⊂**1**]$^-$ and [Cl⊂**2**]$^-$ are estimated to be larger than 10^4 M^{-1} by ^{1}H NMR experiments. The [Cl⊂**1**]$^-$ complex is also present as a mixture of two conformers in solution with a slight increase on the amount of the minor component in comparison to DCM.[45] Using ITC experiments, we determined accurate but apparent binding constant values for the two anionic complexes and demonstrated that the cation effect of the salts is markedly reduced in this solvent. We also determined that in acetone the difference in energy between [Cl⊂**1**]$^-$ and [Cl⊂**2**]$^-$ is in the range of 1.0 – 0.5 kcal mol^{-1} in favor of the later.

2.4 Experimental Section

2.4.1 General information and instruments

All manipulations were performed under N_2 or Ar atmosphere using standard Schlenk techniques. Anhydrous solvents were obtained by distillation from appropriate drying agents. All solvents were of HPLC grade quality. Reagents were obtained from Sigma Aldrich and used without further purification: 1,3,5-triaza-7-phosphatricyclo[3.3.1.13.7]decane 97% (PTA), tetrabutylammonium chloride (TBACl), methyltrioctylammonium chloride (MTOACl), tetramethylammonium chloride (TMACl) and tetraethylammonium chloride (TEACl). The preparation of [AuCl(PTA)][26] and 10α, 20α-bis(4-[ethynylphenyl]calix[4]pyrrole was carried out following reported procedures.[24,25] Infrared spectra were recorded on a FI-IR 520 Nicolet Spectrophotometer. Absorption spectra were recorded on a Varian Cary 100 Bio UV-spectrophotometer and emission spectra on a Horiba-Jobin-Ybon SPEX Nanolog spectrofluorimeter. ^{1}H, ^{31}P{^{1}H} and COSY NMR spectra were recorded using a Bruker 400 UltrashieldTM (400 MHz for ^{1}H and 100 MHz for ^{13}C), Bruker Avance 500 UltrashieldTM (500 MHz for ^{1}H and 162 MHz for ^{31}P{^{1}H}) or Bruker Avance 500 with cryoprobe (500 MHz for ^{1}H and 162 MHz for ^{31}P{^{1}H}) spectrometers. Dichloromethane-*d*$_2$ (CD_2Cl_2) and acetone-*d*$_6$ [$(CD_3)_2CO$] were purchased from Sigma Aldrich and chemical shifts are given in ppm, relative to TMS. All NMR *J* values are given in Hz. 2D NMR experiments were helpful for the proton assignment. ElectroSpray-Mass spectra (+) were recorded on a Fisons VG Quattro spectrometer.

2.4.2 Synthesis and characterization data

[Au{10α,20α-bis(4-[ethynylphenyl])calix[4]pyrrole}-(PTA)] (1): A solution of [AuCl(PTA)] (32 mg, 0.08 mmol) in CH_2Cl_2 (5 mL) was added to a solution of KOH (5 mg, 0.089 mmol) and 10α,20α-bis(4-[ethynylphenyl])calix[4]pyrrole **2** (50 mg, 0.083 mmol) in a mixture of MeOH (10 mL) and DCM (4 mL). After 2 hours of stirring at room temperature, the resulting pale yellow solution was concentrated to *ca.* 10 mL, and hexane (10 mL) was added to precipitate a pale yellow solid. The filtered solid was recrystallized in DCM/Hexane solution and isolated by filtration.[46] Yield: 60% (45 mg). ^{1}H-NMR (400 MHz, $(CD_3)_2CO$): 8.77 (br, 2H, N-H), 8.71 (br, 2H, N-H), 7.33 (d, 2H, *J* = 8.42 Hz), 7.12 (d, 2H, *J* = 8.42 Hz), 6.92 (d, 2H, *J* = 8.42 Hz), 6.77 (d, 2H, *J* = 8.42 Hz), 5.78 (m, 4H), 5.60 (s, 2H), 5.56 (s, 2H), 4.65 (d, 3H, *J* = 12.88 Hz, N-C*H*$_2$-N), 4.50 (d, 3H, *J* = 12.88 Hz, N-C*H*$_2$-N), 4.36 (s, 6H, P-C*H*$_2$-N), 3.58 (s, 1H, C≡C-*H*), 1.87 (s, 3H, CH_3), 1.83 (s, 3H, CH_3), 1.65 (s, 6H, CH_3), 1.48 (s, 6H, CH_3). ^{31}P{^{1}H}-NMR (162 MHz, $(CD_3)_2CO$, 298 K, δ ppm): -47.0 ppm. ES-MS (+) m/z: 954.40 ([M + H]$^{+}$, calc.: 954.40). IR (KBr, cm^{-1}): 3413 *v*(N-H), 3105 *v*(C≡C-H), 2092 *v*(C≡C), 1637 *v*(C=O), 1590 *v*(C=N).

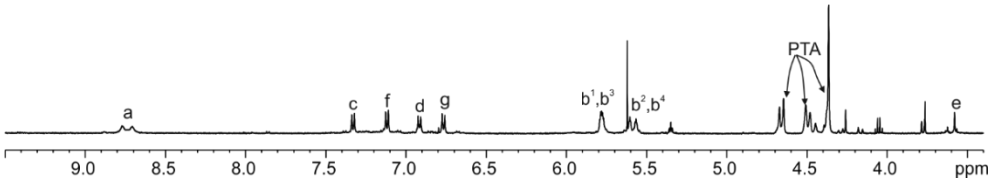

Figure 2.10. ^{1}H NMR (500 MHz, $(CD_3)_2CO$, 298 K) spectrum of **1**. See scheme 2.1 for proton assignment.

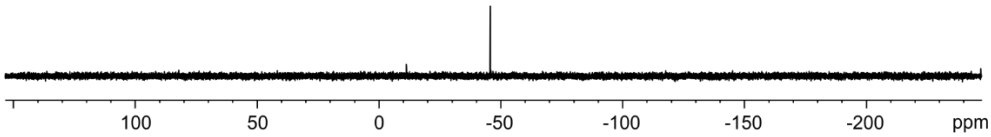

Figure 2.11. $^{31}P\{^{1}H\}$ NMR (162 MHz, $(CD_3)_2CO$, 298 K) spectrum of **1**.

2.4.3 X-ray structure of **2** in 1,3-alternate conformation

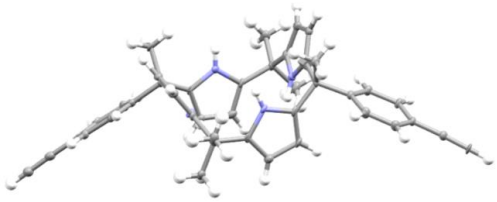

Figure 2.12. X-ray structure of **2** in 1,3-alternate conformation. The structure is shown in ORTEP view with thermal ellipsoids set at 50% probability.

2.4.4 ^{1}H NMR spectroscopic titration experiments of **1** in CD_2Cl_2

NMR titrations were performed by preparing a 1 mM solution of host **1** in CD_2Cl_2. Subsequently, 0.5 mL of the solution was transferred to a NMR tube. The remaining solution was used to prepared the MTOACl solution at 20-30-fold higher concentration. Thus, the concentration of the host was maintained constant throughout the titration. The host solution was titrated by adding incremental amounts of the salt solution and registering a ^{1}H NMR spectrum after each addition.

MTOACl

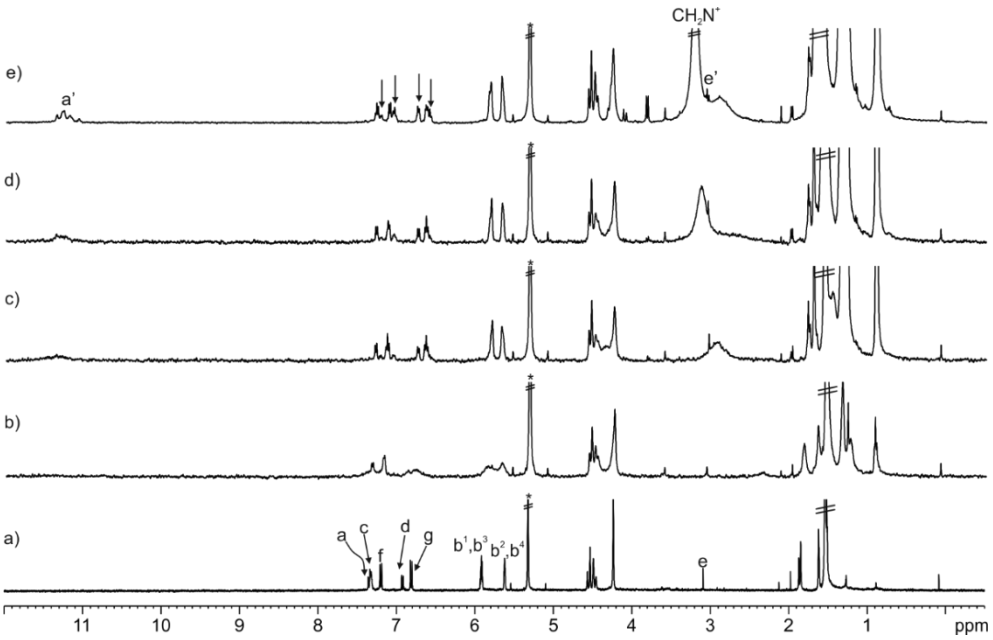

Figure 2.13. ^{1}H NMR (400 MHz, CD_2Cl_2, 298 K) spectra of the titration of **1** with incremental amounts of MTOACl: a) 0; b) 0.5; c) 1; d) 2 and e) 3 equiv. *Residual solvent peak. Primed letters correspond to proton signals of bound **1**. Black arrows correspond to a new set of emerging proton signals of the bound receptor **1**.

2.4.5 ^{1}H NMR spectroscopic titration experiments of **2** in $(CD_3)_2CO$

NMR titrations were performed by preparing a 1 mM solution of host **2** in $(CD_3)_2CO$. Subsequently, 0.5 mL of the solution was transferred to a NMR tube. The remaining solution was used to prepared the MTOACl solution at 20-30-fold higher concentration. Thus, the concentration of the host was maintained constant throughout the titration. The host solution was titrated by adding incremental amounts of the salt solution and registering a ^{1}H NMR spectrum after each addition.

MTOACl

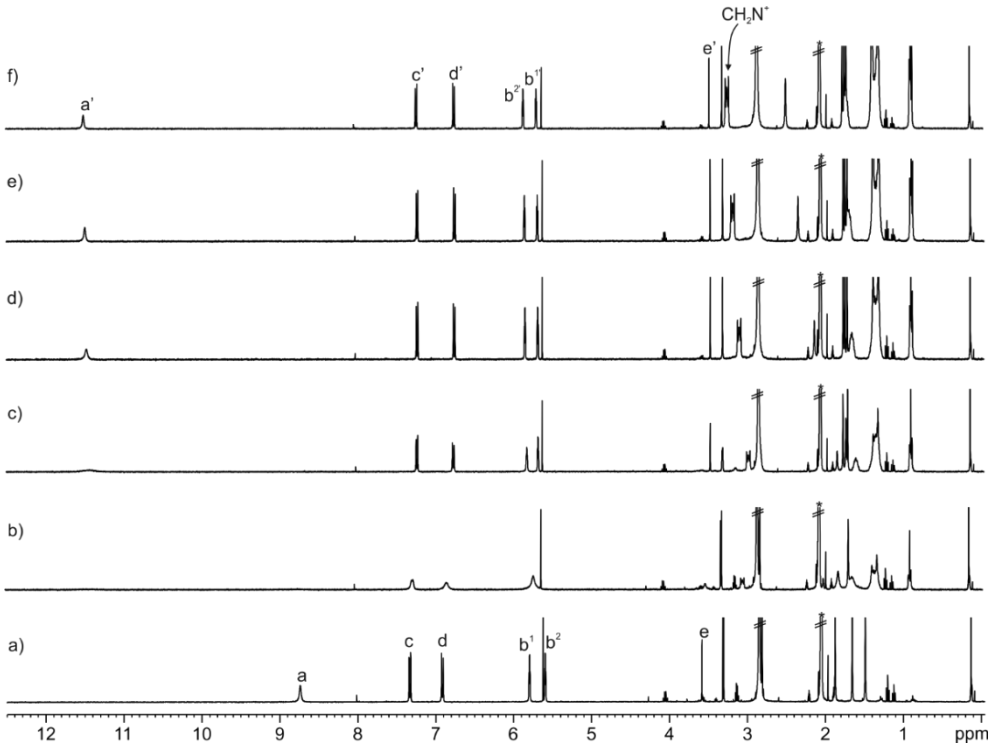

Figure 2.14. ^{1}H NMR (400 MHz, $(CD_3)_2CO$, 298 K) spectra of the titration of **2** with incremental amounts of MTOACl; a) 0; b) 0.5; c) 1; d) 1.5; e) 2 and f) 2.5 equiv. *Residual solvent peak. See Scheme 2.1 for proton assignment. Primed letters correspond to proton signals of bound **2**.

2.4.6 ^{1}H NMR spectroscopic titration experiments of **1** in $(CD_3)_2CO$

NMR titrations were performed by preparing a 0.4 mM solution of host **1** in $(CD_3)_2CO$. Subsequently, 0.5 mL of the solution was transferred to a NMR tube. The remaining solution was used to prepared the titrant's solution (TBACl, MTOACl or TEACl) at 20-30-fold higher concentration. Thus, the concentration of the host was maintained constant throughout the titration. The host solution was titrated by adding incremental amounts of the salt solution and registering a ^{1}H NMR spectrum after each addition. Due to the reduced solubility of TMACl in acetone, we performed solid-liquid extraction experiment to acquire the spectra.

TBACl

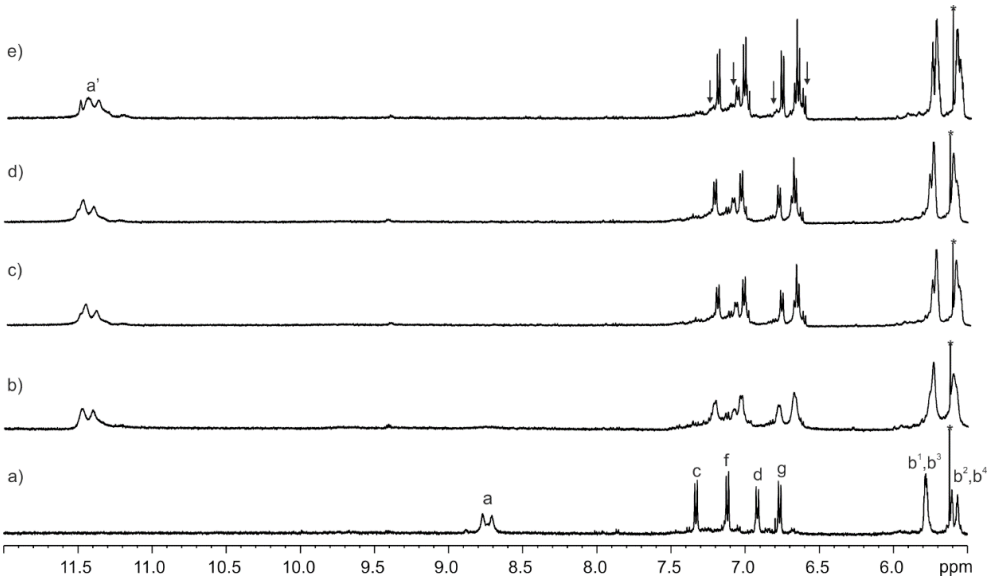

Figure 2.15. Selected region of the ^{1}H NMR (500 MHz with cryoprobe, $(CD_3)_2CO$, 298 K) spectra of the titration of **1** (0.4 mM) with incremental amounts of TBACl: a) 0; b) 0.5; c) 1; d) 2 and e) 3 equiv. *Residual solvent peak. Primed letters correspond to proton signals of bound **1**. Black arrows correspond to a new set of emerging proton signals for the bound receptor **1**.

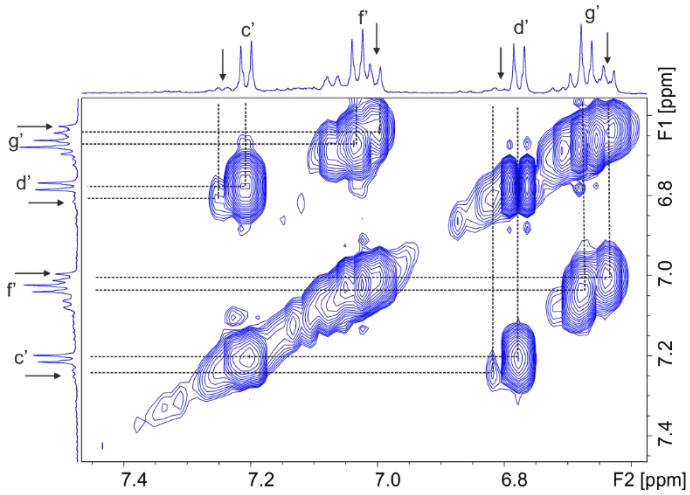

Figure 2.16. Selected region of the COSY NMR (500 MHz, $(CD_3)_2CO$, 298 K) spectrum of a 3:1 mixture of TBACl and **1**. Primed letters correspond to proton signals of bound **1**. Black arrows correspond to a new set of emerging signals for the bound receptor **1**.

MTOACl

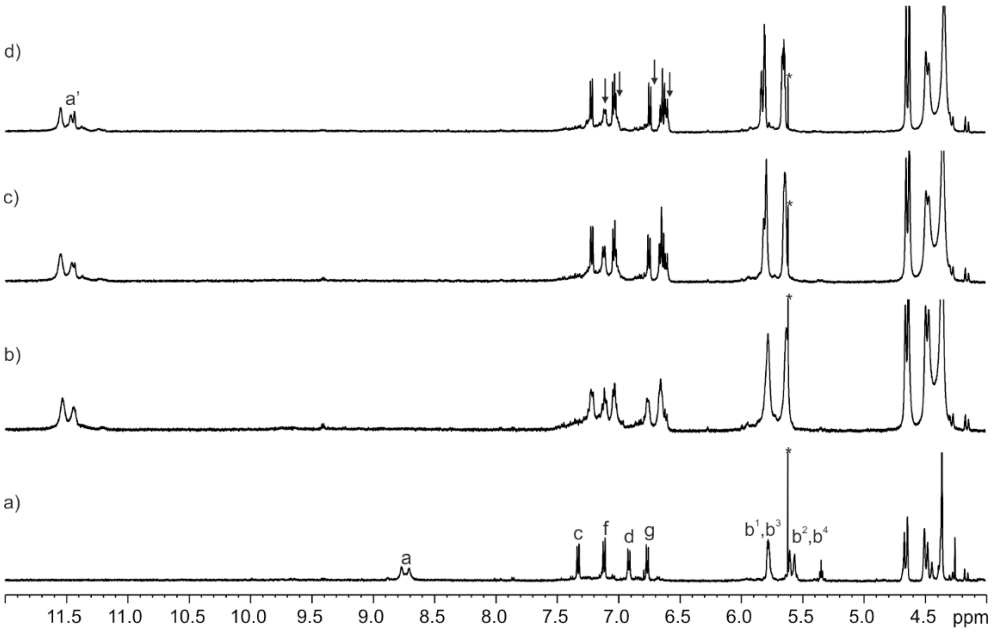

Figure 2.17. Selected region of the ^{1}H NMR (500 MHz with cryoprobe, $(CD_3)_2CO$, 298 K) spectra of the titration of **1** (0.4 mM) with incremental amount of MTOACl: a) 0; b) 0.5; c) 1 and d) 2 equiv. *Residual solvent peak. Primed letters correspond to proton signals of bound **1**. Black arrows correspond to a new set of emerging proton signals for bound receptor **1**.

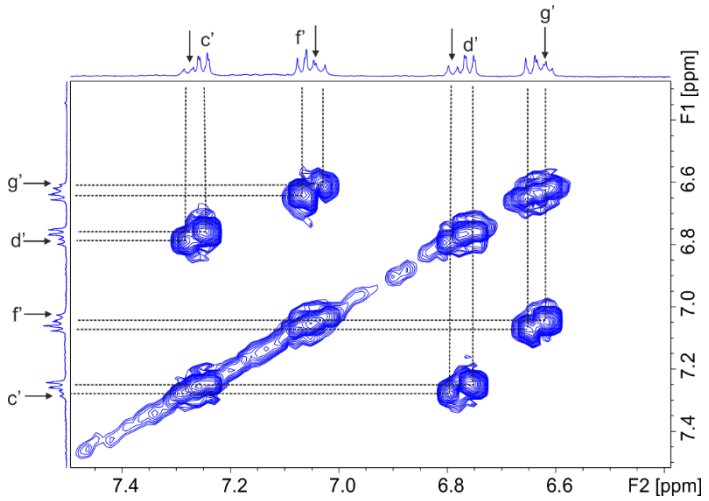

Figure 2.18. Selected region of the COSY NMR (500 MHz, $(CD_3)_2CO$, 298 K) spectrum of a 3:1 mixture of MTOACl and **1**. Primed letters correspond to proton signals of bound **1**. Black arrows correspond to a new set of emerging signals for the bound receptor **1**.

TMACl

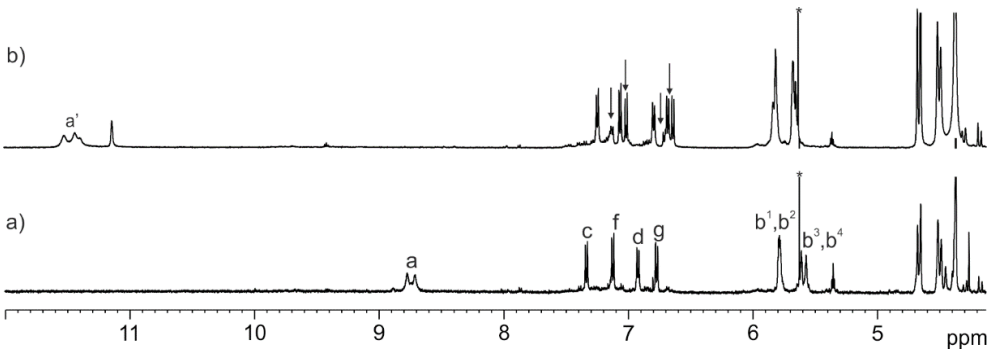

Figure 2.19. Selected regions of the ^{1}H NMR (500 MHz with cryoprobe, $(CD_3)_2CO$, 298 K) spectra acquired before a) and after b) a solid-liquid extraction of TMACl with 0.4 mM solution of **1** in $(CD_3)_2CO$. See Scheme 2.1 for proton assignment.

TEACl

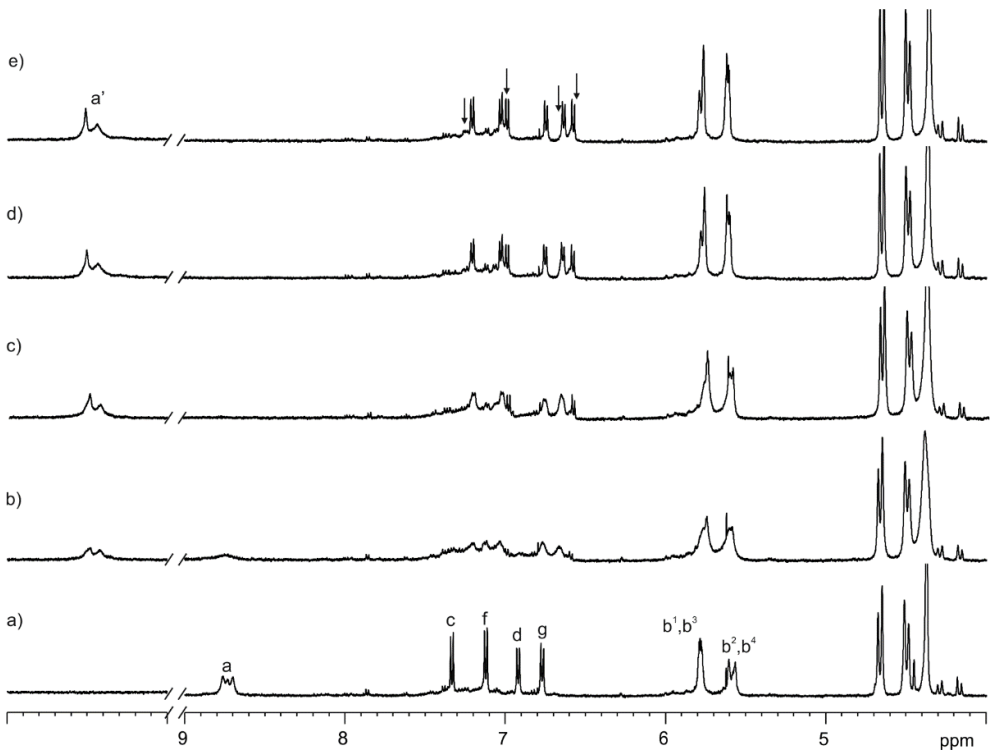

Figure 2.20. Selected regions of the ^{1}H NMR (500 MHz with cryoprobe, $(CD_3)_2CO$, 298 K) spectra of the titration of **1** (0.4 mM) with incremental amounts of TEACl: a) 0; b) 0.5; c) 1; d) 2 and e) 3 equiv. See Scheme 2.1 for proton assignment. Black arrows correspond to a new set of emerging proton signals for bound receptor **1**.

2.4.7 ITC titration experiments of **2** with MTOACl in DCM

ITC experiments were performed using a MicroCal VP-ITC MicroCalorimeter with the VP viewer 2000 software. Dichloromethane titrations of **2** with MTOACl were carried out at 288 K by adding small aliquots (8 µL, 16 s) of a 2.8 mM solution of MTOACl into a 0.35 mM solution of **2**. The association constant and the thermodynamic parameters of binding process were derived using the "one set of sites" model included in the Microcal software.

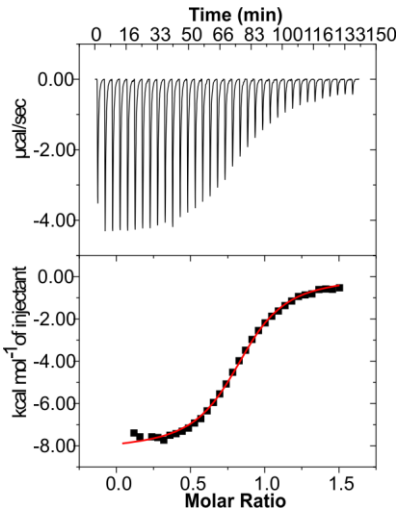

Figure 2.21. (Top) Raw data for the ITC titrations of receptor **2** with MTOACl at 288 K in dichloromethane. Bottom) Normalized integration of heat vs MTOACl/**2** molar ratio; the fit of the experimental data to the one set of sites binding isotherm (red line) is also shown. [MTOACl] = 2.8 mM and [**2**] = 0.35 mM.

2.4.8 ITC titration experiments in acetone

ITC experiments were performed using a MicroCal VP-ITC MicroCalorimeter with the VP Viewer 2000 software. Dichloromethane titrations of **2** with MTOACl were carried out at 288 K by adding small aliquots (8 µL, 16 s) of a 2.8 mM solution of MTOACl into a 0.35 mM solution of **2**. The association constant and the thermodynamic parameters of binding process were derived using the "one set of sites" model included in the Microcal software. Acetone ITC experiments of **1** and **2** with the different alkylammonium salts were performed at 288 K by injecting small aliquots (8 µL, 16 s) of a 5.4 mM acetone solution of the salt using a computer controlled microsyringe into a 0.3-0.4 mM solution of the host in the same solvent. Moreover, for receptor **2**, reverse titrations (i.e. 8 µL injections of a 8.5 mM solution of **2** in acetone to a 1.1 mM guest solution in the same solvent) were also performed producing very similar results. Reverse titrations were not performed with receptor **1** due to the limited solubility of this receptor in acetone. The association constants and the thermodynamic parameters of binding processes were obtained from the fit of the titration data to a simple 1:1 binding model using HypΔH software.

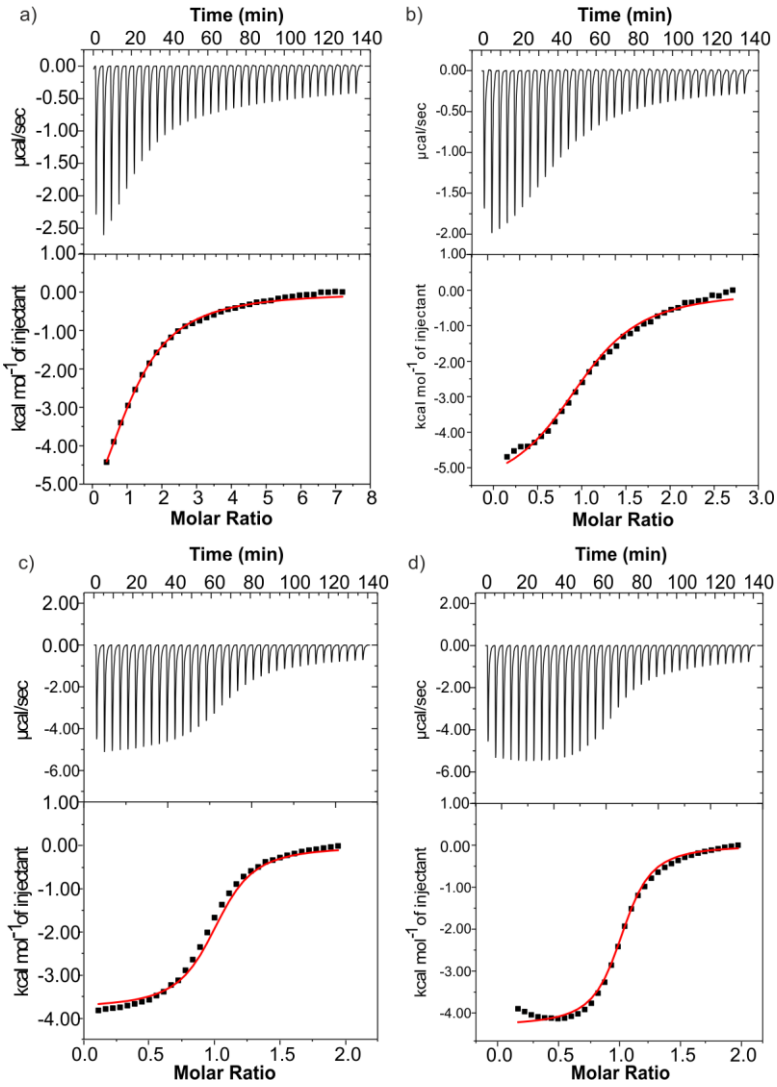

Figure 2.22. Top panels show raw data (heat vs. time) for the titration of guest into host: a) TBAClⵚ**2**; b) MTOAClⵚ**2**; c) TBAClⵚ**1** and d) MTOAClⵚ**1**. Titrations were performed at 288 K. Bottom panels represent integrated data fitted to the one set of sites binding isotherm (red line) is also shown.

2.5 References and Notes

[1] P. A. Gale, J. L. Sessler, V. Kral, V. Lynch, *J. Am. Chem. Soc.* **1996**, *118*, 5140-5141.

[2] P. A. Gale, J. L. Sessler, V. Kral, *Chem. Commun.* **1998**, 1-8.

[3] Y.-D. Wu, D.-F. Wang, J. L. Sessler, *J. Org. Chem.* **2001**, *66*, 3739-3746.

[4] L. Adriaenssens, C. Estarellas, A. Vargas Jentzsch, M. Martinez Belmonte, S. Matile, P. Ballester, *J. Am. Chem. Soc.* **2013**, *135*, 8324-8330.

[5] L. Adriaenssens, G. Gil-Ramirez, A. Frontera, D. Quinonero, E. C. Escudero-Adan, P. Ballester, *J. Am. Chem. Soc.* **2014**, *136*, 3208-3218.

[6] Y. Han, G.-L. Wang, J.-J. Sun, J. Sun, C.-G. Yan, *Tetrahedron* **2013**, *69*, 10604-10609.

[7] J. S. Park, K. Y. Yoon, D. S. Kim, V. M. Lynch, C. W. Bielawski, K. P. Johnston, J. L. Sessler, *Proc. Natl. Acad. Sci. U. S. A.* **2011**, *108*, 20913-20917.

[8] G. Bruno, G. Cafeo, F. H. Kohnke, F. Nicolo, *Tetrahedron* **2007**, *63*, 10003-10010.

[9] J. R. Romero, G. Aragay, P. Ballester, *Chem. Sci.* **2017**, *8*, 491-498.

[10] S. K. Kim, J. L. Sessler, *Acc. Chem. Res.* **2014**, *47*, 2525-2536.

[11] I. W. Park, J. Yoo, S. Adhikari, J. S. Park, J. L. Sessler, C. H. Lee, *Chem-Eur J* **2012**, *18*, 15073-15078.

[12] D. E. Gross, F. P. Schmidtchen, W. Antonius, P. A. Gale, V. M. Lynch, J. L. Sessler, *Chem. - Eur. J.* **2008**, *14*, 7822-7827.

[13] J. L. Sessler, D. E. Gross, W.-S. Cho, V. M. Lynch, F. P. Schmidtchen, G. W. Bates, M. E. Light, P. A. Gale, *J. Am. Chem. Soc.* **2006**, *128*, 12281-12288.

[14] R. Custelcean, L. H. Delmau, B. A. Moyer, J. L. Sessler, W.-S. Cho, D. Gross, G. W. Bates, S. J. Brooks, M. E. Light, P. A. Gale, *Angew. Chem., Int. Ed.* **2005**, *44*, 2537-2542.

[15] S. L. Cockroft, *Chem* **2017**, *3*, 383-384.

[16] R. B. P. Elmes, K. A. Jolliffe, *Chem. Commun.* **2015**, *51*, 4951-4968.

[17] M. Ferrer, L. Giménez, A. Gutiérrez, J. C. Lima, M. Martínez, L. Rodríguez, A. Martín, R. Puttreddy, K. Rissanen, *Dalton Trans.* **2017**, *46*, 13920-13934.

[18] F. K.-W. Hau, K.-L. Cheung, N. Zhu, V. W.-W. Yam, *Org. Chem. Front.* **2019**, *6*, 1205-1213.

[19] V. W.-W. Yam, K.-L. Cheung, L.-H. Yuan, K. M.-C. Wong, K.-K. Cheung, *Chem. Commun.* **2000**, 1513-1514.

[20] X. He, W. H. Lam, N. Zhu, V. W.-W. Yam, *Chem. - Eur. J.* **2009**, *15*, 8842-8851.

[21] J. C. Lima, L. Rodriguez, *Chem. Soc. Rev.* **2011**, *40*, 5442-5456.

[22] S. Wan, W. Lu, *Angew. Chem., Int. Ed.* **2017**, *56*, 1784-1788.

[23] C. J. Borman, R. Custelcean, B. P. Hay, N. L. Bill, J. L. Sessler, B. A. Moyer, *Chem. Commun.* **2011**, *47*, 7611-7613.

[24] V. Valderrey, E. C. Escudero-Adán, P. Ballester, *Angew. Chem., Int. Ed.* **2013**, *52*, 6898-6902.

[25] V. Valderrey, E. C. Escudero-Adán, P. Ballester, *J. Am. Chem. Soc.* **2012**, *134*, 10733-10736.

[26] E. Vergara, S. Miranda, F. Mohr, E. Cerrada, E. R. T. Tiekink, P. Romero, A. Mendía, M. Laguna, *Eur. J. Inorg. Chem.* **2007**, *2007*, 2926-2933.

[27] R. Gavara, J. C. Lima, L. Rodríguez, *Photochem. Photobiol. Sci.* **2016**, *15*, 635-643.

[28] L. Rodríguez, M. Ferrer, R. Crehuet, J. Anglada, J. C. Lima, *Inorg. Chem.* **2012**, *51*, 7636-7641.

[29] E. Aguiló, A. J. Moro, M. Outis, J. Pina, D. Sarmento, J. S. Seixas de Melo, L. Rodríguez, J. C. Lima, *Inorg. Chem.* **2018**, *57*, 13423-13430.

[30] Y. Liu, A. Sengupta, K. Raghavachari, A. H. Flood, *Chem* **2017**, *3*, 411-427.

[31] Protonics Software http://www.hyperquad.co.uk/HypSpec.htm.

[32] R. M. Fuoss, *J. Am. Chem. Soc.* **1958**, *80*, 5059-5061.

[33] A. D. Becke, *Phys. Rev. A* **1988**, *38*, 3098-3100.

[34] J. P. Perdew, *Phys. Rev. B* **1986**, *33*, 8822-8824.

[35].S. Grimme, J. Antony, S. Ehrlich, H. Krieg, *J. Chem. Phys.* **2010**, *132*.

[36] G. W. T. M. J. Frisch, H. B. Schlegel, G. E. Scuseria, M. A. Robb, J. R. Cheeseman, G. Scalmani, V. Barone, G. A. Petersson, H. Nakatsuji, X. Li, M. Caricato, A. Marenich, J. Bloino, B. G. Janesko, R. Gomperts, B. Mennucci, H. P. Hratchian, J. V. Ortiz, A. F. Izmaylov, J. L. Sonnenberg, D. Williams-Young, F. Ding, F. Lipparini, F. Egidi, J. Goings, B. Peng, A. Petrone, T. Henderson, D. Ranasinghe, V. G. Zakrzewski, J. Gao, N. Rega, G. Zheng, W. Liang, M. Hada, M. Ehara, K. Toyota, R. Fukuda, J. Hasegawa, M. Ishida, T. Nakajima, Y. Honda, O. Kitao, H. Nakai, T. Vreven, K. Throssell, J. A. Montgomery, Jr., J. E. Peralta, F. Ogliaro, M. Bearpark, J. J. Heyd, E. Brothers, K. N. Kudin, V. N. Staroverov, T. Keith, R. Kobayashi, J. Normand, K. Raghavachari, A. Rendell, J. C. Burant, S. S. Iyengar, J. Tomasi, M. Cossi, J. M. Millam, M. Klene, C. Adamo, R. Cammi, J. W. Ochterski, R. L. Martin, K. Morokuma, O. Farkas, J. B. Foresman, and D. J. Fox, Gaussian, Inc. in *Gaussian 09, Revision A 02,*, *Vol.* Wallingford CT, **2016**.

[37] ^{1}H NMR titrations of model compound **6** with TBACl and MTOACl in DCM or acetone do not show noticeable changes in the acquired ^{1}H NMR spectra of **6** before and after the addition of the salts. These findings indicate that Au chloride interactions are not significant.

[38] CCDC 1965694-1965695 contain the supplementary crystallographic data for this paper. These data are provided free of charge by the Cambridge Crystallographic Data Centre.

[39] The ^{1}H NMR titrations of the parent ligand **2** in acetone solution with the two salts provided identical results (see Experimental Section for details). We concluded that **2** acts mainly as homotopic receptor for ion pair binding in acetone and that the stability constant of the anionic chloride complex $[Cl\subset\mathbf{2}]^-$ is larger than 10^4 M^{-1}.

[40].A. Frontera, P. Gamez, M. Mascal, T. J. Mooibroek and J. Reedijk, *Angew. Chem., Int. Ed.* **2011**, *50*, 9564-9583.

[41].A. Frontera and P. Ballester in *CHAPTER 3 Anion–π Interactions: Theoretical Studies, Supramolecular Chemistry and Catalysis*, *Vol.* The Royal Society of Chemistry, **2017**, pp. 39-97.

[42] ^{1}H NMR titration experiments of **1** with tetraethylammonium chloride (TEACl) in acetone also supports the presence of two conformers for the chloride complex in solution (see Experimental Section).

[43] The ^{1}H NMR spectrum acquired after the solid-liquid extraction of tetramethylammonium chloride (TMACl) by **1** dissolved in acetone was similar to the one obtained after the addition of 1-2 equiv. of MTOACl to an acetone solution of the same receptor. The ^{1}H NMR spectrum displayed two different sets of proton signals. This observation indicated the presence of the anionic complex in solution as a mixture of two conformers (see Experimental Section)

[44] We also performed ITC experiments of receptors **1** and **2** with tetraethylammonium chloride (TEACl) in acetone. In both cases, the binding constant values obtained from the fit of the experimental data to a simple 1:1 binding model are between those determined for MTOACl and TBACl (see Experimental Section).

[45] Recent experiments performed in organic solutions, after the publication, indicating that the organometallic receptor **1** and its derivatives evolved over time. This findings suggested that our previous hypothesis about the two conformational complexes was not fully correct.

[46] For some reactions runs, the isolation of pure **1** required multiple precipitations and produced lower yields. This result suggests that the initially isolated pale yellow solid is a mixture of starting material, mono- and bis-gold complex. An increase in the number of equivalents of AuCl(PTA) allowed the isolation, although in low yields, of the bis-gold complex following multiple precipitations.

Chapter 3

Hydrolysis of Aliphatic *Bis*-isonitriles in the Presence of a Polar Super Aryl-Extended Calix[4]pyrrole Container

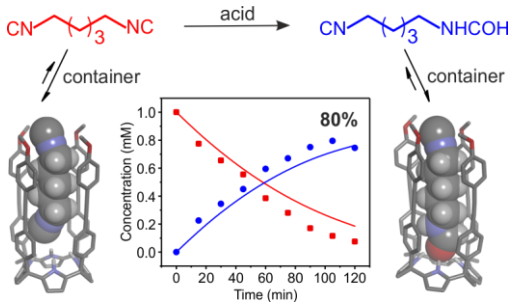

Part of this chapter has been published in:

Q. Sun, L. Escobar, P. Ballester, *Angew. Chem., Int. Ed.* **2021**, *60*, 10359-10365.

UNIVERSITAT ROVIRA I VIRGILI
ARYL AND SUPER ARYL-EXTENDED CALIX[4]PYRROLES: SYNTHESIS AND APPLICATIONS
Qingqing Sun

3.1 Introduction

Molecular containers have been used to mediate and catalyze chemical transformations, as well as to alter the selectivity of reactions occurring in bulk solution.[1,2,3,4,5,6,7,8,9,10,11,12] In solution the *mono*-functionalization of symmetric difunctional compounds featuring independent reacting groups, *i.e.,* the chemical modification of one group has little effect on the reactivity of the other, yields statistical mixtures of products. Generally, such mixtures arising from the reaction makes the purification and isolation of the desired *mono*-reacted (non-symmetric) product challenging and troublesome. The improvement of the selectivity in desymmetrization reactions should increase their application in synthetic strategies. Molecular containers featuring non-polar cavities have been used as reaction flasks to address the *mono*-functionalization problem.[9] For example, Rebek and co-workers employed a water-soluble octa-methyl tetra-benzimidazolone resorcin[4]arene cavitand for increasing the selectivity of: the reduction of *α*,*ω*-*bis*-azides to *mono*-amines,[13] the hydrolysis of *α*,*ω*-*bis*-esters to *mono*-acids, in both acid and basic media,[14] and obtaining *mono*-epoxides from *α*,*ω*-*bis*-enes.[15] In all cases, the product distributions were exceptional, containing the *mono*-functionalized or *mono*-reacted compound in significantly larger extents than the statistically predicted upper limit (36.8%) assuming identical rate constants, $k_1 = k_2$, for each site.[14]

In these applications, the function of the molecular container doubles as supramolecular water-solubilizing and protecting group. The binding of the water-insoluble symmetric substrates to the cavitand produces soluble 1:1 inclusion complexes. The bound symmetric guests adopt folded *J*-conformations, which interconvert rapidly on the ^{1}H NMR chemical shift time scale, most likely, through a “yo-yo” motion.[16,17] The *J*-shape of the bound guest provokes an alternative exposure of only one of the two reactive ends to the bulk solution. The exposed end reacts at the interface of the inclusion complex and water. Subsequently, the equilibrium between the reacted and unreacted ends of the bound guest is modified owing to their different hydrophobicities. Typically, the unreacted site (being less polar) is preferentially hidden from the water/cavitand interface, and its further reaction is inhibited. The selectivity for the *mono*-functionalization reaction, compared to that in the absence of the container, is increased.

The groups of Gibb,[18,19] Nitschke[20] and Dalcanale,[21] among others,[22] have also reported beautiful examples of molecular containers able to sequester reactive groups from external reagents. Both polar and steric factors have strong impacts on the transition state’s energy of reactive groups sequestered in molecular containers.[23,24]

We reported the synthesis and binding properties of water-soluble aryl-extended (AE-C[4]P)[25,26] and super aryl-extended calix[4]pyrrole (SAE-C[4]P)[27] receptors containing *polar* aromatic cavities. We demonstrated that in aqueous solution an AE-C[4]P binds formamides with high affinity, $K_a > 10^4$ M^{-1}. There is selectivity for the *cis*-isomer of primary and secondary formamides,[25] despite the energetic preference for a *trans*-conformation when free in solution.[28] Water-soluble SAE-C[4]Ps

were also effective in the binding of polar neutral substrates such as pyridyl *N*-oxides, $K_a > 10^5$ M^{-1}.[27] The cone conformation of AE-C[4]Ps and SAE-C[4]Ps, *i.e.,* **1** (Figure 3.1a and Figure 3.3), creates sizeable polar aromatic cavities. In water, their inclusion complexes are stabilized not only by the hydrophobic effect and CH-π, NH-π and π-π interactions[29] but also by the establishment of four convergent hydrogen bonds between the pyrrole NHs of the calix[4]pyrrole unit of the receptor and the oxygen atom of the bound guest.[30]

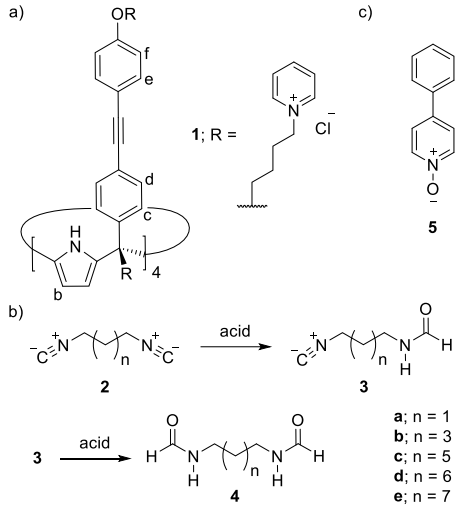

Figure 3.1. a) Chemical structure of SAE-C[4]P **1**; b) Stepwise reaction scheme of the acid-catalyzed hydrolysis of *bis*-isonitrile **2** to give *mono*-formamide **3** and *bis*-formamide **4**; c) Line-drawing structure of 4-phenylpyridine *N*-oxide **5** used as competitive binding guest.

In bulk solution, the acid-catalyzed hydrolysis[31] of long-chain aliphatic *α*,*ω*-*bis*-isonitriles provides the *mono*-hydrolyzed formamide-isonitrile as a statistical mixture with the unreacted starting material and the doubly-hydrolyzed compound (Figure 3.1b). Formamide and isonitrile (isocyanide) functional groups display orthogonal reactivity. Isonitriles participate in multi-component reactions,[32] and are easily attached to biomolecules, making long-chain aliphatic *α*,*ω*-formamide-isonitriles valuable intermediates in organic and bio-organic synthesis. The efficient binding of primary formamides exhibited by water-soluble calix[4]pyrrole receptors and their supramolecular sequestering and protecting abilities suggested an improved selectivity in the hydrolysis reaction of symmetric aliphatic *α*,*ω*-*bis*-isonitriles; we report on these developments here.

Initially, we examined the binding of SAE-C[4]P **1** in water to a series of difunctional aliphatic guests: *bis*-isonitriles **2**, *mono*-formamides **3** and *bis*-formamides **4** (Figure 3.1b). We investigated the acid-catalyzed hydrolysis of a series of *bis*-isonitriles **2a**-**e** in the absence and in the presence of receptor **1** (1 equiv.). The results showed that the presence of **1** induces yield enhancements for the *mono*-formamides (non-symmetric) **3a**-**e** with respect to the statistical mixture of products

obtained in the absence of the receptor. The largest yield enhancement was obtained for the *mono*-formamide **3b**. The modifications in the composition of the reaction mixture and the observed diminution in reaction rates are related to the formation of stable inclusion complexes of the reacting substrates (**2** and **3**) with receptor **1**.

3.2 Results and Discussion

The interaction of SAE-C[4]P **1** with *bis*-isonitrile **2b** and *mono*- and *bis*-formamides, **3b** and **4b**, in D_2O solution was followed using ^1H NMR spectroscopy (see Experimental Section). The ^1H NMR spectrum of a millimolar D_2O solution of free **1** shows broad proton signals due to aggregation or intermediate dynamics between conformational changes (cone and alternate). The addition of 1 equiv. of the *mono*-formamide **3b** provoked the sharpening of the signals of receptor **1**. In addition, the five methylene units of **3b** appeared upfield shifted, locating them within the four aromatic walls of SAE-C[4]P **1**. The addition of more than 1 equiv. of **3b** produced a separate set of signals corresponding to the protons of the free guest (Figure 3.2c).

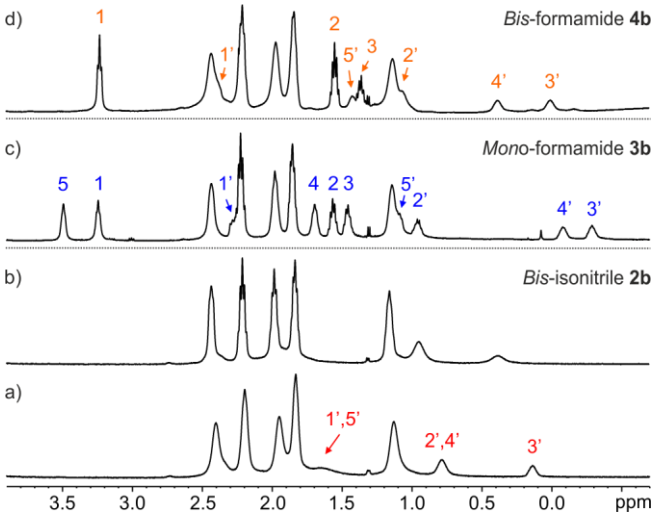

Figure 3.2. Selected region of the ^1H NMR spectra (500 MHz with cryoprobe, D_2O, 313 K) registered for the titration of SAE-C[4]P **1** with *bis*-isonitrile **2b**: a) 0.5 and b) 1 equiv. added. Panels c) and d) display the identical region of the ^1H NMR spectra (298 K) of mixtures containing **1** with 2 equiv. of *mono*-formamide **3b** and *bis*-formamide **4b**, respectively. Primed numbers correspond to the proton signals of bound species: **2b** (in red), **3b** (in blue) and **4b** (in orange).

These results indicated the formation of a 1:1 inclusion complex, **3b⊂1**, for which we can estimate a stability constant value (K_a) larger than 10^4 M^{-1}, with a binding process displaying slow exchange dynamics on the ^1H NMR chemical shift time scale. The five methylene signals of bound **3b** showed quite different upfield shifts ($\Delta\delta < 0$), which reflect the dissimilar anisotropic shielding provided by the four walls of **1** along its aromatic cavity. In contrast to the observations made in inclusion complexes of resorcin[4]arene cavitands,[9] the magnitudes of the upfield shifts are not

directly related to the various depth of the guest's alkyl chain included in the SAE-C[4]P **1**. For example, the formyl proton of bound **3b** appeared at δ = 4.39 ppm ($\Delta\delta$ = - 3.60 ppm) (see Experimental Section, Figure 3.31).

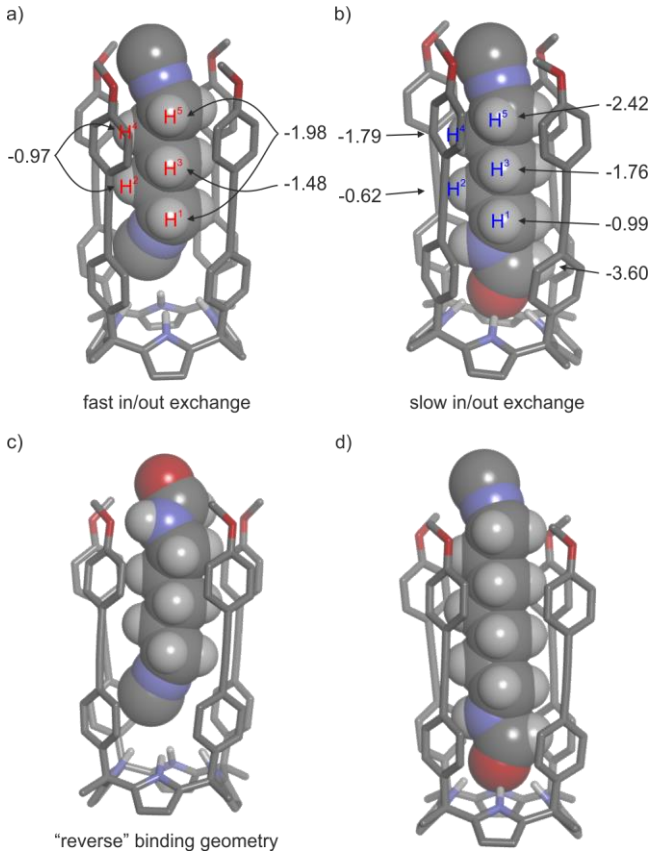

Figure 3.3. Gas-phase energy-minimized structures at the BP86[33,34]-Def2SVP-D3[35] level of theory of simplified 1:1 inclusion complexes: a) **2b⊂1**; b) **3b⊂1**; c) "reverse" binding geometry for **3b⊂1** and d) **3c⊂1**. The complexation-induced shifts (CIS, $\Delta\delta$) experienced by all the non-polar proton signals of the bound guests, **2b** and **3b**, and the dynamics of their in/out chemical exchange process on the ^{1}H NMR chemical shift time scale are indicated. Receptor **1** is shown in line-stick representation with non-polar hydrogen atoms omitted for clarity. Bound guests are depicted as CPK models. The water-solubilizing groups at the upper and lower rims of **1** are pruned to methyl groups. See Figure 3.1 for the line-drawing structures of the compounds.

We observed analogous complexation-induced shifts (CIS, $\Delta\delta$) in the binding of the *cis*-isomers of phenyl and alkyl formamides with a water-soluble AE-C[4]P.[25] This places the *cis*-formamide group of **3b** in the closed and polar aromatic cavity of calix[4]pyrrole **1**.[36] In turn, this arrangement fixes the geometry of the **3b⊂1** complex by placing the isonitrile end of **3b** close to the open rim of the receptor (Figure 3.3b). The two methylene groups *alpha* (H^1) and *beta* (H^2) with respect to the formamide end of **3b** are significantly less shielded ($\Delta\delta$ = -0.99 and -0.62 ppm, respectively). This

is due to their location in the cavity region of **1** surrounded by the alkynyl linkers, which impart a reduced magnetic shielding. In striking contrast, the remaining three methylene units, specially the one *alpha* to the isonitrile end (H^5), although being less deep in the cavity of **1**, experienced more intense shielding ($\Delta\delta$ = -2.42 ppm). These larger CIS derive from the placement of the methylene groups in the upper non-polar aromatic cavity of **1**. In this location, they are exposed to the strong shielding effect exerted by the four terminal phenyl substituents of the receptor. We did not observe additional signals that could be assigned to the hydrogen atoms of the "reverse" binding geometry of the **3b⊂1** complex (Figure 3.3c). Remarkably, the chemical exchange between free and bound **3b** was fast on the EXSY time scale (t_{mix} = 0.3 s). The observed chemical exchange cross-peaks were used for unequivocal assignment of the proton signals of bound **3b**. The exclusive observation of i + 2 NOE peaks between the methylene proton signals of bound **3b** supports the extended conformation of its alkyl chain.

Table 3.1. Binding constant values (K_a) determined using ITC experiments for the 1:1 complexes of receptor **1** with guests **2b**-**4b** in water at 313 K and their corresponding free energies (ΔG). Error values in K_a are reported as standard deviations and propagated to ΔG. The heat capacities (ΔC_p) were calculated using the ΔH values of ITC experiments performed at 298 and 313 K.

Guest	K_a (M^{-1}) x 10^{-5}	ΔG (kcal·mol^{-1})	ΔC_p (cal·mol^{-1}·K^{-1})
2b	1.3 ± 0.1	7.3 ± 0.1	-240
3b[a]	6.9 ± 0.9	8.3 ± 0.1	-193
4b[a]	9.2 ± 0.1	8.5 ± 0.1	-233

[a] The reported K_a values are apparent (K_{app}) because only the *cis*-isomer of the guests binds the receptor. K_a and K_{app} have similar magnitudes when the percentage of the *cis*-isomer in solution is significant, as is the case here. See reference 25 for a more detailed analysis of the ratio between these constant values.

The binding of the symmetric *bis*-formamide **4b** with the SAE-C[4]P **1** produced identical results (see Figure 3.2d and Experimental Section). That is, a 1:1 inclusion complex of **4b** with $K_a > 10^4$ M^{-1}, and slow bound/free exchange dynamics on the ^{1}H NMR chemical shift time scale. Fast exchange with the free counterpart on the EXSY time scale was detected, but not tumbling of the bound guest on the same time scale. We observed five separate signals for the methylene protons of bound **4b**. The lack of symmetry and the magnitude of the upfield shifts experienced by the methylene signals in the **4b⊂1** complex indicated that a *cis*-formamide end is bound by the calix[4]pyrrole unit of **1** while the other formamide end, in *cis* (15%) and *trans* (85%) conformation, occupies the upper non-polar aromatic cavity. We performed the assessment of the binding constant values for the **3b⊂1** and **4b⊂1** complexes using ITC experiments (Table 3.1).

A bound symmetric difunctional guest, having five methylene groups and experiencing fast tumbling on the ^{1}H NMR chemical shift time scale inside the cavity of **1**, should lead to the

observation of only three signals. At 313 K, we observed only three upfield shifted signals in the ^{1}H NMR spectrum of mixtures of the symmetric *bis*-isonitrile **2b** (0.5-1 equiv.) with **1** (Figure 3.2a,b). In this case, however, the binding process displayed fast exchange dynamics on the chemical shift time scale. This latter characteristic serves to explain the symmetric pattern of the proton signals of bound **2b** without the need to invoke fast tumbling of the bound guest. The addition of more than 1 equiv. of **2b** did not induce further changes in the proton signals of **1** (Figure 3.22). This observation allows us to estimate that the binding constant value of the **2b⊂1** complex is also larger than 10^4 M^{-1}. The CIS of the methylene protons of bound **2b** were calculated by extrapolating the fit of its chemical shift changes experienced in the titration of **1** using a theoretical 1:1 binding model (Figure 3.33). The calculated values represent average chemical shifts of the two separate signals expected for both *alpha*- and *beta*-methylene protons in a **2b⊂1** complex experiencing slow dynamics on the chemical shift time scale for its binding and tumbling processes (see CIS for **2b⊂1** in Figure 3.3a). The calculated average CIS values for the two separate *alpha*- and *beta*-methylene proton signals observed for **3b⊂1** or the symmetric *bis*-formamide **4b** in the **4b⊂1** complex are in line with those of the *bis*-isonitrile **2b** in the **2b⊂1** complex. This result suggests that **2b** also adopts an extended conformation when included in the cavity of **1**. In this conformation, one of the two isonitrile groups of **2b** is more accessible to water molecules in the interface between the open end of the SAE-C[4]P **1** and the bulk solution. ITC experiments provided a more accurate value for K_a (**2b⊂1**) (Table 3.1). We calculated large and negative heat capacity values (ΔC_p) for all binding processes. This result indicates that the formation of the complexes, **2b**-**4b⊂1**, is mainly driven by the hydrophobic effect.[37,38] Based on the above, we hypothesized that in the **2b⊂1** complex, the rate of the hydrolysis reaction producing the *mono*-formamide **3b** should be different from that in the bulk solution.

Assuming that the reaction occurs preferentially at the water/SAE-C[4]P interface (isonitrile end located at the open cavity of the container), the resulting *mono*-formamide **3b** will locate the non-reacted isonitrile end buried in the polar cavity of **1** protected from bulk water. This would result in the "reverse" binding geometry of the **3b⊂1** complex (Figure 3.3c). However, as mentioned above, the ^{1}H NMR spectrum of the **3b⊂1** complex (Figure 3.2c) did not show additional proton signals hinting to the presence of this isomer in solution. Nevertheless, we cannot rule out its existence to a reduced extent (< 10^{-4} M). Our expectations were that the inclusion of the *bis*-isonitrile **2b** and the *mono*-formamide **3b** in the cavity of **1** might produce a reduction in the hydrolysis reaction rates of their isonitrile ends exposed at the water/container interface in comparison to the bulk solution. Possible reasons of this putative effect include: a limited exposure to bulk water molecules and a reduced solvation of the transition state. It is worth mentioning that the superior binding properties of SAE-C[4]P **1** for the *mono*-formamide **3b** will reduce its concentration in solution to a large extent.[39]

In order to test our hypotheses, we studied the hydrolysis reaction of *bis*-isonitrile **2b** chaperoned by the synthetic container **1** in water. In doing so, we also wanted to evaluate the potential application of **1** in addressing the *mono*-functionalization problem of **2b**. We performed the hydrolysis reaction by adding 5 equiv. of citric acid as a solution (0.5 M in D_2O) to an NMR tube containing an equimolar mixture (1 mM) of **2b** and **1** in 0.5 mL of D_2O (final pD ~ 3). We monitored the progress of the reaction at 313 K using ^1H NMR spectroscopy (Figure 3.90). The distribution of the species as a function of time was determined using the integral values of the methylene proton signals in the corresponding inclusion complexes.[40] Alternatively, we added 1.2 equiv. of 4-phenylpyridine *N*-oxide **5** (Figure 3.1c) to the reaction mixture at different time intervals (Figure 3.93). *N*-oxide **5** is a competitive guest[27] that displaces the reacting species bound in the cavity of **1** to the bulk solution. Next, we used the integral values of the proton signals of the displaced guests to determine their concentrations. The two methodologies produced similar results.

The formation of the *mono*-formamide **3b** was evident from the loss of symmetry of its inclusion complex. Please note that we assigned a preferred binding geometry for the **3b⊂1** complex fixing the formamide group in the calix[4]pyrrole unit and having an extended conformation for the alkyl spacer (*vide supra*). After *ca.* 2 h, the composition of the reaction mixture contained the *mono*-formamide **3b** in an amount close to 80% (Figure 3.4c). This result suggests that the remaining isonitrile group in the **3b⊂1** complex is less accessible to bulk water. It also represents a significant improvement of the theoretical 36.8% predicted by Rebek and co-workers in the *mono*-functionalization of symmetrical difunctional substrates having independent reacting groups.[14] The isolation of the *mono*-formamide **3b** was possible by extracting it from the neutralized aqueous solution using ethyl acetate (Figure 3.100).

$$\mathbf{2b}\subset\mathbf{1} \xrightarrow{k_1} \mathbf{3b}\subset\mathbf{1} \quad (1)$$

$$\mathbf{3b}\subset\mathbf{1} \xrightarrow{k_2} \mathbf{4b}\subset\mathbf{1} \quad (2)$$

In analogy to the Rebek's report,[14] we fit the experimental concentration data *vs* time to a theoretical kinetic model of two consecutive first-order irreversible reaction steps, Eqs. 1 and 2 (model 1), using COPASI kinetic modeling software. From the fit of the data, we obtained the rate constant values $k_1 = 1.7 \times 10^{-2}$ min^{-1} and $k_2 = 2.3 \times 10^{-3}$ min^{-1} (Figure 3.4a, dashed lines). Based on this model, the determined rate constant values for the hydrolysis reactions in the water/container interface show that the first step (Eq. 1) is seven-fold faster than the second one (Eq. 2). This result is difficult to reconcile with the experimental observation made for the **3b⊂1** complex, which preferentially locates the reactive isonitrile end at the open cavity of the container not providing an increased protection for its hydrolysis. Moreover, model 1 disregards that the reactions can also take place in the bulk solution by assuming that the rates are very slow and the concentration of the free substrates negligible. However, the *bis*-isonitrile **2b** and the *mono*-formamide **3b** are perfectly soluble in water at millimolar concentrations.

Using identical conditions, we performed the hydrolysis experiment of the *bis*-isonitrile **2b** in the absence of container **1**. The reaction profile showed also a good fit to two consecutive first-order irreversible reactions, Eqs. 3 and 4 (model 2), with k_3 = 7.0 x 10^{-2} min^{-1} and k_4 = 3.5 x 10^{-2} min^{-1} (Figure 3.4b, solid lines).

$$\mathbf{2b} \xrightarrow{k_3} \mathbf{3b} \quad (3)$$

$$\mathbf{3b} \xrightarrow{k_4} \mathbf{4b} \quad (4)$$

The selectivity of the reaction for the *mono*-formamide **3b** reached a maximum of 50%, in agreement with the theoretical statistical distribution for identical microscopic reaction rate constants. As could be expected from a protective/sequestering effect of the container, the calculated rate constant values in the absence of **1** increased more than four-fold with respect to those determined above. For this reason, the 50% maximum concentration of **3b** was obtained after 20 min of reaction compared to *ca.* 2 h needed to produce **3b** in an extent of 80% in the presence of **1**.

Having determined the rate constants for the hydrolysis reaction of **2b** in the bulk solution and the binding constants of the inclusion complexes of **1** with all the species at 313 K, we decided to mathematically analyze the hydrolysis data in the presence of **1** using a more elaborate kinetic model. This model includes two consecutive irreversible reactions occurring in the bulk solution, Eqs. 3 and 4, and the reversible formation of three complexes: **2b⊂1**, **3b⊂1** and **4b⊂1**, Eqs. 5-7 (model 3). It also assumes that the rates of the hydrolysis reaction of the bound substrates are negligible.

$$\mathbf{2b} + \mathbf{1} \underset{}{\overset{K_a(\mathbf{2b}\subset\mathbf{1})}{\rightleftharpoons}} \mathbf{2b}\subset\mathbf{1} \quad (5)$$

$$\mathbf{3b} + \mathbf{1} \underset{}{\overset{K_a(\mathbf{3b}\subset\mathbf{1})}{\rightleftharpoons}} \mathbf{3b}\subset\mathbf{1} \quad (6)$$

$$\mathbf{4b} + \mathbf{1} \underset{}{\overset{K_a(\mathbf{4b}\subset\mathbf{1})}{\rightleftharpoons}} \mathbf{4b}\subset\mathbf{1} \quad (7)$$

Fixing k_3 and k_4 to the values determined in the absence of **1**, and K_a (**2b⊂1**), K_a (**3b⊂1**) and K_a (**4b⊂1**) to the measured magnitudes (Table 3.1), within experimental error, also produced a reasonable fit to the experimental distribution of the species for the time course of the hydrolysis reaction of **2b** chaperoned by **1** (Figure 3.4c, solid lines).

Remarkably, the theoretical kinetic models 1 and 3 produced quite different results in the simulations of the time course for the hydrolysis reaction of **2b** chaperoned by 1.5 equiv. of **1**. Model 1 considers that the hydrolysis reactions take place exclusively in the bound substrates and forecasts no changes in reaction rates.[41] Conversely, model 3 assuming that only the free species are hydrolyzed in the bulk aqueous solution projects a significant reduction in reaction rates owing

to the increased sequestering effect of the free reacting species by complexation with the additionally added container.

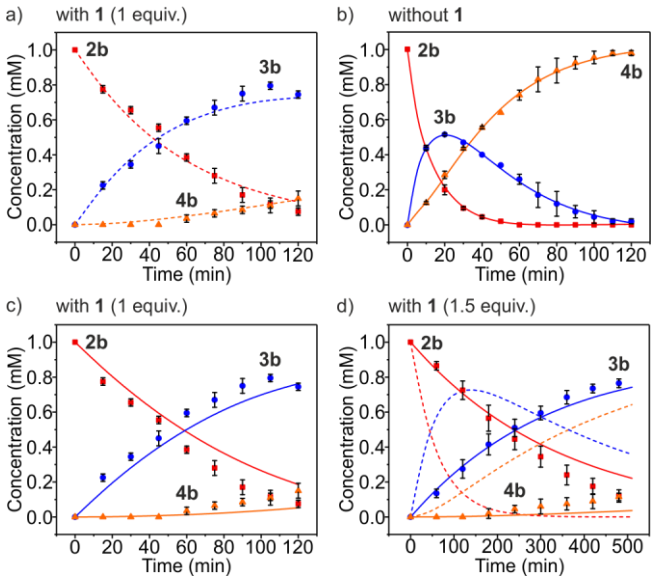

Figure 3.4. Plots of the concentration of the species *vs* time for the acid-catalyzed hydrolysis of *bis*-isonitrile **2b**: a) with 1 equiv. of **1**; b) without container; c) with 1 equiv. of **1** and d) with 1.5 equiv. of **1**. Dashed lines represent fit/simulation of the kinetic data to model 1 in a) and d). Solid lines represent fit/simulation of the kinetic data to model 2 in b) and model 3 in c) and d). Error bars are standard deviations.

In order to evaluate which of the two models was most reliable, we experimentally undertook the hydrolysis of **2b** in the presence of 1.5 equiv. of **1**. Figure 3.4d displays the experimental time course of the reaction (points). The dashed and solid lines represent the simulated kinetic profiles using models 1 and 3, respectively. The simulation of the experimental data to model 3 is good, suggesting that it better explains the observed selectivity enhancement in the acid-catalyzed hydrolysis of **2b**. In short, container **1** sequesters **2b** and **3b** offering protection to their isonitrile end groups towards the hydrolysis reaction. The hydrolysis of the substrates occurs mainly as the free species present in the bulk solution. Because the concentrations of the free reactants are very low, their hydrolysis reaction rates are reduced. This is specially the case for the *mono*-formamide **3b**, whose concentration free in solution becomes relevant when close to 80% of **2b** has reacted.

To evaluate the scope and generality of the sequestering and protection effect delivered by the synthetic chaperone **1** in improving the selectivity for the acid-catalyzed hydrolysis of symmetric aliphatic *α*,*ω*-*bis*-isonitriles, we used a series of shorter and longer homologues of **2b** (Figure 3.1b). In the case of the *bis*-isonitrile **2a**, having a spacer with three methylene groups, the reaction selectivity for the *mono*-formamide **3a** was reduced to 70% and the reaction rate was just slightly diminished compared to that in the absence of **1**. The maximum percentage of **3a** was

obtained after 40 min of reaction instead of *ca.* 2 h required for **3b**. Taking into account the smaller binding affinities of the shorter substrates **2a** and **3a** for **1** (see Experimental Section), compared to the longer counterparts **2b** and **3b**, the obtained results can be simply explained by invoking an attenuation in the sequestering effect of the container. Also in this case, model 3 provides a good fit to the obtained hydrolysis kinetic data (Figure 3.89).

Longer *bis*-isonitriles **2c**-**e**, having seven to nine methylene groups as spacers, and their corresponding *mono*-formamides **3c**-**e** (Figure 3.1b) display higher affinity for receptor **1** (Tables 3.14 and 3.15). As mentioned above, the hydrophobic effect is an important component in the binding of the homologous series of difunctional aliphatic guests by **1**. The selectivity of the *mono*-formamides **3c**-**e** in the hydrolysis reactions of **2c**-**e** (1% DMSO/D_2O)[42] reaches values of 55-65%. The achievement of these selectivities require extensive reaction times (3 – 8 h). On the other hand, the hydrolysis reactions of **2c**-**e** in the absence of **1** (see Experimental section) produced similar results to those discussed above for **2b**.[43] Taking together, these results suggest that the longer symmetric difunctional substrates being more hydrophobic are present in reduced concentrations in the bulk solution. On the other hand, the formed inclusion complexes with **1** might provide a decrease in the hydrolysis rate of the bound isonitrile end group that is located close to the open cavity of the container but not inhibition (total protection). This is due to the increased protrusion of the isonitrile end groups of these complexes into the water/container interface (see Figure 3.3d for the energy-minimized structure of the **3c⊂1** complex).

3.3 Conclusions

In summary, we demonstrated that, in water solution, the octa-pyridinium SAE-C[4]P **1** forms highly stable 1:1 inclusion complexes with a series of symmetric and non-symmetric difunctional aliphatic guests: *bis*-isonitriles, *bis*-formamides and formamide-isonitriles. The *cis*-conformation of the formamide end group is preferentially included in the deep aromatic cavity of **1**. Four hydrogen bonds are established between the oxygen atom of the *cis*-formamide and the four pyrrole NHs of the calix[4]pyrrole unit of **1**. The large and negative heat capacity values measured for the complexation processes indicate that the hydrophobic effect is important for binding. Remarkably, the complexation induced shifts (CIS) experienced by the methylene groups in the bound guests are not related to its depth in the aromatic cavity of **1**. The addition of 1 equiv. of container **1** to the acid-catalyzed hydrolyses of the *bis*-isonitriles modifies the reaction selectivity towards the *mono*-formamides and the reaction rates compared to those in the bulk aqueous solution. The mathematical analysis of the kinetic data suggests that the influence of the container **1** is mainly related to sequestration, due to complexation, of the reacting substrates from solution. In addition, the hydrolysis reaction of the isonitrile group in the bound substrates occurs with rate constants that are smaller than in solution. The protection level offered by **1** to the hydrolysis reaction of the bound guests depends on their length. For substrates having a spacer of five methylene groups (**2b** and **3b**), their hydrolysis reaction seems to be inhibited in the bound state. The right

combination of binding affinity and protection offered by **1** leads, after *ca.* 2 h of reaction time, to a maximum of 80% selectivity for the *mono*-formamide **3b** in the hydrolysis of the *bis*-isonitrile **2b**. To the best of our knowledge, the effect exerted by a synthetic container, featuring a polar aromatic cavity (**1**), on the chemical selectivity of a desymmetrization reaction in water solution and its proposed function mechanism are unprecedented.[44]

3.4 Experimental Section

3.4.1 General information and instruments

Reagents were obtained from commercial suppliers and used without further purification unless otherwise stated. All solvents were commercially obtained and used without further purification except pyrrole which was distilled and freshly used. Dry solvents were taken from a solvent system MB SPS 800. THF, Et_3N, DIPEA and iPr_2NH were dried, distilled and degassed by three freeze-pump-thaw cycles before used in the cross-coupling reactions. Routine ^1H NMR and ^{13}C NMR spectra were recorded on a Bruker Avance 300 (300 MHz for ^1H NMR and 75 MHz for ^{13}C NMR), Bruker Avance 400 (400 MHz for ^1H NMR and 100 MHz for ^{13}C NMR), Bruker Avance 500 (500 MHz for ^1H NMR and 125 MHz for ^{13}C NMR) or Bruker Avance 500 with cryoprobe (500 MHz for ^1H NMR and 125 MHz for ^{13}C NMR). Deuterated solvents used are indicated in the characterization and chemical shifts are given in ppm. Residual solvent peaks were used as reference.[45] All NMR *J* values are given in Hz. COSY, NOESY, ROESY, HMQC and HMBC experiments were recorded to help with the assignment of ^1H and ^{13}C signals. High Resolution Mass Spectra (HRMS) were obtained on a Bruker HPLC-TOF (MicroTOF Focus) with ESI as ionization mode and Bruker HPLC-QqTOF (MaXis Impact) with ESI as ionization mode. ITC experiments were performed using a MicroCal VP-ITC MicroCalorimeter with the VP Viewer 2000 software. The association constants and the thermodynamic parameters were obtained from the fit of the titration data to the "one set of sites" binding model using the MicroCal ITC Data Analysis module. Column chromatography was performed with silica gel technical grade (Sigma-Aldrich), pore size 60 Å, 230-400 mesh particle size, 40-63 μm particle size and Thin Layer Chromatography (TLC) analysis on silica gel 60 F254.

3.4.2 Theoretical kinetic models used for the fit and simulation of the reaction profiles

Hydrolysis of *bis*-isonitriles in the absence of container

The kinetic data (concentration *vs.* time) obtained from the acid-catalyzed hydrolysis of *bis*-isonitriles **2a**-**e** in water were fit to the corresponding theoretical kinetic model using the Parameter Estimation module of COPASI Software Version 4.25. We introduced the theoretical kinetic model shown below that considers two consecutive first-order reactions.

Model 2

1) **2** → **3**; k_3
2) **3** → **4**; k_4

k_3 and k_4 are the rate constants for the hydrolysis reactions of 1) *bis*-isonitrile **2** and 2) *mono*-formamide **3**, respectively. The experimental data were fit to the theoretical kinetic model returning the rate constants k_3 and k_4.

Hydrolysis of *bis*-isonitriles in the presence of container **1**

The reaction profiles for the acid-catalyzed hydrolysis of *bis*-isonitriles **2a**-**c** in the presence of the super aryl-extended calix[4]pyrrole **1**, were fit/simulated using the Time Course or Parameter Estimation modules of COPASI Software Version 4.25. We used two different theoretical kinetic models shown below. On the one hand, model 1 considers two consecutive first-order reactions for the hydrolysis of the substrates in the inclusion complexes. On the other hand, model 3 considers the two consecutive first-order reactions for the hydrolysis of the substrates free in solution and the formation of their corresponding inclusion complexes.

Model 1

1) **2⊂1** → **3⊂1**; k_1
2) **3⊂1** → **4⊂1**; k_2

k_1 and k_2 are the rate constants for the hydrolysis reactions of 1) *bis*-isonitrile **2** and 2) *mono*-formamide **3**, respectively, in the inclusion complexes. The experimental data were fit to the theoretical kinetic model returning the rate constants k_1 and k_2.

Model 3

1) **2** → **3**; k_3
2) **3** → **4**; k_4
3) **2** + **1** → **2⊂1**; k_5
4) **2⊂1** → **2** + **1**; k_6
5) **3** + **1** → **3⊂1**; k_7
6) **3⊂1** → **3** + **1**; k_8
7) **4** + **1** → **4⊂1**; k_9
8) **4⊂1** → **4** + **1**; k_{10}

k_3 and k_4 are the rate constants for the hydrolysis reactions of 1) *bis*-isonitrile **2** and 2) *mono*-formamide **3**, respectively, in the bulk solution. We fixed the values of k_3 and k_4, within experimental error, obtained in the hydrolysis reaction of the substrates in the absence of container (model 2).

The six rates constants k_5-k_{10} are pairwise related by three reversible equilibrium binding constants:

K_a (**2⊂1**) = k_5/k_6; K_a (**3⊂1**) = k_7/k_8; K_a (**4⊂1**) = k_9/k_{10}

The binding constant values (K_a) used were those determined by NMR titrations and ITC experiments, within experimental error.

We assumed dissociation rate constants k_6, k_8 and k_{10} in the order of 3 s^{-1}. For a K_a (guest⊂**1**) = 10^5 M^{-1} it will translate into k_5, k_7 or k_9 = 10^5 M^{-1} x 3 s^{-1} = 3 x 10^5 $M^{-1}{\cdot}s^{-1}$. We also need to provide the software with initial concentrations of the substrate **2** and the container **1**. We computed the simulations and compared with the experimental reaction profiles.

The comparison between experimental and simulated reaction profiles indicated that model 3 is better than model 1 to explain the selectivity enhancement in the acid-catalyzed hydrolysis of **2** in the presence of container **1**.

3.4.3 Synthesis and characterization data

Bis-isonitriles **2a-e**

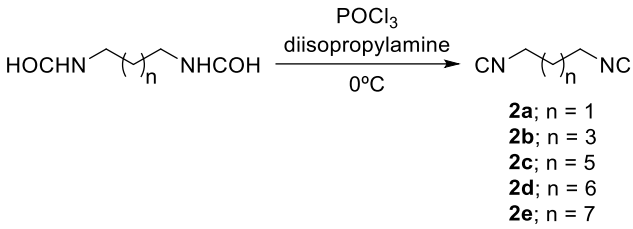

Scheme 3.1. Synthesis of compounds **2a-e.**

General procedure

Bis-isonitriles **2a**-**e** were prepared following similar procedures previously described in the literature.[46,47] The corresponding *bis*-formamide **4a**-**e** (1.90 mmol) was dissolved in dry CH_2Cl_2 (0.56 M of reactant). Subsequently, dry diisopropylamine (19 mmol) was added. The solution mixture was cooled to 0°C and phosphoryl chloride (5.30 mmol) was added dropwise. The reaction was stirred at 0°C for 2 h. After that, the crude was poured into ice water (10 mL) containing K_2CO_3 (2 g). The resulting emulsion was stirred for 1 h at r.t. The organic layer was separated and the crude was further extracted with CH_2Cl_2. The combined organic layers were dried (Na_2SO_4), filtered and concentrated. The crude was purified by silica gel column chromatography to afford the product as a yellow oil.

Characterization

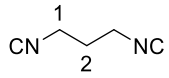

2a

Bis-isonitrile **2a**: Yield = 55%. Rf = 0.3 (2:1 Hexane:EtOAc). ^{1}H NMR (400 MHz, D_2O, 298 K): δ (ppm) = 3.72 (m, 4H); 2.11 (m, 2H). $^{13}C\{^{1}H\}$ NMR (100 MHz, D_2O, 298 K): δ (ppm) = 152.5; 38.5; 27.6. MS (EI) *m/z*: $[C_5H_5N_2]^+$ 93.0.

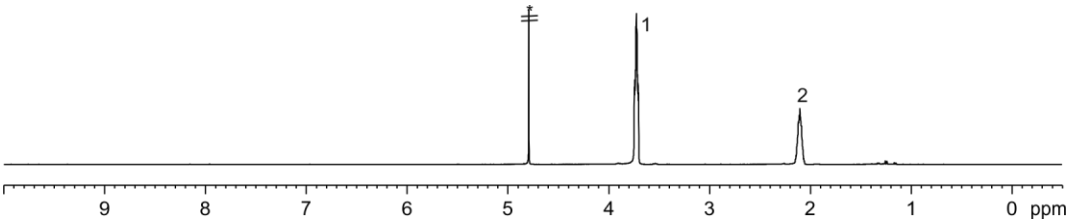

Figure 3.5. ^{1}H NMR (400 MHz, D_2O, 298 K) spectrum of **2a**. *Residual solvent peak.

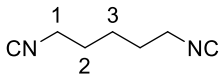

2b

Bis-isonitrile **2b**: Yield = 56%. Rf = 0.3 (4:1 Hexane:EtOAc). ^{1}H NMR (400 MHz, $CDCl_3$, 298 K): δ (ppm) = 3.47 (m, 4H); 1.79 (m, 4H); 1.65 (m, 2H). $^{13}C\{^{1}H\}$ NMR (100 MHz, $CDCl_3$, 298 K): δ (ppm) = 156.8; 41.4; 28.3; 23.4. The ^{1}H NMR spectrum ($CDCl_3$) is in agreement with that reported in literature.[48]

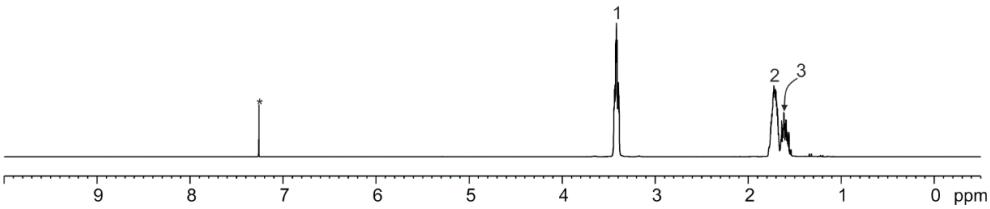

Figure 3.6. ^{1}H NMR (400 MHz, $CDCl_3$, 298 K) spectrum of **2b**. *Residual solvent peak.

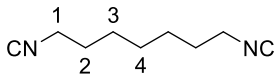

2c

Bis-isonitrile **2c**: Yield = 54%. Rf = 0.3 (4:1 Hexane:EtOAc). ^{1}H NMR (500 MHz, $CDCl_3$, 298 K): δ (ppm) = 3.39 (m, 4H); 1.69 (m, 4H); 1.48 (m, 4H); 1.38 (m, 2H). $^{13}C\{^{1}H\}$ NMR (125 MHz, $CDCl_3$,

298 K): δ (ppm) = 156.1; 41.6; 29.0; 28.0; 26.2. The ^{1}H NMR spectrum ($CDCl_3$) is in agreement with that reported in literature.[49]

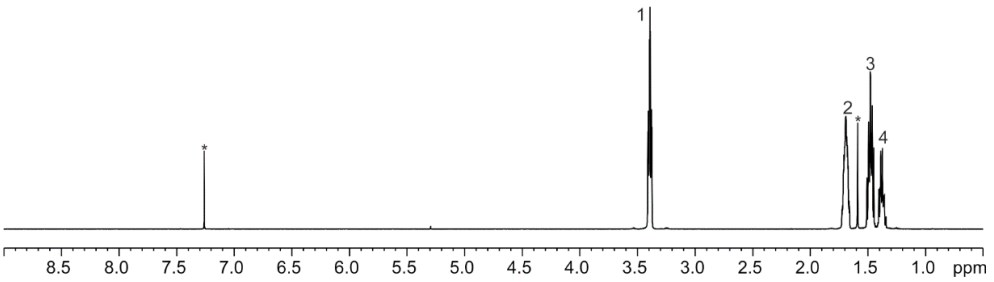

Figure 3.7. ^{1}H NMR (500 MHz, $CDCl_3$, 298 K) spectrum of **2c**. *Residual solvent peaks.

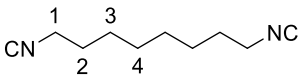

2d

Bis-isonitrile **2d**: Yield = 59%. Rf = 0.3 (4:1 Hexane:EtOAc). ^{1}H NMR (500 MHz, $CDCl_3$, 298 K): δ (ppm) = 3.38 (m, 4H); 1.67 (m, 4H); 1.44 (m, 4H); 1.35 (m, 4H). $^{13}C\{^1H\}$ NMR (125 MHz, $CDCl_3$, 298 K): δ (ppm) = 156.0; 41.7; 29.2; 28.6; 26.4. The ^{1}H NMR spectrum ($CDCl_3$) is in agreement with that reported in literature.[49]

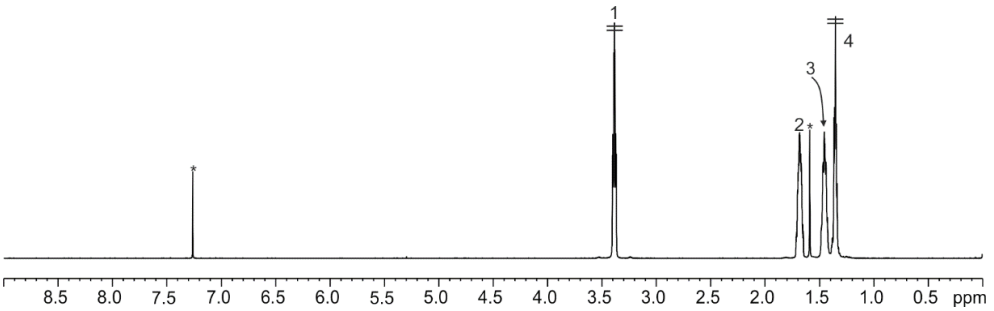

Figure 3.8. ^{1}H NMR (500 MHz, $CDCl_3$, 298 K) spectrum of **2d**. *Residual solvent peaks.

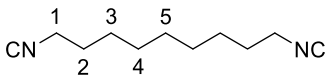

2e

Bis-isonitrile **2e**: Yield = 57%. Rf = 0.3 (4:1 Hexane:EtOAc). ^{1}H NMR (400 MHz, $CDCl_3$, 298 K): δ (ppm) = 3.38 (m, 4H); 1.67 (m, 4H); 1.43 (m, 4H); 1.32 (m, 6H). $^{13}C\{^1H\}$ NMR (100 MHz, $CDCl_3$, 298 K): δ (ppm) = 155.8; 41.7; 29.2; 28.7; 26.4. MS (EI) *m*/*z*: $[C_{11}H_{17}N_2]^+$: 177.1.

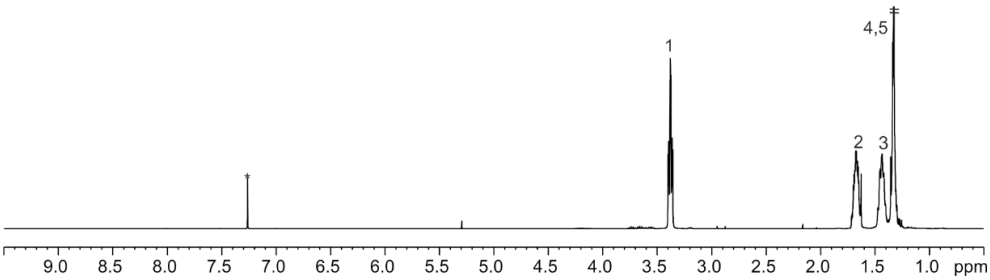

Figure 3.9. ^{1}H NMR (400 MHz, $CDCl_3$, 298 K) spectrum of **2e**. *Residual solvent peak.

Mono-formamide **3a**-**e**

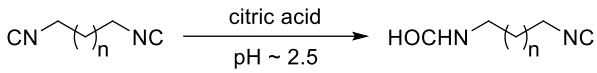

3a; n = 1
3b; n = 3
3c; n = 5
3d; n = 6
3e; n = 7

Scheme 3.2. Synthesis of compounds **3a**-**e**.

General procedure

Mono-formamides **3a**-**e** were prepared following similar procedures previously described in literature.[31] The corresponding *bis*-isonitrile **2a**-**e** (0.19 mmol) was dissolved in water (0.01 M of reactant) and citric acid (1.0 mL from a 0.5 M solution in water) was added. The reaction was stirred at r.t. for 40 min. After that, the reaction was quenched with aqueous saturated $NaHCO_3$ (10 mL). The crude was extracted with ethyl acetate and the organic layer was dried (Na_2SO_4), filtered and concentrated. The crude was purified by column chromatography on silica gel to afford the product as a yellow oil.

Characterization

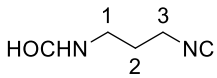

3a

Mono-formamide **3a**: Yield = 22%. Rf = 0.2 (EtOAc). ^{1}H NMR (500 MHz with cryoprobe, D_2O, 298 K): δ (ppm) = 8.08 (s, 0.85H); 8.04 (s, 0.15H); 3.57 (m, 2H); 3.41 (t, J = 6.6 Hz, 2H); 1.93 (m, 2H). $^{13}C\{^{1}H\}$ NMR (125 MHz with cryoprobe, D_2O, 298 K): δ (ppm) = 165.0; 151.8; 39.5; 35.5; 28.2 (*trans*-isomer, major isomer in solution). HRMS (ESI-TOF) *m*/*z*: $[M+Na]^+$ Calcd for $C_5H_8N_2NaO$ 135.0529; Found 135.0529.

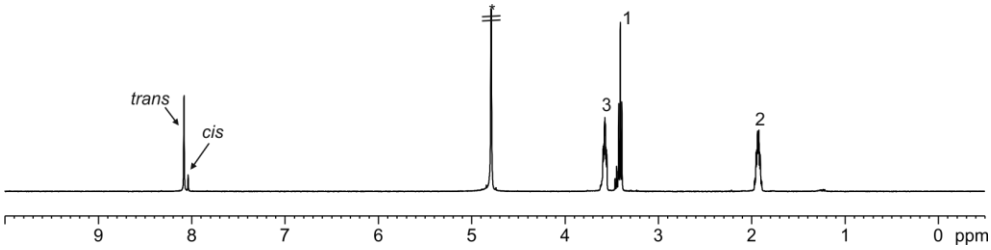

Figure 3.10. ^{1}H NMR (500 MHz with cryoprobe, D_2O, 298 K) spectrum of **3a**. *Residual solvent peak.

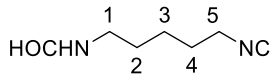

3b

Mono-formamide **3b**: Yield = 23%. Rf = 0.2 (EtOAc). ^{1}H NMR (500 MHz with cryoprobe, D_2O, 298 K): δ (ppm) = 8.04 (s, 0.85H); 7.98 (s, 0.15H); 3.51 (m, 2H); 3.26 (t, J = 6.7 Hz, 2H); 1.71 (m, 2H); 1.58 (m, 2H); 1.48 (m, 2H). ^{13}C{^{1}H} NMR (125 MHz with cryoprobe, D_2O, 298 K): δ (ppm) = 164.1; 150.5; 42.1; 37.9; 27.7; 27.4; 22.8 (*trans*-isomer, major isomer in solution). HRMS (ESI-TOF) *m*/*z*: $[M+Na]^+$ Calcd for $C_7H_{12}N_2NaO$ 163.0842; Found 163.0835.

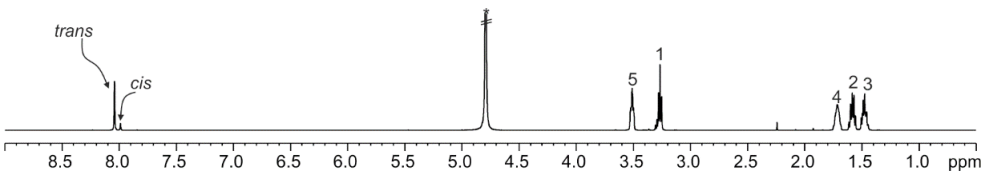

Figure 3.11. ^{1}H NMR (500 MHz with cryoprobe, D_2O, 298 K) spectrum of **3b**. *Residual solvent peak.

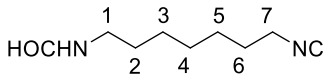

3c

Mono-formamide **3c**: Yield = 23%. Rf = 0.2 (EtOAc). ^{1}H NMR (500 MHz with cryoprobe, D_2O, 298 K): δ (ppm) = 8.03 (s, 0.85H); 7.98 (s, 0.15H); 3.49 (m, 2H); 3.24 (m, 2H); 1.69 (m, 2H); 1.55 (m, 2H); 1.44 (m, 2H); 1.36 (m, 4H). ^{13}C{^{1}H} NMR (125 MHz with cryoprobe, D_2O, 298 K): δ (ppm) = 164.5; 150.1; 41.5; 37.9; 28.1; 27.3; 25.7; 25.4, 25.2 (*trans*-isomer, major isomer in solution). HRMS (ESI-TOF) *m*/*z*: $[M+Na]^+$ Calcd for $C_9H_{16}N_2NaO$ 191.1155; Found 191.1152.

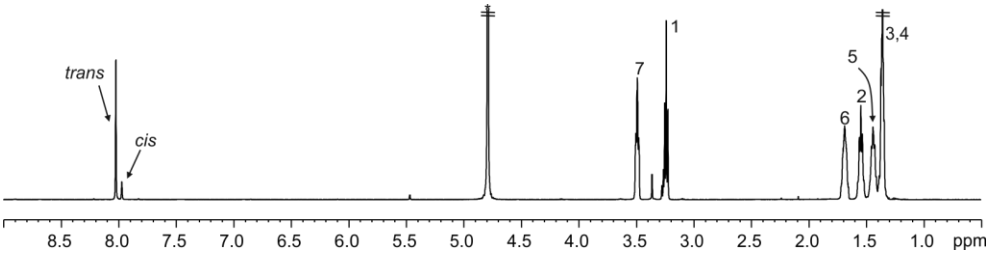

Figure 3.12. ^{1}H NMR (500 MHz with cryoprobe, D_2O, 298 K) spectrum of **3c**. *Residual solvent peak.

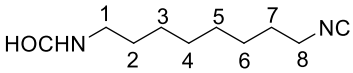

3d

Mono-formamide **3d**: Yield = 27%. Rf = 0.2 (EtOAc). ^{1}H NMR (500 MHz with cryoprobe, $CDCl_3$, 298 K): δ (ppm) = 8.17 (s, 0.85H); 8.05 (d, J = 11.8 Hz, 0.15H); 5.48 (br s, 1H); 3.38 (m, 2H); 3.30 (m, 1.7H); 3.22 (m, 0.3H); 1.68 (m, 2H); 1.53 (m, 2H); 1.44 (m, 2H); 1.34 (m, 6H). ^{13}C{^{1}H} NMR (125 MHz with cryoprobe, $CDCl_3$, 298 K): δ (ppm) = 161.6; 156.1; 41.8; 38.2; 31.4; 29.7; 29.1; 28.7; 26.8; 26.3 (*trans*-isomer, major isomer in solution). HRMS (ESI-TOF) *m*/*z*: [M+Na]$^{+}$ Calcd for $C_{10}H_{18}N_2NaO$ 205.1311; Found 205.1305.

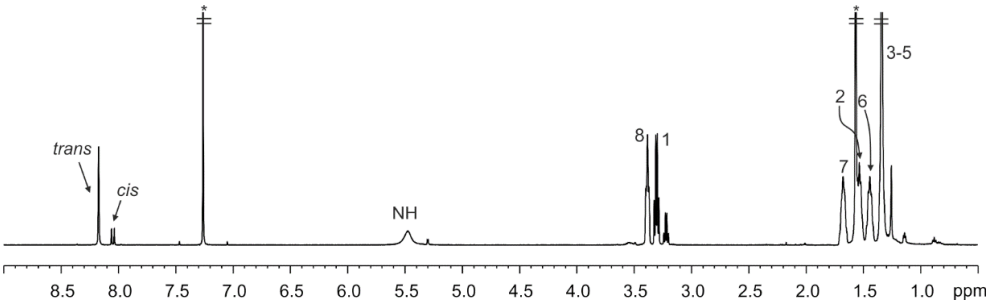

Figure 3.13. ^{1}H NMR (500 MHz with cryoprobe, $CDCl_3$, 298 K) spectrum of **3d**. *Residual solvent peaks.

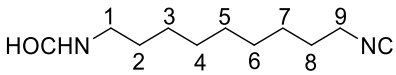

3e

Mono-formamide **3e**: Yield = 21%. Rf = 0.2 (EtOAc). ^{1}H NMR (500 MHz with cryoprobe, $CDCl_3$, 298 K): δ (ppm) = 8.17 (s, 0.85H); 8.04 (d, J = 11.8 Hz, 0.15H); 5.51 (br s, 1H); 3.38 (t, J = 5.6 Hz, 2H); 3.30 (m, 1.7H); 3.21 (m, 0.3H); 1.67 (m, 2H); 1.52 (m, 2H); 1.43 (m, 2H); 1.32 (m, 8H). ^{13}C{^{1}H} NMR (125 MHz with cryoprobe, $CDCl_3$, 298 K): δ (ppm) = 161.2; 155.7; 41.7; 38.3; 31.4; 29.7; 29.4; 29.2; 28.7; 26.9; 26.4 (*trans*-isomer, major). HRMS (ESI-TOF) *m*/*z*: [M+Na]$^{+}$ Calcd for $C_{11}H_{20}N_2NaO$ 219.1468; Found 219.1463.

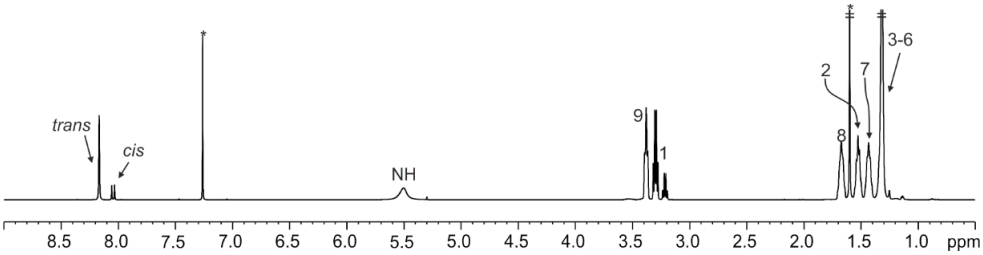

Figure 3.14. ^{1}H NMR (500 MHz with cryoprobe, $CDCl_3$, 298 K) spectrum of **3e**. *Residual solvent peaks.

Table 3.2. *Cis*/*trans* isomeric ratio of compounds **3a**-**e** measured by integration of the corresponding proton signals in the ^{1}H NMR spectrum.

Solvent	***cis*/*trans* ratio**
$CDCl_3$	15:85
D_2O	15:85

Bis-formamides **4a**-**e**

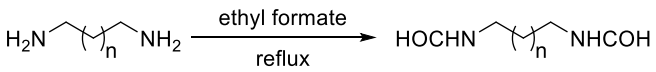

4a; n = 1
4b; n = 3
4c; n = 5
4d; n = 6
4e; n = 7

Scheme 3.3. Synthesis of compounds **4a**-**e**.

General procedure

A solution of the corresponding *bis*-amine (4.90 mmol) in ethyl formate (0.50 M of reactant) was refluxed overnight. After that, the crude was concentrated under reduced pressure. The crude was purified by silica gel column chromatography (acetone) to afford the product as a white solid.

Characterization

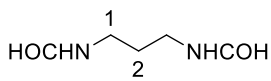

4a

Bis-formamide **4a**: Yield = 85%. ^{1}H NMR (400 MHz, D_2O, 298 K): δ (ppm) = 8.05 (s, 1.7H); 7.98 (s, 0.3H); 3.29 (m, 4H); 1.78 (m, 2H). $^{13}C\{^{1}H\}$ NMR (100 MHz, D_2O, 298 K): δ (ppm) = 165.0; 35.3; 27.9 (*trans*,*trans*-isomer, major isomer in solution). HRMS was reported previously in literature.[50]

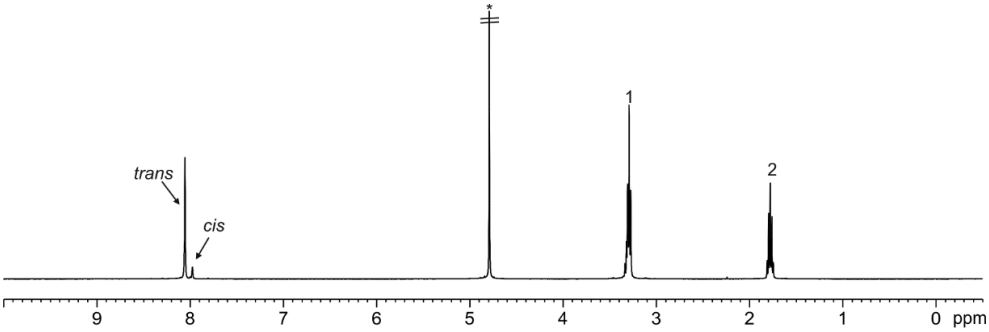

Figure 3.15. ^{1}H NMR (400 MHz, D_2O, 298 K) spectrum of **4a**. *Residual solvent peak.

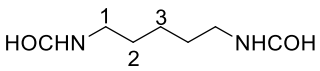

4b

Bis-formamide **4b**: Yield = 85%. ^{1}H NMR (400 MHz, D_2O, 298 K): δ (ppm) = 8.18 (s, 1.7H); 8.04 (s, 0.3H); 3.32 (m, 4H); 1.57 (m, 4H); 1.38 (m, 2H). The ^{1}H NMR spectrum ($CDCl_3$) is in agreement with that reported in literature.[51]

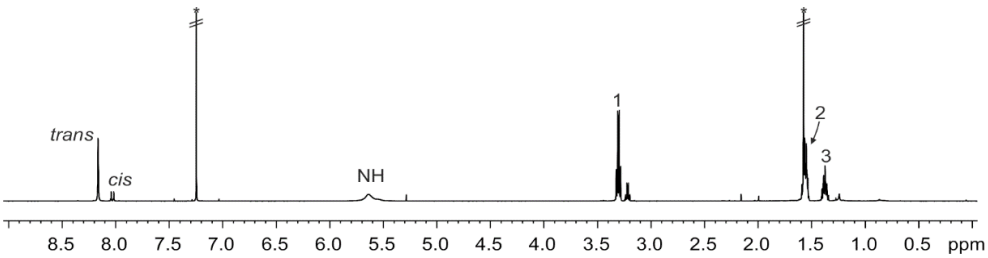

Figure 3.16. ^{1}H NMR (400 MHz, $CDCl_3$, 298 K) spectrum of **4b**. *Residual solvent peaks.

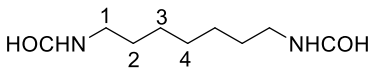

4c

Bis-formamide **4c**: Yield = 93%. ^{1}H NMR (400 MHz, $CDCl_3$, 298 K): δ (ppm) = 8.15 (s, 1.7H); 8.03 (d, J = 11.9 Hz, 0.3H); 5.82 (br s, 2H); 3.38 (m, 3.4H); 3.21 (m, 0.6H); 1.52 (m, 4H); 1.33 (m, 6H). ^{13}C{^{1}H} NMR (100 MHz, $CDCl_3$, 298 K): δ (ppm) = 161.5; 41.7; 38.1; 29.5; 26.7 (*trans,trans*-isomer, major isomer in solution). HRMS (ESI-TOF) *m/z*: $[M+Na]^+$ Calcd for $C_9H_{18}N_2NaO_2$ 209.1260; Found 209.1252.

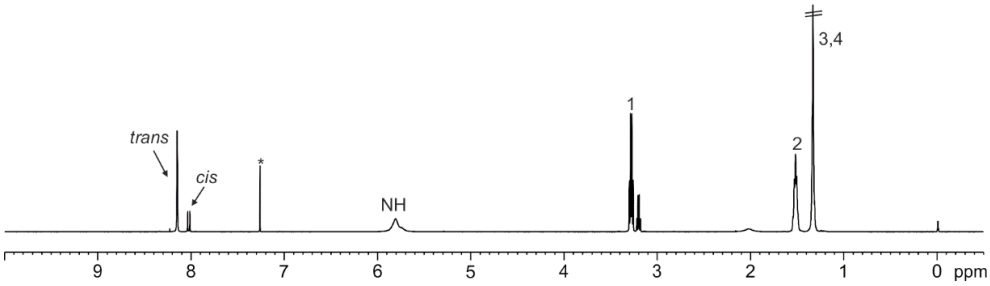

Figure 3.17. ^{1}H NMR (400 MHz, $CDCl_3$, 298 K) spectrum of **4c**. *Residual solvent peak.

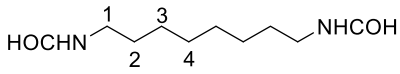

4d

Bis-formamide **4d**: Yield = 85%. ^{1}H NMR (500 MHz, D_2O, 298 K): δ (ppm) = 8.02 (s, 1.7H); 7.97 (s, 0.3H); 3.23 (m, 4H); 1.53 (m, 4H); 1.33 (m, 8H). The ^{1}H NMR spectrum ($CDCl_3$) is in agreement with that reported in literature.[17]

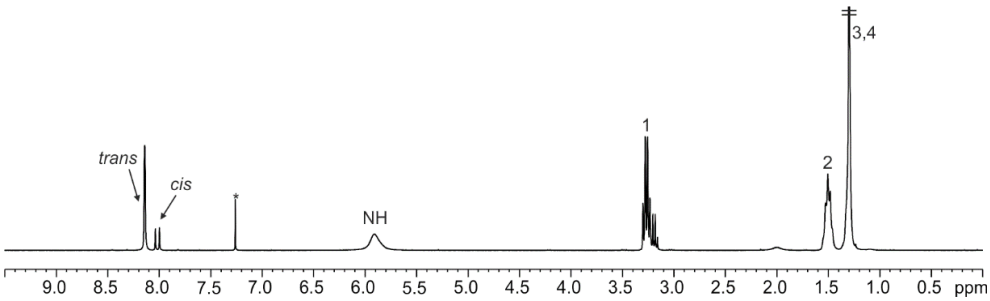

Figure 3.18. ^{1}H NMR (400 MHz, $CDCl_3$, 298 K) spectrum of **4d**. *Residual solvent peak.

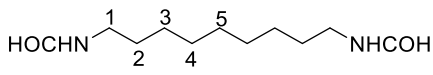

4e

Bis-formamide **4e**: Yield = 96%. ^{1}H NMR (400 MHz, $CDCl_3$, 298 K): δ (ppm) = 8.16 (s, 1.7H); 8.03 (d, J = 11.8 Hz, 0.3H); 5.69 (br, 2H); 3.29 (m, 3.4H); 3.21 (m, 0.6H); 1.51 (m, 4H); 1.30 (m, 10H). The ^{1}H NMR spectrum ($CDCl_3$) was in agreement with that reported in literature.[17]

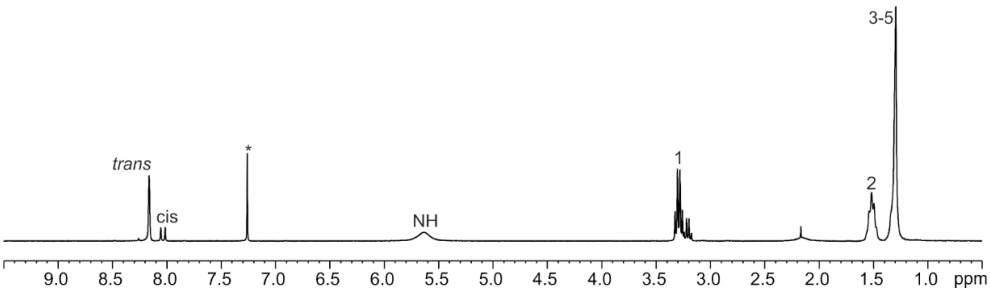

Figure 3.19. ^{1}H NMR (400 MHz, $CDCl_3$, 298 K) spectrum of **4e**. *Residual solvent peak.

Table 3.3. *Cis/trans* isomeric ratio of compounds **4a**-**e** measured by integration of the corresponding proton signals in the ^{1}H NMR spectrum.

Solvent	***cis*/*trans* ratio**
$CDCl_3$	15:85
D_2O	15:85

3.4.4 NMR binding studies and 2D spectra (NOESY, ROESY and DOSY) used in the characterization of selected inclusion complexes

A solution of the host (1 mM) was prepared in D_2O. Subsequently, 0.5 mL of the solution were placed in an NMR tube. A solution of the guest **2a**-**b**, **3a**-**c** or **4a**-**c** was prepared at 20-30-fold higher concentration using the host's solution ([G] = 20-30 mM and [H] = 1 mM). For guests **2c**-**e**, **3d**-**e** and **4d**-**e**, a solution was prepared at 100-fold higher concentration using $(CD_3)_2SO$ ([G] = 100 mM). Immediately, the host solution was titrated by manually injecting incremental amounts of the titrant's solutions using a micro-syringe. A ^{1}H NMR spectrum of the mixture was acquired after each injection and vigorous hand shaking of the NMR tube for few seconds.

NMR binding studies of *bis*-isonitriles **2a**-**e** with octa-pyridinium **1**

Bis-isonitrile **2a**

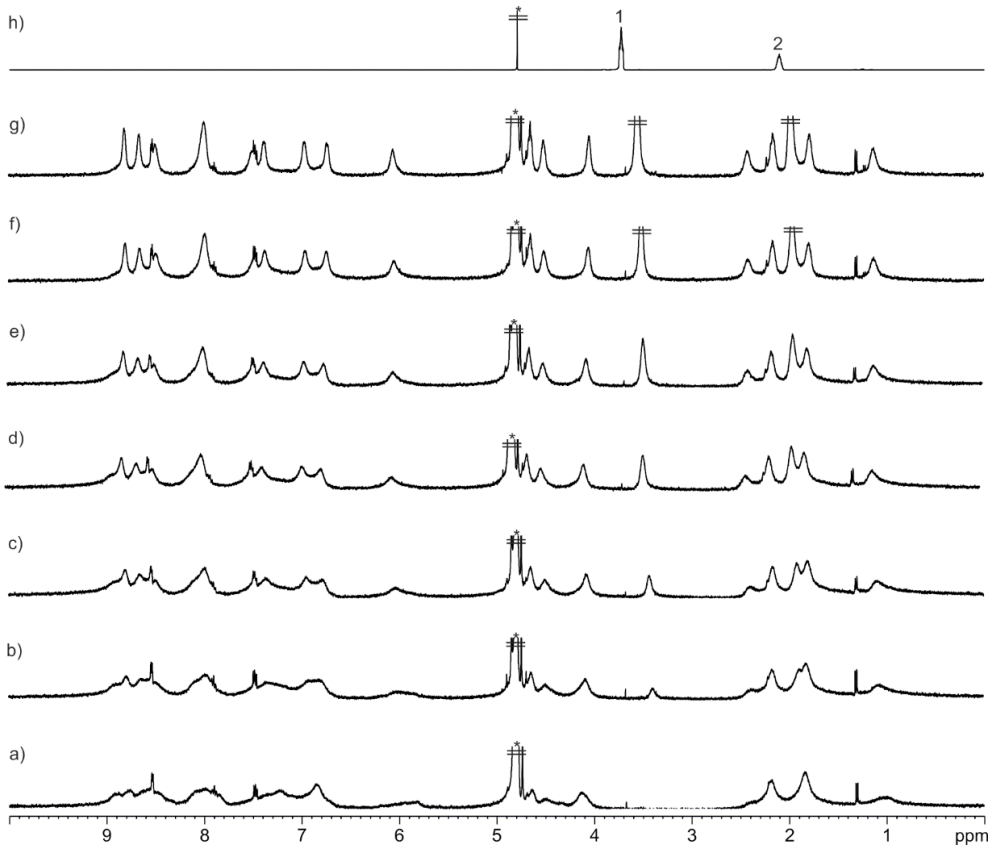

Figure 3.20. ^{1}H NMR (400 MHz, D_2O, 298 K) spectra of the titration of octa-pyridinium **1** with **2a**: a) 0; b) 0.5; c) 1; d) 1.5; e) 2; f) 3 and g) 5 equiv.; h) **2a**. *Residual solvent peak.

Bis-isonitrile **2b**

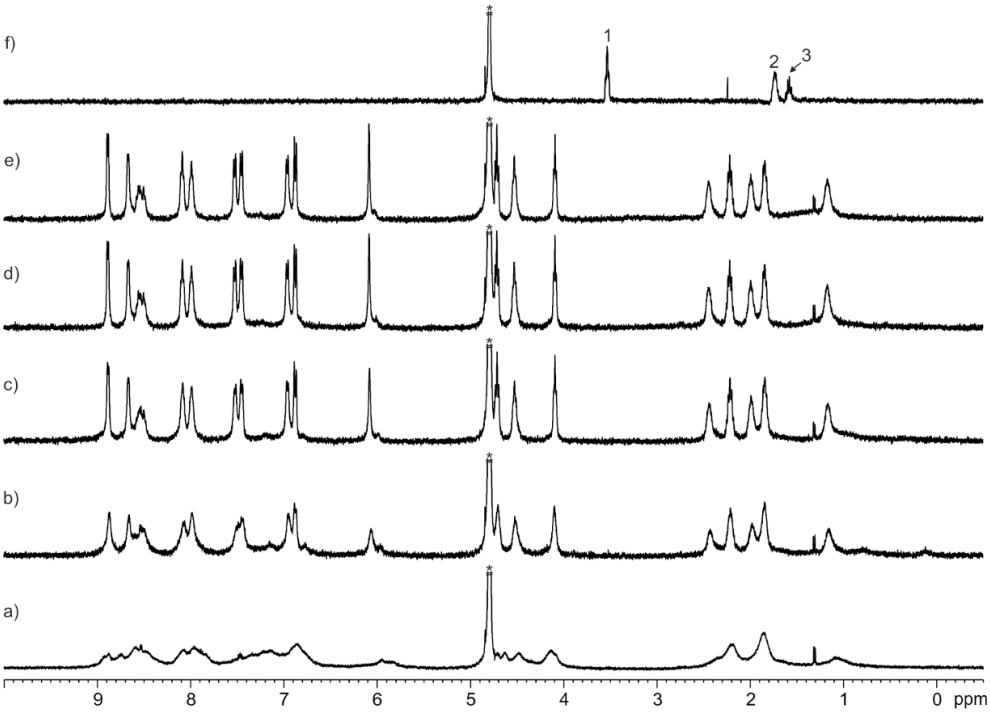

Figure 3.21. ^{1}H NMR (400 MHz, D_2O, 298 K) spectra of the titration of octa-pyridinium **1** with **2b**: a) 0; b) 0.5; c) 1; d) 1.5 and e) 2 equiv.; f) **2b**. *Residual solvent peak.

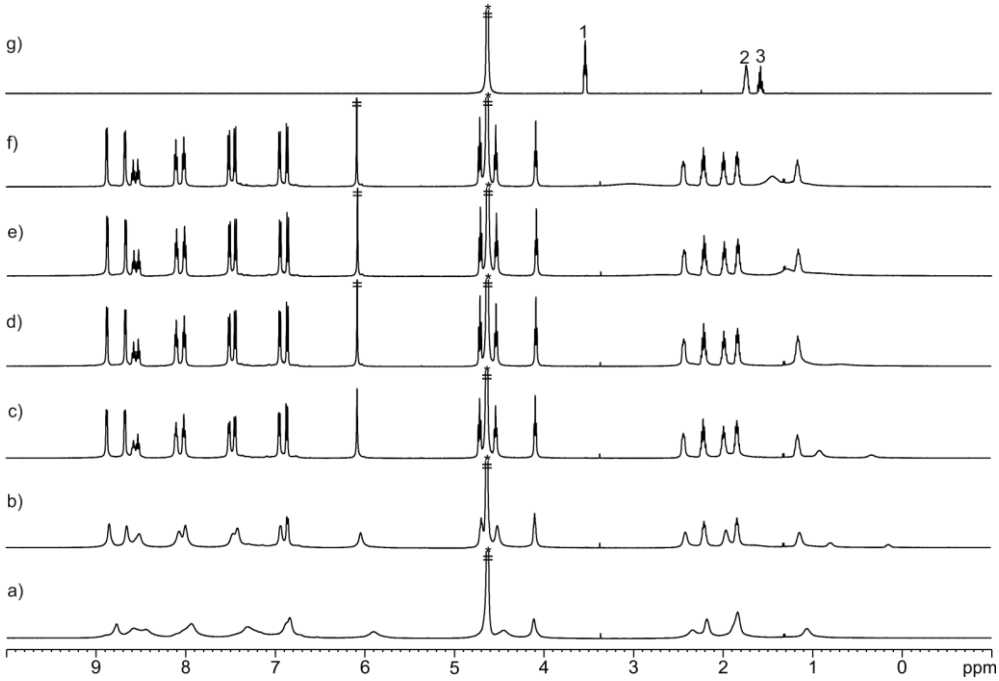

Figure 3.22. Selected ^{1}H NMR (500 MHz with cryoprobe, D_2O, 313 K) spectra of the titration of octa-pyridinium **1** with **2b**: a) 0; b) 0.5; c) 1; d) 1.5; e) 2 and f) 3 equiv.; g) **2b**. *Residual solvent peak.

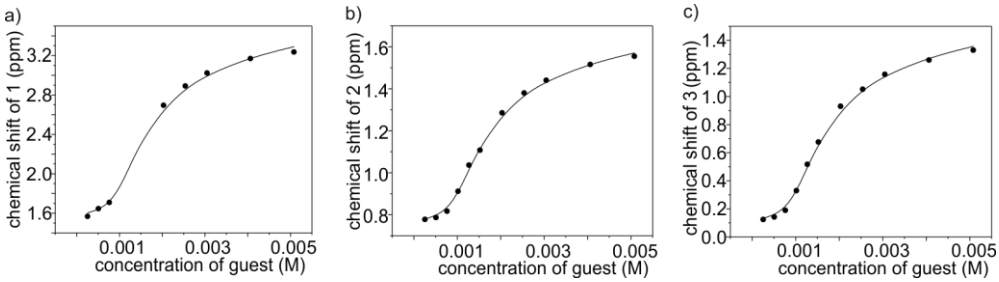

Figure 3.23. Fit of the NMR titration data at 313 K (proton signals H^1, H^2 and H^3 of bis-isonitrile **2b**) to a theoretical 1:1 binding model. The fit returned a binding constant value K_a (**2b**⊂**1**) > 10^4 M^{-1}.

Table 3.4. Chemical shifts of free (δ_{free}) and bound (δ_{bound}) *bis*-isonitrile **2b** and complexation-induced shifts ($\Delta\delta$) at 313 K. The fit of the NMR titration data to a theoretical 1:1 binding model returned the chemical shifts of the proton signals of bound **2b**.

Signal	δ_{free} (ppm)	δ_{bound} (ppm)	$\Delta\delta$ (ppm)
1	3.50	1.52	-1.98
2	1.71	0.74	-0.97
3	1.55	0.07	-1.48

Bis-isonitrile **2c**

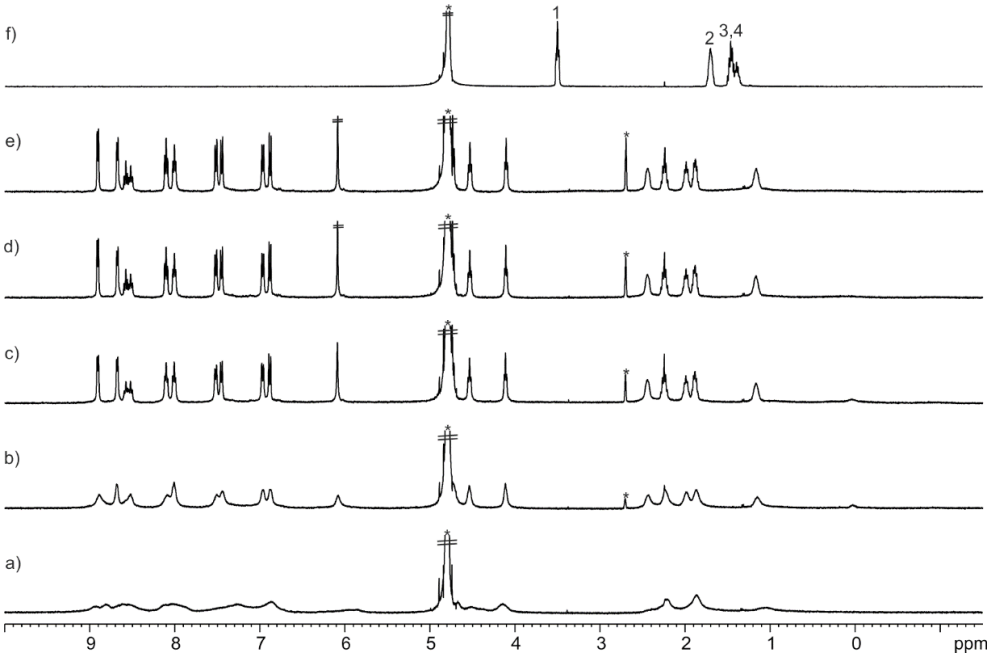

Figure 3.24. ^{1}H NMR (400 MHz, D_2O, 298 K) spectra of the titration of octa-pyridinium **1** with **2c**: a) 0; b) 0.5; c) 1; d) 1.5 and e) 2 equiv.; f) **2c**. *Residual solvent peaks.

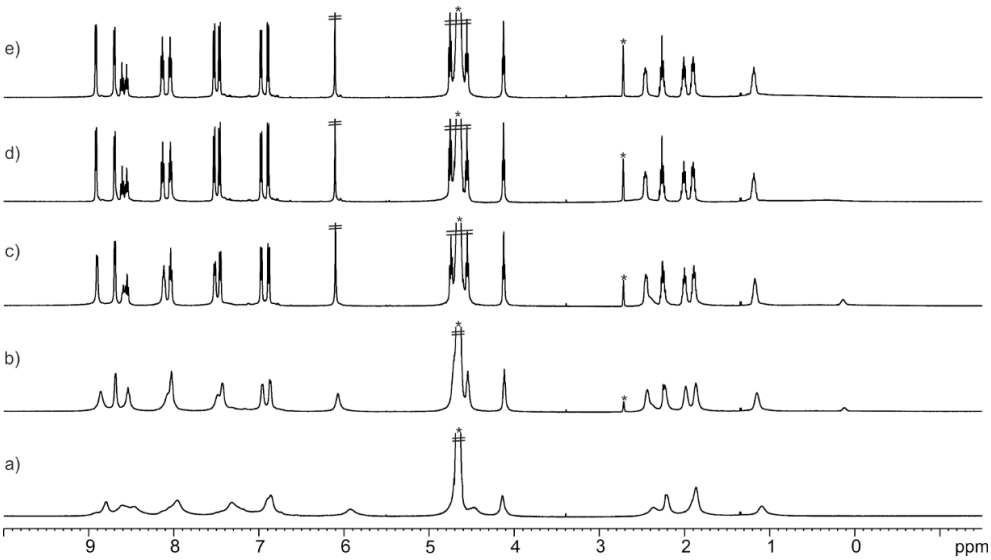

Figure 3.25. ^{1}H NMR (500 MHz with cryoprobe, D_2O, 313 K) spectra of the titration of octa-pyridinium **1** with **2c**: a) 0; b) 0.5; c) 1; d) 1.5 and e) 2 equiv. *Residual solvent peaks.

Bis-isonitrile **2d**

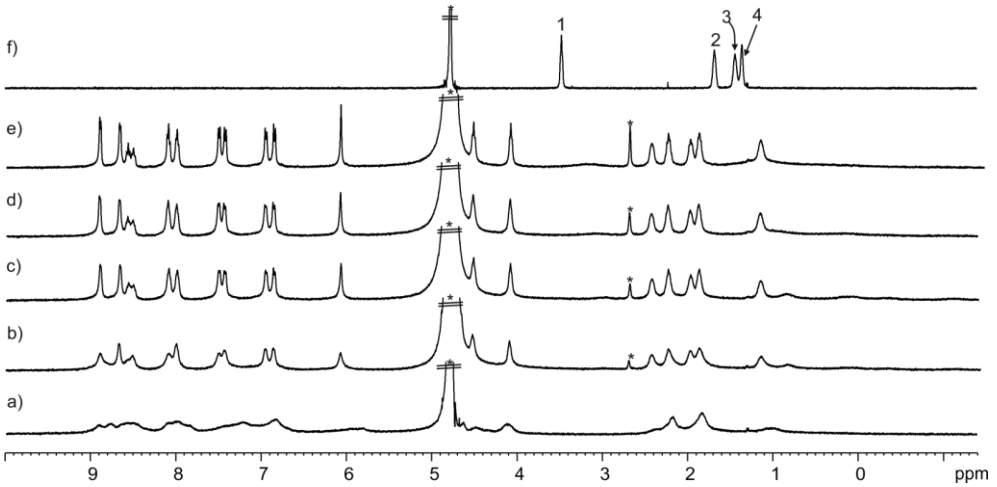

Figure 3.26. ^{1}H NMR (400 MHz, D_2O, 298 K) spectra of the titration of octa-pyridinium **1** with **2d**: a) 0; b) 0.5; c) 1; d) 1.5 and e) 2 equiv.; f) **3d**. *Residual solvent peaks.

Bis-isonitrile **2e**

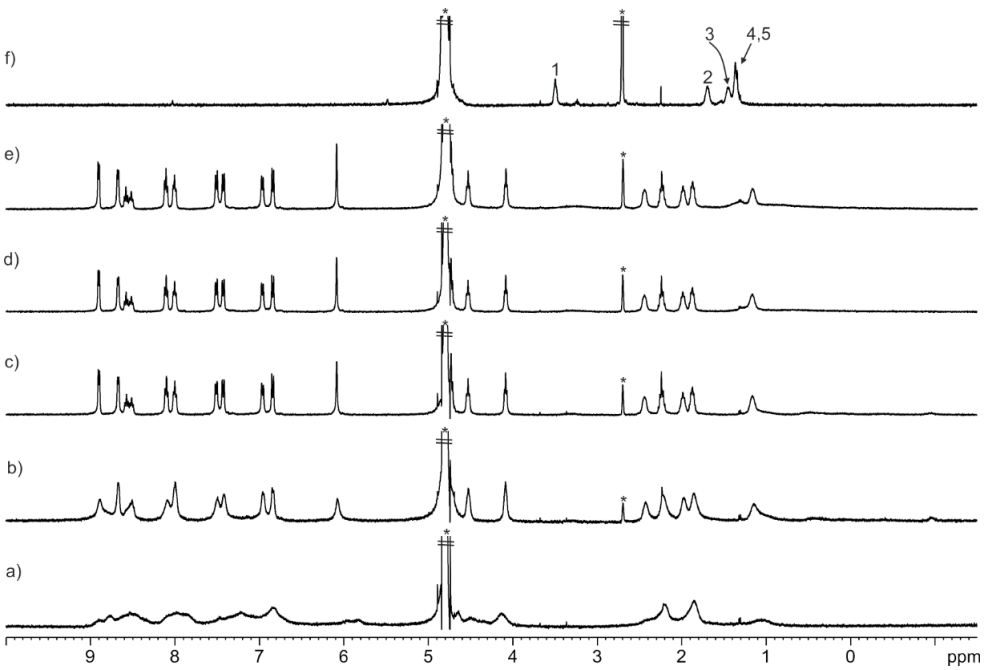

Figure 3.27. ^{1}H NMR (400 MHz, D_2O, 298 K) spectra of the titration of octa-pyridinium **1** with **2e**: a) 0; b) 0.5; c) 1; d) 1.5 and e) 2 equiv.; f) **2e**. *Residual solvent peaks.

NMR binding studies of *mono*-formamides **3a**-**e** with octa-pyridinium **1**

Mono-formamide **3a**

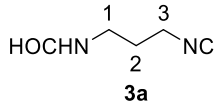

3a

Figure 3.28. Line-drawing structure of **3a**. Numbers indicate proton signals of guest.

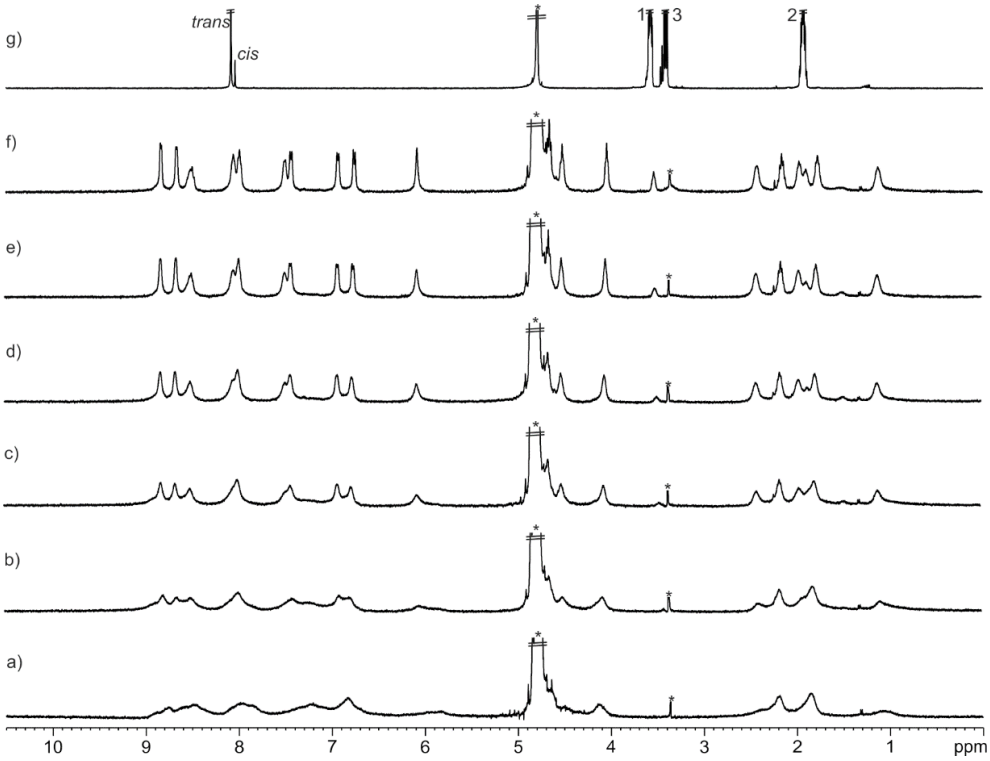

Figure 3.29. ^{1}H NMR (400 MHz, D_2O, 298 K) spectra of the titration of octa-pyridinium **1** with **3a**: a) 0; b) 0.5; c) 1; d) 1.5; e) 2 and f) 3 equiv.; g) **3a**. *Residual solvent peaks.

Mono-formamide **3b**

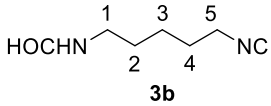

3b

Figure 3.30. Line-drawing structure of **3b**. Numbers indicate proton signals of guest.

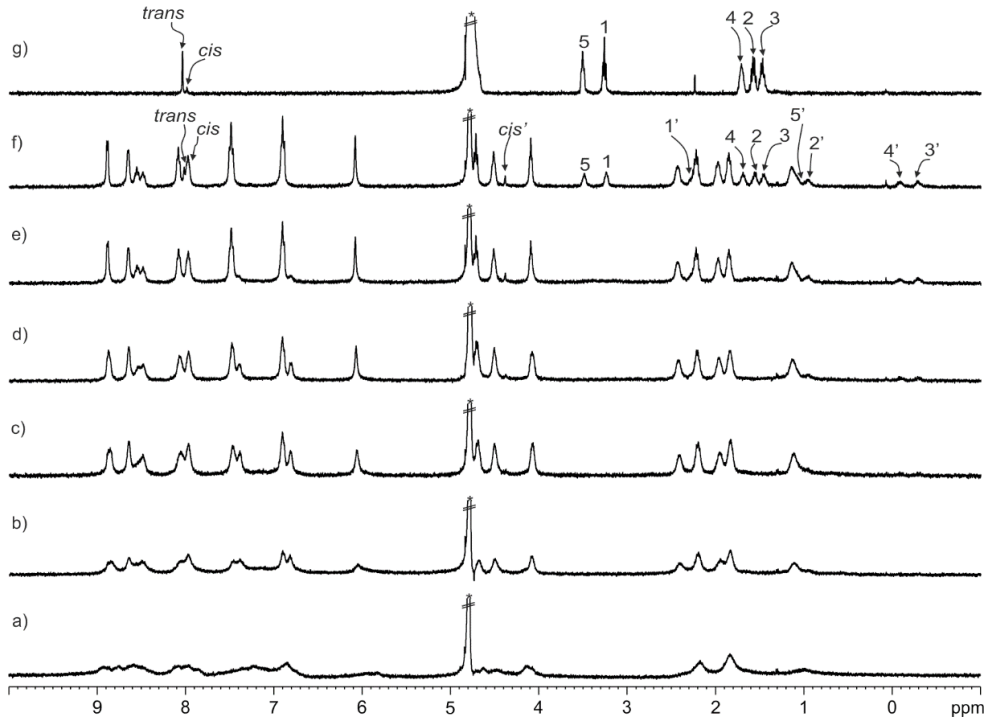

Figure 3.31. ^{1}H NMR (400 MHz, D_2O, 298 K) spectra of the titration of octa-pyridinium **1** with **3b**: a) 0; b) 0.5; c) 1; d) 1.5; e) 2 and f) 3 equiv.; g) **3b**. Primed labels correspond to proton signals of bound *cis*-**3b**. *Residual solvent peak.

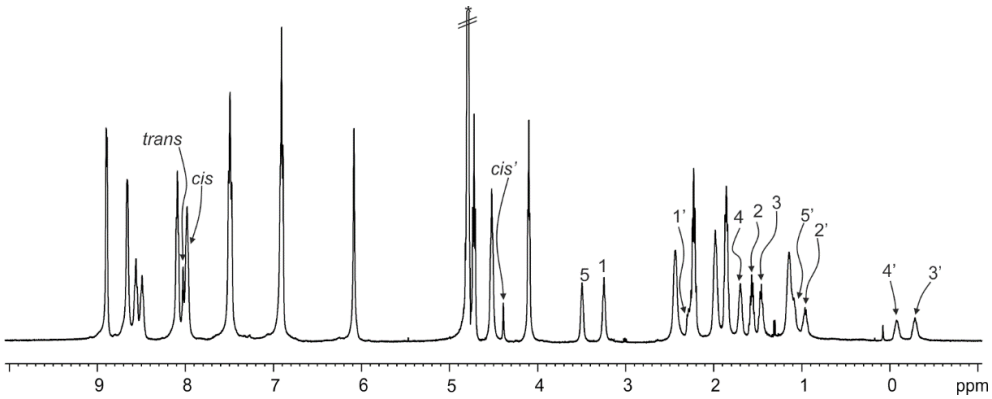

Figure 3.32. ^{1}H NMR (500 MHz with cryoprobe, D_2O, 298 K) spectrum of *mono*-formamide **3b** and octa-pyridinium **1** (ca. 2:1 ratio). Primed labels correspond to proton signals of bound *cis*-**3b**. *Residual solvent peak.

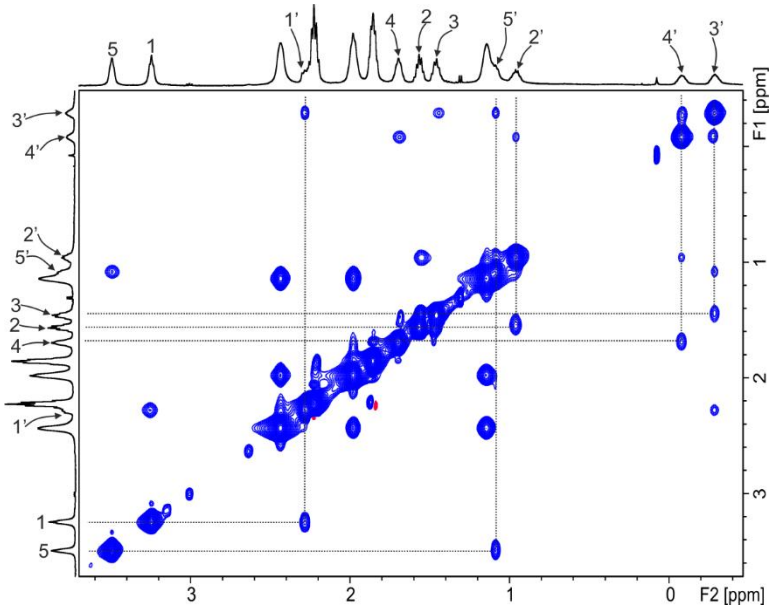

Figure 3.33. Selected region of the ^{1}H-^{1}H EXSY NMR (500 MHz with cryoprobe, D_2O, 298 K, mixing time = 0.3 s) spectrum of *mono*-formamide **3b** and octa-pyridinium **1** (ca. 2:1 ratio). Primed numbers correspond to proton signals of bound *cis*-**3b**.

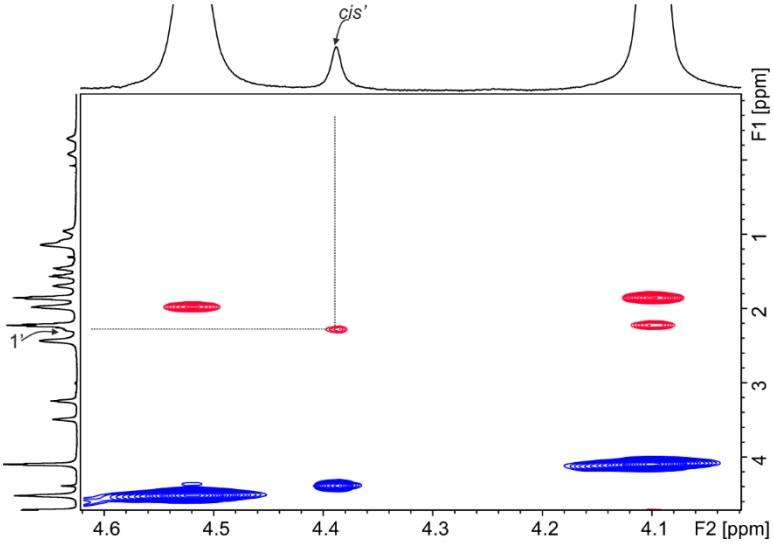

Figure 3.34. Selected region of the ^{1}H-^{1}H ROESY NMR (500 MHz with cryoprobe, D_2O, 298 K, spin lock = 0.3 s) spectrum of *mono*-formamide **3b** and octa-pyridinium **1** (ca. 2:1 ratio). A ROESY cross-peak between 1' and the singlet at 4.39 ppm (*cis'*) of bound formamide is highlighted. This observation confirmed that the signal corresponds to the *cis*-formyl proton of bound **3b**.

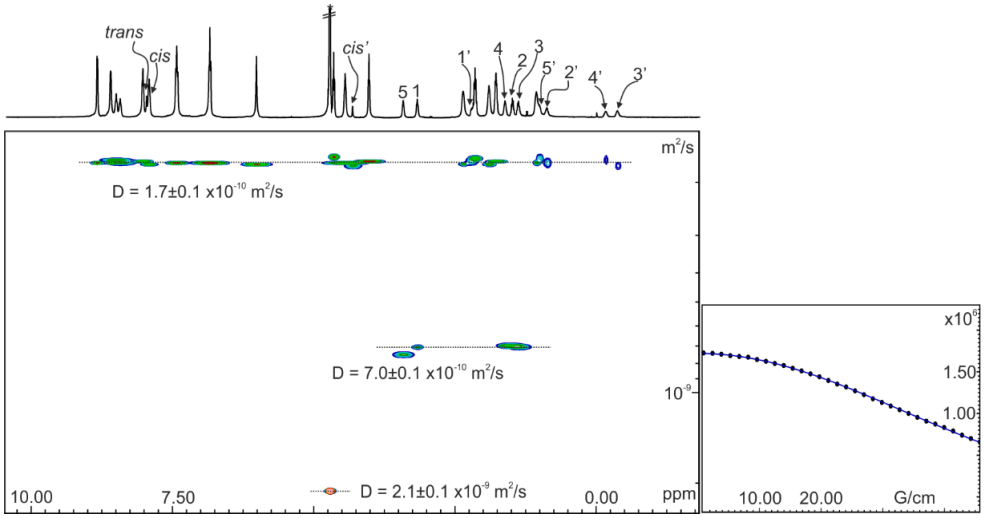

Figure 3.35. left) ^{1}H pseudo 2D DOSY (500 MHz with cryoprobe, D_2O, D20 = 0.01 s, P30 = 3.5 ms, 298 K) plot of *mono*-formamide **3b** and octa-pyridinium **1** (*ca.* 2:1 ratio). right) Fit of the *beta*-pyrrole signal to a *mono*-exponential function using Dynamics Center from Bruker. Primed labels correspond to proton signals of bound *cis*-**3b**. *Residual solvent peak.

Table 3.5. Experimental chemical shifts of free (δ_{free}) and bound (δ_{bound}) *mono*-formamide **3b**, complexation-induced shifts ($\Delta\delta$) and calculated chemical shifts (calc. δ_{bound}).[52]

Signal	δ_{free} (ppm)	δ_{bound} (ppm)	$\Delta\delta$ (ppm)	calc. δ_{bound}
trans	8.04	-	-	-
cis	7.99	4.39	-3.60	4.54
1	3.27	2.28	-0.99	2.67
2	1.58	0.96	-0.62	1.76
3	1.47	-0.29	-1.76	0.12
4	1.71	-0.08	-1.79	-0.74
5	3.51	1.09	-2.42	0.16

Mono-formamide **3c**

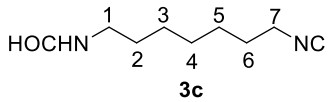

3c

Figure 3.36. Line-drawing structure of **3c**. Numbers indicate proton signals of guest.

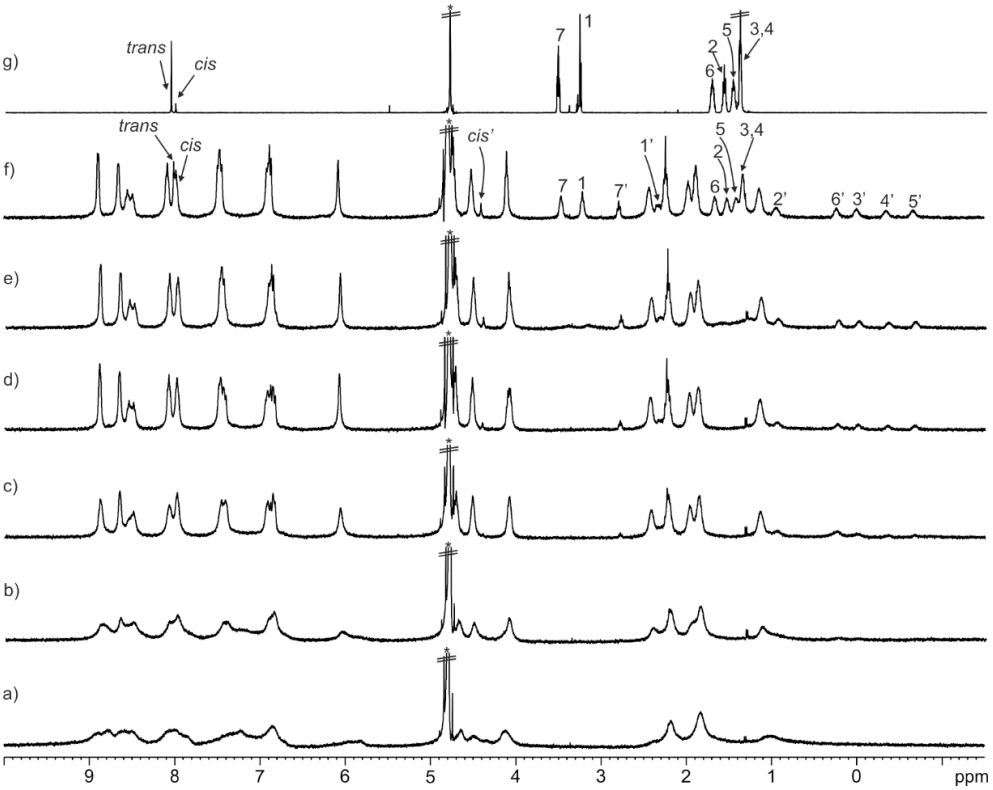

Figure 3.37. ^{1}H NMR (400 MHz, D_2O, 298 K) spectra of the titration of octa-pyridinium **1** with **3c**: a) 0; b) 0.5; c) 1; d) 1.5; e) 2 and f) 3 equiv.; g) **3c**. Primed labels correspond to proton signals of bound *cis*-**3c**. *Residual solvent peak.

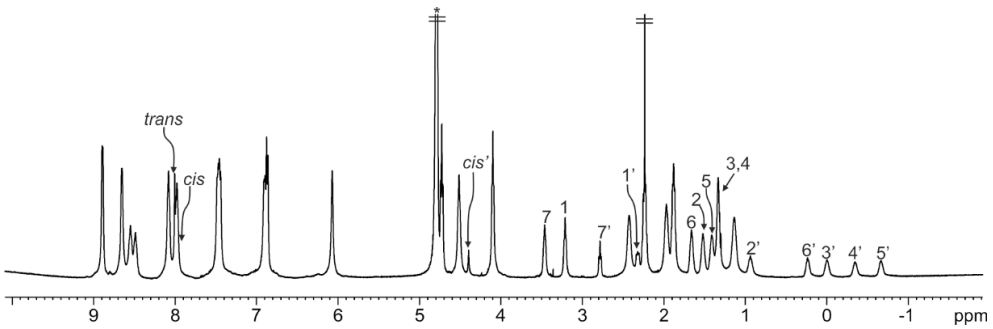

Figure 3.38. ^{1}H NMR (500 MHz with cryoprobe, D_2O, 298 K) spectrum of mono-formamide **3c** and octa-pyridinium **1** *(ca*. 3:1 ratio). Primed labels correspond to proton signals of bound *cis*-**3c**. *Residual solvent peak.

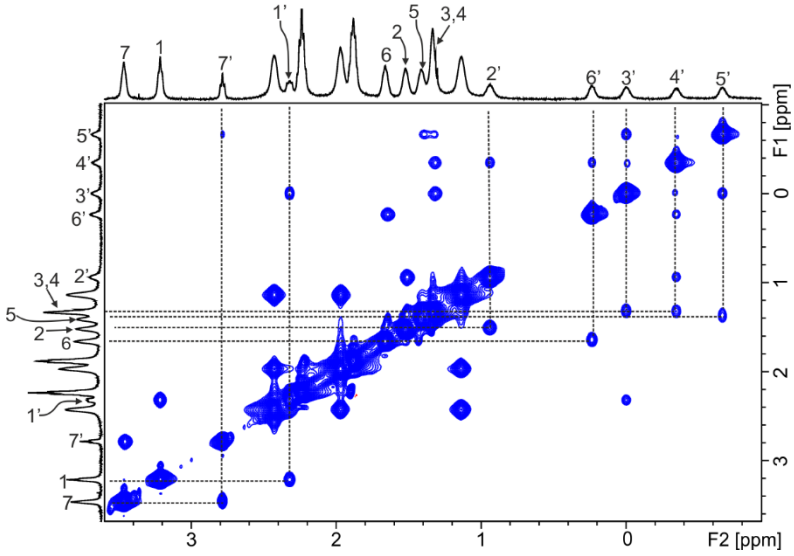

Figure 3.39. Selected region of the ^{1}H-^{1}H EXSY NMR (500 MHz with cryoprobe, D_2O, 298 K, mixing time = 0.3 s) spectrum of mono-formamide **3c** and octa-pyridinium **1** (*ca.* 3:1 ratio). Primed numbers correspond to proton signals of bound *cis*-**3c**.

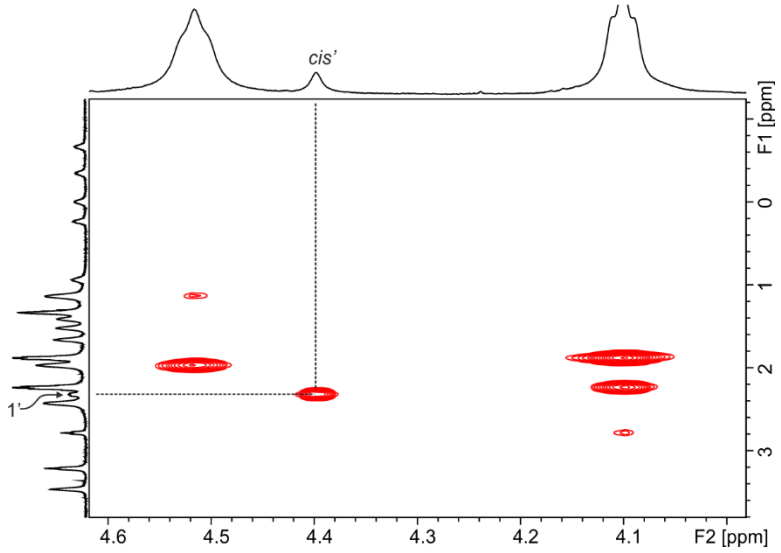

Figure 3.40. Selected region of the ^{1}H-^{1}H ROESY NMR (500 MHz with cryoprobe, D_2O, 298 K, spin lock = 0.3 s) spectrum of *mono*-formamide **3c** and octa-pyridinium **1** (*ca.* 3:1 ratio). A ROESY cross-peak between 1' and the singlet at 4.39 ppm (*cis'*) of bound formamide is highlighted. This observation confirmed that the signal corresponds to the *cis*-formyl proton of bound **3c**.

Table 3.6. Experimental chemical shifts of free (δ_{free}) and bound (δ_{bound}) *mono*-formamide **3c** and complexation-induced shifts ($\Delta\delta$).

Signal	δ_{free} (ppm)	δ_{bound} (ppm)	$\Delta\delta$ (ppm)
trans	8.03	-	-
cis	7.98	4.39	-3.59
1	3.24	2.37	-0.87
2	1.55	0.99	-0.56
3	1.36	0.08	-1.28
4	1.36	-0.24	-1.60
5	1.44	-0.55	-1.99
6	1.69	0.29	-1.40
7	3.49	2.82	-0.67

<u>*Mono*-formamide **3d**</u>

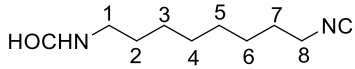

3d

Figure 3.41. Line-drawing structure of **3d**. Numbers indicate proton signals of guest.

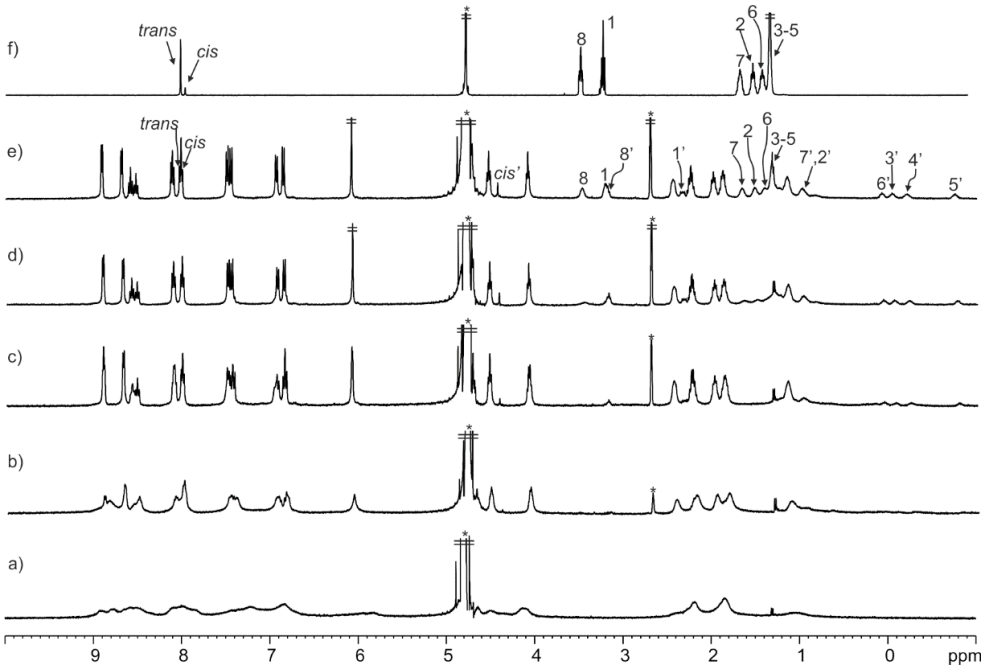

Figure 3.42. ^{1}H NMR (400 MHz, D_2O, 298 K) spectra of the titration of octa-pyridinium **1** with **3d**: a) 0; b) 0.5; c) 1; d) 1.5 and e) 2 equiv.; f) **3d**. Primed labels correspond to proton signals of bound *cis*-**3d**. *Residual solvent peaks.

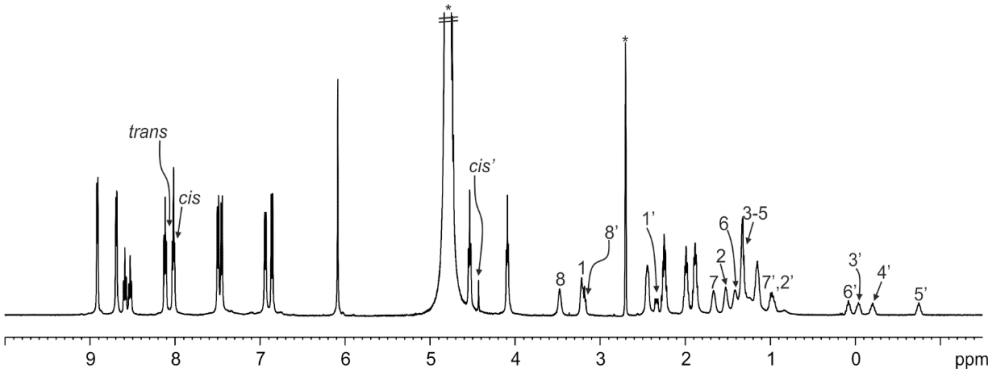

Figure 3.43. ^{1}H NMR (500 MHz with cryoprobe, D_2O, 298 K) spectrum of *mono*-formamide **3d** and octa-pyridinium **1** (*ca.* 2:1 ratio). Primed labels correspond to proton signals of bound *cis*-**3d**. *Residual solvent peaks.

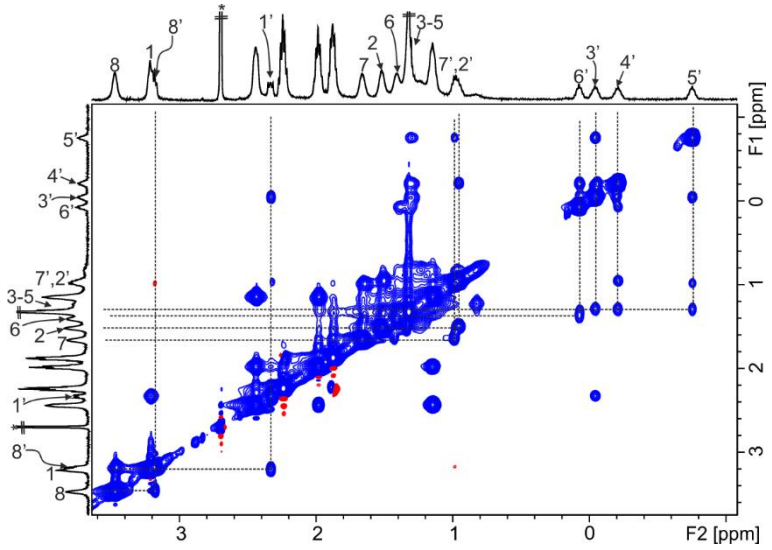

Figure 3.44. Selected region of the ^{1}H-^{1}H EXSY NMR (500 MHz with cryoprobe, D_2O, 298 K, mixing time = 0.3 s) spectrum of *mono*-formamide **3d** and octa-pyridinium **1** (*ca.* 2:1 ratio). Primed numbers correspond to proton signals of bound *cis*-**3d**. *Residual solvent peak.

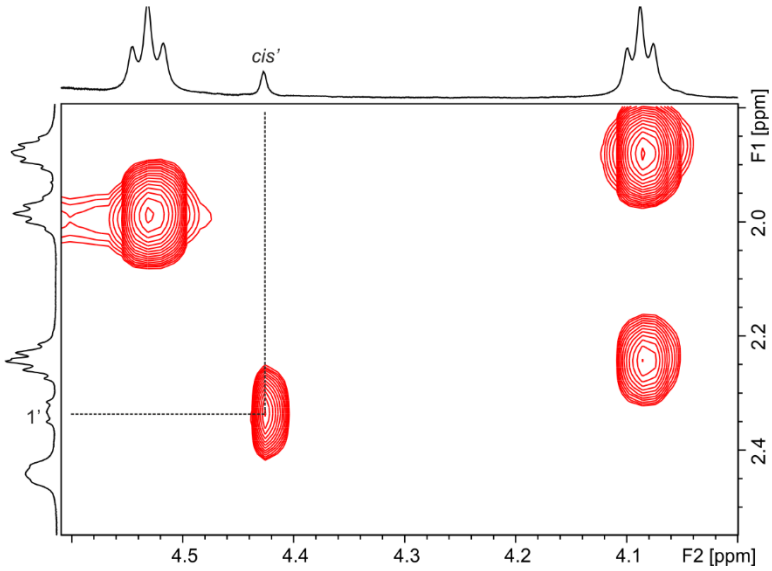

Figure 3.45. Selected region of the ^{1}H-^{1}H ROESY NMR (500 MHz with cryoprobe, D_2O, 298 K, spin lock = 0.3 s) spectrum of *mono*-formamide **3d** and octa-pyridinium **1** (*ca.* 2:1 ratio). A ROESY cross-peak between 1' and the singlet at 4.45 ppm (*cis'*) of bound formamide is highlighted. This observation confirmed that the signal corresponds to the *cis*-formyl proton of bound **3d**.

Table 3.7. Experimental chemical shifts of free (δ_{free}) and bound (δ_{bound}) *mono*-formamide **3d** and complexation-induced shifts ($\Delta\delta$).

Signal	δ_{free} (ppm)	δ_{bound} (ppm)	$\Delta\delta$ (ppm)
trans	8.03	-	-
cis	7.98	4.45	-3.53
1	3.21	2.33	-0.88
2	1.52	0.98	-0.54
3	1.32	-0.04	-1.36
4	1.32	-0.21	-1.53
5	1.32	-0.75	-2.07
6	1.41	0.07	-1.34
7	1.66	0.98	-0.68
8	3.47	3.18	-0.29

<u>*Mono*-formamide **3e**</u>

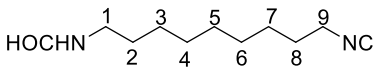

3e

Figure 3.46. Line-drawing structure of **3e**. Numbers indicate proton signals of guest.

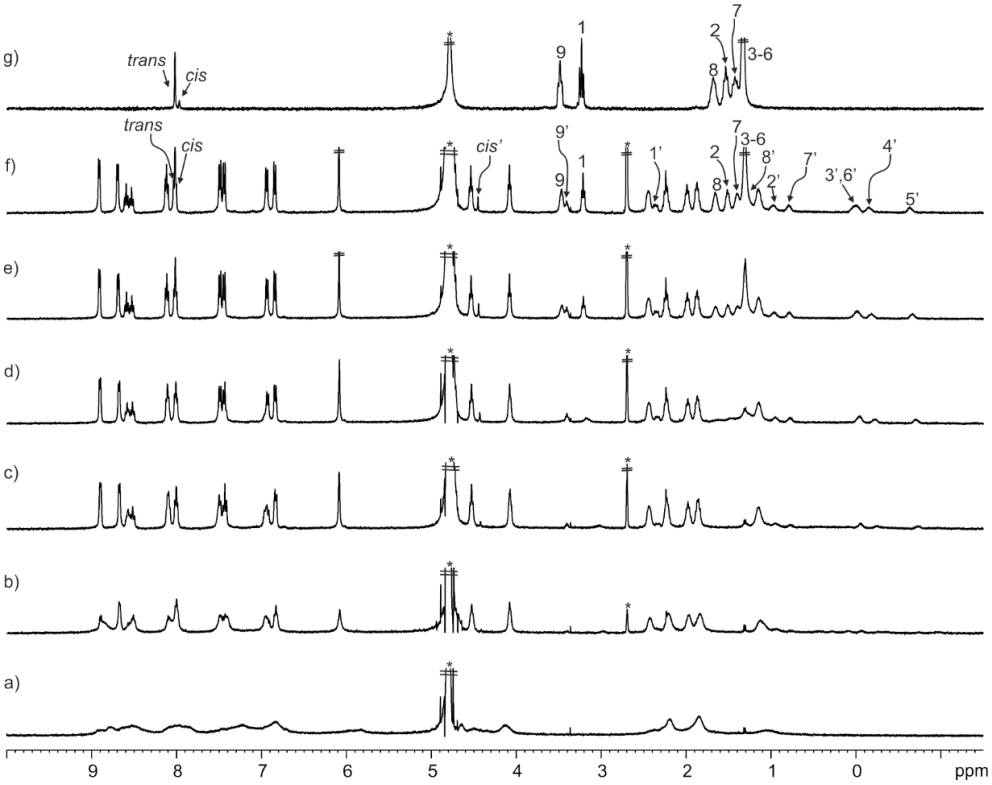

Figure 3.47. ^{1}H NMR (400 MHz, D_2O, 298 K) spectra of the titration of octa-pyridinium **1** with **3e**: a) 0; b) 0.5; c) 1; d) 1.5; e) 2 and f) 2.5 equiv.; g) **3e**. Primed labels correspond to proton signals of bound *cis*-**3e**. *Residual solvent peaks.

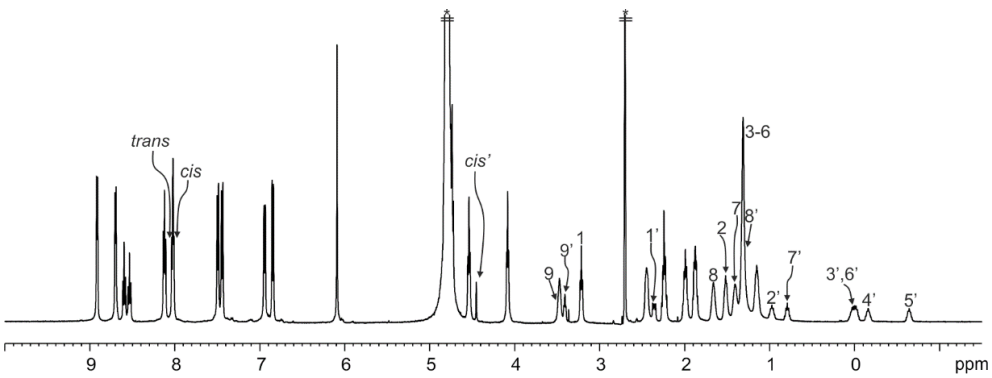

Figure 3.48. ^{1}H NMR (500 MHz with cryoprobe, D_2O, 298 K) spectrum of mono-formamide **3e** and octa-pyridinium **1** (*ca*. 2.5:1 ratio). Primed labels correspond to proton signals of bound *cis*-**3e**. *Residual solvent peaks.

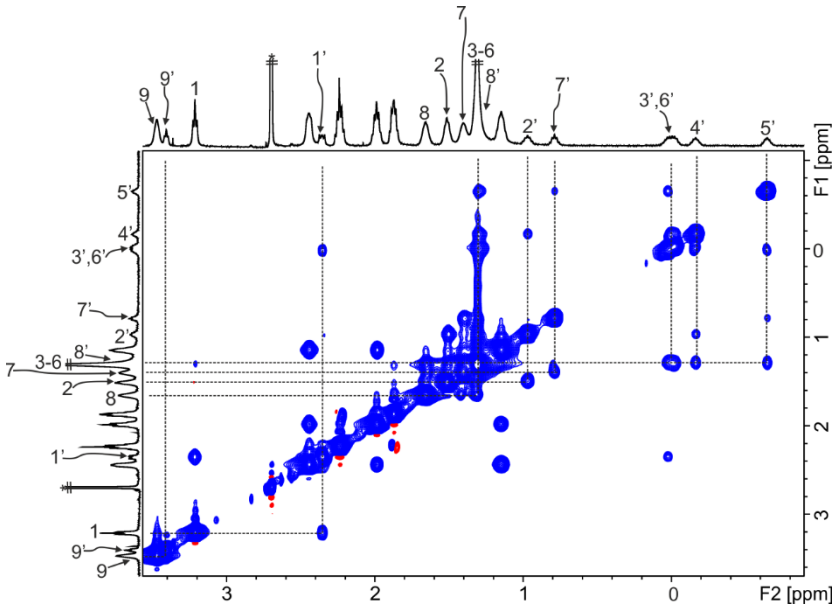

Figure 3.49. Selected region of the ^{1}H-^{1}H EXSY NMR (500 MHz with cryoprobe, D_2O, 298 K, mixing time = 0.3 s) spectrum of *mono*-formamide **3e** and octa-pyridinium **1** (*ca.* 2.5:1 ratio). Primed numbers correspond to proton signals of bound *cis*-**3e**. *Residual solvent peak.

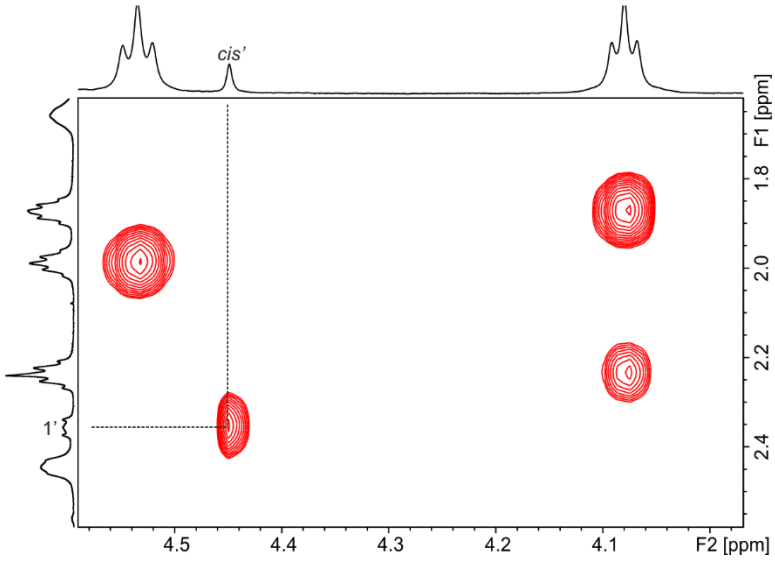

Figure 3.50. Selected region of the ^{1}H-^{1}H ROESY NMR (500 MHz with cryoprobe, D_2O, 298 K, spin lock = 0.3 s) spectrum of *mono*-formamide **3e** and octa-pyridinium **1** (*ca.* 2.5:1 ratio). A ROESY cross-peak between 1' and the singlet at 4.45 ppm (*cis'*) of bound formamide is highlighted. This observation confirmed that the signal corresponds to the *cis*-formyl proton of bound **3e**.

Table 3.8. Experimental chemical shifts of free (δ_{free}) and bound (δ_{bound}) *mono*-formamide **3e** and complexation-induced shifts ($\Delta\delta$).

Signal	δ_{free} (ppm)	δ_{bound} (ppm)	$\Delta\delta$ (ppm)
trans	8.04	-	-
cis	7.99	4.45	-3.54
1	3.22	2.38	-0.84
2	1.52	0.99	-0.53
3	1.32	0.04	-1.28
4	1.32	-0.11	-1.43
5	1.32	-0.59	-1.91
6	1.32	0.04	-1.28
7	1.41	0.80	-0.61
8	1.67	1.32	-0.35
9	3.48	3.41	-0.07

NMR binding studies of *bis*-formamides **4a**-**e** with octa-pyridinium **1**

Bis-formamide **4a**

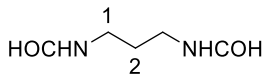

4a

Figure 3.51. Line-drawing structure of **4a**. Numbers indicate proton signals of free guest.

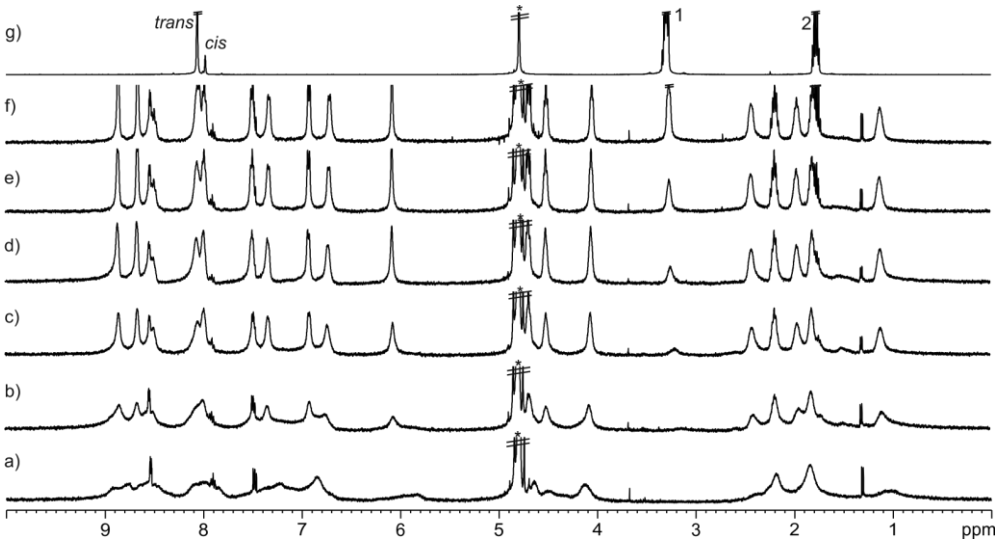

Figure 3.52. ^{1}H NMR (400 MHz, D_2O, 298 K) spectra of the titration of octa-pyridinium **1** with **4a**: a) 0; b) 0.5; c) 1; d) 1.5; e) 2 and f) 3 equiv.; g) **4a**. *Residual solvent peak.

Bis-formamide **4b**

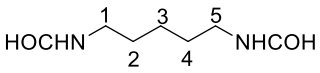

4b

Figure 3.53. Line-drawing structure of **4b**. Numbers indicate proton signals of bound guest.

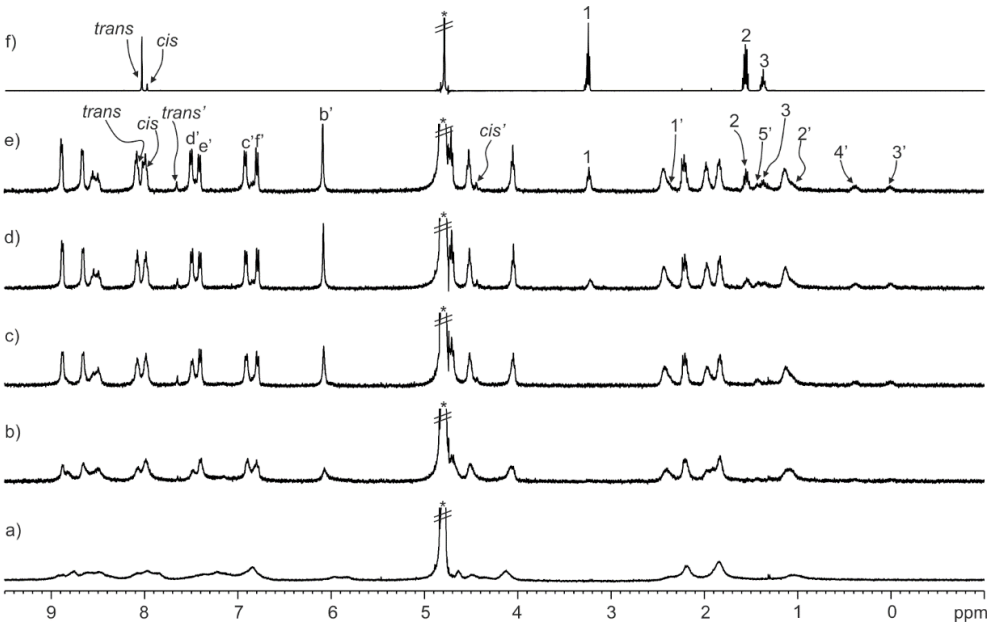

Figure 3.54. ^{1}H NMR (400 MHz, D_2O, 298 K) spectra of the titration of octa-pyridinium **1** with **4b**: a) 0; b) 0.5; c) 1; d) 1.5 and e) 2 equiv.; f) **4b**. Primed labels correspond to proton signals of bound *trans,cis*-**4b**. *Residual solvent peak.

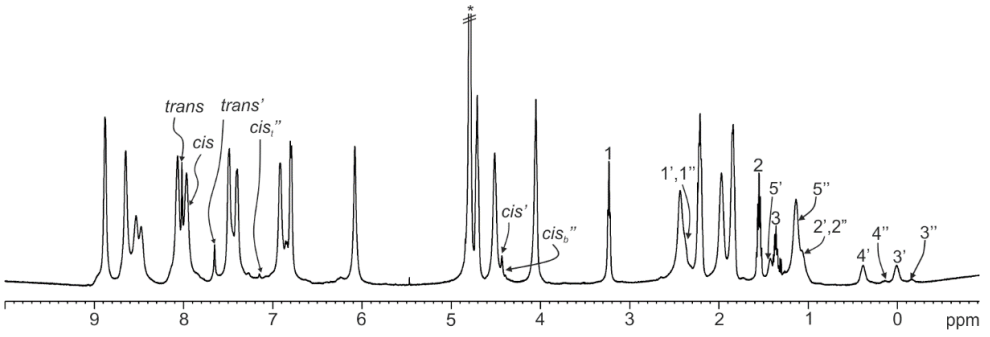

Figure 3.55. ^{1}H NMR (500 MHz with cryoprobe, D_2O, 298 K) spectrum of *bis*-formamide **4b** and octa-pyridinium **1** (*ca.* 2:1 ratio). Primed labels correspond to proton signals of bound *trans,cis*-**4b** and doubly primed labels correspond to proton signals of bound *cis,cis*-**4b** (*cis*$_t$*''* is assigned to the formyl proton at the upper rim and *cis*$_b$*''* is assigned to the formyl proton of the *cis*-formamide bound to the calix[4]pyrrole unit). *Residual solvent peak.

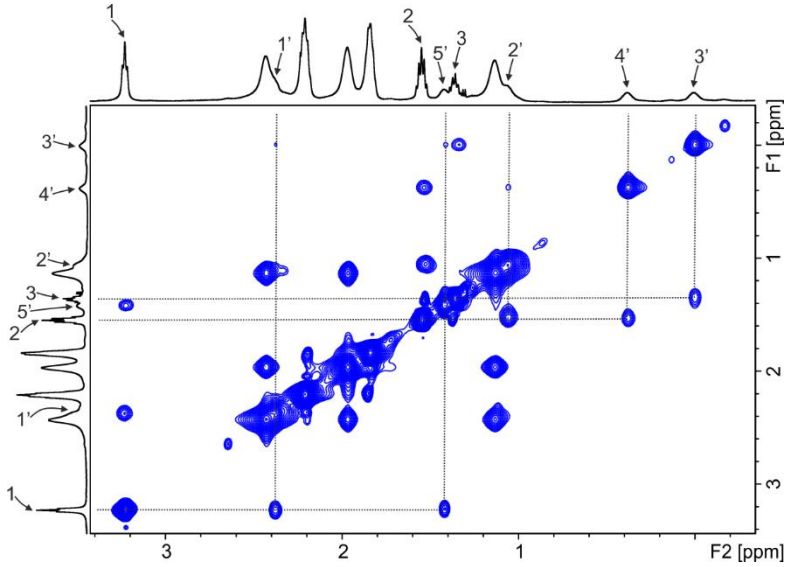

Figure 3.56. Selected region of the ^{1}H-^{1}H EXSY NMR (500 MHz with cryoprobe, D_2O, 298 K, mixing time = 0.3 s) spectrum of *bis*-formamide **4b** and octa-pyridinium **1** (*ca.* 2:1 ratio). Primed numbers correspond to proton signals of bound *trans*,*cis*-**4b**.

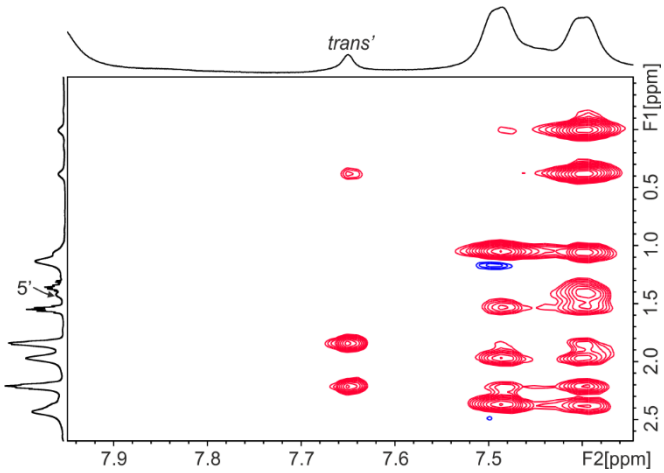

Figure 3.57. Selected region of the ^{1}H-^{1}H ROESY NMR (500 MHz with cryoprobe, D_2O, 298 K, spin lock = 0.3 s) spectrum of *bis*-formamide **4b** and octa-pyridinium **1** (ca. 2:1 ratio). A ROESY cross-peak between 5' and the singlet at 7.65 ppm (trans') of bound *trans,cis*-**4b** is not observed. This confirmed that the signal corresponds to the *trans*-formamide end of **4b**.

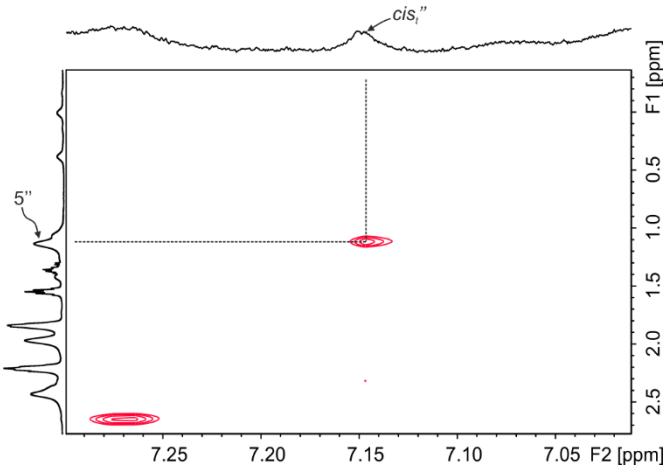

Figure 3.58. Selected region of the ^{1}H-^{1}H ROESY NMR (500 MHz with cryoprobe, D_2O, 298 K, spin lock = 0.3 s) spectrum of *bis*-formamide **4b** and octa-pyridinium **1** (*ca.* 2:1 ratio). A ROESY cross-peak between 5'' and *cis*$_i$'' of bound *cis*,*cis*-**4b** is observed due to the *cis*-conformation of the formamide at the upper rim of the receptor's cavity.

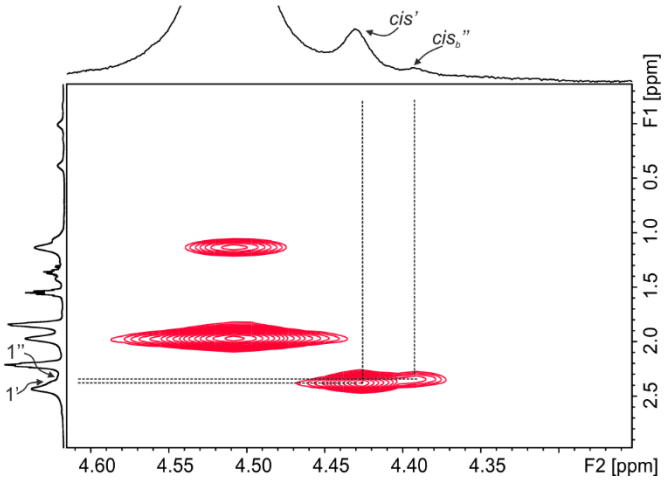

Figure 3.59. Selected region of the ^{1}H-^{1}H ROESY NMR (500 MHz with cryoprobe, D_2O, 298 K, spin lock = 0.3 s) spectrum of *bis*-formamide **4b** and octa-pyridinium **1** (ca. 2:1 ratio). ROESY cross-peaks between 1' and 1'' with the signals at 4.44 and 4.39 ppm, respectively, are highlighted. The observed cross-peaks confirmed that the buried formamide groups of bound *trans,cis*-**4b** and *cis,cis*-**4b** adopt a *cis*-conformation.

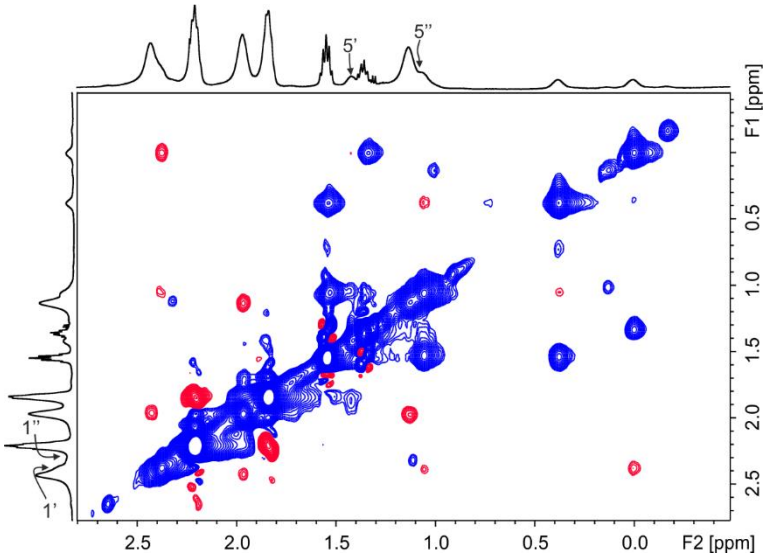

Figure 3.60. Selected region of the ^{1}H-^{1}H ROESY NMR (500 MHz with cryoprobe, D_2O, 298 K, spin lock = 0.3 s) spectrum of *bis*-formamide **4b** and octa-pyridinium **1** (ca. 2:1 ratio). ROESY cross-peaks between 1' and 5' of bound *trans,cis*-**4b** and 1'' and 5'' of bound *cis,cis*-**4b** are not observed. These indicated that the guests adopt extended conformations in the receptor's cavity

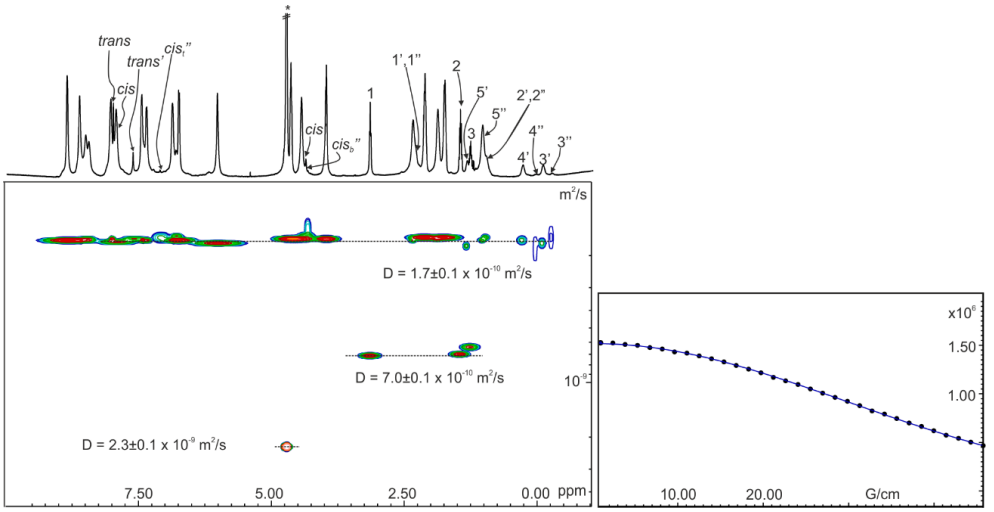

Figure 3.61. left) ^{1}H pseudo 2D DOSY (500 MHz with cryoprobe, D_2O, D20 = 0.01 s, P30 = 4 ms, 298 K) plot of *bis*-formamide **4b** and octa-pyridinium **1** (ca. 2:1 ratio). right) Fit of the beta-pyrrole signal to a mono-exponential function using Dynamics Center from Bruker. Primed labels correspond to proton signals of bound *trans,cis*-**4b** and doubly primed labels correspond to proton signals of bound *cis,cis*-**4b**. *Residual solvent peak.

Table 3.9. Experimental chemical shifts of free (δ_{free}) and bound (δ_{bound}) *trans*,*cis*-**4b**, complexation-induced shifts ($\Delta\delta$) and calculated chemical shifts (calc. δ_{bound}).[52]

Signal	δ_{free} (ppm)	δ_{bound} (ppm)	$\Delta\delta$ (ppm)	calc. δ_{bound}
trans	8.03	7.65	-0.38	7.52
cis	7.98	4.44	-3.54	4.48
1	3.25	2.38	-0.87	2.89
2	1.56	1.06	-0.50	1.71
3	1.37	0.01	-1.36	0.79
4	-	0.38	-1.18	-0.70
5	-	1.43	-1.82	1.41

Bis-formamide **4c**

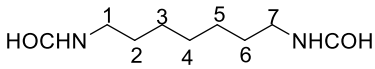

4c

Figure 3.62. Line-drawing structure of **4c**. Numbers indicate proton signals of bound guest.

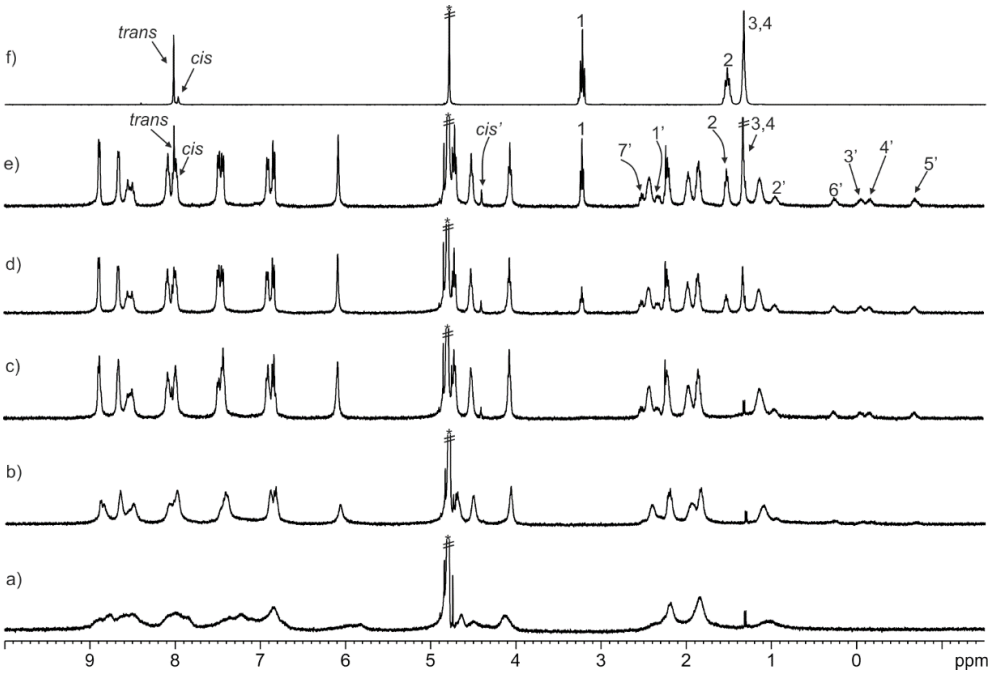

Figure 3.63. ^{1}H NMR (400 MHz, D_2O, 298 K) spectra of the titration of octa-pyridinium **1** with **4c**: a) 0; b) 0.5; c) 1; d) 1.5 and e) 2 equiv.; f) **4c**. *Residual solvent peak.

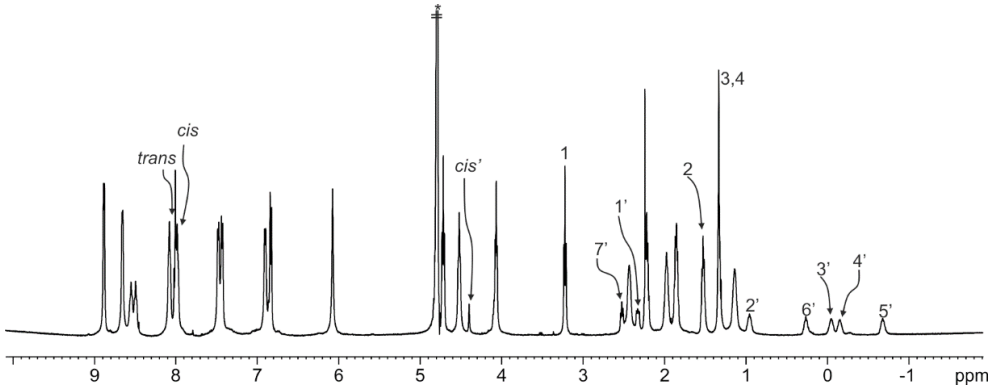

Figure 3.64. ^{1}H NMR (500 MHz with cryoprobe, D_2O, 298 K) spectrum of *bis*-formamide **4c** and octa-pyridinium **1** (ca. 2:1 ratio). Primed labels correspond to proton signals of bound *trans*,*cis*-**4c**. *Residual solvent peak.

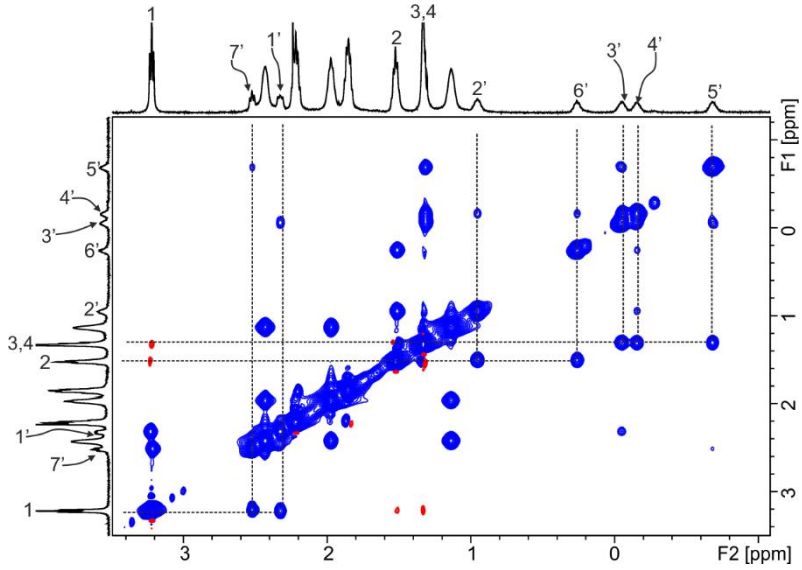

Figure 3.65. Selected region of the ^{1}H-^{1}H EXSY NMR (500 MHz with cryoprobe, D_2O, 298 K, mixing time = 0.3 s) spectrum of *bis*-formamide **4c** and octa-pyridinium **1** (*ca.* 2:1 ratio). Primed numbers correspond to proton signals of bound *trans*,*cis*-**4c**.

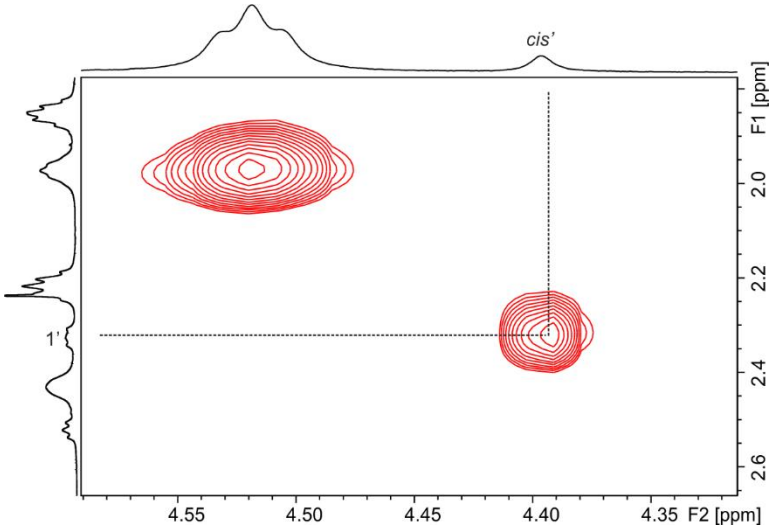

Figure 3.66. Selected region of the ^{1}H-^{1}H ROESY NMR (500 MHz with cryoprobe, D_2O, 298 K, spin lock = 0.3 s) spectrum of *bis*-formamide **4c** and octa-pyridinium 1 (*ca.* 2:1 ratio). A ROESY cross-peak between 1' and the singlet at 4.39 ppm (*cis'*) of bound formamide is highlighted. This observation confirmed that the signal corresponds to the *cis*-formyl proton of bound *trans,cis*-**4c**.

Table 3.10. Experimental chemical shifts of free (δ_{free}) and bound (δ_{bound}) *trans,cis*-**4c** and complexation-induced shifts ($\Delta\delta$).

Signal	δ_{free} (ppm)	δ_{bound} (ppm)	$\Delta\delta$ (ppm)
trans	8.04	-	-
cis	7.99	4.39	-3.60
1	3.22	2.32	-0.90
2	1.52	0.95	-0.57
3	1.33	-0.05	-1.38
4	1.33	-0.16	-1.49
5	-	-0.69	-2.02
6	-	0.25	-1.27
7	-	2.52	-0.70

Bis-formamide **4d**

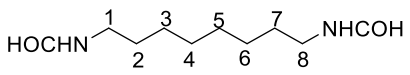

4d

Figure 3.67. Line-drawing structure of **4d**. Numbers indicate proton signals of bound guest.

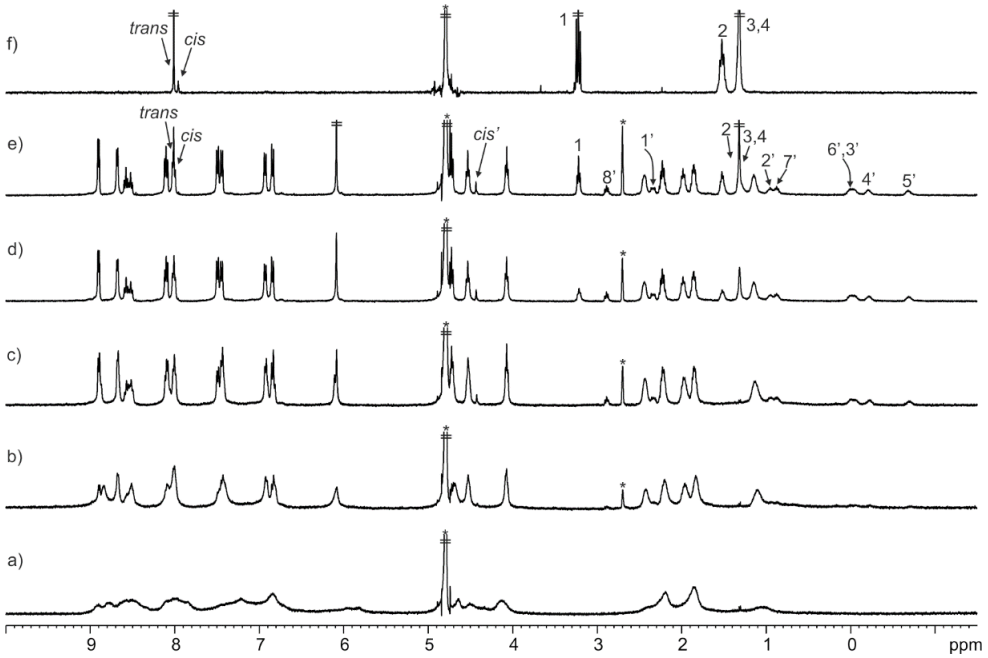

Figure 3.68. ^{1}H NMR (400 MHz, D_2O, 298 K) spectra of the titration of octa-pyridinium **1** with **4d**: a) 0; b) 0.5; c) 1; d) 1.5 and e) 2 equiv.; f) **4d**. Primed labels correspond to proton signals of bound *trans,cis*-**4d**. *Residual solvent peaks.

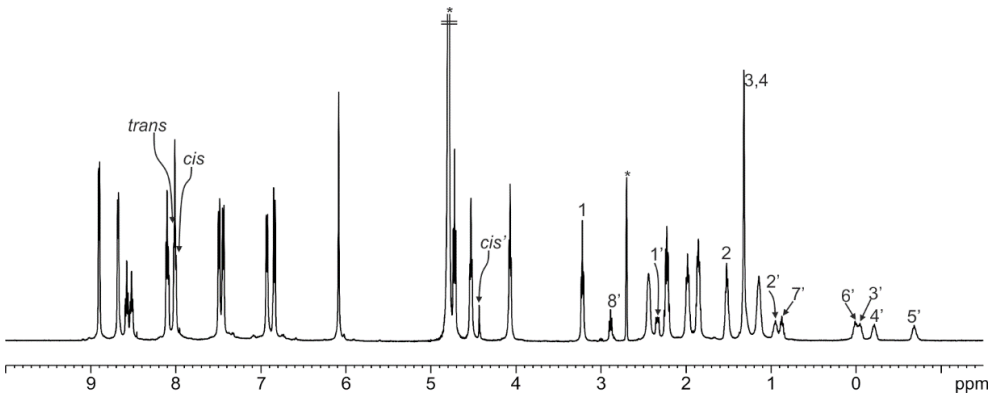

Figure 3.69. ^{1}H NMR (500 MHz with cryoprobe, D_2O, 298 K) spectrum of *bis*-formamide **4d** and octa-pyridinium **1** (ca. 2:1 ratio). Primed labels correspond to proton signals of bound *trans,cis*-**4d**. *Residual solvent peaks.

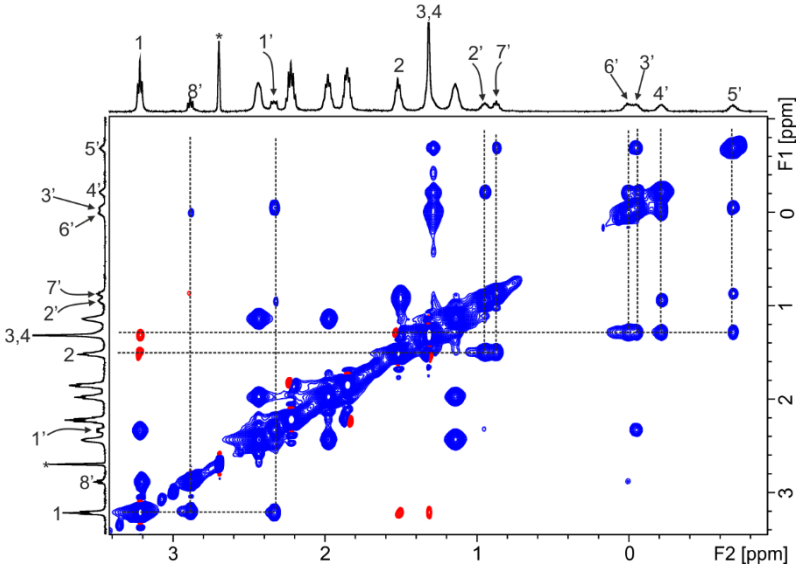

Figure 3.70. Selected region of the ^{1}H-^{1}H EXSY NMR (500 MHz with cryoprobe, D_2O, 298 K, mixing time = 0.3 s) spectrum of *bis*-formamide **4d** and octa-pyridinium **1** (*ca.* 2:1 ratio). Primed numbers correspond to proton signals of bound *trans*,*cis*-**4d**.

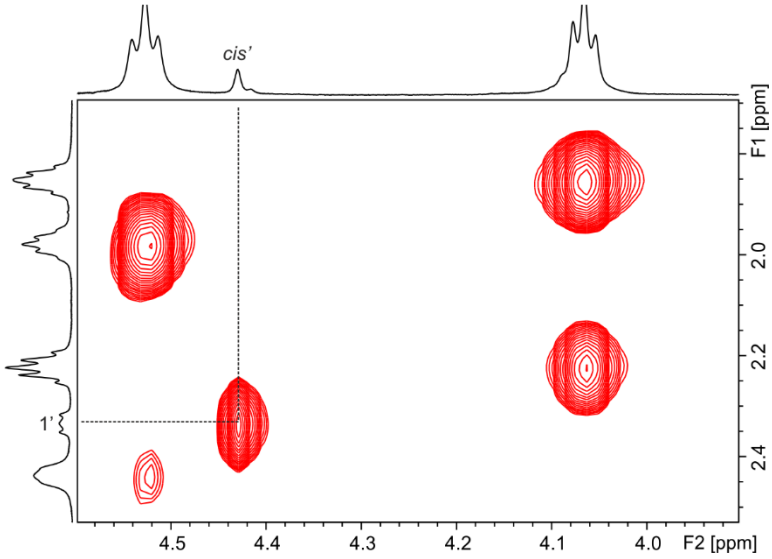

Figure 3.71. Selected region of the ^{1}H-^{1}H ROESY NMR (500 MHz with cryoprobe, D_2O, 298 K, spin lock = 0.3 s) spectrum of *bis*-formamide **4d** and octa-pyridinium **1** (*ca.* 2:1 ratio). A ROESY cross-peak between 1' and the singlet at 4.45 ppm (*cis'*) of bound formamide is highlighted. This observation confirmed that the signal corresponds to the *cis*-formyl proton of bound *trans,cis*-**4d**.

Table 3.11. Experimental chemical shifts of free (δ_{free}) and bound (δ_{bound}) *trans,cis*-**4d** and complexation-induced shifts ($\Delta\delta$).

Signal	δ_{free} (ppm)	δ_{bound} (ppm)	$\Delta\delta$ (ppm)
trans	8.02	-	-
cis	7.97	4.45	-3.52
1	3.23	2.33	-0.90
2	1.53	0.95	-0.58
3	1.33	-0.05	-1.38
4	1.33	-0.21	-1.54
5	-	-0.69	-2.02
6	-	0.01	-1.32
7	-	0.87	-0.66
8	-	2.88	-0.35

Bis-formamide **4e**

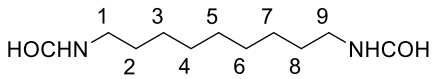

4e

Figure 3.72. Line-drawing structure of **4e**. Numbers indicate proton signals of bound guest.

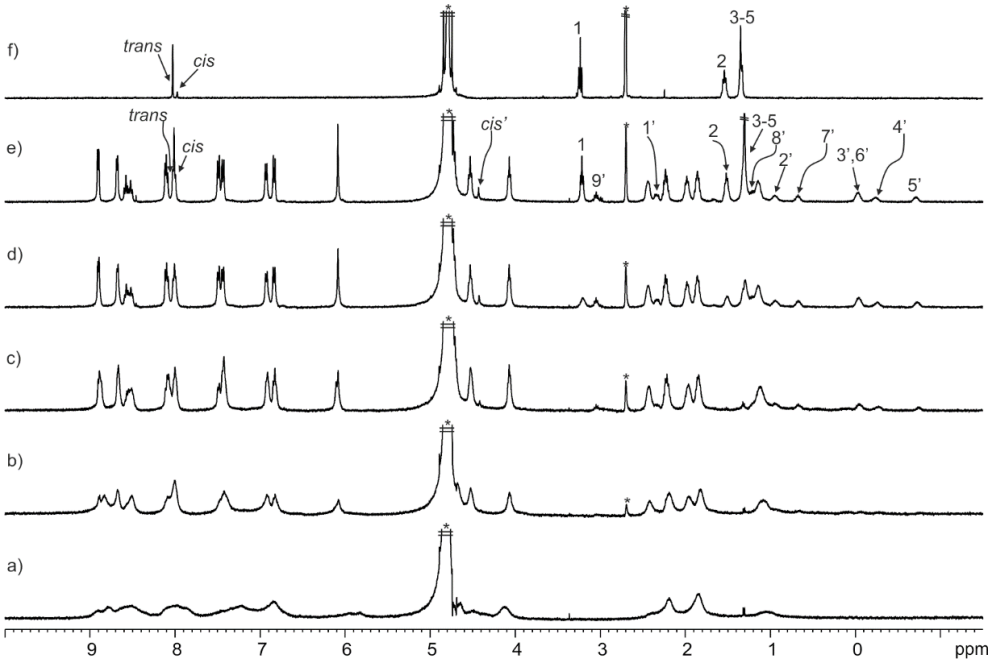

Figure 3.73. ^{1}H NMR (400 MHz, D_2O, 298 K) spectra of the titration of octa-pyridinium **1** with **4e**: a) 0; b) 0.5; c) 1; d) 1.5 and e) 2 equiv.; f) **4e**. Primed labels correspond to proton signals of bound *trans,cis*-**4e**. *Residual solvent peaks.

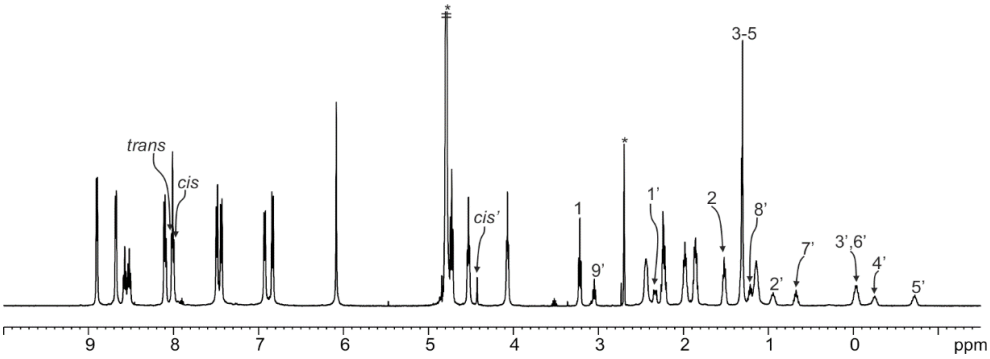

Figure 3.74. ^{1}H NMR (500 MHz with cryoprobe, D_2O, 298 K) spectrum of *bis*-formamide **4e** and octa-pyridinium **1** (*ca.* 2:1 ratio). Primed labels correspond to proton signals of bound *trans,cis*-**4e**. *Residual solvent peaks.

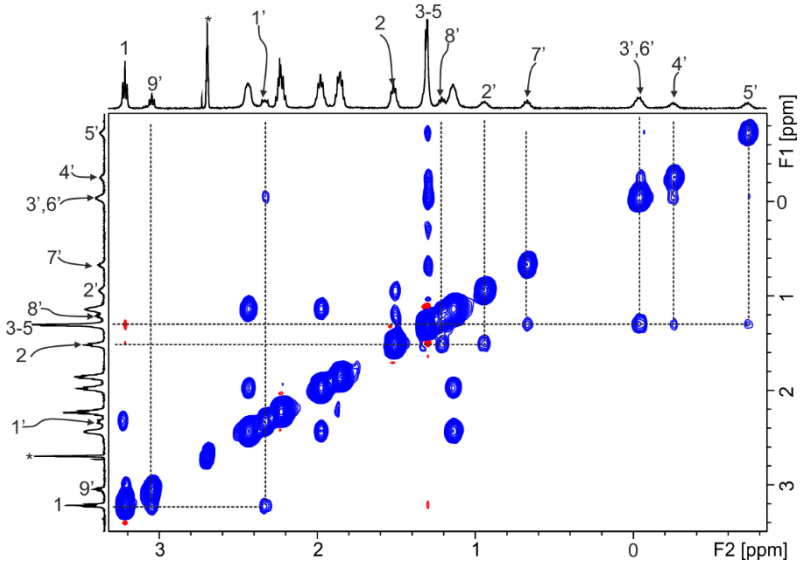

Figure 3.75. Selected region of the ^{1}H-^{1}H EXSY NMR (500 MHz with cryoprobe, D_2O, 298 K, mixing time = 0.3 s) spectrum of *bis*-formamide **4e** and octa-pyridinium **1** (*ca.* 2:1 ratio). Primed numbers correspond to proton signals of bound *trans*,*cis*-**4e**.

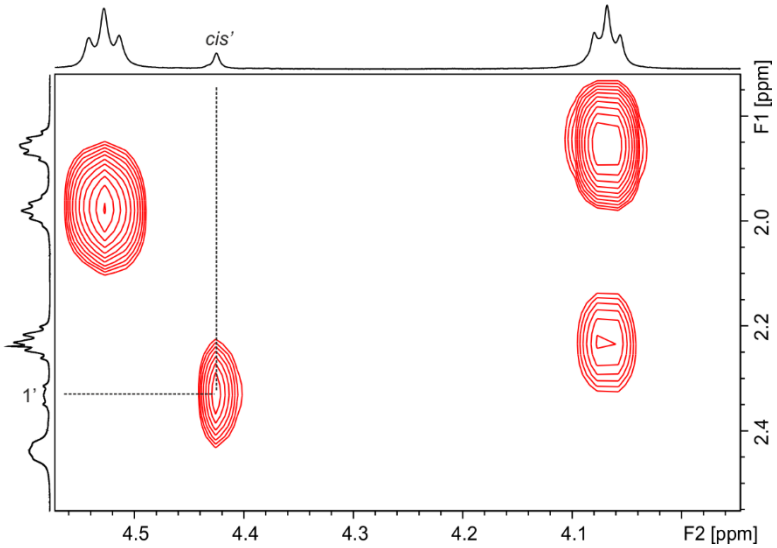

Figure 3.76. Selected region of the ^{1}H-^{1}H ROESY NMR (500 MHz with cryoprobe, D_2O, 298 K, spin lock = 0.3 s) spectrum of *bis*-formamide **4e** and octa-pyridinium **1** (*ca.* 2:1 ratio). A ROESY cross-peak between 1' and the singlet at 4.45 ppm (*cis'*) of bound formamide is highlighted. This observation confirmed that the signal corresponds to the *cis*-formyl proton of bound *trans,cis*-**4e**.

Table 3.12. Experimental chemical shifts of free (δ_{free}) and bound (δ_{bound}) *trans,cis*-**4e** and complexation-induced shifts ($\Delta\delta$).

Signal	δ_{free} (ppm)	δ_{bound} (ppm)	$\Delta\delta$ (ppm)
trans	8.03	-	-
cis	7.98	4.45	-3.53
1	3.21	2.33	-0.88
2	1.52	0.95	-0.57
3	1.30	-0.03	-1.33
4	1.30	-0.24	-1.54
5	1.30	-0.71	-2.01
6	-	-0.03	-1.33
7	-	0.67	-0.63
8	-	1.22	-0.30
9	-	3.05	-0.16

3.4.5 ITC experiments in water solution

Titrations were carried out in water solution at 298 or 313 K by adding small aliquots (8 µL, 32 s) of a solution of guest into a solution of the host. The concentration of the guest's solution was 7-8 times more concentrated than the host's solution (see corresponding figures for details).

Bis-isonitrile **2b**

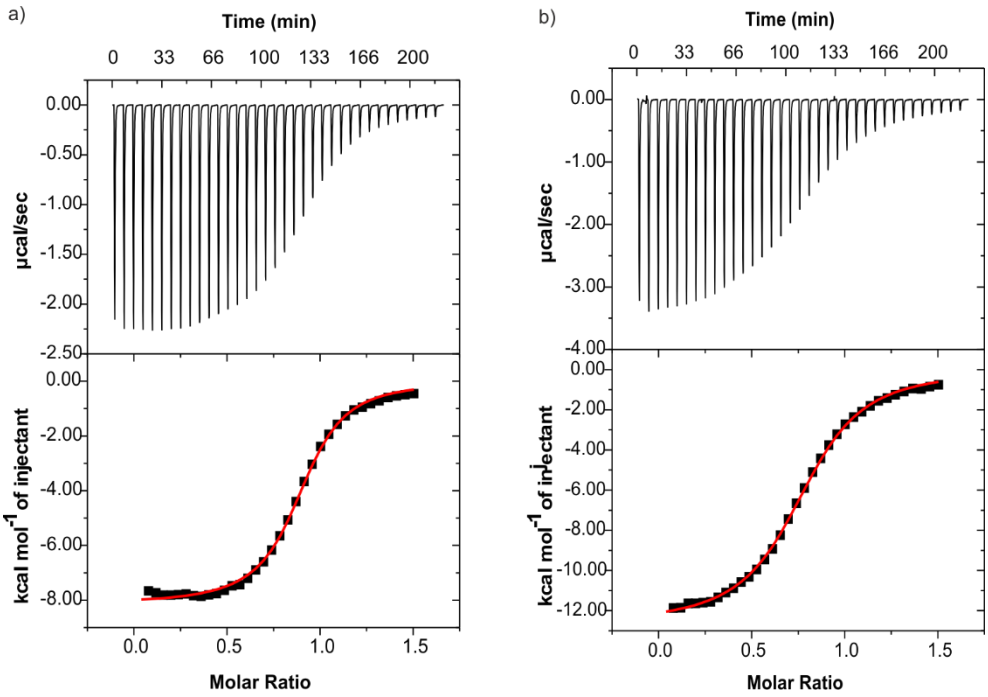

Figure 3.77. top) Trace shows raw data for the titrations of guest into host: [**2b**] = 1.4 mM and [**1**] = 0.2 mM. Titrations were performed in H_2O at a) 298 and b) 313 K. bottom) Binding isotherms of the calorimetric titrations shown on top. The enthalpy of binding for each injection is plotted versus the molar ratio of guest/host in the cell. The continuous line represents the least-squares-fit of the data to the "one set of sites" binding model.

Table 3.13. Binding constants (K_a) and thermodynamic parameters (ΔH, $T\Delta S$ and ΔG) obtained from the ITC experiments of **2b** and **1** at 298 or 313 K. Errors in K_a and ΔH are reported as standard deviations.

Complex	T (K)	K_a (M^{-1})	ΔH (kcal·mol^{-1})	$T\Delta S$ (kcal·mol^{-1})	ΔG (kcal·mol^{-1})
2b⊂1	298	3.5±0.1 x 10^5	-8.5±0.5	-1.0±0.5	-7.5±0.1
	313	1.3±0.1 x 10^5	-12.1±0.1	-4.8±0.1	-7.3±0.1

Mono-formamide **3a, b** and **e**

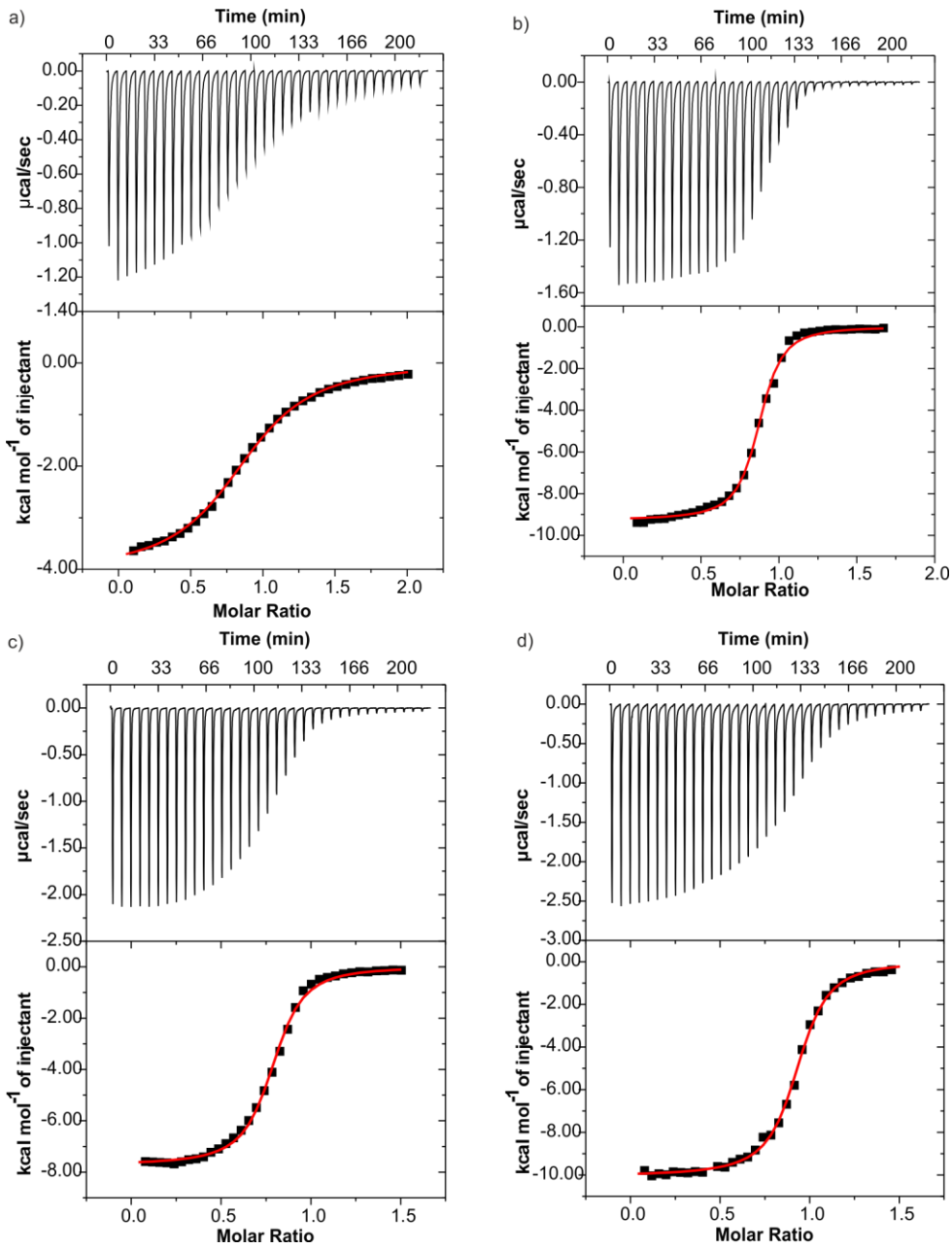

Figure 3.78. top) Trace shows raw data for the titration of guest into host: a) [**3a**] = 2.8 mM and [**1**] = 0.35 mM; b) [**3e**] = 1.4 mM and [**1**] = 0.2 mM. Titration was performed in H_2O at 298 K. [**3b**] = 1.4 mM and [**1**] = 0.2 mM performed in H_2O at c) 298 K and d) 333 K. bottom) Binding isotherm of the calorimetric titration shown on top. The enthalpy of binding for each injection is plotted versus the molar ratio of guest/host in the cell. The continuous line represents the least-squares-fit of the data to the "one set of sites" binding model.

Bis-formamide **4a, b** and **e**

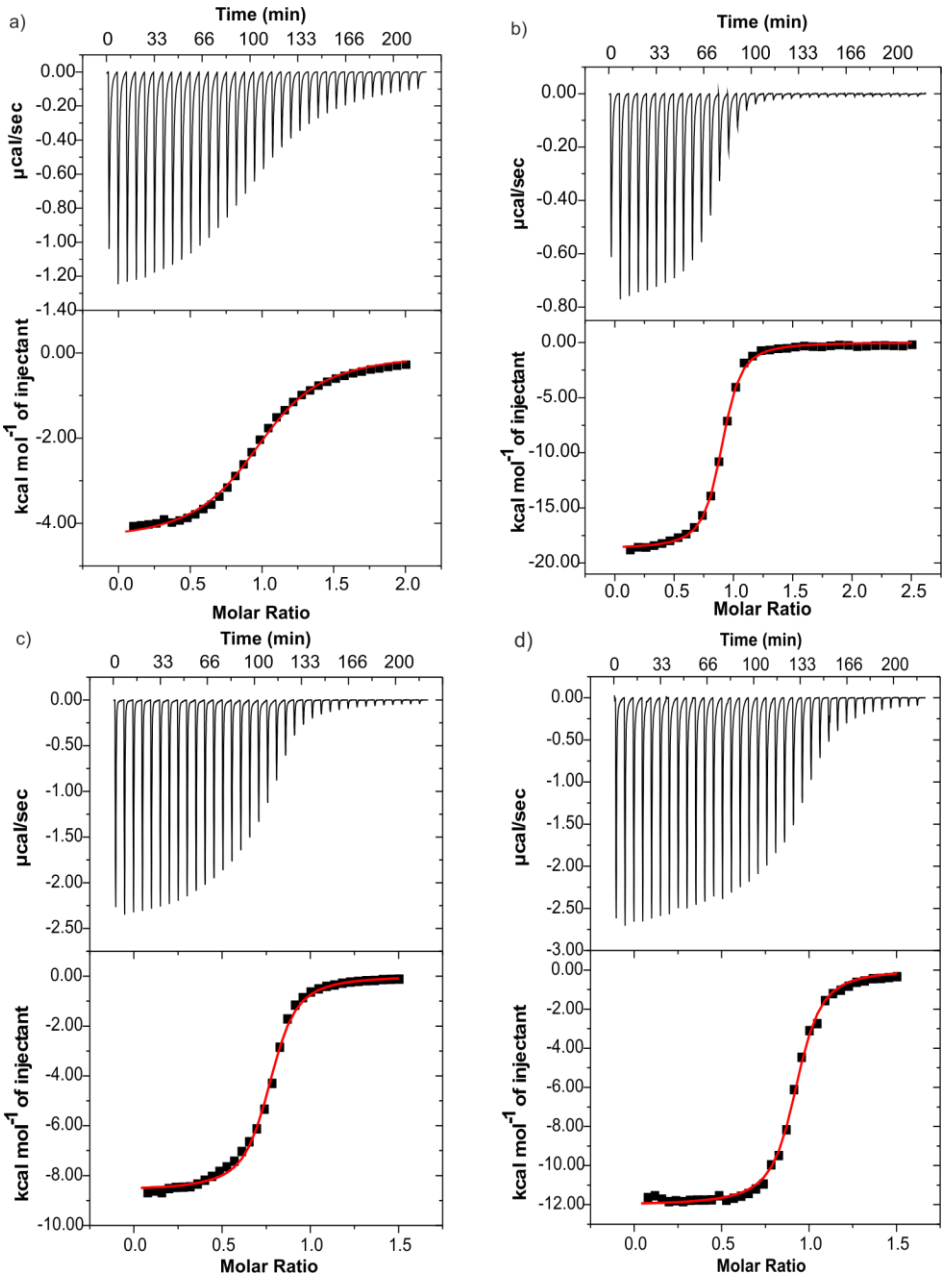

Figure 3.79. top) Trace shows raw data for the titration of guest into host: a) [**4a**] = 2.8 mM and [**1**] = 0.35 mM; b) [**4e**] = 0.35 mM and [**1**] = 0.03 mM. Titration was performed in H_2O at 298 K. [**4b**] = 1.4 mM and [**1**] = 0.2 mM performed in H_2O at: c) 298 K and d) 333K. bottom) Binding isotherm of the calorimetric titration shown on top. The enthalpy of binding for each injection is plotted versus the molar ratio of guest/host in the cell. The continuous line represents the least-squares-fit of the data to the "one set of sites" binding model.

Table 3.14. Binding constants (K_a) and thermodynamic parameters (ΔH, $T\Delta S$ and ΔG) obtained from the ITC experiments of **3a**, **b**, **e** and **1** at 298 or 313 K. Errors in K_a and ΔH are reported as standard deviations.

Complex	*T* (K)	K_a (M^{-1})[a]	ΔH (kcal·mol^{-1})	$T\Delta S$ (kcal·mol^{-1})	ΔG (kcal·mol^{-1})
3a⊂1	298	5.0±0.5 x 10^4	-3.7±0.4	2.7±0.4	-6.4±0.1
3b⊂1	298	5.7±0.4 x 10^5	-7.3±0.6	0.6±0.5	-7.9±0.1
	313	6.9±0.9 x 10^5	-10.2±0.3	-1.9±0.3	-8.3±0.1
3e⊂1	298	9.2±0.5 x 10^5	-9.9±0.9	-1.8±0.9	-8.1±0.1

[a] The reported K_a values are apparent because only the *cis*-isomer of the guests bind to the calix[4]pyrrole unit of the receptor.

Table 3.15. Binding constants (K_a) and thermodynamic parameters (ΔH, $T\Delta S$ and ΔG) obtained from the ITC experiments of **4a**, **b**, **e** and **1** at 298 or 313 K. Errors in K_a and ΔH are reported as standard deviations.

Complex	*T* (K)	K_a (M^{-1})	ΔH (kcal·mol^{-1})	$T\Delta S$ (kcal·mol^{-1})	ΔG (kcal·mol^{-1})
4a⊂1	298	6.1±0.3 x 10^4	-4.3±0.2	2.2±0.2	-6.5±0.1
4b⊂1	298	6.7±0.1 x 10^5	-8.6±0.1	-0.7±0.1	-7.9±0.1
	313	9.2±0.1 x 10^5	-12.1±0.1	-3.6±0.1	-8.5±0.1
4e⊂1	298	5.0±0.5 x 10^6	-18.6±0.2	-9.5±0.2	-9.1±0.1

[a] The reported K_a values are apparent because only the *cis*-isomer of the guests bind to the calix[4]pyrrole unit of the receptor.

3.4.6 Hydrolysis reactions monitored by ^{1}H NMR spectroscopy

Stability of *bis*-formamide **4b** and container **1** under reaction conditions

Separate solutions of compound **1** or **4b** (1 mM) were prepared in D_2O. Subsequently, 0.5 mL of the compound's solution were added to an NMR tube. A solution of citric acid (0.5 M) was prepared in D_2O. Citric acid (5 mM) was added to the previous solution. The pD of the solution was *ca.* 3. The NMR tube was heated in an oil bath at 40ºC. ^{1}H NMR spectra were acquired at different time intervals.

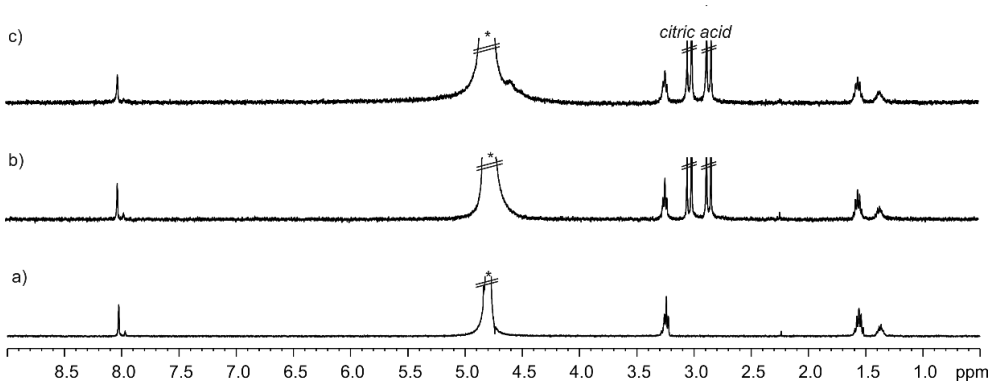

Figure 3.80. ^{1}H NMR (300 MHz, D_2O, 298 K) spectra: a) *bis*-formamide **4b**; b) addition of citric acid (5 mM) and c) after 1 h at 40°C. *Residual solvent peak.

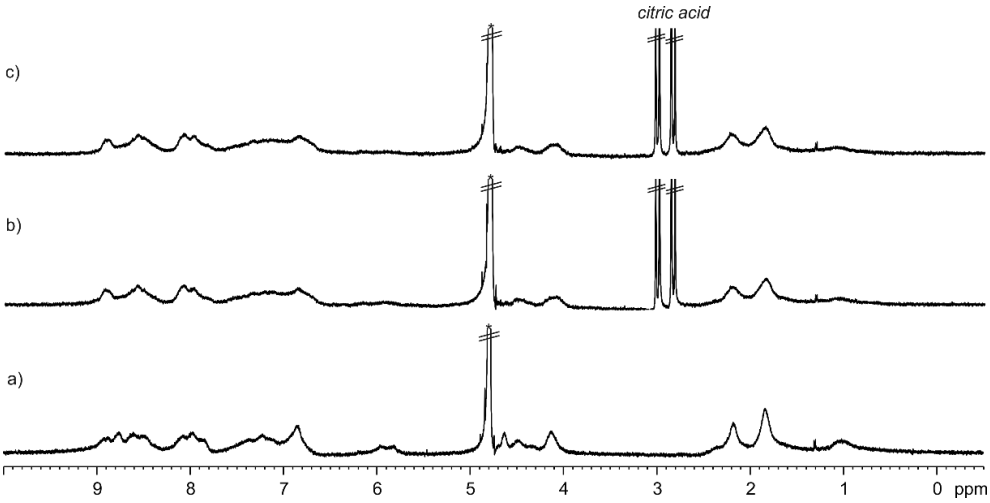

Figure 3.81. ^{1}H NMR (400 MHz, D_2O, 298 K) spectra: a) octa-pyridinium **1**; b) addition of citric acid (5 mM) and c) after 1 h at 40ºC. *Residual solvent peak.

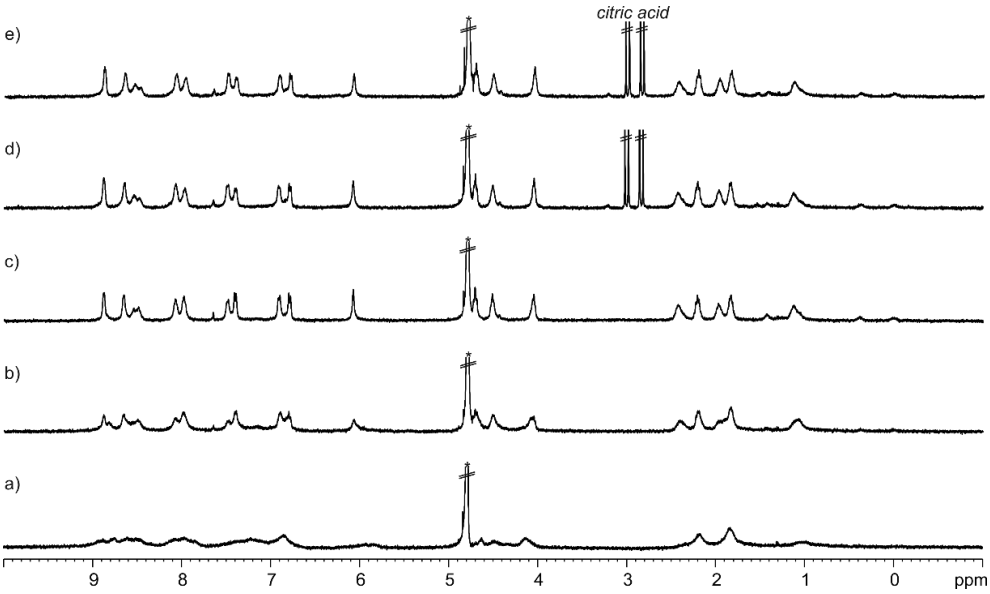

Figure 3.82. ^{1}H NMR (400 MHz, D_2O, 298 K) spectra: a) octa-pyridinium **1**; addition of *bis*-formamide **4b**: b) 0.5 and c) 1 equiv.; d) addition of citric acid (5 mM) and e) after 1 h at 40ºC. *Residual solvent peak.

The ^{1}H NMR spectra shown above indicated that **1** and **4b** are stable in acidic aqueous solution (5 mM citric acid, pD ~ 3).

Hydrolysis of *bis*-isonitriles **2a**-**e** in the absence of container

A solution of *bis*-isonitrile **2a**-**e** (1-2 mM) was prepared in D_2O. Subsequently, 0.5 mL of the solution were placed in an NMR tube. A solution of citric acid (0.5 M) was prepared in D_2O. Citric acid (5 mM) was added to the previous solution. The pD of the aqueous solution was *ca.* 3. The NMR spectrum of the solution was acquired. After that, the NMR tube was heated in an oil bath or in the spectrometer probe at 40ºC. NMR spectra were acquired at different time intervals (see figure footnotes for details). Integration of the proton signals allowed the determination of the concentrations of the species in the hydrolysis reactions of **2a**,**b**.

Bis-isonitrile **2a**

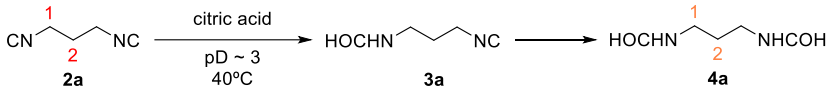

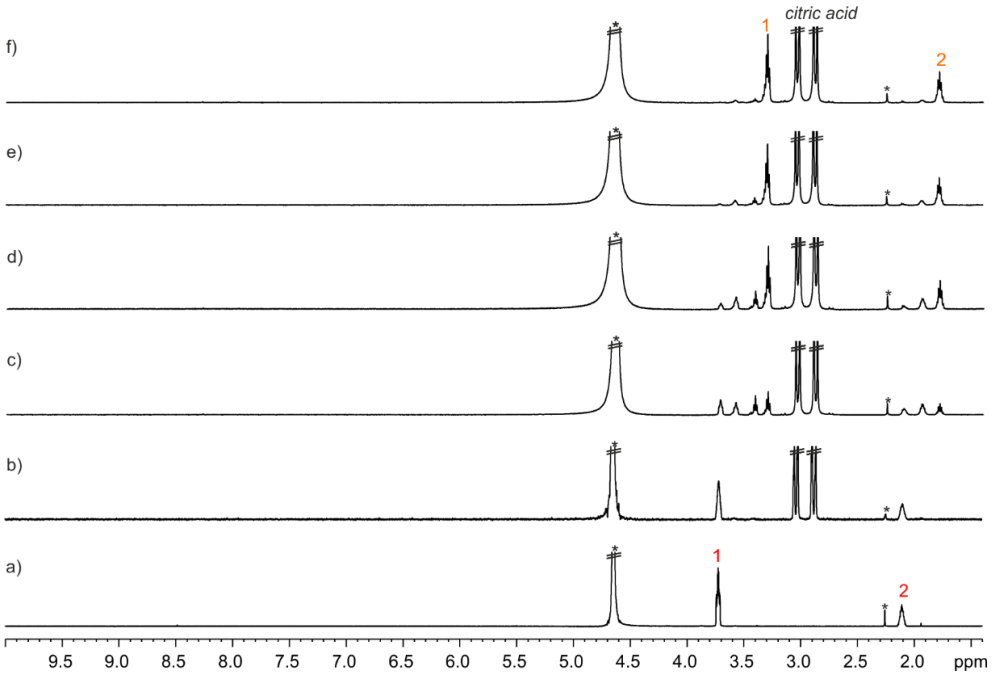

Figure 3.83. Selected ^{1}H NMR (500 MHz with cryoprobe, D_2O, 313 K) spectra: a) *bis*-isonitrile **2a**; b) addition of citric acid (5 mM); after c) 30; d) 60; e) 90 and f) 120 min. *Residual solvent peak.

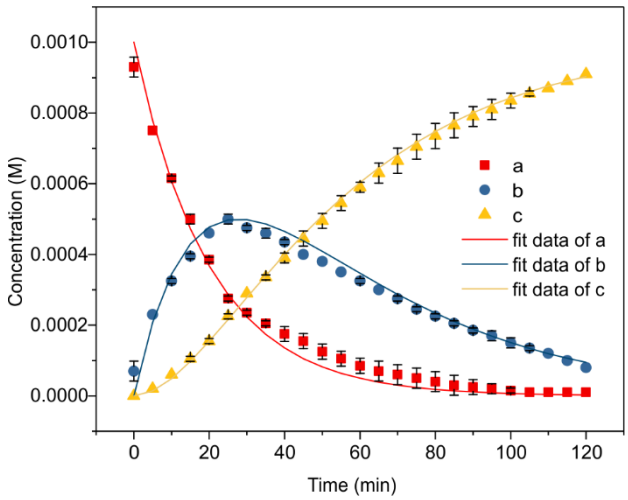

Figure 3.84. Concentration (M) *vs*. time (min) for the hydrolysis of *bis*-isonitrile **2a** (0.001 M) in acidic aqueous solution (5 mM citric acid, pD ~ 3) at 40ºC: a) *bis*-isonitrile **2a**; b) *mono*-formamide **3a** and c) *bis*-formamide **4a**. Lines represent fit of the experimental data to the theoretical kinetic model 2 (Section 3.4.2). Error bars are standard deviations.

Table 3.16. Rate constants (k_3 and k_4) returned from the fit of the experimental data (**2a** in the bulk solution) to the theoretical kinetic model 2.

Reaction	Rate constant (min^{-1})
2a → **3a**	k_3 = 5.0±1.0 x 10^{-2}
3a → **4a**	k_4 = 2.5±0.5 x 10^{-2}

Bis-isonitrile **2b**

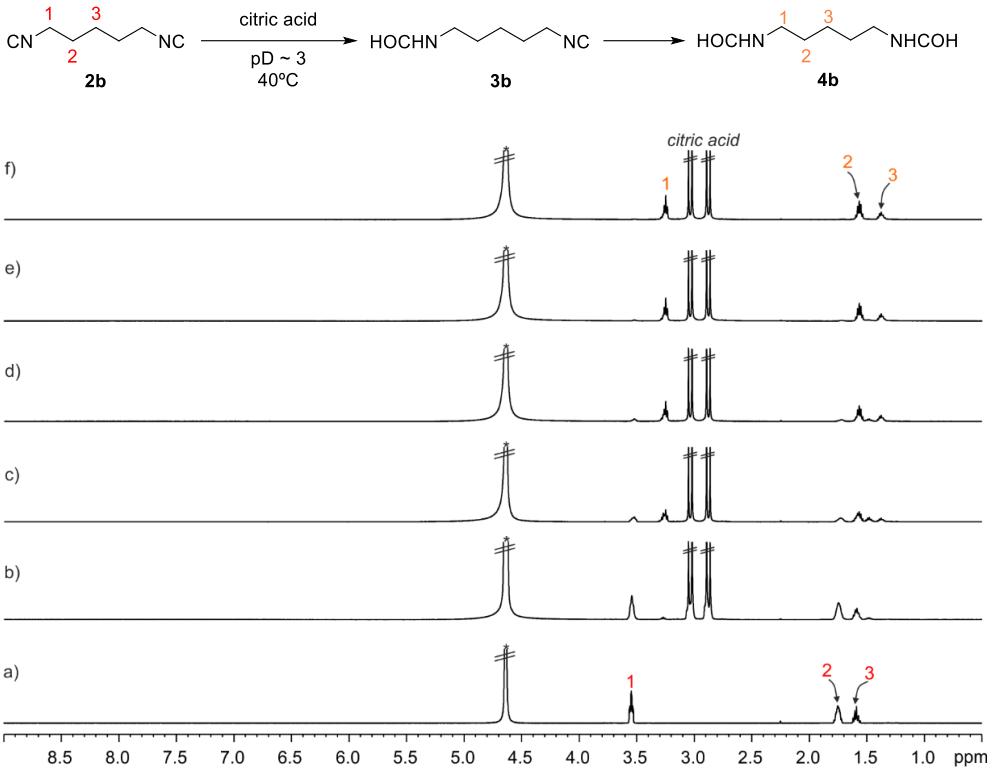

Figure 3.85. Selected ^{1}H NMR (500 MHz with cryoprobe, D_2O, 313 K) spectra: a) *bis*-isonitrile **2b**; b) addition of citric acid (5 mM); after c) 30; d) 60; e) 90 and f) 120 min. *Residual solvent peak.

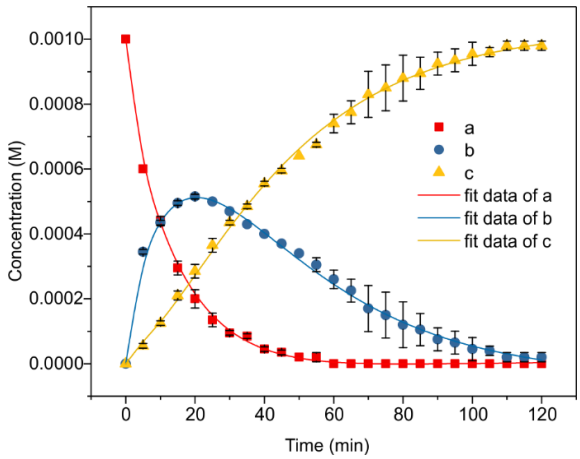

Figure 3.86. Concentration (M) *vs.* time (min) for the hydrolysis of *bis*-isonitrile **2b** (0.001 M) in acidic aqueous solution (5 mM citric acid, pD ~ 3) at 40ºC: a) *bis*-isonitrile **2b**; b) *mono*-formamide **3b** and c) *bis*-formamide **4b**. Lines represent fit of the experimental data to the theoretical kinetic model 2 (Section 3.4.2). Error bars are standard deviations.

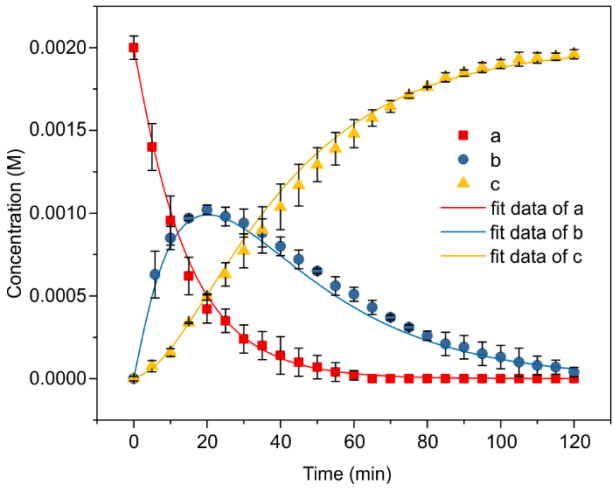

Figure 3.87. Concentration (M) *vs.* time (min) for the hydrolysis of *bis*-isonitrile **2b** (0.002 M) in acidic aqueous solution (5 mM citric acid, pD ~ 3) at 40ºC: a) *bis*-isonitrile **2b**; b) *mono*-formamide **3b** and c) *bis*-formamide **4b**. Lines represent fit of the experimental data to the theoretical kinetic model 2 (Section 3.4.2). Error bars are standard deviations.

Table 3.17. Rate constants (k_3 and k_4) returned from the fit of the experimental data (**2b** in the bulk solution) to the theoretical kinetic model 2.

Reaction	Rate constant (min^{-1})
2b → **3b**	k_3 = 7.0±1.0 x 10^{-2}
3b → **4b**	k_4 = 3.5±0.5 x 10^{-2}

Note: The characteristic proton signals of *mono*-formamides **3c**-**e** overlap with those of the starting materials, *bis*-isonitriles **2c**-**e**, and the products, *bis*-formamides **4c**-**e**. This fact precluded the

determination of the concentrations of the species in the hydrolysis reactions by integration of the corresponding proton signals.

Hydrolysis of *bis*-isonitriles **2a**-**e** in the presence of container **1**

A solution of octa-pyridinium **1** (1 mM) was prepared in D_2O. Subsequently, 0.5 mL of the solution were placed in an NMR tube. A solution of *bis*-isonitrile **2a**,**b** was prepared at 20-30-fold higher concentration (20-30 mM). For *bis*-isonitriles **2c**-**e**, a solution of the guest was prepared at 80-100-fold higher concentration in $(CD_3)_2SO$ (80-100 mM). Immediately, the 0.5 mL of the receptor's solution was titrated by manually injecting incremental amounts of the titrant's solution using a micro-syringe. A ^1H NMR spectrum of the mixture was acquired after each injection and vigorous hand shaking of the NMR tube for few seconds. A solution of citric acid (0.5 M) was prepared in D_2O. Citric acid (5 mM) was added to the previous solution. The pD of the aqueous solution was *ca.* 3. The NMR spectrum of the solution was acquired. After that, the NMR tube was heated in an oil bath or in the spectrometer probe at 40ºC. NMR spectra were acquired at different time intervals (see figure footnotes for details). The concentrations of the species in the hydrolysis reactions were determined by: a) integration of the proton signals of the bound guests and/or b) integration of the proton signals of the guests released to the bulk solution upon addition of a competitive guest, *i.e.* 4-phenylpyridine *N*-oxide (1.2 equiv.).

Bis-isonitrile **2a**

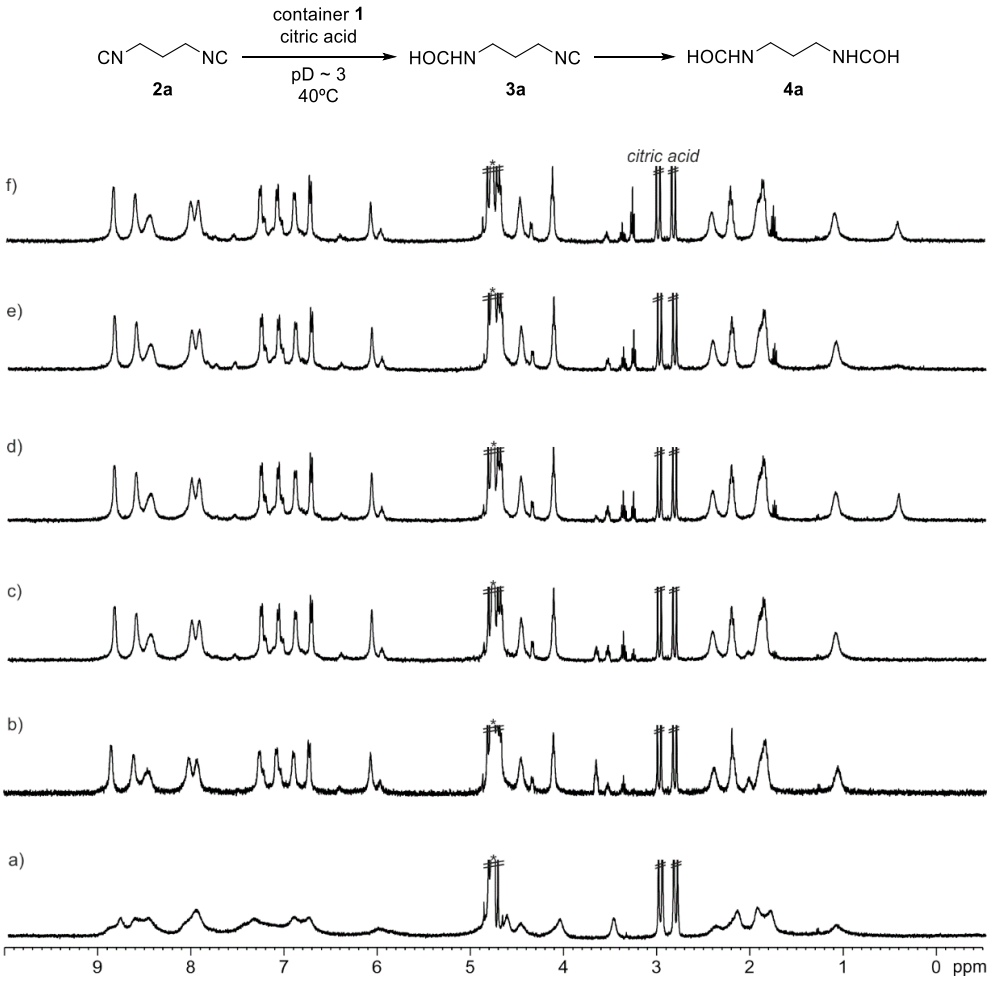

Figure 3.88. ^{1}H NMR (400 MHz, D_2O, 298 K) spectra of the hydrolysis reaction of *bis*-isonitrile **2a** in the presence of octa-pyridinium **1**: a) **1**; **2a** (1 equiv.) and citric acid (5 mM); addition of 4-phenylpyridine *N*-oxide (1.2 equiv.) to a): after b) 15; c) 30; d) 60; e) 90 and f) 120 min at 40°C. *Residual solvent peak.

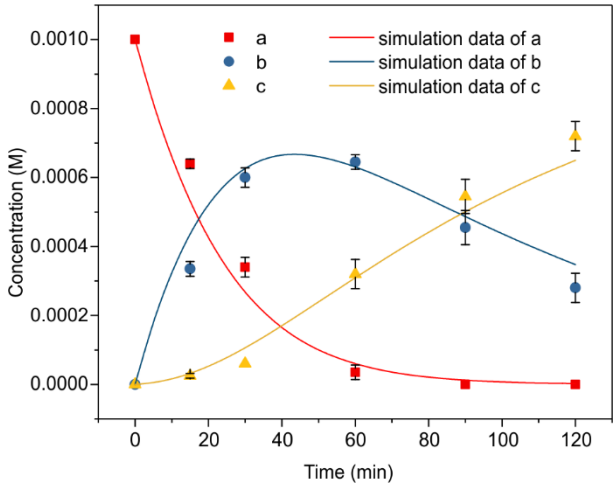

Figure 3.89. Concentration (M) *vs.* time (min) for the hydrolysis of *bis*-isonitrile **2a** (0.001 M) in the presence of octa-pyridinium **1** (0.001 M) in acidic aqueous solution (5 mM citric acid, pD ~ 3) at 40ºC obtained by NMR integration of the free species upon addition of 4-phenylpyridine *N*-oxide: a) *bis*-isonitrile **2a**; b) *mono*-formamide **3a** and c) *bis*-formamide **4a**. Lines represent simulation of the reaction profile using the theoretical kinetic model 3 (Section 3.4.2). Error bars are standard deviations.

Table 3.18. Rate and equilibrium constant values used for the simulation of the reaction profile (**2a** in the presence of container **1**).

Reaction	Constant
2a → **3a**	k_3 = 8.0 x 10^{-2} min^{-1}
3a → **4a**	k_4 = 4.0 x 10^{-2} min^{-1}
2a + **1** ⇆ **2a⊂1**	K_a = 2.0 x 10^{3} M^{-1}
3a + **1** ⇆ **3a⊂1**	K_a = 1.0 x 10^{4} M^{-1}
4a + **1** ⇆ **4a⊂1**	K_a = 2.0 x 10^{4} M^{-1}

Note that the fixed constant values, k_3, k_4, K_a (**2a⊂1**), K_a (**3a⊂1**) and K_a (**4a⊂1**), are in line with those determined/estimated by analysis of the hydrolysis reaction of *bis*-isonitrile **2a** in the absence of container and ITC experiments with receptor **1**.

Bis-isonitrile **2b**

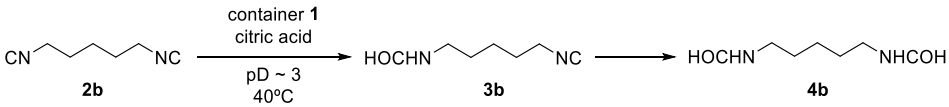

In the presence of 1 equiv. of container **1**

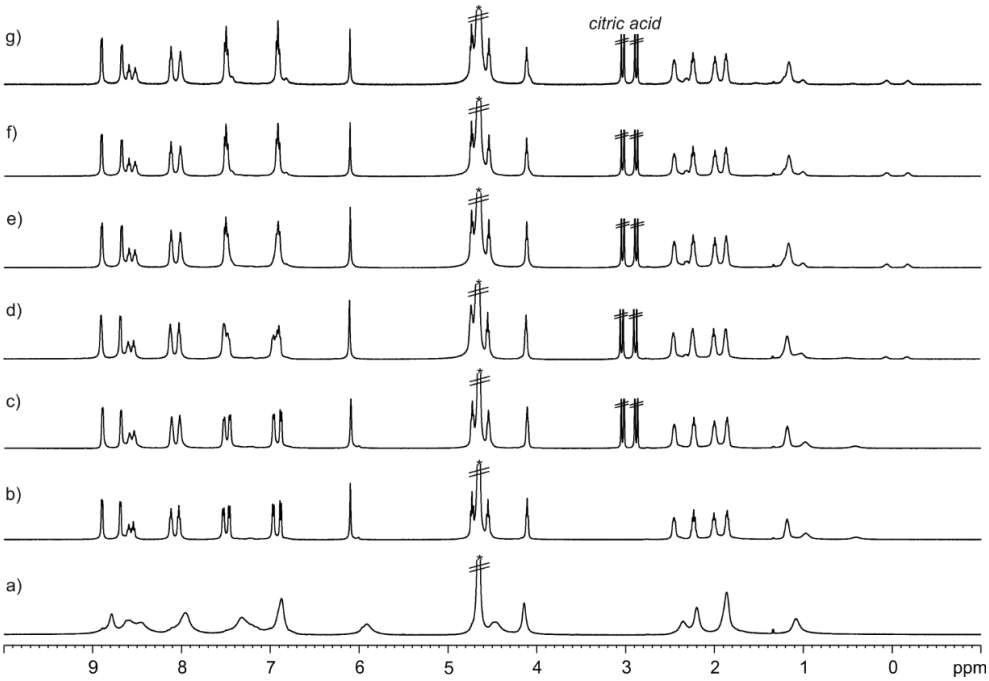

Figure 3.90. Selected ^{1}H NMR (500 MHz with cryoprobe, D_2O, 313 K) spectra of the hydrolysis reaction of *bis*-isonitrile **2b** in the presence of octa-pyridinium **1**: a) **1**; b) addition of **2b** (1 equiv.); c) addition of citric acid (5 mM); after d) 30; e) 60; f) 90 and g) 120 min. *Residual solvent peak.

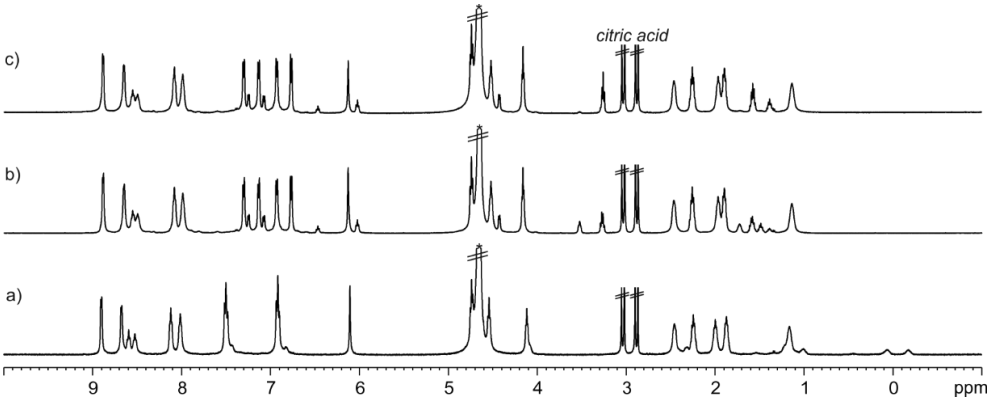

Figure 3.91. ^{1}H NMR (500 MHz with cryoprobe, D_2O, 313 K) spectra: a) octa-pyridinium **1**, *bis*-isonitrile **2b** (1 equiv.) and citric acid (5 mM) after 2 h at 40ºC; b) addition of 4-phenylpyridine *N*-oxide (1.2 equiv.) and c) after 1 h at 40ºC. *Residual solvent peak.

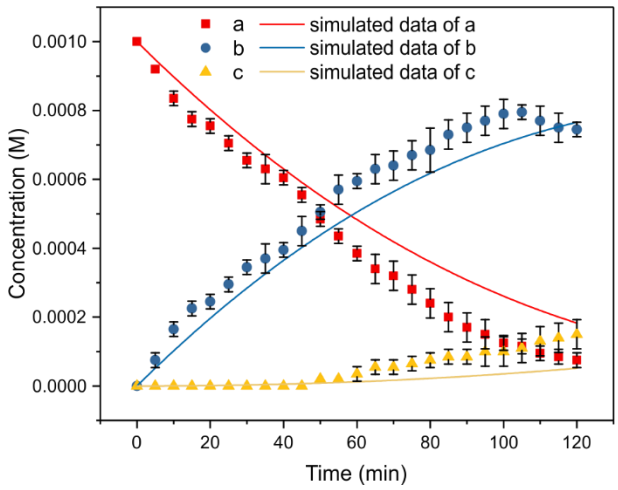

Figure 3.92. Concentration (M) *vs*. time (min) for the hydrolysis of *bis*-isonitrile **2b** (0.001 M) in the presence of octa-pyridinium **1** (0.001 M) in acidic aqueous solution (5 mM citric acid, pD ~ 3) at 40ºC obtained by NMR integration of the proton signals of the bound species: a) *bis*-isonitrile **2b**; b) *mono*-formamide **3b** and c) *bis*-formamide **4b**. Lines represent simulation of the reaction profile using the theoretical kinetic model 3 (Section 3.4.2). Error bars are standard deviations.

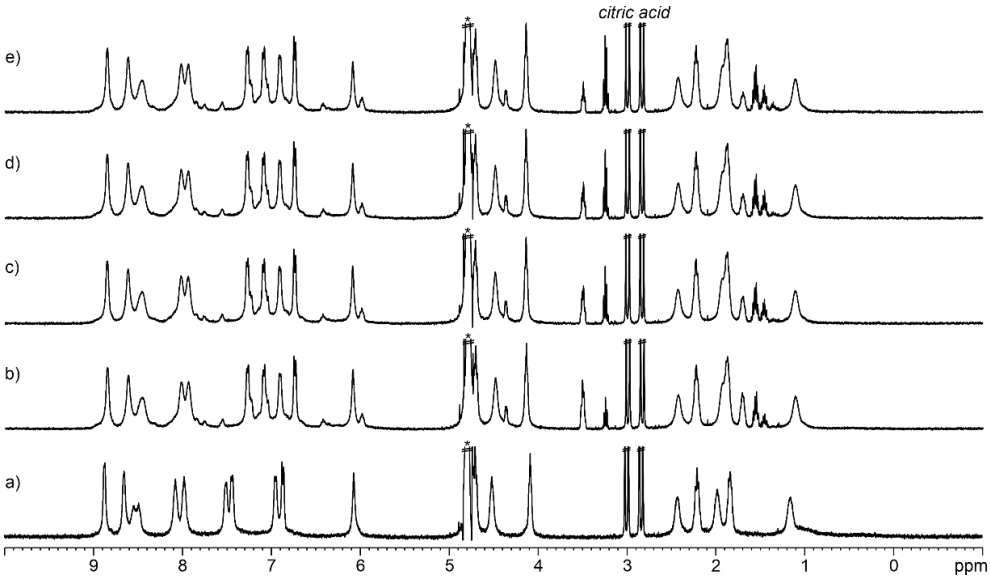

Figure 3.93. ^{1}H NMR (400 MHz, D_2O, 298 K) spectra of the hydrolysis reaction of *bis*-isonitrile **2b** in the presence of octa-pyridinium **1**: a) **1**, **2b** (1 equiv.) and citric acid (5 mM); addition of 4-phenylpyridine *N*-oxide (1.2 equiv.) to a): after b) 30; c) 60; d) 90 and e) 120 min at 40ºC. *Residual solvent peak.

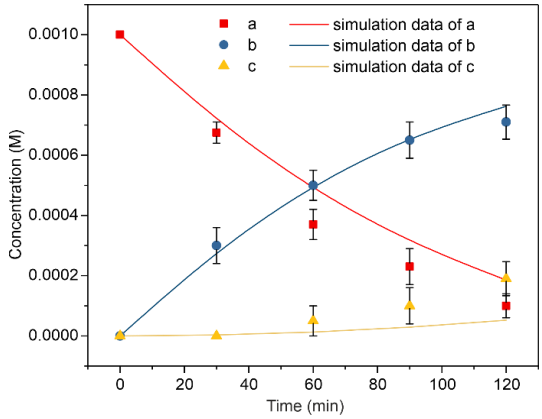

Figure 3.94. Concentration (M) *vs.* time (min) for the hydrolysis of *bis*-isonitrile **2b** (0.001 M) in the presence of octa-pyridinium **1** (0.001 M) in acidic aqueous solution (5 mM citric acid, pD ~ 3) at 40ºC obtained by NMR integration of the free species upon addition of 4-phenylpyridine *N*-oxide: a) *bis*-isonitrile **2b**; b) *mono*-formamide **3b** and c) *bis*-formamide **4b**. Lines represent simulation of the reaction profile using the theoretical kinetic model 3 (Section 3.4.2). Error bars are standard deviations.

In the presence of 1.5 equiv. of container **1**

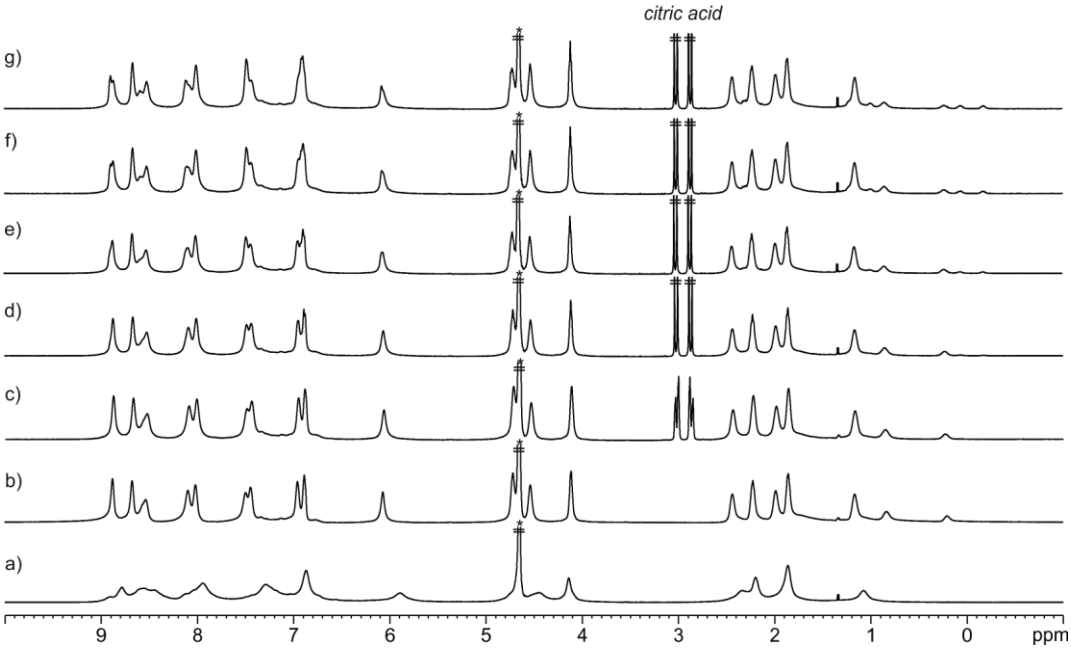

Figure 3.95. Selected ^{1}H NMR (500 MHz with cryoprobe, D_2O, 313 K) spectra of the hydrolysis reaction of *bis*-isonitrile **2b** (1 mM) in the presence of octa-pyridinium **1** (1.5 mM): a) **1**; b) addition of **2b**; c) addition of citric acid (5 mM); after d) 30; e) 60; f) 90 and g) 120 min. *Residual solvent peak.

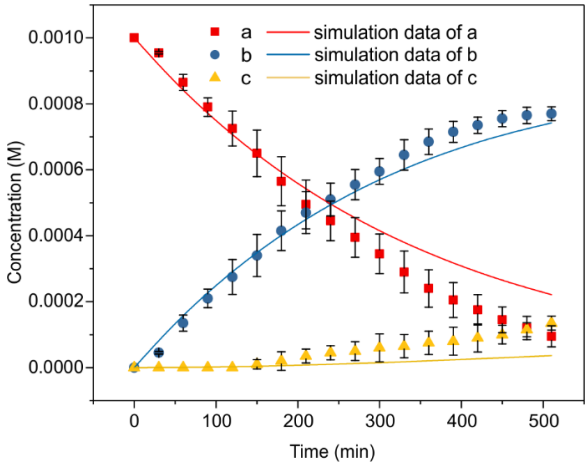

Figure 3.96. Concentration (M) *vs.* time (min) for the hydrolysis of *bis*-isonitrile **2b** (0.001 M) in the presence of octa-pyridinium **1** (0.0015 M) in acidic aqueous solution (5 mM citric acid, pD ~ 3) at 40ºC obtained by NMR integration of the proton signals of the bound species: a) *bis*-isonitrile **2b**; b) *mono*-formamide **3b** and c) *bis*-formamide **4b**. Lines represent simulation of the reaction profile using the theoretical kinetic model 3 (Section 3.4.2). Error bars are standard deviations.

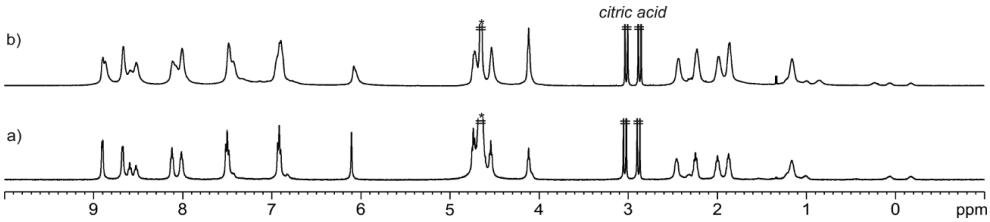

Figure 3.97. Comparison of the ^{1}H NMR (500 MHz with cryoprobe, D_2O, 313 K) spectra of the hydrolysis reaction of *bis*-isonitrile **2b** (1 mM) using citric acid (5 mM) after 120 min in the presence of octa-pyridinium **1**: a) 1 and b) 1.5 equiv.*Residual solvent peak.

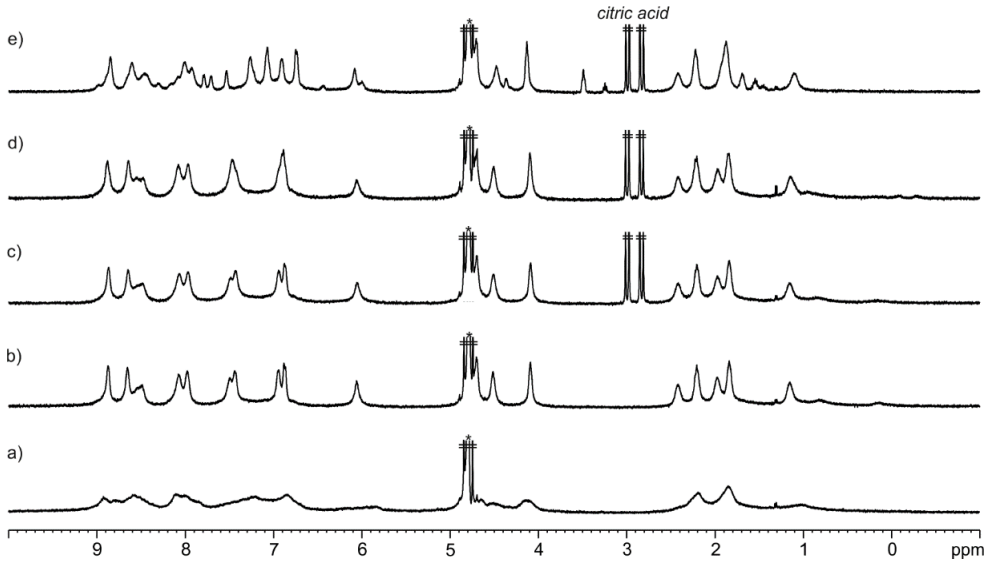

Figure 3.98. ^{1}H NMR (400 MHz, D_2O, 298 K) spectra of the hydrolysis reaction of *bis*-isonitrile **2b** (1 mM) in the presence of octa-pyridinium **1** (1.5 mM): a) **1**; b) addition of **2b**; c) addition of citric acid (5 mM); d) after 120 min at 40ºC and e) addition of 4-phenylpyridine *N*-oxide (excess). *Residual solvent peak.

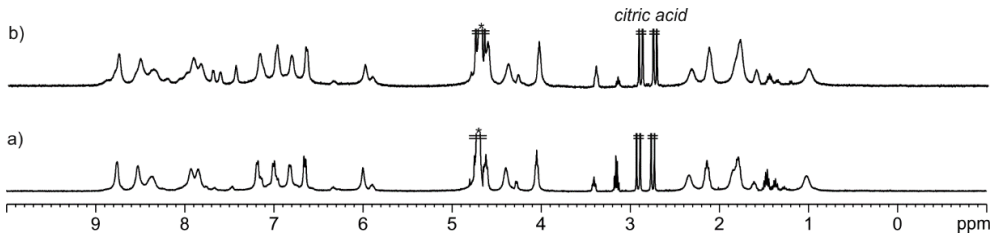

Figure 3.99. Comparison of the ^{1}H NMR (400 MHz, D_2O, 298 K) spectra of the hydrolysis reaction of *bis*-isonitrile **2b** (1 mM) using citric acid (5 mM) after 120 min in the presence of octa-pyridinium **1**: a) 1 and b) 1.5 equiv. 4-Phenylpyridine *N*-oxide (excess) was added before the acquisition of the ^{1}H NMR spectra. *Residual solvent peak.

In the presence of 1.5 equiv. of container **1**, the acid-catalyzed hydrolysis of *bis*-isonitrile **2b** gave 39% of *mono*-formamide **3b** after 120 min.

Table 3.19. Rate and equilibrium constant values used for the simulation of the reaction profile (**2b** in the presence of container **1**).

Reaction	Rate constants
2b → **3b**	k_3 = 8.0 x 10^{-2} min^{-1}
3b → **4b**	k_4 = 4.0 x 10^{-2} min^{-1}
2b + **1** ⇆ **2b⊂1**	K_a = 5.0 x 10^4 M^{-1}
3b + **1** ⇆ **3b⊂1**	K_a = 5.0 x 10^5 M^{-1}
4b + **1** ⇆ **4b⊂1**	K_a = 9.0 x 10^5 M^{-1}

Note that the fixed constant values, k_3, k_4, K_a (**2b⊂1**), K_a (**3b⊂1**) and K_a (**4b⊂1**), are in line with those determined by analysis of the hydrolysis reaction of *bis*-isonitrile **2b** in the absence of container and ITC experiments with receptor **1**, within the error.

Extraction experiment of *mono*-formamide **3b**

Bis-isonitrile **2b** (1 mM), octa-pyridinium **1** (1 mM) and citric acid (5 mM) in D_2O solution (2.5 mL, pD ~ 3) were heated at 40ºC for 100 min. After that, the solution was neutralized by adding aqueous saturated $NaHCO_3$ until pD ~ 7.4. The resulting aqueous solution was concentrated to 0.5 mL volume by freeze drying. The crude was extracted with EtOAc (10x0.5 mL). The organic layer was dried (Na_2SO_4), filtered and concentrated. Finally, a ^{1}H NMR spectrum was acquired.

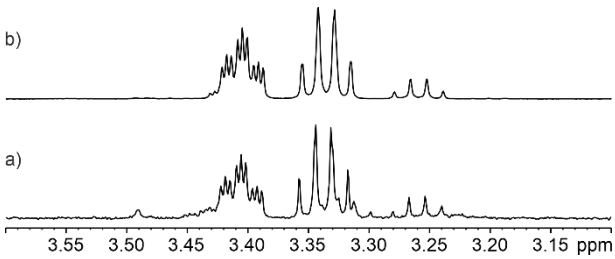

Figure 3.100. Selected region of the ^{1}H NMR (500 MHz, $CDCl_3$, 298 K) spectra: a) extracted crude from the acid-catalyzed hydrolysis of *bis*-isonitrile **2b** (1 mM) in the presence of octa-pyridinium **1** (1 mM) after 100 min and b) pure *mono*-formamide **3b**. In a) *mono*-formamide **3b** is the major compound in the extracted crude, together with trace amounts of *bis*-isonitrile **2b** and *bis*-formamide **4b**. The competitive guest, 4-phenylpyridine *N*-oxide, was also partially extracted.

Bis-isonitrile **2c**

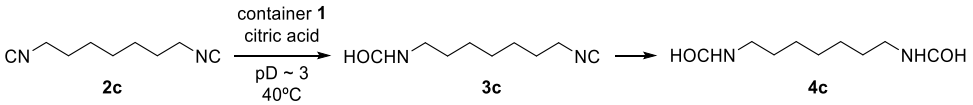

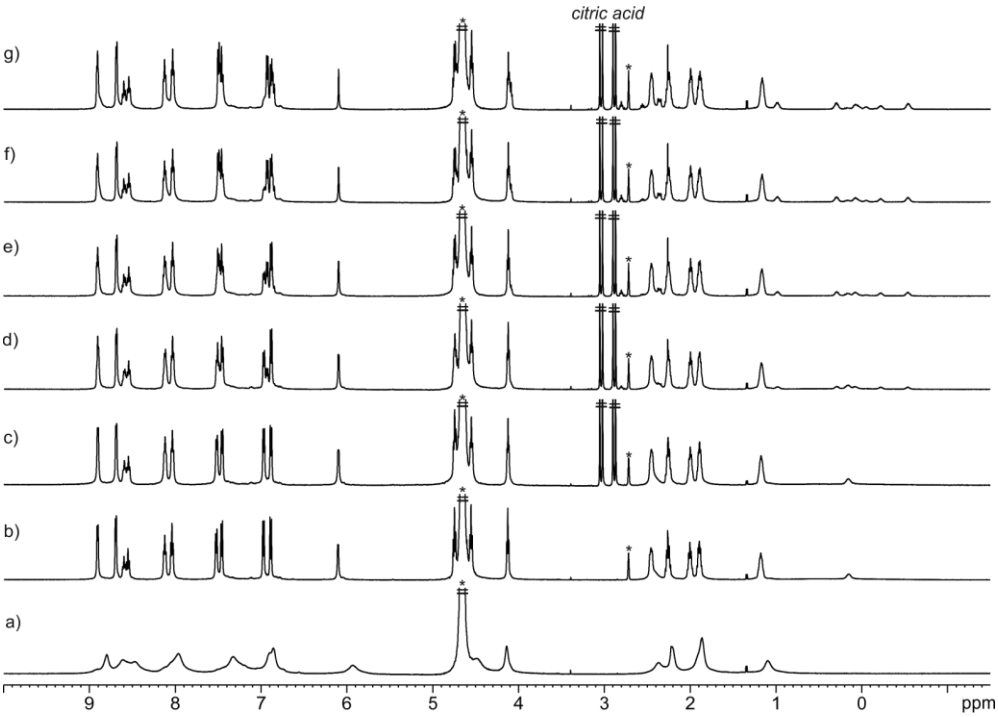

Figure 3.101. Selected ^{1}H NMR (500 MHz with cryoprobe, D_2O, 313 K) spectra of the hydrolysis reaction of *bis*-isonitrile **2c** in the presence of octa-pyridinium **1**: a) **1**; b) addition of **2c** (1 equiv.); c) addition of citric acid (5 mM); after d) 120; e) 240; f) 360 and g) 480 min. *Residual solvent peaks.

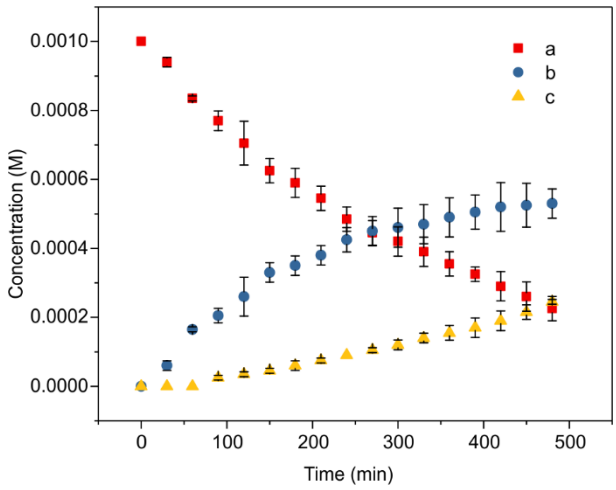

Figure 3.102. Concentration (M) *vs*. time (min) for the hydrolysis of *bis*-isonitrile **2c** (0.001 M) in the presence of octa-pyridinium **1** (0.001 M) in acidic aqueous solution (5 mM citric acid, pD ~ 3) at 40ºC obtained by NMR integration of the proton signals of the bound species: a) *bis*-isonitrile **2c**; b) *mono*-formamide **3c** and c) *bis*-formamide **4c**. Error bars are standard deviations.

Bis-isonitrile **2d**

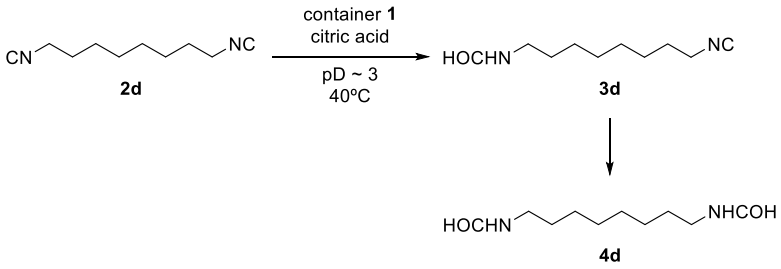

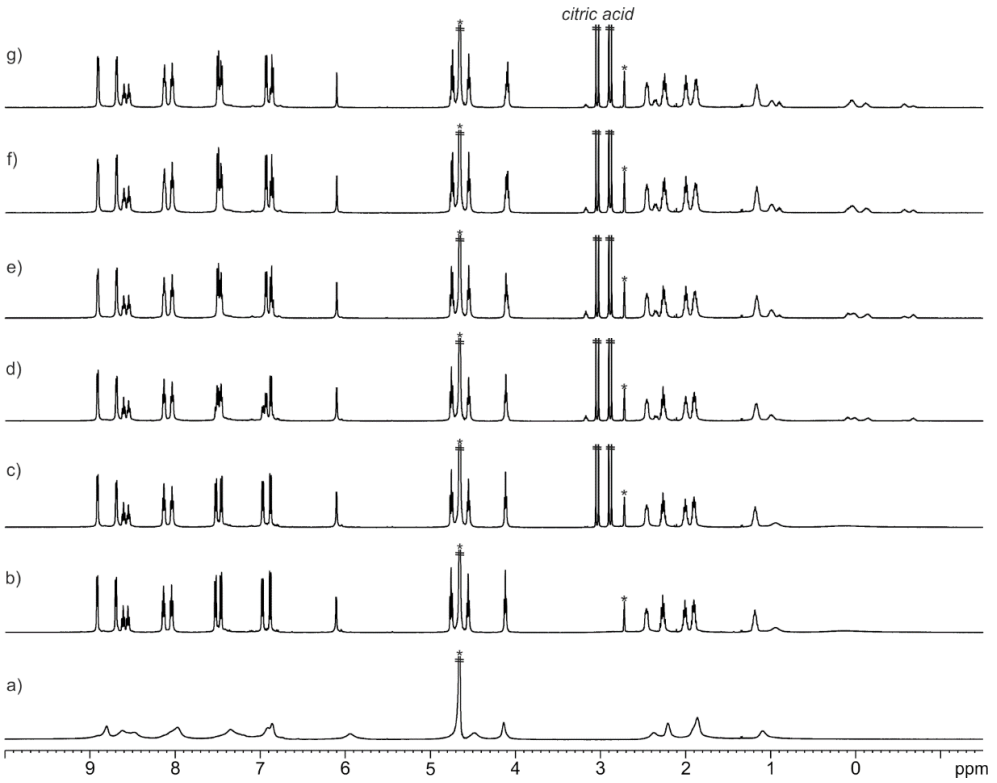

Figure 3.103. Selected ^{1}H NMR (500 MHz with cryoprobe, D_2O, 313 K) spectra of the hydrolysis reaction of *bis*-isonitrile **2d** in the presence of octa-pyridinium **1**: a) **1**; b) addition of **2d** (1 equiv.); c) addition of citric acid (5 mM); after d) 120; e) 240; f) 360 and g) 480 min. *Residual solvent peaks.

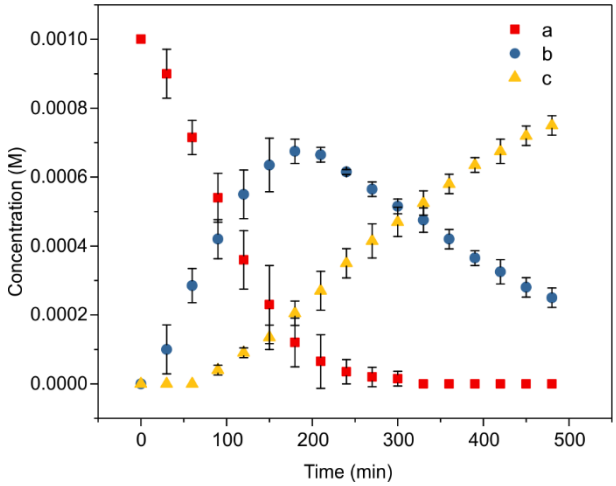

Figure 3.104. Concentration (M) *vs*. time (min) for the hydrolysis of *bis*-isonitrile **2d** (0.001 M) in the presence of octa-pyridinium **1** (0.001 M) in acidic aqueous solution (5 mM citric acid, pD ~ 3) at 40ºC obtained by NMR integration of the proton signals of the bound species: a) *bis*-isonitrile **2d**; b) *mono*-formamide **3d** and c) *bis*-formamide **4d**. Error bars are standard deviations.

Bis-isonitrile **2e**

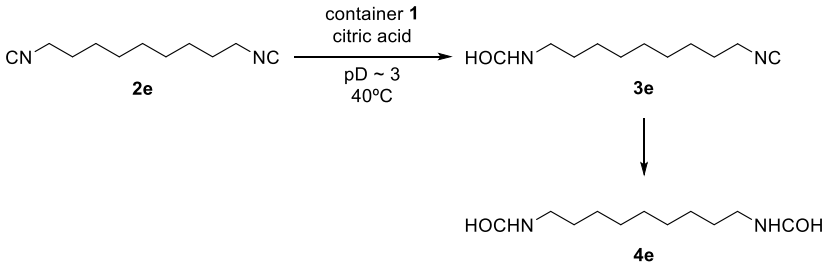

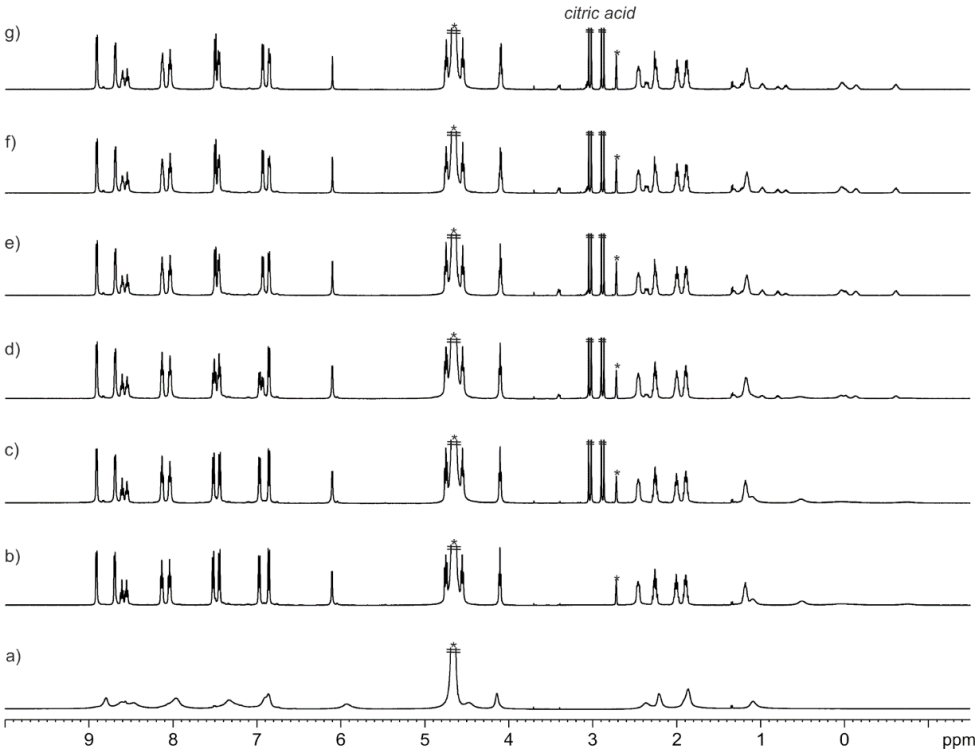

Figure 3.105. Selected ^{1}H NMR (500 MHz with cryoprobe, D_2O, 313 K) spectra of the hydrolysis reaction of *bis*-isonitrile **2e** in the presence of octa-pyridinium **1**: a) **1**; b) addition of **2e** (1 equiv.); c) addition of citric acid (5 mM); after d) 120; e) 240; f) 360 and g) 480 min. *Residual solvent peaks.

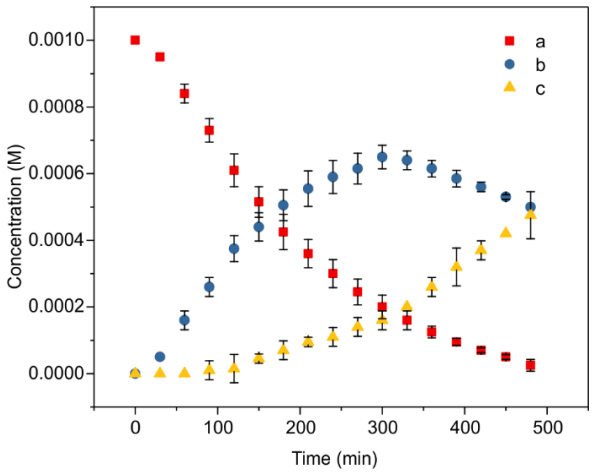

Figure 3.106. Concentration (M) *vs.* time (min) for the hydrolysis of *bis*-isonitrile **2e** (0.001 M) in the presence of octa-pyridinium **1** (0.001 M) in acidic aqueous solution (5 mM citric acid, pD ~ 3) at 40ºC obtained by NMR integration of the proton signals of the bound species: a) *bis*-isonitrile **2e**; b) *mono*-formamide **3e** and c) *bis*-formamide **4e**. Error bars are standard deviations.

3.4.7 Hydrolysis reactions of **2c**-**e** monitored by GC-FID due to signal overlap in the ^{1}H NMR kinetic analysis

Calibration curves

Standard solutions of *bis*-isonitriles **2c**-**e**, *mono*-formamides **3c**-**e** and *bis*-formamides **4c**-**e**, were prepared in CH_2Cl_2 solution at different, known concentrations (0.0004-0.020 M). The standard solutions were analyzed using a Clarus Gas Chromatography (GC) system equipped with a Flame Ionization Detector (FID) and an Elite-5 capillary column (30 x 0.25 mm, 0.25 µm). Integration of the chromatographic peaks provided the values of their corresponding areas. The analysis of the area versus the concentration of the standard solutions for each specie followed a linear relationship.

Partition coefficients

A solution of *bis*-isonitrile **2c**-**e** (1 mM), *mono*-formamide **3c**-**e** (1 mM) and *bis*-formamide **4c**-**e** (1 mM) was prepared in H_2O (V_w = 2 mL). Then, the equimolar mixture of compounds in water was extracted using CH_2Cl_2 (3x4 mL; n = 3 extractions; V_o = 4 mL). The combined organic layers were dried (Na_2SO_4), filtered and concentrated. The extracted mixture was redissolved in CH_2Cl_2 (0.1 mL) and analyzed by GC-FID. Using the calibration curves and the volume of the analyzed sample, we calculated the number of moles of each specie extracted in the combined organic layers (n_o). Based on the calculated number of moles in the combined organic layers (n_o) and the initial number of moles for each specie (n_i), we calculated the partition coefficients (*P*) using Equation 3,[53,54] which is defined for n extractions (in this case, n = 3) using an equal volume of organic solvent (in this case, V_o = 4 mL).

1) $P = [A]_o/[A]_w$; $[A]_o$ and $[A]_w$ are the concentrations of specie A at equilibrium between the organic and aqueous layers.

2) $n_i = n_o + n_w$; n_i is the initial number of moles of A in the aqueous layer; n_o is the number of moles of A in the combined organic layers after n extractions and n_w is the number of moles of A that remains in the aqueous layer.

3) $n_o/n_i = 1 - [1/(1 + (PV_o/V_w))^n] = 1 - f$

Hydrolysis of *bis*-isonitriles **2c**-**e** in the absence of container in water containing 1% $(CH_3)_2SO$

A solution of *bis*-isonitrile **2c**-**e** was prepared in $(CH_3)_2SO$ (100 mM). Subsequently, 0.14 mL of the $(CH_3)_2SO$ solution were diluted with water to prepare a 1 mM solution (14 mL containing 1% $(CH_3)_2SO$). A solution of citric acid (0.5 M) was also prepared in H_2O. Subsequently, citric acid (5 mM) was added to the previous solution. The pH of the aqueous solution was *ca*. 3. After that, the reaction was heated in an oil bath at 40°C. Fractions of the aqueous solution were taken (2 mL) at

different time intervals (see figure footnotes for details). The crude was extracted with CH_2Cl_2 (3x4 mL). The combined organic layers were dried (Na_2SO_4), filtered and concentrated. The extracted crude was redissolved in CH_2Cl_2 (0.1 mL) and analyzed by GC-FID. The number of moles of each species extracted in the combined organic layers (n_o) were calculated using the corresponding calibration curve. Finally, the total number of moles (n_t) of each compound was calculated using Equation 4. Based on the total number of moles, we calculated the concentration of each specie throughout the hydrolysis reaction (% and M).

4) $n_t = n_o/(1 - f)$; *f* parameter is defined in Equation 3.

Bis-isonitrile **2c**

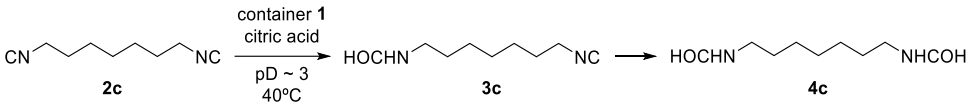

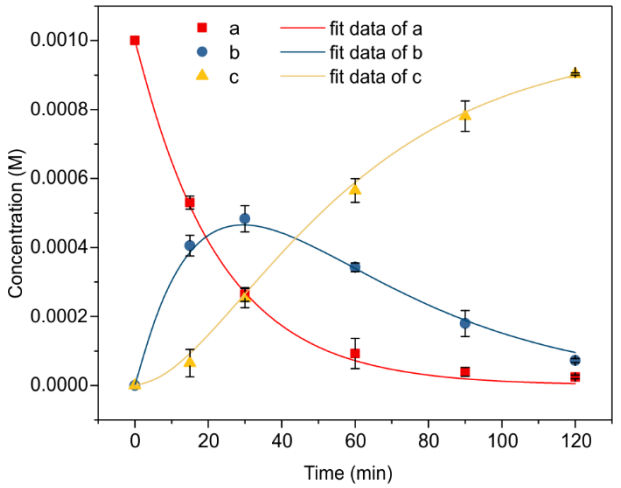

Figure 3.107. Concentration (M) *vs*. time (min) for the hydrolysis reaction of *bis*-isonitrile **2c** (0.001 M) in acidic aqueous solution (5 mM citric acid, pD ~ 3) at 40°C obtained by GC-FID analysis: a) *bis*-isonitrile **2c**; b) *mono*-formamide **3c** and c) *bis*-formamide **4c**. Lines represent fit of the experimental data to the theoretical kinetic model 2 (Section 3.4.2). Error bars are standard deviations.

Table 3.20. Rate constants (k_3 and k_4) returned from the fit of the experimental data (**2c** in water solution containing 1% $(CH_3)_2SO$) to the theoretical kinetic model 2.

Reaction	Rate constant (min^{-1})
2c → **3c**	k_3 = 6.0±2.0 x 10^{-2}
3c → **4c**	k_4 = 3.0±1.0 x 10^{-2}

Bis-isonitrile **2d**

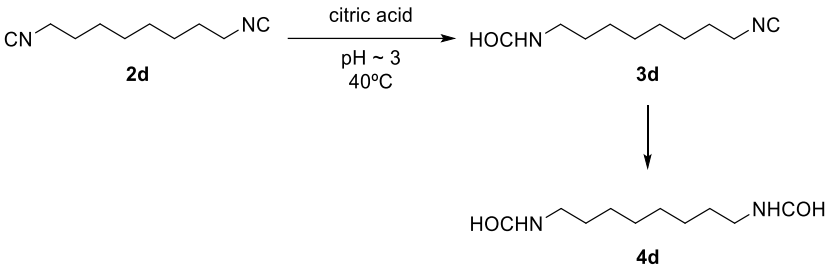

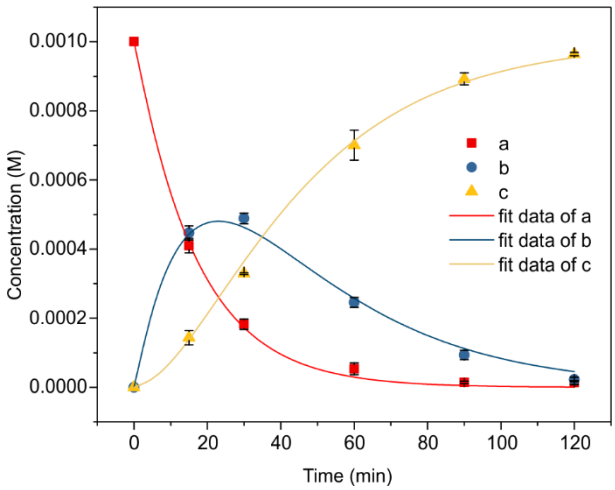

Figure 3.108. Concentration (M) *vs*. time (min) for the hydrolysis reaction of *bis*-isonitrile **2d** (0.001 M) in acidic aqueous solution (5 mM citric acid, pD ~ 3) at 40°C obtained by GC-FID analysis: a) *bis*-isonitrile **2d**; b) *mono*-formamide **3d** and c) *bis*-formamide **4d**. Lines represent fit of the experimental data to the theoretical kinetic model 2 (Section 3.4.2). Error bars are standard deviations.

Table 3.21. Rate constants (k_3 and k_4) returned from the fit of the experimental data (**2d** in water solution containing 1% $(CH_3)_2SO$) to the theoretical kinetic model 2.

Reaction	Rate constant (min^{-1})
2d → **3d**	$k_3 = 6.0 \pm 1.0 \times 10^{-2}$
3d → **4d**	$k_4 = 3.0 \pm 1.0 \times 10^{-2}$

Bis-isonitrile **2e**

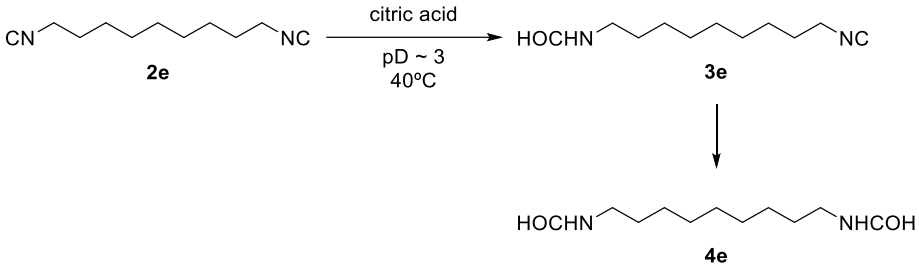

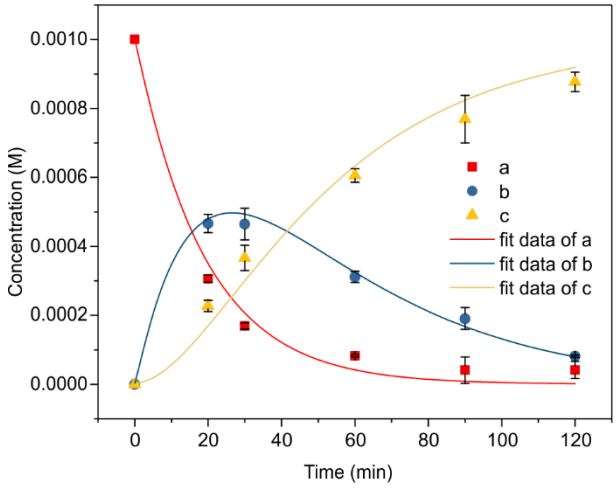

Figure 3.109. Concentration (M) *vs*. time (min) for the hydrolysis reaction of *bis*-isonitrile **2e** (0.001 M) in acidic aqueous solution (5 mM citric acid, pD ~ 3) at 40°C obtained by GC-FID analysis: a) *bis*-isonitrile **2e**; b) *mono*-formamide **3e** and c) *bis*-formamide **4e**. Lines represent fit of the experimental data to the theoretical kinetic model 2 (Section 3.4.2). Error bars are standard deviations.

Table 3.22. Rate constants (k_3 and k_4) returned from the fit of the experimental data (**2e** in water solution containing 1% $(CH_3)_2SO$) to the theoretical kinetic model.

Reaction	Rate constant (min^{-1})
2e → **3e**	k_3 = 6.0±1.0 x 10^{-2}
3e → **4e**	k_4 = 3.0±1.0 x 10^{-2}

3.4.8 Comparison of the results for the hydrolysis reaction of *bis*-isonitrile **2e** in the presence of container **1** monitored using GC-FID and ^{1}H NMR spectroscopy

A solution of octa-pyridinium **1** (1 mM) was prepared in H_2O (12 mL). A solution of *bis*-isonitrile **2e** was prepared at 80-100-fold higher concentration (80-100 mM) in $(CH_3)_2SO$ due to the limited solubility of the guest in water. Immediately, *bis*-isonitrile **2e** (1 equiv.) was added to the receptor's solution. A solution of citric acid (0.5 M) was also prepared in H_2O. Subsequently, citric acid (5 mM) was added to the previous solution. The pH of the aqueous solution was *ca*. 3. After that, the

reaction was heated in an oil bath at 40°C. Fractions of the aqueous solution were taken (2 mL) at different time intervals (see figure footnotes for details). 4-Phenylpyridine *N*-oxide (1.2 equiv.) was added to the latter aqueous solution in order to release the bound guests from the receptor's cavity to the bulk. The crude was extracted with CH_2Cl_2 (3x4 mL). The combined organic layers were dried (Na_2SO_4), filtered and concentrated. The extracted crude was redissolved in CH_2Cl_2 (0.1 mL) and analyzed by GC-FID. The number of moles of each specie extracted in the combined organic layers (n_o) was determined using the corresponding calibration curve. Finally, the total number of moles of each specie (n_t) was calculated using Equation 4. Based on the total number of moles, we calculated the concentration of each specie in the hydrolysis reaction (% and M).

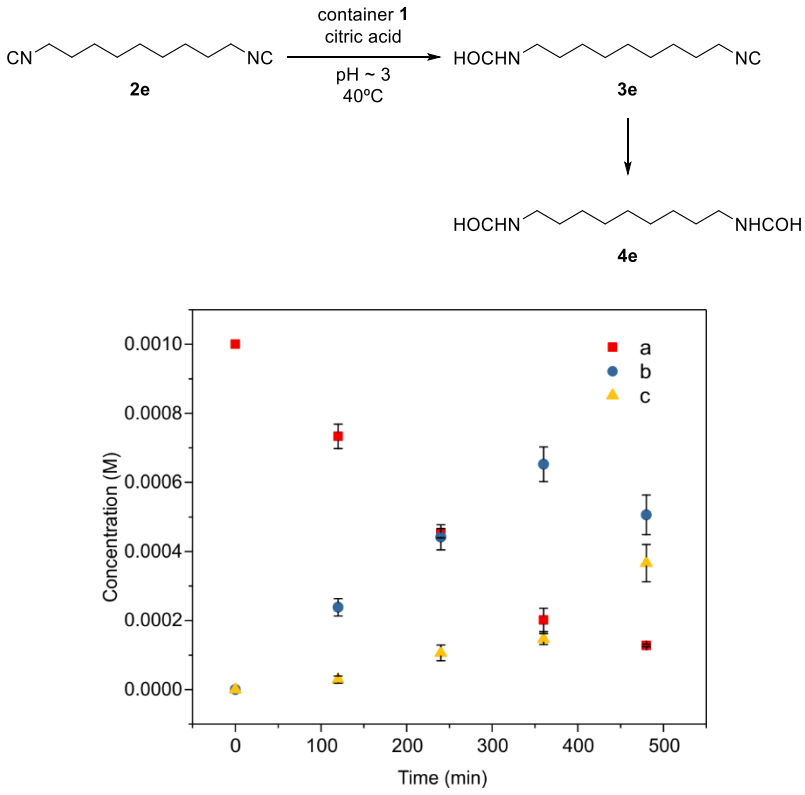

Figure 3.110. Concentration (M) vs. time (min) for the hydrolysis of *bis*-isonitrile **2e** (0.001 M) in the presence of octa-pyridinium **1** (0.001 M) in acidic aqueous solution (5 mM citric acid, pD ~ 3) at 40ºC obtained by GC-FID analysis: a) *bis*-isonitrile **2e**; b) *mono*-formamide **3e** and c) *bis*-formamide **4e**. Error bars are standard deviations.

The reaction profiles obtained by NMR and GC-FID analyses of the acid-catalyzed hydrolysis of *bis*-isonitrile **2e** in the presence of container **1** (1 equiv.) were similar.

3.4.9 Energy-minimized structures of some inclusion complexes

Simple molecular modeling studies were performed at the DFT level of theory (BP86-Def2SVP-D3) using Turbomole Version 7.0.[33,34,55] or Molecular Mechanics (MM3) using SCIGRESS Version FJ 2.6.

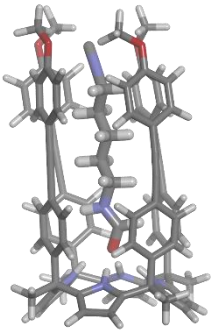

Figure 3.111. Energy-minimized structure (BP86-Def2SVP-D3 DFT level of theory) of the simplified 1:1 inclusion complex of octa-pyridinium **1** with *cis*-**3b**. The receptor and bound guest are depicted in stick representation. Water-solubilizing groups at the upper and lower rims of **1** were pruned to methyl groups to simplify the calculation.

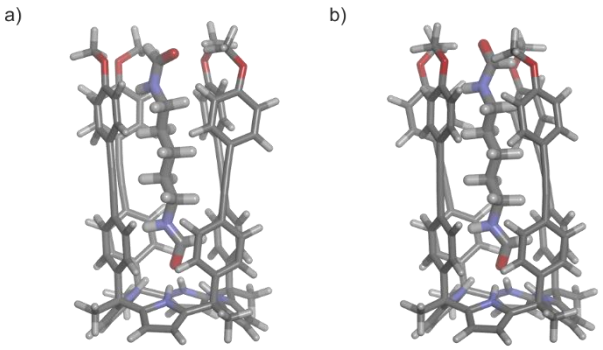

Figure 3.112. Energy-minimized structures (BP86-Def2SVP-D3 DFT level of theory) of the simplified 1:1 inclusion complexes of octa-pyridinium **1** with a) *trans,cis*-**4b** and b) *cis,cis*-**4b**. The receptor and bound guests are depicted in stick representation. Water-solubilizing groups at the upper and lower rims of **1** were pruned to methyl groups to simplify the calculations.

3.5 References and Notes

[1] J. Kang, J. Rebek, *Nature* **1997**, *385*, 50-52.

[2] M. Yoshizawa, M. Tamura, M. Fujita, *Science* **2006**, *312*, 251-254.

[3] M. D. Pluth, R. G. Bergman, K. N. Raymond, *Science* **2007**, *316*, 85-88.

[4] V. Ramamurthy, *Acc. Chem. Res.* **2015**, *48*, 2904-2917.

[5] W. Cullen, M. C. Misuraca, C. A. Hunter, N. H. Williams, M. D. Ward, *Nat. Chem.* **2016**, *8*, 231-236.

[6] A. Palma, M. Artelsmair, G. L. Wu, X. Y. Lu, S. J. Barrow, N. Uddin, E. Rosta, E. Masson, O. A. Scherman, *Angew. Chem., Int. Ed.* **2017**, *56*, 15688-15692.

[7] C. M. Hong, R. G. Bergman, K. N. Raymond, F. D. Toste, *Acc. Chem. Res.* **2018**, *51*, 2447-2455.

[8] N. W. Wu, I. D. Petsalakis, G. Theodorakopoulos, Y. Yu, J. Rebek, *Angew. Chem., Int. Ed.* **2018**, *57*, 15091-15095.

[9] Y. Yu, J. Rebek, Jr., *Acc. Chem. Res.* **2018**, *51*, 3031-3040.

[10] K. Wang, X. Cai, W. Yao, D. Tang, R. Kataria, H. S. Ashbaugh, L. D. Byers, B. C. Gibb, *J. Am. Chem. Soc.* **2019**, *141*, 6740-6747.

[11] H. Takezawa, T. Kanda, H. Nanjo, M. Fujita, *J. Am. Chem. Soc.* **2019**, *141*, 5112-5115.

[12] H. Takezawa, K. Shitozawa, M. Fujita, *Nat. Chem.* **2020**, *12*, 574-578.

[13] D. Masseroni, S. Mosca, M. P. Mower, D. G. Blackmond, J. Rebek, *Angew. Chem., Int. Ed.* **2016**, *55*, 8290-8293.

[14] Q. X. Shi, M. P. Mower, D. G. Blackmond, J. Rebek, *Proc. Natl. Acad. Sci. U. S. A.* **2016**, *113*, 9199-9203.

[15] V. Angamuthu, F.-U. Rahman, M. Petroselli, Y. Li, Y. Yu, J. Rebek, *Org. Chem. Front.* **2019**, *6*, 3220-3223.

[16] K. D. Zhang, D. Ajami, J. V. Gavette, J. Rebek, *J. Am. Chem. Soc.* **2014**, *136*, 5264-5266.

[17] Y.-S. Li, L. Escobar, Y.-J. Zhu, Y. Cohen, P. Ballester, J. Rebek, Y. Yu, *Proc. Natl. Acad. Sci. U. S. A.* **2019**, *116*, 19815-19820.

[18] S. Liu, H. Gan, A. T. Hermann, S. W. Rick, B. C. Gibb, *Nat. Chem.* **2010**, *2*, 847-852.

[19] K. Wang, J. H. Jordan, B. C. Gibb, *Chem. Commun.* **2019**, *55*, 11695-11698.

[20] M. M. J. Smulders, J. R. Nitschke, *Chem. Sci* **2012**, *3*, 785-788.

[21] R. M. Yebeutchou, E. Dalcanale, *J. Am. Chem. Soc.* **2009**, *131*, 2452-2453.

[22] A. Galan, P. Ballester, *Chem. Soc. Rev.* **2016**, *45*, 1720-1737.

[23] P. Mal, B. Breiner, K. Rissanen, J. R. Nitschke, *Science* **2009**, *324*, 1697-1699.

[24] C. M. Hong, M. Morimoto, E. A. Kapustin, N. Alzakhem, R. G. Bergman, K. N. Raymond, F. D. Toste, *J. Am. Chem. Soc.* **2018**, *140*, 6591-6595.

[25] L. Escobar, A. Diaz-Moscoso, P. Ballester, *Chem. Sci.* **2018**, *9*, 7186-7192.

[26] G. Peñuelas-Haro, P. Ballester, *Chem. Sci.* **2019**, *10*, 2413-2423.

[27] L. Escobar, P. Ballester, *Org. Chem. Font.* **2019**, *6*, 1738-1748.

[28] V. P. Manea, K. J. Wilson, J. R. Cable, *J. Am. Chem. Soc.* **1997**, *119*, 2033-2039.

[29] L. M. Salonen, M. Ellermann, F. Diederich, *Angew. Chem., Int. Ed.* **2011**, *50*, 4808-4842.

[30] B. Verdejo, G. Gil-Ramirez, P. Ballester, *J. Am. Chem. Soc.* **2009**, *131*, 3178-3179.

[31] Y. Y. Lim, A. R. Stein, *Can. J. Chem.* **1971**, *49*, 2455-2459.

[32] H. Stockmann, A. A. Neves, S. Stairs, K. M. Brindle, F. J. Leeper, *Org. Biomol. Chem.* **2011**, *9*, 7303-7305.

[33] J. P. Perdew, *Phys. Rev. B* **1986**, *33*, 8822-8824.

[34] A. D. Becke, *Phys. Rev. A* **1988**, *38*, 3098-3100.

[35] S. Grimme, J. Antony, S. Ehrlich, H. Krieg, *J. Chem. Phys.* **2010**, *132*, 154104.

[36] The observation of a cross-peak in the ROESY NMR spectrum between the formyl proton included in the calix[4]pyrrole unit and the corresponding *alpha*-methylene protons supports the *cis*-conformation of the buried formamide group.

[37] N. V. Prabhu, K. A. Sharp, *Annu. Rev. Phys. Chem.* **2005**, *56*, 521-548.

[38].L. Escobar, P. Ballester, Chem. Rev. (Washington, DC, U. S.) **2021**, *121*, 2445-2514.

[39] M. Petroselli, V. Angamuthu, F.-U. Rahman, X. Zhao, Y. Yu, J. Rebek, *J. Am. Chem. Soc.* **2020**, *142*, 2396-2403.

[40] If all binding constant values of the complexes have similar magnitudes (see Table 3.1), this methodology can be used to calculate the total concentration of the reacting species (free + bound) because their distribution is reflected by the relative concentrations of the complexes.

[41] The simulation of the time course for the hydrolysis reaction of **2b** in the presence of 1.5 equiv. of **1** using a kinetic model composed of Eqs. 1, 2, 5, 6 and 7 produced a similar result to that obtained using model 1.

[42] The hydrolysis reaction of longer *bis*-isonitriles **2c**-**e** in the presence of container **1** was performed in 1% DMSO/D_2O due to solubility reasons.

[43] Due to the overlap of proton signals and reduced solubility, we used GC-FID to monitor the reaction kinetics in the control hydrolysis experiments of the longer *bis*-isonitriles **2c**-**e**. The addition of 1% of DMSO did not produce a modification of the maximum selectivity of the *mono*-formamide.

[44] Previous reports on the use of molecular containers in controlling the selectivity of desymmetrization reactions in water made exclusive use of non-polar binding cavities.

[45] G. R. Fulmer, A. J. M. Miller, N. H. Sherden, H. E. Gottlieb, A. Nudelman, B. M. Stoltz, J. E. Bercaw, K. I. Goldberg, *Organometallics* **2010**, *29*, 2176-2179.

[46] A. Sehlinger, P. K. Dannecker, O. Kreye, M. A. R. Meier, *Macromolecules* **2014**, *47*, 2774-2783.

[47] W. Konrad, F. R. Bloesser, K. S. Wetzel, A. C. Boukis, M. A. R. Meier, C. Barner-Kowollik, *Chem.--Eur. J.* **2018**, *24*, 3413-3419.

[48] K. A. Waibel, R. Nickisch, N. Möhl, R. Seim, M. A. R. Meier, *Green Chem.* **2020**, *22*, 933-941.

[49] A. V. Gulevich, L. S. Koroleva, O. V. Morozova, V. N. Bakhvalova, V. N. Silnikov and V. G. Nenajdenko, *Beilstein J. Org. Chem.* **2011**, *7*, 1135–1140.

[50] Y.-X. Luan, T. Zhang, W.-W. Yao, K. Lu, L.-Y. Kong, Y.-T. Lin, M. Ye, *J. Am. Chem. Soc.* **2017**, *139*, 1786-1789.

[51] W. F. Li, X. F. Wu, *Chem.--Eur. J.* **2015**, *21*, 14943-14948.

[52] M. Kollwitz, J. Gauss, *Chem. Phys. Lett.* **1996**, *260*, 639-646.

[53] A. J. Leo, *Chem. Rev. (Washington, DC, U. S.)* **1993**, *93*, 1281-1306.

[54] D. R. Palleros, *J. Chem. Educ.* **1995**, *72*, 319-321.

[55] R. Ahlrichs, M. Bar, M. Haser, H. Horn, C. Kolmel, *Chem. Phys. Lett.* **1989**, *162*, 165-169.

UNIVERSITAT ROVIRA I VIRGILI
ARYL AND SUPER ARYL-EXTENDED CALIX[4]PYRROLES: SYNTHESIS AND APPLICATIONS
Qingqing Sun

Chapter 4

Self-Assembly of a Water-Soluble, Endohedrally Functionalized Pd(II)-Cage Using Polar Guests as Templates

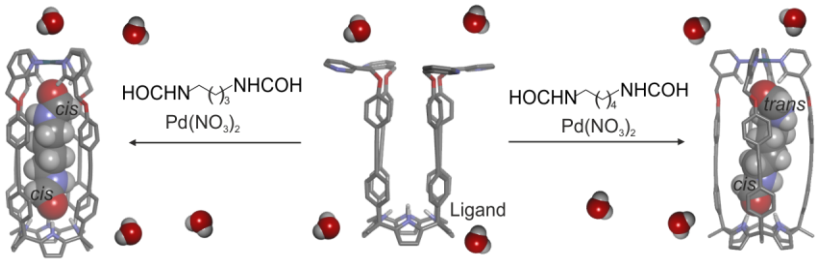

Unpublished results

UNIVERSITAT ROVIRA I VIRGILI
ARYL AND SUPER ARYL-EXTENDED CALIX[4]PYRROLES: SYNTHESIS AND APPLICATIONS
Qingqing Sun

4.1 Introduction

Self-assembly is an effective synthetic strategy for the construction of molecular coordination cages (CCs).[1,2,3] CCs self-assemble in organic solvents and in water. Their molecular components are multi-topic aromatic ligands (L) and metal coordination ions (M). The inclusion of size, shape and charge complementary guests in CCs enables not only selective molecular recognition but also controlling the properties, reactivities and on-demand catch and release of molecular cargo.[3,4,5,6,7] The inclusion of polar guests demands the functionalization of the aromatic cavities of the cages with polar groups (*e.g.* hydrogen bond donors/acceptors).[8,9] However, the extensive use of aromatic panels in shaping the cage's aromatic cavity makes this endeavour synthetically difficult. For this reason, examples of endohedrally functionalized CCs are still scarce in literature.[10,11]

Custelcean *et al.*[12,13] and Kaifer *et al.*[14] reported tetrahedral $[L_6•M_4]^{8+}$ CCs (M(II) = Fe, Ni or Zn) assembled from ditopic chelating ligands featuring urea groups as spacer units. The 6 ligands are located at the edges of the tetrahedron offering 12 NH hydrogen bond donors to the cage's interior. This characteristic makes the $[L_6•M_4]^{8+}$ cages suitable hosts for the binding of tetrahedral oxoanions, such as sulfate, in aqueous solution. The encapsulated anion is stabilized by a combination of coulombic and hydrogen-bonding interactions. In the same vein, Hooley *et al.* assembled $[L_6•Fe_4]^{8+}$ CCs featuring inwardly-directed hydroxyl[15] and carboxylic acid[16] groups in acetonitrile solution. Interestingly, the latter CC, bearing carboxylic acid functions, was applied as catalyst in the hydrolysis of acetals[16] and in the oxa-Pictet-Spengler cyclization reaction.[17] The incorporation of polar groups in the interior of a tetrahedral $[L_4•Fe_4]^{12+}$ CC, assembled from tritopic azaphosphatrane-based ligands, was shown by Nitschke *et al*.[18,19] In this case, the 4 ligands occupy the faces of the tetrahedral cage and provide up to 4 $^{+}$P-H donors converging in the cavity. The $[L_4•Fe_4]^{12+}$ cage is capable of binding anions in water. More recently, the same group demonstrated the encapsulation of D-glucose (a neutral and polar guest) by an endohedrally functionalized $[L_3•Fe_2]^{4+}$ helicate in 50:1 acetonitrile/water solution mixture.[20] The oxygen atoms of the bound guest establish multiple hydrogen-bonding interactions with the inwardly-directed urea NHs of the helicate.

Recently, we described the self-assembly of the uni-molecular mono-metallic Pd(II)-cage, [**1a**•Pd]$^{2+}$, (Scheme 4.1), in a 2:1 $CDCl_3/CD_3CN$ solution mixture. The tetra-topic pyridyl ligand, **1a**, shaping the cage's aromatic cavity is based on a "four wall" super aryl-extended calix[4]pyrrole (SAE-C[4]P) scaffold.[21] The Pd(II)-cage, [**1a**•Pd]$^{2+}$, features two different and converging polar binding sites. One of them is defined by the four pyrrole NHs of the C[4]P core. The other one is constituted by the four inwardly-directed pyridyl *α*-CH protons[22] (Figure 4.1b). Notably, the assembly of the CC requires the filling of its cavity with suitable polar molecules *i.e.* co-encapsulation of two diverging CD_3CN molecules. The bound guests not only fill the 55% of the cage's cavity volume but also satisfy the hydrogen-bonding donor characteristics of its two polar

binding sites. In particular, the CD_3CN bound to the C[4]P core stabilizes the ligand's cone conformation, which is mandatory for the emergence of the Pd(II)-cage (Figure 4.1b). We also investigated the inclusion/exchange mechanisms of the guest operating in the [**1a**•Pd]$^{2+}$ CC. We proposed a "french doors" mechanism, involving the concerted rotation of the four *meso*-aromatic substituents of the Pd(II)-cage, for the in/out exchange of planar (2D) pyridyl *N*-oxide derivatives. In contrast, we postulated the existence of a partial ligand-metal dissociation mechanism in the in/out exchange processes of sterically more demanding (3D) *N*-oxides *i.e.* quinuclidine-*N*-oxide.[23]

Herein, we report the self-assembly of a structurally related mono-metallic cage, [**2**•Pd]$^{6+}$, in water solution. We also describe the synthesis of the tetra-cationic ligand precursor **2**$^{4+}$, the water soluble version of the SAE-C[4]P tetra-pyridyl ligand, **1a** (Scheme 4.1a). In analogy to the observations made in organic solvents, the assembly of the water soluble [**2**•Pd]$^{6+}$ CC requires the inclusion of appropriate guests filling the cage's cavity and satisfying the hydrogen bonding characteristics of its two polar binding sites. We show that the cage's assembly occurs by including neutral, mono- and ditopic polar guests (*i.e.* pyridyl *N*-oxide derivatives, *N*-pentyl *mono*-formamide and α,ω-aliphatic *bis*-formamides). Remarkably, these polar guests are difficult to bind in water using synthetic receptors. Using ^{1}H NMR spectroscopy, we study the conformational arrangement adopted by the *bis*-formamides included in the water-soluble [**2**•Pd]$^{6+}$ CC. We report solid-state structures of the analogous inclusion complexes of the organic soluble [**1a**•Pd]$^{2+}$ counterpart supporting the results obtained in water. Finally, we investigate the dynamics and thermodynamics of guest exchange in water using selected cage complexes and competitive pair-wise binding experiments.

4.2 Results and Discussion

Synthesis

The tetra-cationic-tetra-pyridyl SAE-C[4]P ligand **2**$^{4+}$ was synthesized in two steps starting from the tetra-*α* isomer of 4-iodophenyl-4'-chlorobutyl C[4]P **3b**[24] (Scheme 4.1a). Firstly, the quadruple Sonogashira cross-coupling reaction between tetra-iodo C[4]P **3b** and pyridyl mono-acetylene **4**[21] afforded, after column chromatography purification of the reaction crude, the tetra-pyridyl-tetra-chloro SAE-C[4]P **1b** in 60% yield. Next, we treated **1b** with excess of pyridine at 110 °C affording the tetra-chloride salt of the tetra-pyridinium SAE-C[4]P **2**$^{4+}$ in 68% yield. Both tetra-pyridyl SAE-C[4]Ps ligands, **1b** and **2**$^{4+}$, were fully characterized by a set of high-resolution spectra (See Experimental Section).

The tetra-pyridyl-tetra-chloro SAE-C[4]P **1b** was also characterized by X-ray diffraction of a single crystal grown from a 1:1 CH_2Cl_2/CH_3CN solution mixture (Figure 4.1a). The solution of the diffracted data revealed that in the solid state the SAE-C[4]P **1b** adopted the cone conformation by including one molecule of CH_3CN.

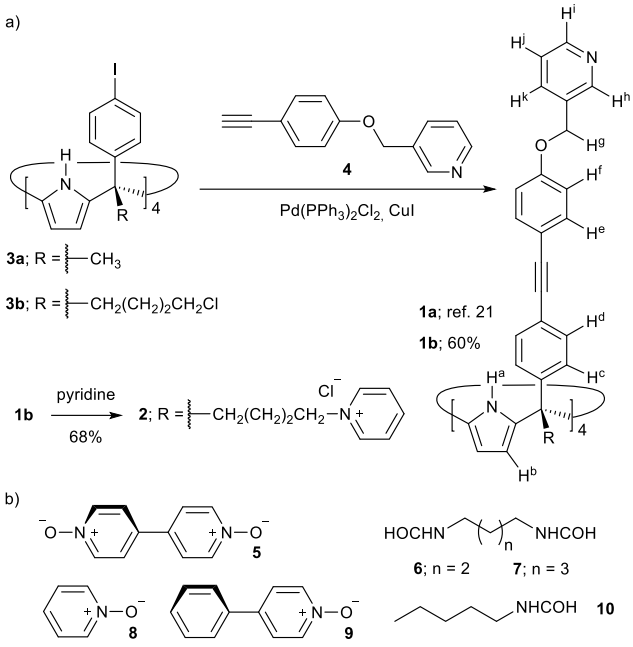

Scheme 4.1. a) Synthesis of tetra-pyridyl SAE-C[4]P ligands **1a**,**b** and $\mathbf{2}^{4+}$. b) Line-drawing structures of guests **5**-**10** used as templates.

The nitrogen atom of the included CH_3CN is hydrogen-bonded to the four pyrrole NHs of the C[4]P core, $d_{average}$ (N···N) ~ 3.3 Å. Moreover, the aromatic cavity of the upper section of **1b** collapses owing to the establishment of intermolecular CH-π and π-π interactions.[25] In the solid state, an additional molecule of CH_3CN occupies the shallow and electron-rich aromatic cavity defined by the pyrrole rings of the C[4]P core in cone conformation. The hydrogen atoms of the externally-bound CH_3CN are involved in CH-π interactions with the pyrrole rings.[26] It is worthy to note that the cone conformation of the C[4]P core of SAE-**1b** seems not to be perturbed by the presence of the *meso*-alkyl substituents.[27]

To our delight, the neutral tetra-pyridyl ligand SAE-**1b** self-assembled almost quantitatively into the mono-metallic Pd(II)-cage, $[\mathbf{1b}{\bullet}Pd]^{2+}$, in a 2:1 $CDCl_3/CD_3CN$ solution mixture by addition of 1 equiv of $[Pd(CH_3CN)_4](BF_4)_2$ (Figure 4.15). Consequently, the *meso*-alkyl substituents of the SAE-C[4]P ligand **1b** also did not have an impact on the assembly of the CC.

Next, we probed the coordination of Pd(II) with the water-soluble tetra-pyridinium-tetra-pyridyl SAE-C[4]P ligand $\mathbf{2}^{4+}$ (Scheme 4.1a) by means of ^1H NMR spectroscopy. At 298 K, the ^1H NMR spectrum of a millimolar D_2O solution of the tetra-pyridyl SAE-ligand $\mathbf{2}^{4+}$ showed broad proton signals[28] (Figure 4.28). Heating the solution at 333 K did not induce noticeable changes of the spectrum (Figure 4.2a).

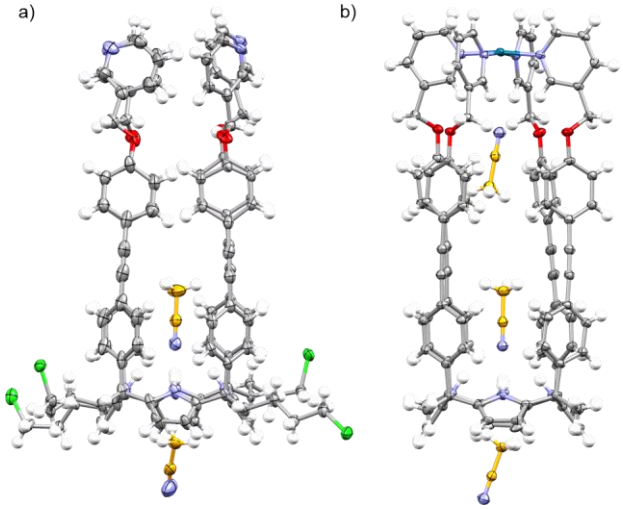

Figure 4.1. X-ray crystal structures of: a) **1b** and b) [**1a**•Pd]$^{2+}$. The structures are shown in ORTEP view with thermal ellipsoids set at 50% probability for the non-hydrogen atoms. Hydrogen atoms are depicted as fixed-size spheres of 0.3 Å radius.

However, the addition of *ca.* 10% DMSO to the r.t. D_2O solution of **2**$^{4+}$ provoked the appearance of sharp proton signals. (Figure 4.70). Taken together, these observations indicated that SAE-C[4]P **2**$^{4+}$ experienced significant aggregation in water solution.[29] We cannot rule out the possibility that the aggregation process makes the conformational exchange dynamics (cone and alternate) of **2**$^{4+}$ to become intermediate on the chemical shift time scale.[24]

The putative assembly of the [**2**•Pd]$^{6+}$ cage would assign an overall six positive charge to the CC. For this reason, we expected that the increase in the repulsive coulombic interactions will induce a reduction in the aggregation tendency of the hexa-cationic CC compared to that of the parent tetra-cationic SAE-ligand **2**$^{4+}$. Nevertheless, the addition of *ca.* 1 equiv. of $Pd(NO_3)_2$ to a millimolar D_2O solution of **2**$^{4+}$ at r.t. produced a suspension. We surmised that the insoluble material derived from the formation of metal-mediated polymeric aggregates. The analysis of the filtered solution, using ^{1}H NMR spectroscopy at 333 K, showed broad proton signals, which did not support the presence of the CC in the solution (Figure 4.29)

As stated above, we learned that the emergence of the CC [**1a**•Pd]$^{2+}$ (Figure 4.1b) in organic solvents required the presence of suitable guests able to fill its cavity and complement the hydrogen-bonding characteristics of its two endohedral polar binding sites. One molecule of 4,4'-bispyridine-*N*,*N*'-dioxide **5** or a combination of one pyridine-*N*-oxide **6** and one molecule of acetonitrile were perfect fits[21,23] (Scheme 4.1b). The *N*-oxides formed 1:1 inclusion complexes with the SAE-C[4]P ligand **1a.** The bound ligand was locked in cone conformation and its pyridyl residues were pre-organized for tetra-coordination to the Pd(II) metal cation.[24]

At 333 K, the ^{1}H NMR spectrum of a D_2O solution containing equimolar amounts of the tetra-cationic SAE-C[4]P ligand **2**$^{4+}$ and the *bis*-*N*-oxide **5** displayed a set of sharp and well-defined proton signals in agreement with C_{4v} symmetry for the receptor (Figure 4.2b). Specifically, the two aromatic protons *alpha* to the nitrogen atom of the pyridyl residues of **2**$^{4+}$, H^h and H^i, resonated as doublets at δ = 8.30 and 8.34 ppm, respectively (Figure 4.2b). The four aromatic protons of the *meso*-biphenyl-ethynyl substituents, H^c-H^d and H^e-H^f, emerged as separate doublets (δ = 7.11, 7.10, 6.90 and 6.73 ppm). The β-pyrrole protons, H^b, appeared as a singlet at δ = 6.07 ppm. We also observed that the protons of the *bis*-*N*-oxide **5** resonated as four doublets, which were notably upfield shifted in comparison to those of the *N*-oxide free in solution. The symmetry loss and the upfield shifts experienced by the protons of the *N*-oxide **5** placed it in the polar and deep aromatic cavity of the SAE-C[4]P **2**$^{4+}$.

The addition of more than 1 equiv. of *bis*-*N*-oxide **5** did not produce changes on the proton signals of the SAE-C[4]P **2**$^{4+}$. However, it caused the emergence of the expected signals for the protons of the free *N*-oxide **5** (Figure 4.33). All the above observations supported the formation of the 1:1 inclusion complex, **5**⊂**2**$^{4+}$, which featured slow exchange binding dynamics on both the ^{1}H NMR and EXSY time scale (t_{mix} = 0.3 s, Figure 4.33), and exhibited a binding constant larger than 10^4 M^{-1}. The cross peaks due to chemical exchange between free and bound **5** and those derived from a COSY experiment served for the unequivocal assignment of the signals of bound **5**. Notably, the complexation induced shifts (CIS) experienced by the aromatic protons of the bound *N*-oxide **5** are not directly related to its depth in the aromatic cavity of **2**$^{4+}$. For example, the protons *alpha* to the nitrogen atoms of **5**, H^1 and H^4, one being deep included and the other close to the water-interphase of the complex, were the most upfield shifted ($\Delta\delta$ (H^1)= -4.03 ppm and $\Delta\delta$ (H^4)= -2.07 ppm) (Figure 4.2, top). The aromatic protons H^2 and H^3, although being deeper included in the cavity of **2**$^{4+}$ than H^4, experienced reduced CIS. This result reflected the dissimilar magnetic anisotropy provided by the biphenyl-ethynyl walls of **2**$^{4+}$.

The inclusion geometry of the **5**⊂**2**$^{4+}$ complex diminishes the aromatic surface of the receptor available to water solvation. Because in water the binding of non-polar residues is mainly driven by the hydrophobic effect, the reduction in aromatic surface accessible to water solvation serves to explain the lower aggregation tendency of the complex compared to that of the free receptor.

Next, we investigated the assembly of the Pd(II) CC starting from the 1:1 inclusion complex **5**⊂**2**$^{4+}$. The addition of *ca.* 1 equiv. of $Pd(NO_3)_2$ to the D_2O solution of the **5**⊂**2**$^{4+}$ complex produced the disappearance of its proton signals and the concomitant emergence of a new set of proton signals also in agreement with C_{4v} symmetry for the ligand. The new set of proton signals was diagnostic of the assembly of the CC inclusion complex **5**⊂[**2**•Pd]$^{6+}$ (Figure 4.2c). At first sight, the assembly process seemed to be almost quantitative. However, we calculated that the CC complex was assembled in a 60% extent based on an internal standard. Most likely, metal-mediated aggregates of **5**⊂**2**$^{4+}$ were also formed whose proton signals broadened beyond detection.[30] For example, the

formation of *N*-Pd(II) coordination bonds in the new species was corroborated by the downfield shifts experienced by the two protons *alpha* to the nitrogen atom of the pyridyl residues, H^h and H^i, ($\Delta\delta$ = +0.79 and +0.71 ppm, respectively) with respect to their chemical shift values in the initial **5⊂2**$^{4+}$ complex.

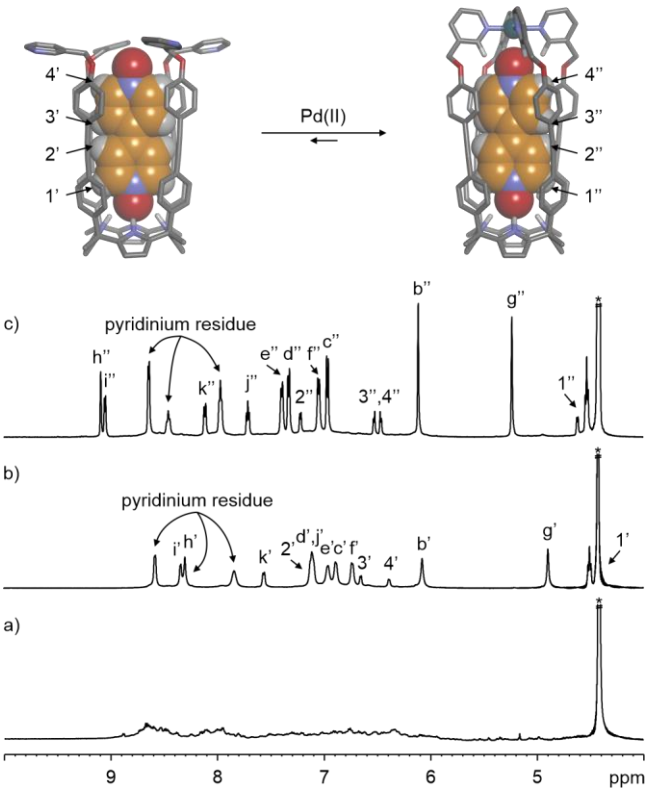

Figure 4.2. (top) Energy minimized structures (MM3) of the simplified **5⊂2**$^{4+}$ and **5⊂[2•**Pd**]**$^{6+}$ complexes including proton assignment of bound **5**. (bottom) Selected region of the ^{1}H NMR (500 MHz with cryoprobe, D_2O, 333 K) spectra of: a) **2**$^{4+}$; b) **5⊂2**$^{4+}$ and c) **5⊂[2•**Pd**]**$^{6+}$. Primed and doubly primed labels correspond to the proton signals of **5⊂2**$^{4+}$ and **5⊂[2•**Pd**]**$^{6+}$, respectively. See Scheme 4.1a for proton assignment of bound **2**$^{4+}$. *Residual solvent peak.

The reduced downfield shift experienced by the *β*-pyrrole protons of the CC's inclusion complex **5⊂[2•**Pd**]**$^{6+}$ ($\Delta\delta$ = +0.04 ppm), H^b, supported that C[4]P core is maintained in the cone conformation. Finally, the proton signals of the *bis*-*N*-oxide **5** included in the metallocage suffered reduced chemical shift changes compared to those in the **5⊂2**$^{4+}$ complex. Previously, we reported analogous observations for the structurally related CC, [**1a•**Pd**]**$^{2+}$, assembled in organic solvents. We showed that the included *bis*-*N*-oxide **5** is too short to establish simultaneous hydrogen-bonding interactions with the two polar binding sites of the cage undergoing a shuttling motion between them (Figure 4.2, top).[21] In the presence of more than 1 equiv. of **5**, the proton signals of the CC inclusion complex, **5⊂[2•**Pd**]**$^{6+}$, did not experience any change (Figure 4.35). Notably, the

protons for free and bound **5** displayed slow dynamics on both the ^{1}H NMR and the EXSY time scales (t_{mix} = 0.3 s). We described similar changes in the exchange dynamics of the inclusion and CC complexes obtained in organic solvents. This difference in dynamics between the free and bound guest in the initial **5**⊂**2**$^{4+}$ complex and the CC complex **5**⊂[**2**•Pd]$^{6+}$ was attributed to a different in/out exchange mechanism for the guest: cone to alternate conformational change of the host in the **5**⊂**2**$^{4+}$ complex and a "french doors" mechanism in the case of the **5**⊂[**2**•Pd]$^{6+}$ CC complex.

We performed a ^{1}H DOSY NMR experiment[31] at 333 K of D_2O solution containing the CC complex **5**⊂[**2**•Pd]$^{6+}$ (Figure 4.36). The signal decay of all protons fits well to the mono-exponential function for the BPLED pulse sequence. The results of the fits returned identical diffusion constant values for both compounds in solution **5** and [**2**•Pd]$^{6+}$, -log *D* = 9.31, supporting that both components are involved in the same diffusive species: the CC inclusion complex **5**⊂[**2**•Pd]$^{6+}$. The extracted diffusion constant was in agreement with the one derived from the analogous organic-soluble CC, [**1a**•Pd]$^{2+}$, indicating that the two versions of CC complexes feature similar dimensions.[32] Taken together, the presented results demonstrated that the formation of the CC [**2**•Pd]$^{6+}$ in D_2O[33] required the presence of the polar *N*-oxide guest **5** to fit its cavity. We estimated that the binding constant of the cage complex **5**⊂[**2**•Pd]$^{6+}$ is larger than 10^4 M^{-1}. At 298 K, the increase in the overall charge provided by the assembly of the CC **5**⊂[**2**•Pd]$^{6+}$ complex, compared to that of the tetra-cationic **5**⊂**2**$^{4+}$ complex, was not enough to eliminate the aggregation of the former. For this reason, the assembly of the CC [**2**•Pd]$^{6+}$ was also studied at 333 K. At this temperature, the ^{1}H NMR spectrum of the CC complex, **5**⊂[**2**•Pd]$^{6+}$, displayed sharp proton signals.

The results obtained with the *bis*-*N*-oxide **5** urged us to investigate the self-assembly of other inclusion complexes of the CC [**2**•Pd]$^{6+}$ in water using different ditopic guests suitable to fit the CC's cavity. Using molecular modelling studies (MM3), we selected the aliphatic *bis*-formamides **6** and **7**, having four and five methylene groups as spacers,[34] respectively (Scheme 4.1b). The extended conformations of both aliphatic *bis*-formamides are good fits to the aromatic cavity of the Pd(II)-cage. In addition, the two terminal formamide groups of **6** and **7** can complement the hydrogen-bonding characteristics of the two distal polar binding sites of the CC's cavity.

At 333 K, the ^{1}H NMR spectrum of a mM equimolar solution of the *bis*-formamide **6**, having four methylene groups as spacer, and the tetra-pyridyl **2**$^{4+}$ in D_2O did not display a set of sharp signals for the receptor as observed when the *bis*-*N*-oxide **5** was used as guest (*vide supra*). In addition, the proton signals of free **6** were easily detected. This result indicated that the putative [**6**⊂**2**]$^{4+}$ complex was formed in solution to a reduced extent.[35]

Gratifyingly, the addition of *ca.* 1 equiv. of $Pd(NO_3)_2$ to the above solution produced a set of sharp and well-defined signals that was diagnostic of the assembly of the CC [**2**•Pd]$^{6+}$ (Figure 4.3a). At the same time, we observed two sets of different intensity protons for the *bis*-formamide **6**. The set

of signals with low intensity corresponded to the protons of free **6**. The more intense set of signals displayed upfield shifts for all protons. We assigned this set of signals to the protons of **6** included in the aromatic cavity of the CC [**2**•Pd]$^{6+}$. In short, the emergence of the CC [**2**•Pd]$^{6+}$ was induced by inclusion of the *bis*-formamide **6** leading to the formation of the CC complex **6**⊂[**2**•Pd]$^{6+}$ in a ~ 60% extent.

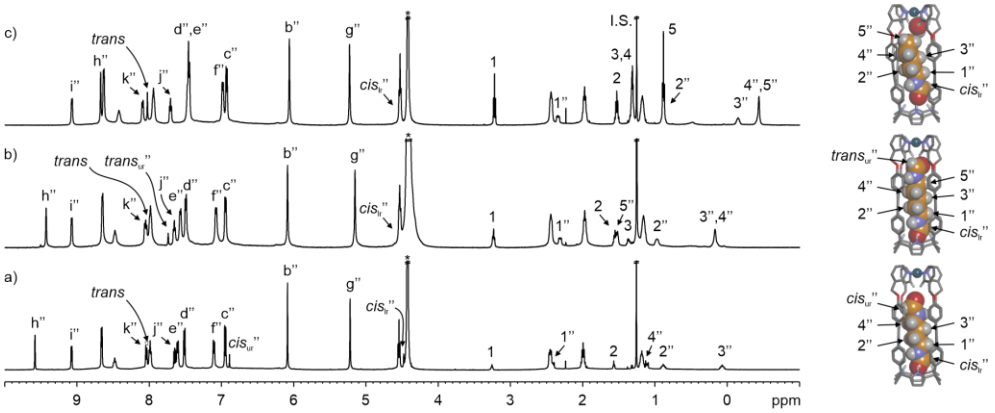

Figure 4.3. (left) ^{1}H NMR (500 MHz with cryoprobe, D_2O, 333 K) spectra of: a) *cis*,*cis*-**6**⊂[**2**•Pd]$^{6+}$; b) *trans*,*cis*-**7**⊂[**2**•Pd]$^{6+}$ and c) *cis*-**10**⊂[**2**•Pd]$^{6+}$, together with free guests in solution. (right) Energy minimized structures (MM3) of the simplified cage complexes. A putative water molecule is bound to *cis*-**10**⊂[**2**•Pd]$^{6+}$. Doubly primed labels correspond to the proton signals of the cage complexes (lr = lower rim and ur = upper rim). See Scheme 4.1 for proton assignment of bound **2**$^{4+}$. I.S. = *tert*-butanol. *Residual solvent peak.

We noticed that one of the formyl protons of bound **6** displayed a significant upfield shift ($\Delta\delta$ = -3.52 ppm), placing it within the four *meso*-aryl substituents of the C[4]P unit[34,36] in the CC [**2**•Pd]$^{6+}$ (Figure 4.3a, right). The other formyl proton also experienced magnetic shielding but to a reduced extent, $\Delta\delta$ = -1.11 ppm, owing to its inclusion in the upper aromatic cavity of the CC. A 2D ROESY experiment of the **6**⊂[**2**•Pd]$^{6+}$ complex showed close-contact intermolecular cross peaks between the later formyl proton and the inwardly directed aromatic protons *alpha* to the nitrogen atoms of the pyridyl groups coordinated to Pd(II) metal. (Figure 4.49).

This observation supported the location of the latter formamide end in the upper aromatic cavity of the CC [**2**•Pd]$^{6+}$. More importantly, the ROESY experiment displayed cross peaks due to intramolecular close-contact between the formyl protons and its corresponding *alpha* methylene groups, H^1 and H^4 (Figure 4.48). This result indicated that there is a selectivity in the inclusion of *bis*-formamide **6** in the aromatic cavity of the [**2**•Pd]$^{6+}$ cage (*i.e*. *cis*,*cis*-isomer). *Bis*-formamide **6** exists in solution as a mixture of three isomers with respect to the possible conformations adopted by the terminal amides: *trans,trans* (~ 76%)*, trans,cis* (~ 20%) *and cis,cis* (~ 4%). The CC [**2**•Pd]$^{6+}$ selectively binds the *cis,cis*-isomer in a fully extended conformation because it provides the best filling of its aromatic cavity and a superior hydrogen-bonding complementary to the two endohedral

polar binding sites (Figure 4.3a, right). We estimated that the stability constant for the *cis*,*cis*-**6**⊂[**2**•Pd]$^{6+}$complex should be larger than 10^5 M^{-1}. Notably, the inwardly directed pyridyl protons *alpha* to the metal-coordinated nitrogen atom in the *cis*,*cis*-**6**⊂[**2**•Pd]$^{6+}$ complex, H^h, shifted further downfield compared to its analogue **5**⊂[**2**•Pd]$^{6+}$ complex (δ = 9.58 *vs* 9.09 ppm, respectively). We interpreted this observation as an evidence of the superior size-complementary of the *cis,cis*-*bis*-formamide **6** for the CC's aromatic cavity in comparison to the *bis*-*N*-oxide **5**.

The homologous *bis*-formamide **7**, possessing an extra methylene group in its alkyl chain spacer, produced similar results to those described for the shorter *bis*-formamide **6** (Figure 4.3b). However, the 2D ROESY experiment of the **7**⊂[**2**•Pd]$^{6+}$ complex did not display intramolecular close-contacts cross peaks between the formyl proton included in the upper aromatic cavity of the CC and the protons of *alpha* methylene. This result suggested that the CC [**2**•Pd]$^{6+}$ showed binding selectivity for the *trans,cis*-isomer of **7** instead of the *cis,cis*-counterpart as displayed in the case of the shorter *bis*-formamide **6**.

Not surprisingly, ^{1}H DOSY NMR experiments performed with the *cis*,*cis*-**6**⊂[**2**•Pd]$^{6+}$ and the *trans*,*cis*-**7**⊂[**2**•Pd]$^{6+}$ CC complexes assigned similar diffusion constant values (log *D* values of -9.32 and -9.31) to the two complexes (Figure 4.51 and 4.58). The calculated magnitudes are almost identical to that determined for the **5**⊂[**2**•Pd]$^{6+}$ CC (*vide supra*) supporting the structural size and shape similarity of the three diffusive species.

Remarkably, the binding geometries assigned in solution to the included *bis*-formamide guests in the *cis*,*cis*-**6**⊂[**2**•Pd]$^{6+}$ and *trans*,*cis*-**7**⊂[**2**•Pd]$^{6+}$ CC complexes were in complete agreement with those obtained from X-ray diffraction analyses of single crystals, grew from organic solutions, of structurally analogues CC complexes: *cis,cis*-**6**⊂[**1a**•Pd]$^{2+}$ and *trans,cis*-**7**⊂[**1a**•Pd]$^{2+}$ (Figure 4.4). Interestingly, the X-ray crystal structure of the *trans,cis*-**7**⊂[**1a**•Pd]$^{2+}$ CC complex evidenced the bending of the larger alkyl spacer to better adapt to the dimensions of the CC's cavity. In complete agreement with the results obtained in solution (ROESY experiment), the solid-state structure of the **7**⊂[**1a**•Pd]$^{2+}$ complex displayed the formamide end hydrogen-bonded to the C[4]P in *cis*-conformation and the opposed end, included in the upper aromatic cavity of the CC, in *trans*-conformation with the formyl oxygen atom hydrogen-bonded to the inwardly directed pyridyl protons *alpha* to the metal coordinated nitrogen atom (Figure 4.4b).

Previously, we described that pyridine-*N*-oxide, **8** (Scheme 4.1b), was also a good guest to induce the assembly of the **8**⊂[**1a**•Pd]$^{2+}$ CC complex in a 2:1 $CDCl_3$:CD_3CN solution mixture.[21,23] The reported X-ray structure of the **8**⊂[**1a**•Pd]$^{2+}$ CC complex evidenced the inclusion of **8** in the C[4]P core and the co-encapsulation of one molecule of acetonitrile in the upper aromatic cavity. In the [**8**•CH_3CN]⊂[**1a**•Pd]$^{2+}$ complex, the inclusion of *N*-oxide **8** was driven by hydrogen-bonding, π-π and CH-π interactions. On the other hand, the nitrogen atom of the acetonitrile acted as hydrogen-bond acceptor of the inwardly directed aromatic protons *alpha* to the nitrogen atom of pyridyl

groups coordinated to the Pd(II). Most likely, the acetonitrile is also involved in attractive cation-dipole interactions.

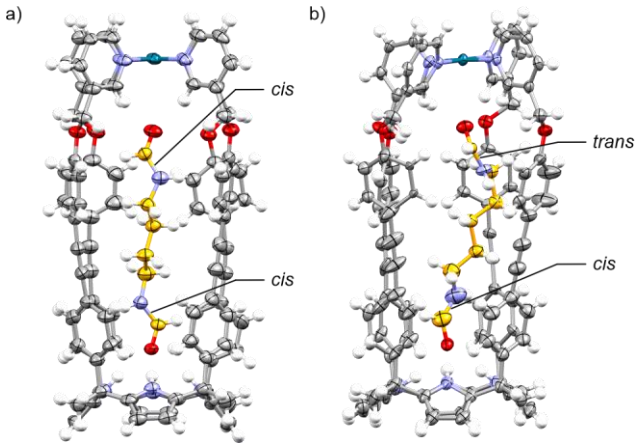

Figure 4.4. X-ray crystal structures of: a) *cis*,*cis*-**6**⊂[**1a**•Pd]$^{2+}$ and b) *trans*,*cis*-**7**⊂[**1a**•Pd]$^{2+}$. The structures are shown in ORTEP view with thermal ellipsoids set at 50% probability for the non-hydrogen atoms. Hydrogen atoms are depicted as fixed-size spheres of 0.3 Å radius.

At 333 K, the ^{1}H NMR spectrum of an equimolar D_2O solution (1 mM) of pyridine-*N*-oxide **8** and the tetra-pyridyl receptor **2**$^{4+}$ showed a diminution in the broadening of the proton signals of the receptor (Figure 4.38). The protons of the free *N*-oxide **8** were visible as sharp signals with reduced intensity compared to those of a 1 mM solution (Figure 4.39). This result suggested us that the 1:1 complex [**8**⊂**2**]$^{4+}$ was formed to some extent. The subsequent addition of 1 equiv. of $Pd(NO_3)_2$ to the solution provoked the appearance of a new set of sharp signals that were diagnostic of the assembly of CC complex **8**⊂[**2**•Pd]$^{6+}$. Because the emergence of the CC complexes require not only the adequate filling of its aromatic cavity but also the functional complementarity of its two endohedral binding sites, we assumed the co-inclusion of one molecule of water with the pyridine *N*-oxide **8** yielding the co-encapsulation complex [**8**•H_2O]⊂[**2**•Pd]$^{6+}$.

Previous and current studies on the self-assembly of the CC [**1a**•Pd]$^{2+}$ in a 2:1 $CDCl_3$:CD_3CN mixture, revealed that monotopic guests like *N*-pentyl-formamide, **10**, or 4-phenyl pyridine *N*-oxide, **9**, formed kinetically and thermodynamically stable 1:1 complexes with the SAE-ligand **1a** but did not induce the emergence of the CC. Instead, Pd(II) mediated oligomers were formed in solution upon the addition of the metal. These results substantiated the double role played by the guest in the emergence of the CC: filling the cavity and complementing the two polar endohedral binding sites.

We became interested in evaluating the two monotopic guests, **9** and **10**, in the assembly of the water-soluble version of the CC, that is [**2**•Pd]$^{6+}$. At 333 K, the ^{1}H NMR spectra of separate

equimolar mixtures of the guests, **9** and **10**, with the SAE-ligand $\mathbf{2}^{4+}$ in D_2O solution showed the formation of the corresponding 1:1 complexes, $\mathbf{9}\subset\mathbf{2}^{4+}$ and $\mathbf{10}\subset\mathbf{2}^{4+}$, in significant extents: sharpening of the proton signals of $\mathbf{2}^{4+}$ and diminution of the intensity for those of the free guest (Figure 4.42 and 4.60).

Surprisingly to us, the addition of 1 equiv. of the metal, as $Pd(NO_3)_2$ salt, produced very different outcomes. In the case of the $\mathbf{9}\subset\mathbf{2}^{4+}$ complex, the addition of the metal produced a ^{1}H NMR spectrum displaying broad and ill-defined proton signals for $\mathbf{2}^{4+}$ and a set of sharp signals for the protons of free **9**. We concluded that the addition of the Pd(II) provoked the formation of metal-mediated oligomeric aggregates of $\mathbf{2}^{4+}$, which may partially bind the *N*-oxide **9** (Figure 4.43). In short, the system expresses an analogous behaviour as the one observed in organic solvents.

In striking contrast, the addition of Pd(II) to the D_2O solution containing the partially formed $\mathbf{10}\subset\mathbf{2}^{4+}$ inclusion complex produced the appearance of a new set of sharp signals that were indicative of the assembly of the CC complex $\mathbf{10}\subset[\mathbf{2}\bullet Pd]^{6+}$. The upfield shift experienced by the formyl proton, $\Delta\delta$ = -3.46 ppm, of bound **10** placed it in the C[*4*]P cavity of the $[\mathbf{2}\bullet Pd]^{6+}$ cage (Figure 4.3a). The *cis*-conformation adopted by the bound formamide **10** was supported by a ROESY experiment. Although, the inwardly directed aromatic protons *alpha* to the nitrogen atom of the Pd-coordinated pyridyl residues in $\mathbf{10}\subset[\mathbf{2}\bullet Pd]^{6+}$ are less downfield shifted than for the $[\mathbf{8}\bullet H_2O]\subset[\mathbf{2}\bullet Pd]^{6+}$ counterpart (8.68 ppm vs 9.44 ppm), we inferred the co-inclusion of a water molecule in order to satisfy the functional complementary of the polar binding site induced by metal coordination (see the putative structure in Figure 4.3a, right). It is worth mentioning that the binding dynamics of the $[\mathbf{10}\bullet H_2O]\subset[\mathbf{2}\bullet Pd]^{6+}$ is slow on the ^{1}H NMR chemical shift time scale, but intermediate on the diffusion time scale of a DOSY experiment. In other words, a typical DOSY experiment (t_d ~ 200 ms) assigned a diffusion constant to bound *cis*-**10** that differed from the one determined for $[\mathbf{2}\bullet Pd]^{6+}$ CC. Likewise, the diffusion constant of the free guest in the above experiment coincides with the value determined using a separate solution containing exclusively the guest (Figure 4.65). The use of a shorter diffusion time (t_d ~ 10 ms) in the DOSY experiment produced the expected coincidence of diffusion constants for bound *cis*-**10** and the CC $[\mathbf{2}\bullet Pd]^{6+}$ (Figure 4.66). This finding indicated that the *cis*-$\mathbf{10}\subset[\mathbf{2}\bullet Pd]^{6+}$ cage complex is kinetically less stable[37] than the CC complexes involving ditopic guests. (*vide supra*).

In water, the binding of the mono- and ditopic guests, **5**-**7** and **8**-**10**, in the polar aromatic cavity of the CC $[\mathbf{2}\bullet Pd]^{6+}$ is mainly driven by the hydrophobic effect (HE).[38] The establishment of hydrogen-bonds, NH-π, π-π and CH-π interactions adds additional selectivity and affinity to the recognition process.[25] The HE must play an important role in the binding of the guests not only by the CC $[\mathbf{2}\bullet Pd]^{6+}$ but also by the SAE-ligand $\mathbf{2}^{4+}$. The *mono*-formamide **10** is bound by $\mathbf{2}^{4+}$ in water, but it does not bind to the analogous neutral SAE-ligand **1b** in a 2:1 $CDCl_3/CD_3CN$ solution[39] (Figure 4.13).

Finally, we studied the kinetics of guest exchange in the encapsulation complexes of the CC [**2**•Pd]$^{6+}$ with *bis*-formamide **6** and pyridine-*N*-oxide **8**. At 333 K, and as discussed above, the ^{1}H NMR spectra of separate equimolar D_2O solutions of [**2**•Pd]$^{6+}$, $Pd(NO_3)_2$, and the respective guest indicated the assembly of the CC complexes *cis*,*cis*-**6**⊂[**2**•Pd]$^{6+}$ and **8**⊂[**2**•Pd]$^{6+}$ in 60% and 30% yield, respectively. We also observed sharp proton signals for the remaining free guest. Particularly for **8**, broad and ill-defined signals assigned to Pd(II)-mediated oligomers of **2**$^{4+}$ were also detectable. After 30s of the addition of 1 equiv. of the *bis*-*N*-oxide **5** to the mixtures, we reanalyzed them using ^{1}H-NMR spectroscopy. The acquired ^{1}H NMR spectra showed that both encapsulated guests, **6** and **8**, were completely replaced by **5** and that the **5**⊂[**2**•Pd]$^{6+}$ CC was present as a 60% extent in the two solutions. As could be expected, the signals of the protons of the free guests increased in intensity owing to their release to the bulk solution. (Figures 4.68 and 4.69). Taken together, these results supported that the **5**⊂[**2**•Pd]$^{6+}$ CC complex is thermodynamically more stable than those of guests **6** and **8**. In addition, the exchange processes of the *bis*-formamide and the pyridyl *N*-oxide, **6** and **8**, by the *bis*-*N*-oxide **5** are fast on the human time scale (< 30 s). In turn, this finding indicated the existence of a "French doors" mechanism for the exchange process. This mechanism has a low energy barrier (~ 20 kcal mol^{-1}) and involves the synchronous rotation of the four *meso*-aromatic substituents of the Pd(II)-cage allowing the simultaneous entrance of the incoming guest **5** and the exiting of the encapsulated one without requiring the dissociation of any Pd-*N* coordination bonds present in the CC.[23]

4.3 Conclusions

In summary, we described the efficient self-assembly of the endohedrally functionalized [**2**•Pd]$^{6+}$ cage in water by encapsulating ditopic and monotopic polar guests, **5**-**7** and **8**-**10**. The parent water-soluble SAE-ligand **2**$^{4+}$ shows a strong tendency to aggregate that is somewhat reduced for the 1:1 complexes formed with the polar guests. The self-assembled encapsulation complexes of the [**2**•Pd]$^{6+}$ CC feature six positive charges, however they are still prone to aggregation in 1 mM D_2O solutions at r.t. Nevertheless, an increase in temperature (333K) or the addition of DMSO (5-10%) reduces this aggregation tendency. On the one hand, the ditopic guests, **5**-**7**, complement the two endohedral polar binding sites of the [**2**•Pd]$^{6+}$ cage and its cavity volume. On the other hand, the monotopic guests, **8** and **10**, are bound only to the C[4]P unit of the CC and partially fill its aromatic cavity. We surmised that in the latter CC complexes a co-included water molecule is bound to the distal polar binding site defined by the inwardly-directed *α*-pyridyl protons. There is conformational selectivity in the encapsulation of *bis*-formamides, **6** and **7**, by the [**2**•Pd]$^{6+}$ CC. Remarkably, *bis*-formamide **6,** having a spacer of four methylene groups, is encapsulated as the least abundant *cis*,*cis*-conformer in solution. Finally, we showed that the displacement of the guests, **6** and **8**, encapsulated in the [**2**•Pd]$^{6+}$ CC by *bis*-*N*-oxide **5** is quantitative and fast on the human time scale (< 30s). This finding proved the superior thermodynamic stability of the **5**⊂[**2**•Pd]$^{6+}$ CC complex and suggested the existence of a "French doors" mechanism for the

exchange process. To the best of our knowledge, the described results are rare examples of guest-induced self-assembly/emergence of polar CCs in water solution.[20] The conformational selectivity displayed by the CC [**2**•Pd]$^{6+}$ in the encapsulation of *bis*-formamide **6** is unprecedented[34,36,40,41]

4.4 Experimental Section

4.4.1 General information and instruments

Reagents were obtained from commercial suppliers and used without further purification unless otherwise stated. All solvents were commercially obtained and used without further purification except pyrrole which was distilled and freshly used. Dry solvents were taken from a solvent system MB SPS 800. THF, Et_3N, DIPEA and iPr_2NH were dried, distilled and degassed by three freeze-pump-thaw cycles before used in the cross-coupling reactions. Pyridine was dried and distilled before use. Routine ^1H NMR and $^{13}C\{^1H\}$ NMR spectra were recorded on a Bruker Avance 300 (300 MHz for ^1H NMR and 75 MHz for ^{13}C NMR), Bruker Avance 400 (400 MHz for ^1H NMR and 100 MHz for ^{13}C NMR), Bruker Avance 500 (500 MHz for ^1H NMR and 125 MHz for ^{13}C NMR) or Bruker Avance 500 with cryoprobe (500 MHz for ^1H NMR and 125 MHz for ^{13}C NMR). Deuterated solvents used are indicated in the characterization and chemical shifts are given in ppm. Residual solvent peaks were used as reference.[42] All NMR *J* values are given in Hz. COSY, NOESY, ROESY, HMQC and HMBC experiments were recorded to help with the assignment of ^1H and ^{13}C signals. High Resolution Mass Spectra (HRMS) were obtained on a Bruker HPLC-TOF (MicroTOF Focus) with ESI as ionization mode and Bruker HPLC-QqTOF (MaXis Impact) with ESI as ionization mode. IR spectra were recorded on a Bruker Optics FTIR Alpha spectrometer equipped with a DTGS detector, KBr beamsplitter at 4 cm^{-1} resolution using a one bounce ATR accessory with diamond windows. Melting points were measured on a MP70 Melting Point System Mettler Toledo. Crystal structure determinations were carried out using a Rigaku MicroMax-007HF diffractometer equipped with a PILATUS 200K detector and a Bruker Apex II Duo equipped with an APEX II detector. Both using MoKα radiation. Crystal structure solution was achieved using VLD and Patterson methods as implemented in SIR2014 v14.10. Least-squares refinement on F2 using all measured intensities was carried out using the program SHELX-2018/3. Column chromatography was performed with silica gel technical grade (Sigma-Aldrich), pore size 60 Å, 230-400 mesh particle size, 40-63 µm particle size and Thin Layer Chromatography (TLC) analysis on silica gel 60 F254.

4.4.2 Synthesis and characterization data

Tetra-*α* 4-iodophenyl-4'-chlorobutyl calix[4]pyrrole **3b**, pyridyl mono-acetylene **4**, tetra-*α* tetra-pyridyl super aryl-extended calix[4]pyrrole **1a** and *bis*-formamide **7** were synthesized following previously reported procedures in the literature.[24,21,34]

Tetra-*α* tetra-pyridyl super aryl-extended calix[4]pyrrole **1b**

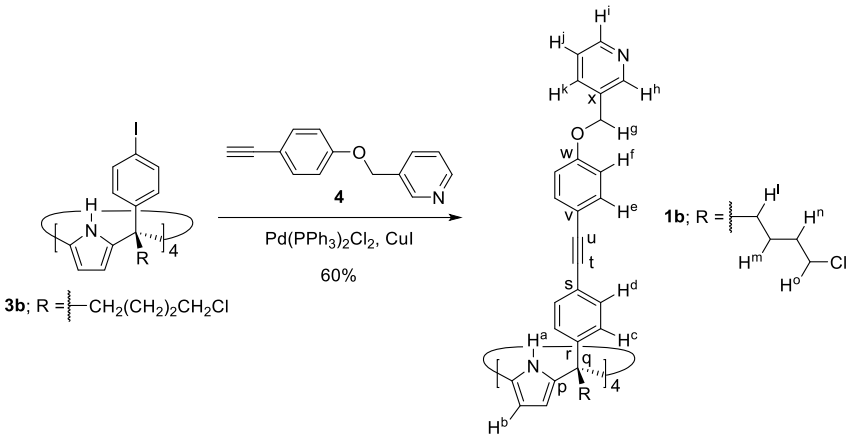

Scheme 4.2. Synthesis of tetra-pyridyl super aryl-extended calix[4]pyrrole **1b**.

Tetra-*α* 4-iodophenyl-4'-chlorobutyl calix[4]pyrrole **3b** (50 mg, 0.03 mmol, 1 equiv.), $Pd(PPh_3)_2Cl_2$ (2.95 mg, 0.004 mmol, 0.03 equiv.), CuI (1.28 mg, 0.007 mmol, 0.05 equiv.) and 3-((4'-ethynylphenoxy)methyl)pyridine **4** (42.20 mg, 0.20 mmol, 1.5 equiv.) were kept under Argon atmosphere. Dry THF (3.6 mL) and dry diisopropylamine (3.6 mL) were added dropwise. The reaction was stirred at r.t. for 24 h. After that, the crude was concentrated, redissolved in CH_2Cl_2 (10 mL) and washed with brine (2×10 mL) and water (10 mL). The organic layer was dried (Na_2SO_4), filtered and concentrated. The crude was purified by column chromatography on silica gel (3 g, 90:10 → 85:15 CH_2Cl_2/isopropanol) to afford the product as a white solid. The product was further purified by recrystallization from 1:1 CH_2Cl_2/CH_3CN (37 mg, 0.02 mmol, 60% yield). Rf = 0.4 (92:8 CH_2Cl_2/isopropanol). ^{1}H NMR (500 MHz with cryoprobe, $(CD_3)_2CO$, 298 K): *δ* (ppm): 8.67 (d, *J* = 1.7 Hz, 4H); 8.53 (dd, *J* = 4.8 Hz, *J* = 1.7 Hz, 4H); 8.48 (s, 4H); 7.82 (ddd, *J* = 7.7 Hz, *J* = 1.7 Hz, *J* = 1.7 Hz, 4H); 7.51-7.49 (m, 8H); 7.42-7.40 (m, 8H); 7.34 (dd, *J* = 7.7 Hz, *J* = 4.8 Hz, 4H); 7.07-7.05 (m, 8H); 7.01-6.99 (m, 8H); 6.05 (d, *J* = 2.7 Hz, 8H); 5.18 (s, 8H); 3.57 (t, *J* = 6.7 Hz, 8H); 2.46-2.43 (m, 8H); 1.71-1.76 (m, 8H); 1.32-1.26 (m, 8H). ^{13}C{^{1}H} NMR (125 MHz with cryoprobe, $(CD_3)_2CO$, 298 K): *δ* (ppm): 159.7; 150.3; 150.1; 147.2; 137.6; 136.1; 133.9; 133.3; 131.9; 130.0; 124.3; 122.8; 116.4; 116.0; 106.4; 90.3; 88.5; 68.4; 49.3; 45.6; 40.9; 33.8; 23.3. MS (MALDI-TOF) *m*/*z*: $[M+H]^+$ Calcd for $C_{116}H_{101}N_8O_4Cl_4$ 1810.6; Found 1810.7. FTIR *ν* (cm^{-1}): 3430; 2950; 1602; 1513; 1428; 1281; 1247; 1018; 829; 771. M.p. > 220ºC (decompose).

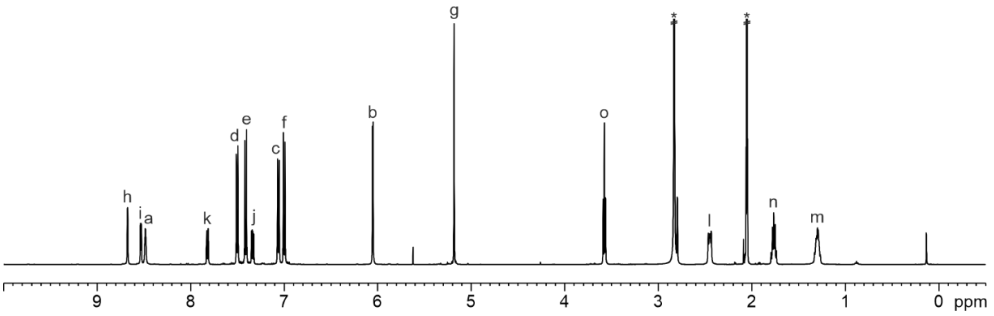

Figure 4.5. ^{1}H NMR (500 MHz with cryoprobe, $(CD_3)_2CO$, 298 K) spectrum of compound **1b**. See Scheme 4.2 for proton assignment. *Residual solvent peaks.

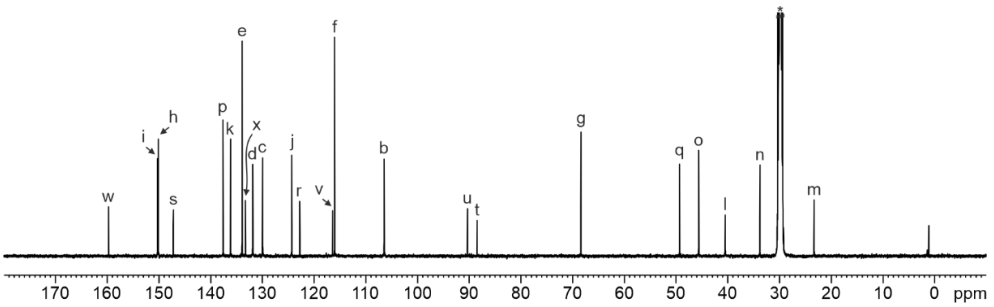

Figure 4.6. $^{13}C\{^{1}H\}$ NMR (125 MHz with cryoprobe, $(CD_3)_2CO$, 298 K) spectrum of compound **1b**. See Scheme 4.2 for carbon assignment. *Residual solvent peak.

Tetra-*α* tetra-pyridyl super aryl-extended calix[4]pyrrole **2**$^{4+}$

Tetra-pyridyl super aryl-extended calix[4]pyrrole **1b** (20 mg, 0.011 mmol, 1 equiv.) was added to a dry-oven schlenk flask and kept under Argon atmosphere. Freshly distilled and dry pyridine (2.2 mL) was added and the reaction was stirred at 110ºC overnight. After that, the reaction was stopped and allowed to reach r.t. The crude was concentrated, and acetone (3 mL) was added and sonicated. The crude was filtered and washed with acetone (3 mL), CH_2Cl_2 (2×3 mL) and hexane (2×3 mL) affording the product as a pale brown solid (16 mg, 0.007 mmol, 68% yield). ^{1}H NMR (500 MHz with cryoprobe, CD_3OD, 333 K): δ (ppm) = 8.87-8.86 (m, 8H); 8.56 (s, 4H); 8.54-8.52 (m, 4H); 8.46 (d, J = 4.8 Hz, 4H); 8.03-8.01 (m, 8H); 7.86 (d, J = 7.8 Hz, 4H); 7.40-7.36 (m, 20 H); 7.02-7.00 (m, 8H); 6.96-6.94 (m, 8H); 5.95 (s, 8H); 5.14 (s, 8H); 4.56 (t, J = 7.4 Hz, 8H); 2.49-2.46 (m, 8H); 1.92-1.98 (m, 8H); 1.30-1.24 (m, 8H). $^{13}C\{^{1}H\}$ NMR (125 MHz with cryoprobe, CD_3OD, 333 K): δ (ppm) = 160.1; 149.8; 149.4; 146.9; 145.8; 137.8; 137.3; 134.7; 134.2; 131.9; 129.8; 129.5; 125.1; 123.4; 117.3; 116.4; 106.8; 68.8; 62.9; 40.3; 32.7; 23.1. HRMS (ESI-TOF) m/z: $[M\text{-}4Cl]^{4+}$ Calcd for $C_{136}H_{120}N_{12}O_4$ 496.2383; Found 496.2398. FTIR v (cm^{-1}): 3363; 3190; 2942; 1600; 1512; 1485; 1241; 1173; 1017; 770. M.p. > 260ºC (decompose).

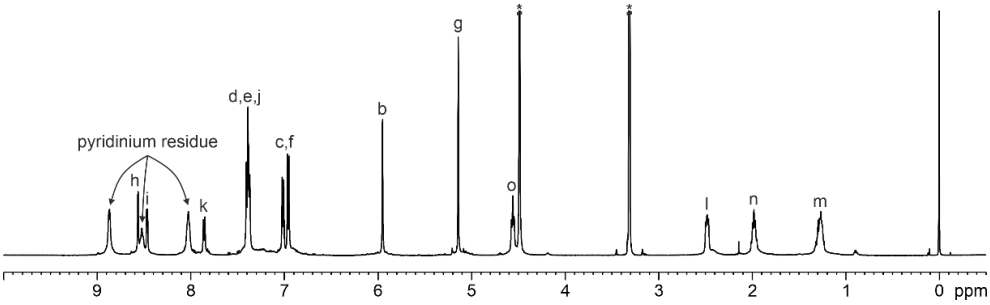

Figure 4.7. ^{1}H NMR (500 MHz with cryoprobe, CD_3OD, 333 K) spectrum of compound **2**$^{4+}$. See See Scheme 4.1 for proton assignment. *Residual solvent peaks.

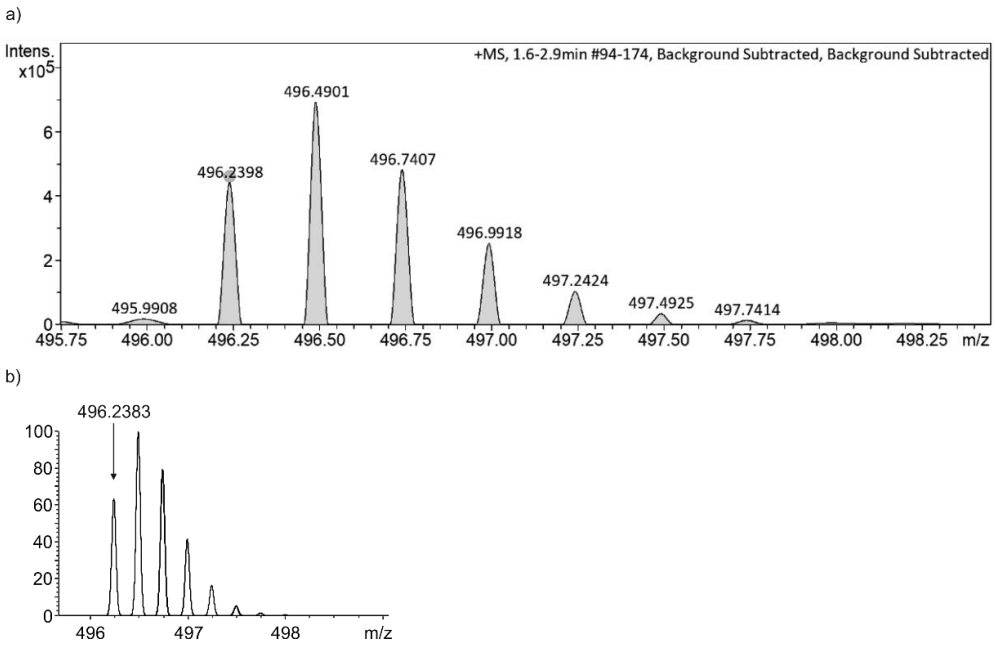

Figure 4.8. a) Experimental and b) theoretical isotopic distributions of $[M\text{-}4Cl]^{4+}$. The exact mass for the mono-isotopic peak in a) and b) is indicated.

Bis-formamide **6**

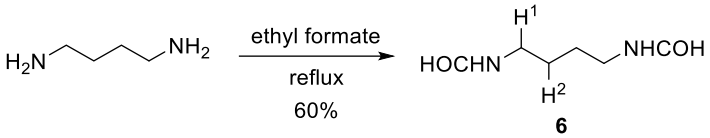

Scheme 4.3. Synthesis of *bis*-formamide **6**.

1,4-*Bis*-aminobutane (0.10 g, 1.12 mmol, 1 equiv.) was dissolved in ethyl formate (0.50 M of reactant). The reaction was heated under reflux conditions overnight. After that, the crude was concentrated under reduced pressure. The crude was purified by silica gel column chromatography (acetone) to afford the product as a white solid (0.10 g, 0.67 mmol, 60% yield). ^{1}H NMR (400 MHz, D_2O, 298 K): δ (ppm) = 8.04 (s, 1.7H); 7.98 (s, 0.3H); 3.28-3.24 (m, 4H); 1.59-1.55 (m, 4H). $^{13}C\{^{1}H\}$ NMR (100 MHz, D_2O, 298 K): δ (ppm) = 164.3; 37.7; 25.8 (*trans*,*trans*-isomer, major isomer in solution). HRMS (ESI-TOF) *m/z*: $[M+Na]^+$ Calcd for $C_6H_{12}N_2NaO_2$ 167.0791; Found 167.0783.

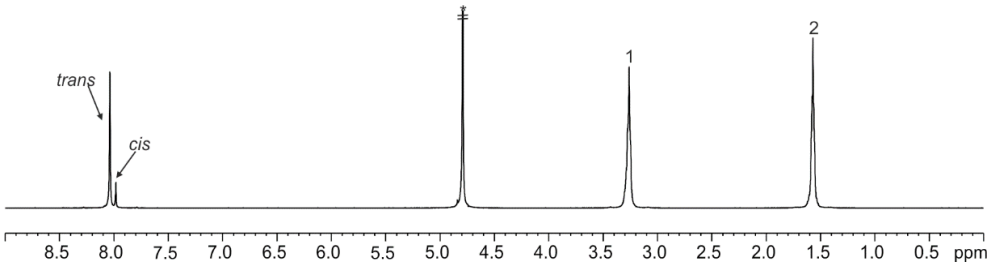

Figure 4.9. ^{1}H NMR (400 MHz, D_2O, 298 K) spectrum of *bis*-formamide **6**. See Scheme 4.3 for proton assignment. *Residual solvent peak.

4.4.3 NMR binding studies of tetra-pyridyl SAE-C[4]P **1b** with *mono*-formamide **10**

A solution of the tetra-pyridyl SAE-C[4]P **1b** (1-2 mM) was prepared in $CDCl_3$ or in 2:1 $CDCl_3/CD_3CN$ solution. Subsequently, 0.5 mL of the solution were placed in an NMR tube. A solution of the guest **10** was prepared at 20-30-fold higher concentration using the host's solution ([G] = 20-30 mM and [H] = 1 mM). The solution of **1b** was titrated by manually injecting incremental amounts of the guest's solution using a micro syringe. A ^1H NMR spectrum of the mixture was acquired after each injection and vigorous hand shaking of the NMR tube for few seconds.

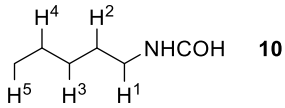

10

Figure 4.10. Line-drawing structure of **10**.

^{1}H NMR titration spectra in $CDCl_3$

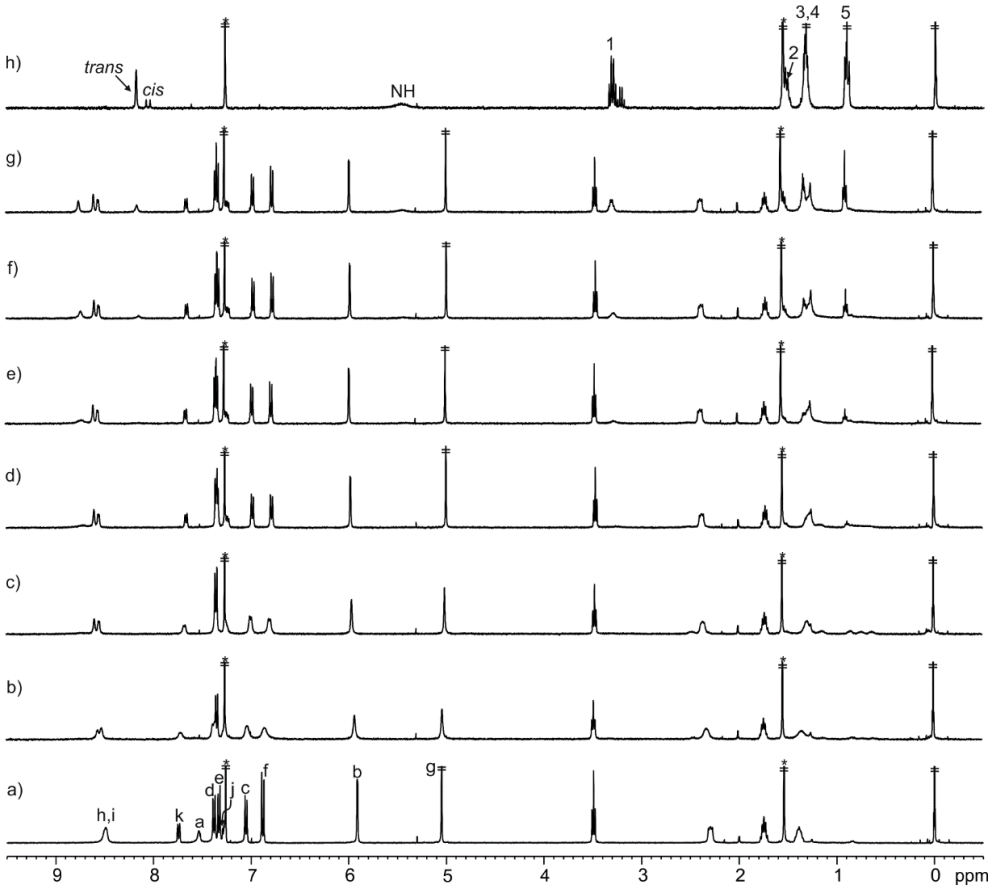

Figure 4.11. Selected ^{1}H NMR (400 MHz, $CDCl_3$, 298 K) spectra of the titration of **1b** with **10**: a) 0; b) 0.5; c) 1; d) 1.5; e) 2; f) 3 and g) 5 equiv.; h) **10**. See Scheme 4.2 and Figure 4.10 for proton assignments. *Residual solvent peaks.

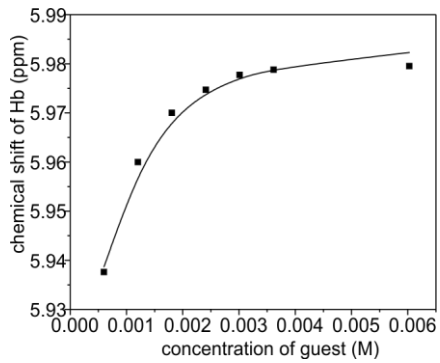

Figure 4.12. Fit of the NMR titration data (proton signal H^b of **1b**) to a theoretical 1:1 binding model. The fit returned an apparent binding constant value K_{app} (**10**⊂**1b**) = 3×10^3 M^{-1}.

^{1}H NMR titration spectra in 2:1 $CDCl_3/CD_3CN$

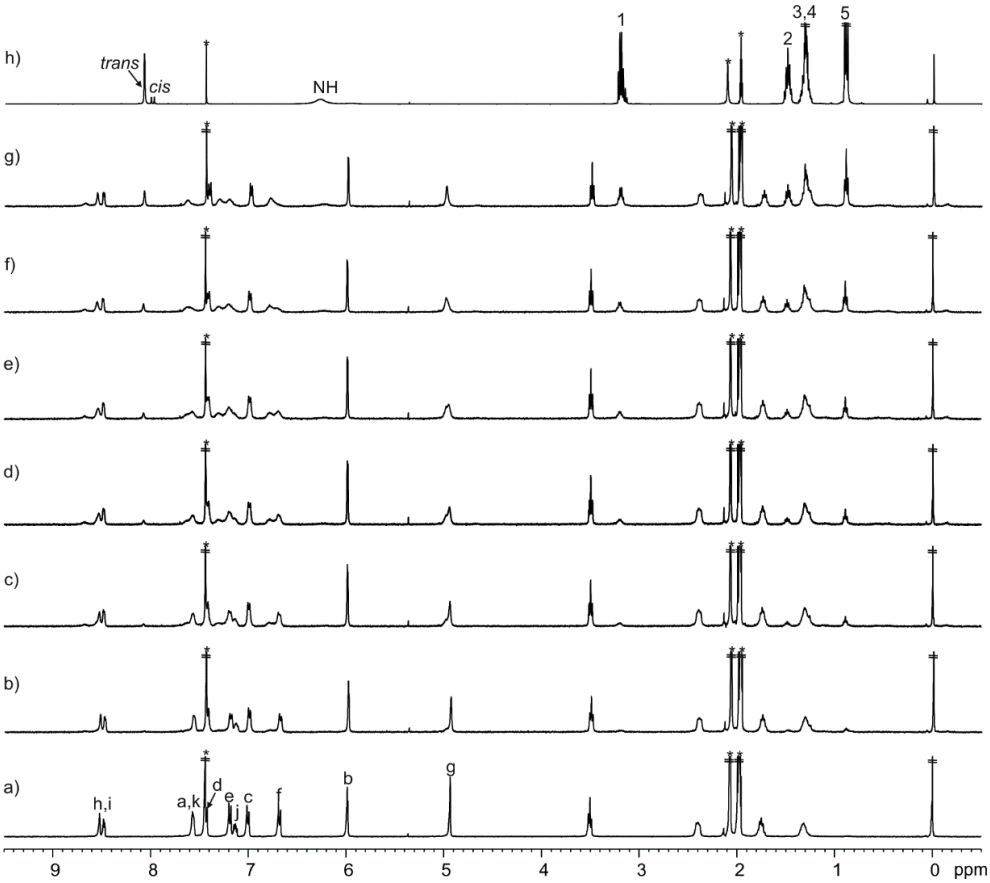

Figure 4.13. Selected ^{1}H NMR (400 MHz, 2:1 $CDCl_3/CD_3CN$, 298 K) spectra of the titration of **1b** with **10**: a) 0; b) 0.5; c) 1; d) 1.5; e) 2; f) 3 and g) 5 equiv.; h) **10**. See Scheme 4.1 and Figure 4.10 for proton assignments. *Residual solvent peaks.

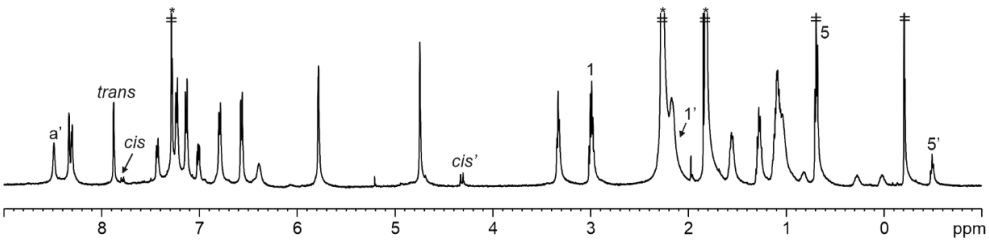

Figure 4.14. ^{1}H NMR (500 MHz, 2:1 $CDCl_3/CD_3CN$, 233 K) spectrum of **1b** with 5 equiv. of **10**. See Scheme 4.1 and Figure 4.10 for proton assignments. *Residual solvent peaks.

Based on the relative integral values of the proton signals of the free and bound components in the ^{1}H NMR spectrum at 233 K, we estimated an apparent binding constant value K_a (**10**⊂**1b**) ~ 7 × 10^2 M^{-1}.

4.4.4 Self-assembly of the [**1b**•Pd]$^{2+}$

A solution of the tetra-pyridyl SAE-C[4]P **1b** (1 mM) and 1,3,5-trimethoxybenzene (internal standard, 1 mM) was prepared in 2:1 $CDCl_3/CD_3CN$ solution. Subsequently, 0.5 mL of the solution were placed in an NMR tube. A solution of $[Pd(CH_3CN)_4](BF_4)_2$ was prepared in 2:1 $CDCl_3/CD_3CN$ at higher concentration (5-7 mM). Immediately, the 0.5 mL of the tetra-pyridyl's solution was titrated by manually injecting incremental amounts of the Pd(II) solution using a micro syringe. A ^{1}H NMR spectrum of the mixture was acquired after each injection and vigorous hand shaking of the NMR tube for few seconds (only 1 equiv. is shown). The solution contained in the NMR tube was thermally equilibrated at 40ºC for 24 h in an oil bath.

Self-assembly of the [**1b**•Pd]$^{2+}$ cage

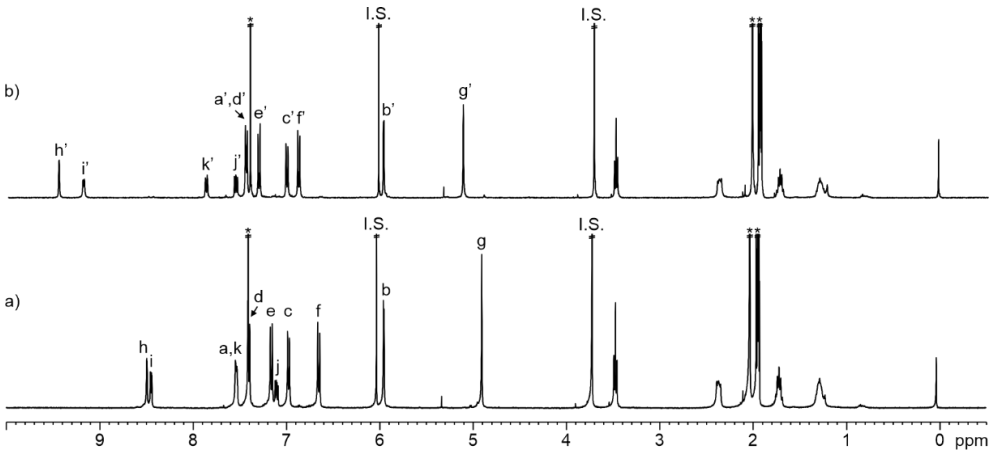

Figure 4.15. ^{1}H NMR (400 MHz, 2:1 $CDCl_3/CD_3CN$, 298 K) spectra of a) **1b**; addition of $[Pd(CH_3CN)_4](BF_4)_2$ to **1b** followed by thermal equilibration (40ºC for 24 h): b) *ca.* 1 equiv. Primed labels correspond to proton signals of [**1b**•Pd]$^{2+}$. The [**1b**•Pd]$^{2+}$ cage was assembled in an extent larger than 90% according to the integration of the I.S. See Scheme 4.1 for proton assignment. 1,3,5-Trimethoxybenzene (I.S.). *Residual solvent peaks.

4.4.5 ^{1}H NMR binding studies of [**1b**•Pd]$^{2+}$ with formamides (**6**, **7** and **10**) and 2D NMR spectra of cage complexes

Guests' solutions (**6**, **7** and **10**, 20-40 mM) were prepared in a 2:1 $CDCl_3/CD_3CN$ solvent mixture. Cage [**1b**•Pd]$^{2+}$ was titrated by manually injecting incremental amounts of the guest's solution using a micro syringe. A ^{1}H NMR spectrum of the mixture was acquired after each injection and vigorous hand shaking of the NMR tube for few seconds.

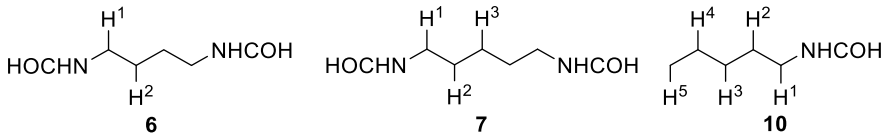

Figure 4.16. Line-drawing structures of **6**, **7** and **10**.

Bis-formamide **6**

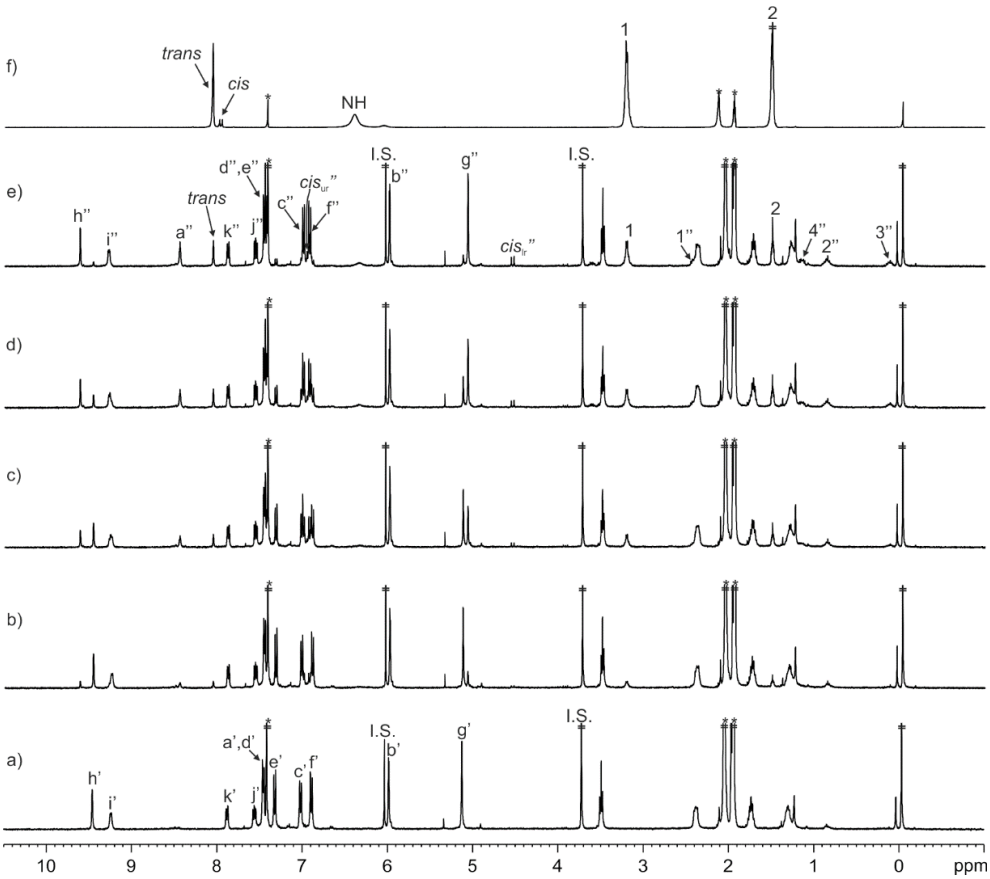

Figure 4.17. ^{1}H NMR (400 MHz, 2:1 $CDCl_3/CD_3CN$, 298 K) spectra of the titration of [**1b**•Pd]$^{2+}$ with **6**: a) 0; b) 0.5; c) 1; d) 1.5 and e) 2 equiv.; f) **6**. Primed labels correspond to proton signals of [**1b**•Pd]$^{2+}$. Doubly primed labels correspond to proton signals of *cis,cis*-**6**⊂[**1b**•Pd]$^{2+}$. See Scheme 4.1 and Figure 4.16 for proton assignments. 1,3,5-Trimethoxybenzene (I.S.). *Residual solvent peaks.

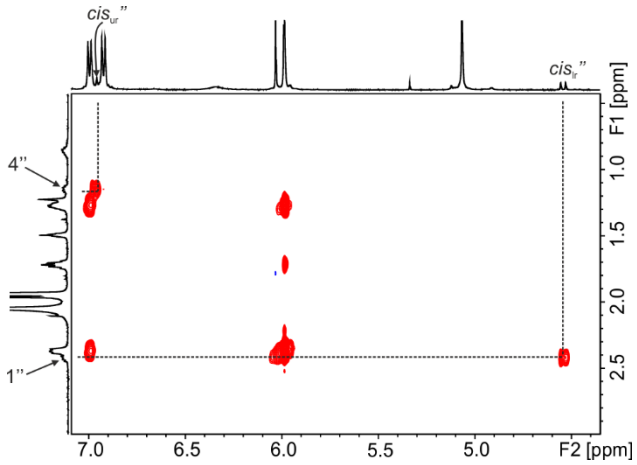

Figure 4.18. Selected region of the ^{1}H-^{1}H ROESY NMR (500 MHz with cryoprobe, 2:1 $CDCl_3/CD_3CN$, 298 K, spin lock = 0.3 s) spectrum of [**1b**•Pd]$^{2+}$ with 2 equiv. of **6**. The ROESY cross-peaks between 1'' and 4'' with the signals at 4.54 and 6.96 ppm, respectively, are highlighted. The observed cross-peaks confirm that the two formamide groups of bound **6** adopt a *cis*-conformation. See Figure 4.21 for proton assignment.

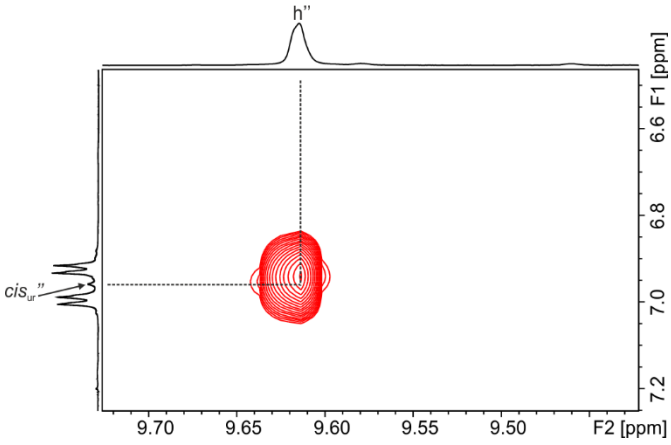

Figure 4.19. Selected region of the ^{1}H-^{1}H ROESY NMR (500 MHz with cryoprobe, 2:1 $CDCl_3/CD_3CN$, 298 K, spin lock = 0.3 s) spectrum of [**1b**•Pd]$^{2+}$ with 2 equiv. of **6**. The ROESY cross-peak between h'' and *cis*$_{ur}$'' is highlighted. The observed cross-peak indicates that one of the formamide groups of bound *cis,cis*-**6** is located in the binding site defined by the inwardly-directed α-pyridyl protons. See Scheme 4.1 and Figure 4.21 for proton assignments.

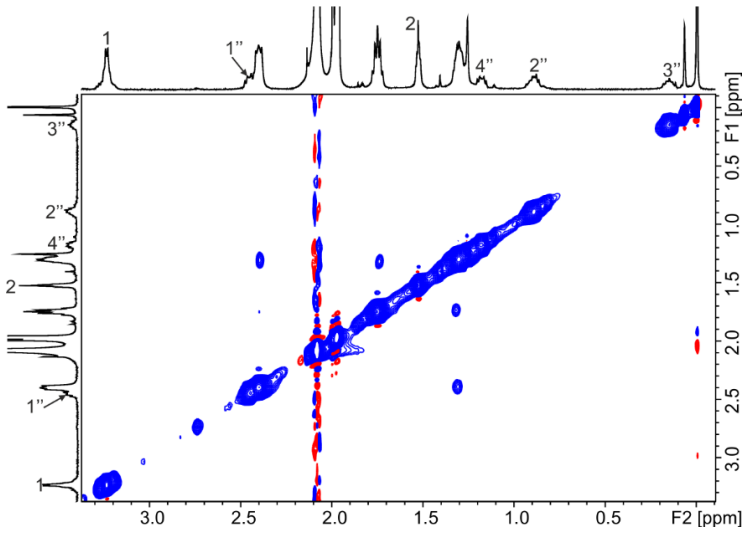

Figure 4.20. Selected region of the ^{1}H-^{1}H EXSY NMR (500 MHz with cryoprobe, 2:1 $CDCl_3/CD_3CN$, 298 K, mixing time = 0.3 s) spectrum of [**1b**•Pd]$^{2+}$ with 2 equiv. of **6**. See Figure 4.16 and Figure 4.21 for proton assignments.

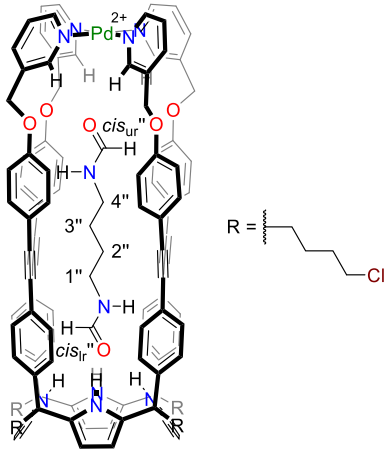

Figure 4.21. Line-drawing structure of the *cis*,*cis*-**6**⊂[**1b**•Pd]$^{2+}$ cage complex.

Table 4.1. Experimental chemical shifts of free (δ_{free}) and bound (δ_{bound}) *bis*-formamide **6** and complexation-induced shifts ($\Delta\delta$).

Signal	δ_{free} (ppm)	Signal	δ_{bound} (ppm)	$\Delta\delta$ (ppm)
trans	8.08	-	-	-
cis	7.99	*cis*$_{lr}$''	4.54	-3.45
-	-	*cis*$_{ur}$''	6.96	-1.03
1	3.23	1''	2.45	-0.78
2	1.53	2''	0.89	-0.64
-	-	3''	0.15	-1.38
-	-	4''	1.17	-2.06

Bis-formamide **7**

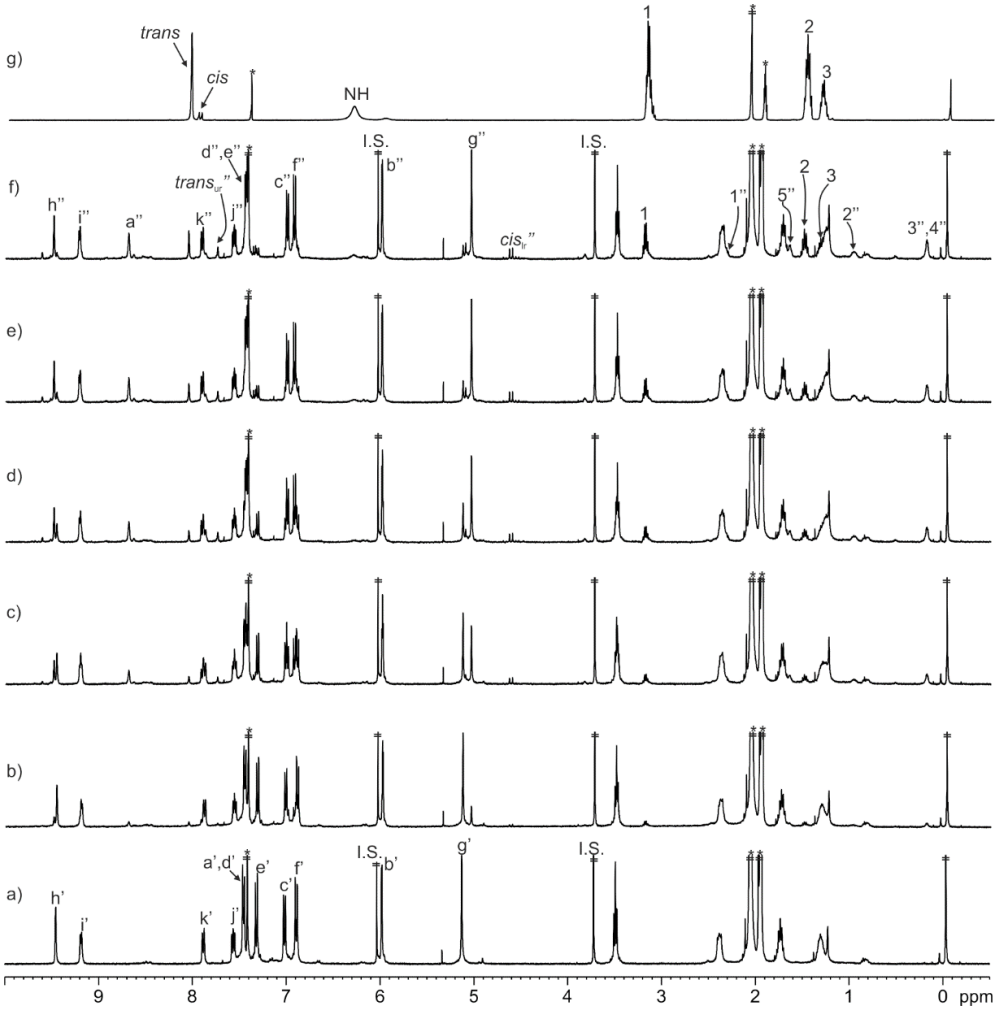

Figure 4.22. ^{1}H NMR (400 MHz, 2:1 $CDCl_3/CD_3CN$, 298 K) spectra of the titration of [**1b**•Pd]$^{2+}$ with **7**: a) 0; b) 0.5; c) 1; d) 1.5; e) 2 and f) 2.5 equiv.; g) **7**. Primed labels correspond to proton signals of [**1b**•Pd]$^{2+}$. Doubly primed labels correspond to proton signals of *trans,cis*-**7**⊂[**1b**•Pd]$^{2+}$. See Scheme 4.1 and Figure 4.16 for proton assignments. 1,3,5-Trimethoxybenzene (I.S.). *Residual solvent peaks.

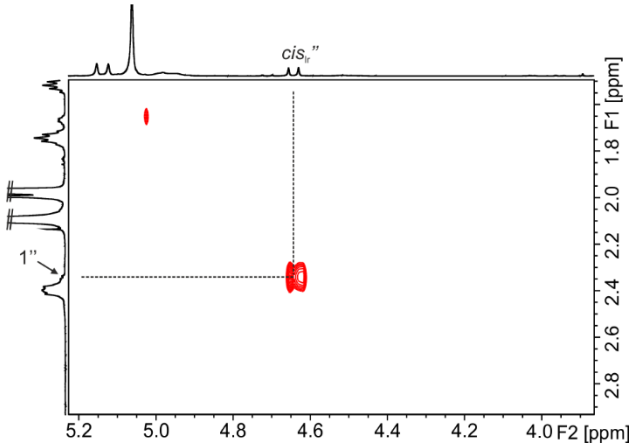

Figure 4.23. Selected region of the ^{1}H-^{1}H ROESY NMR (500 MHz with cryoprobe, 2:1 $CDCl_3/CD_3CN$, 298 K, spin lock = 0.3 s) spectrum of [**1b**•Pd]$^{2+}$ with 2.5 equiv. of **7**. The ROESY cross-peak between 1'' and the signal at 4.61 ppm is highlighted. The observed cross-peak confirms that one of the formamide groups of bound **7** adopts a *cis*-conformation. See Figure 4.26 for proton assignment.

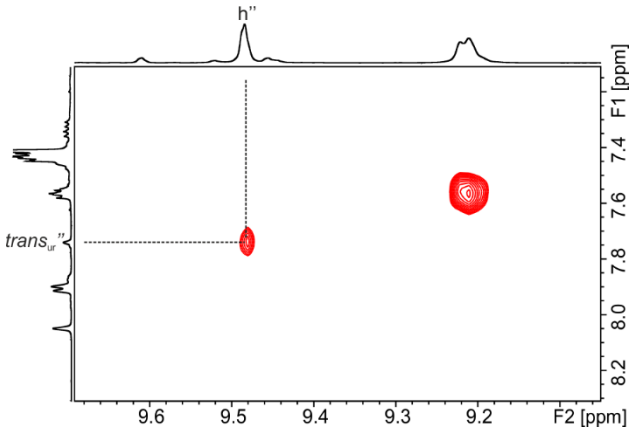

Figure 4.24. Selected region of the ^{1}H-^{1}H ROESY NMR (500 MHz with cryoprobe, 2:1 $CDCl_3/CD_3CN$, 298 K, spin lock = 0.3 s) spectrum of [**1b**•Pd]$^{2+}$ with 2.5 equiv. of **7**. The ROESY cross-peak between h'' and *trans*$_{ur}$'' is highlighted. The observed cross-peak indicates that one of the formamide groups of bound *trans,cis*-**7** is located in the binding site defined by the inwardly-directed α-pyridyl protons. See Scheme 4.1 and Figure 4.26 for proton assignments.

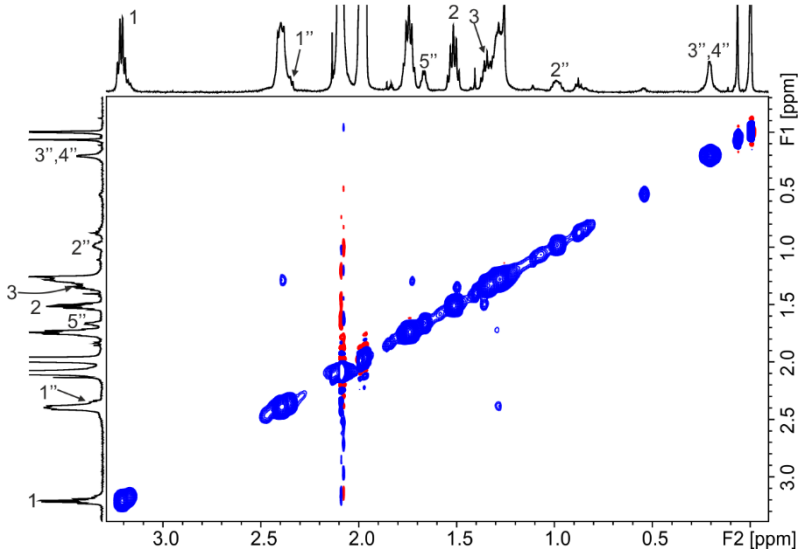

Figure 4.25. Selected region of the ^{1}H-^{1}H EXSY NMR (500 MHz with cryoprobe, 2:1 $CDCl_3/CD_3CN$, 298 K, mixing time = 0.3 s) spectrum of [**1b**•Pd]$^{2+}$ with 2.5 equiv. of **7**. See Figure 4.16 and Figure 4.26 for proton assignments.

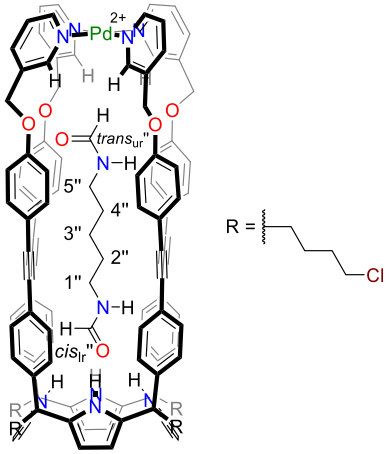

Figure 4.26. Line-drawing structure of the *trans,cis*-**7**⊂[**1b**•Pd]$^{2+}$ cage complex.

Table 4.2. Experimental chemical shifts of free (δ_{free}) and bound (δ_{bound}) *bis*-formamide **7** and complexation-induced shifts ($\Delta\delta$).

Signal	δ_{free} (ppm)	Signal	δ_{bound} (ppm)	$\Delta\delta$ (ppm)
trans	8.08	*trans*$_{ur}$''	7.76	-0.32
cis	7.99	*cis*$_{lr}$''	4.61	-3.38
1	3.21	1''	2.36	-0.85
2	1.52	2''	0.99	-0.53
3	1.34	3''	0.21	-1.13
-	-	4''	0.21	-1.31
-	-	5''	1.67	-1.54

Mono-formamide **10**

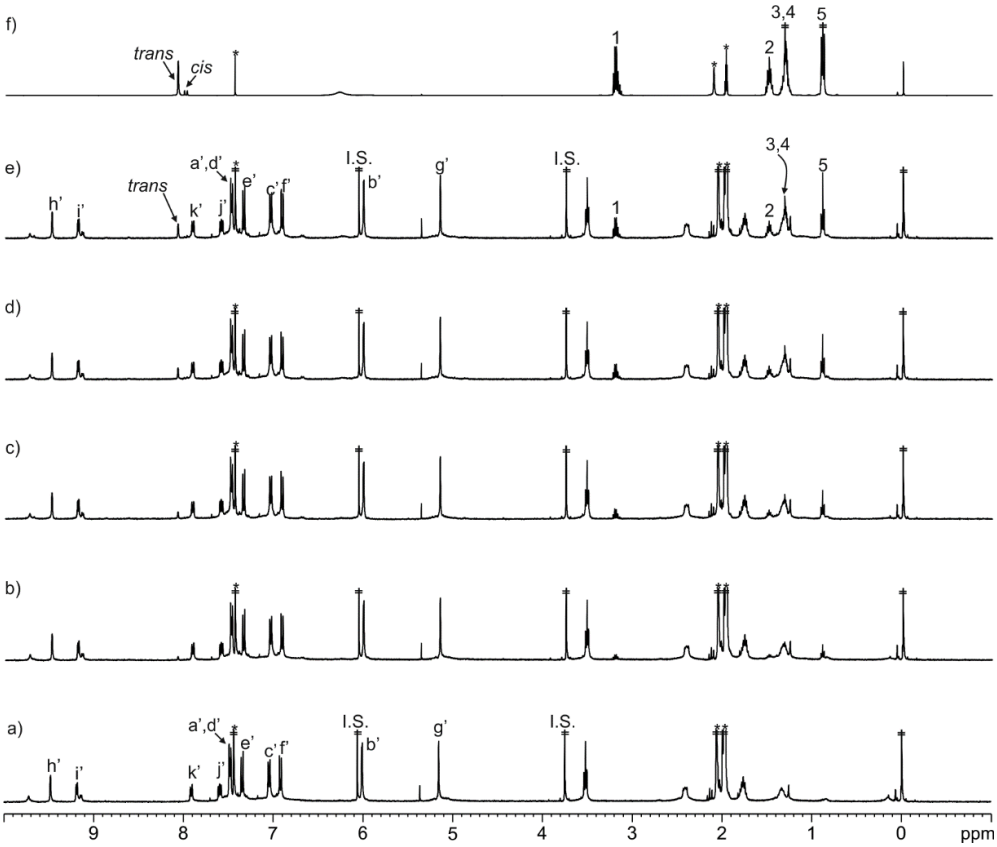

Figure 4.27. ^{1}H NMR (400 MHz, 2:1 $CDCl_3/CD_3CN$, 298 K) spectra of the titration of [**1b**•Pd]$^{2+}$ with **10**: a) 0; b) 0.5; c) 1; d) 1.5 and e) 2 equiv.; f) **10**. Primed labels correspond to proton signals of [**1b**•Pd]$^{2+}$. See Scheme 4.1 and Figure 4.16 for proton assignments. 1,3,5-Trimethoxybenzene (I.S.). *Residual solvent peaks.

The addition of 2 equiv. of *mono*-formamide **10** to a millimolar solution of [**1b**•Pd]$^{2+}$ in 2:1 $CDCl_3/CD_3CN$ did not produce noticeable changes in the proton signals of the Pd(II)-cage.

4.4.6 Self-assembly of the [**2**•Pd]$^{2+}$ using *N*-oxides and formamides (**5**-**10**) as templates, 2D NMR spectra of cage complexes and DOSY experiments

A suspension of the tetra-pyridyl SAE-C[4]P **2**$^{4+}$ (1 mM) and *tert*-butanol (internal standard, 1 mM) was prepared in D_2O solution. The suspension was heated at 50-60°C for 1 h leading to a clear solution. A solution of the guest (**5**-**10**) was prepared in D_2O solution at higher concentration (10-20 mM). Immediately, the guest (1-2 equiv.) was added to the solution of **2**$^{4+}$. After that, 0.5 mL of the solution were placed in an NMR tube and variable temperature (VT) ^{1}H NMR experiments were performed (see figure footnotes for details).

Later, a solution of $Pd(NO_3)_2$ salt (10-30 mM) was prepared in D_2O solution. Subsequently, Pd(II) (*ca.* 1 equiv.) was added to the D_2O solution containing the tetra-pyridyl **2**$^{4+}$ and the guest. VT ^{1}H NMR experiments (see figure footnotes for details) were performed after vigorous hand shaking of the NMR tube for few seconds.

Attempt of the self-assembly of the [**2**•Pd]$^{6+}$ cage without template

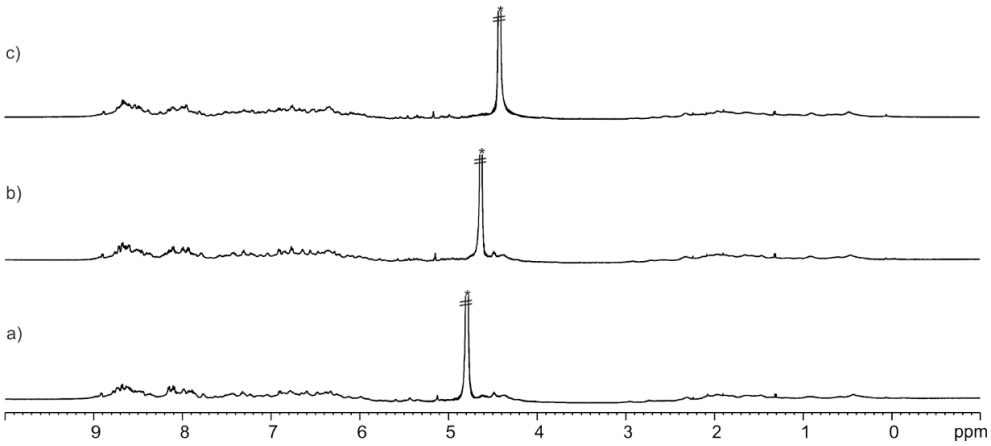

Figure 4.28. VT ^{1}H NMR (500 MHz with cryoprobe, D_2O) spectra of **2**$^{4+}$: a) 298; b) 313 and c) 333 K. *Residual solvent peak.

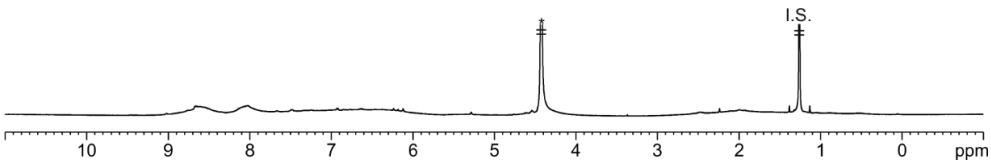

Figure 4.29. ^{1}H NMR (500 MHz with cryoprobe, D_2O, 333 K) spectrum of **2**$^{4+}$ with *ca.* 1 equiv. of $Pd(NO_3)_2$. *tert*-Butanol (I.S.). *Residual solvent peak.

Self-assembly of the [**2**•Pd]$^{2+}$ with pyridine *N*-oxides **5**, **8** and **9**

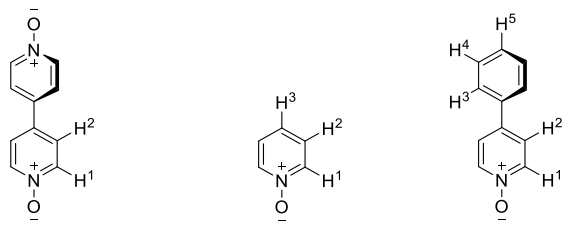

5 **8** **9**

Figure 4.30. Line-drawing structures of pyridine *N*-oxides **5**, **8** and **9**.

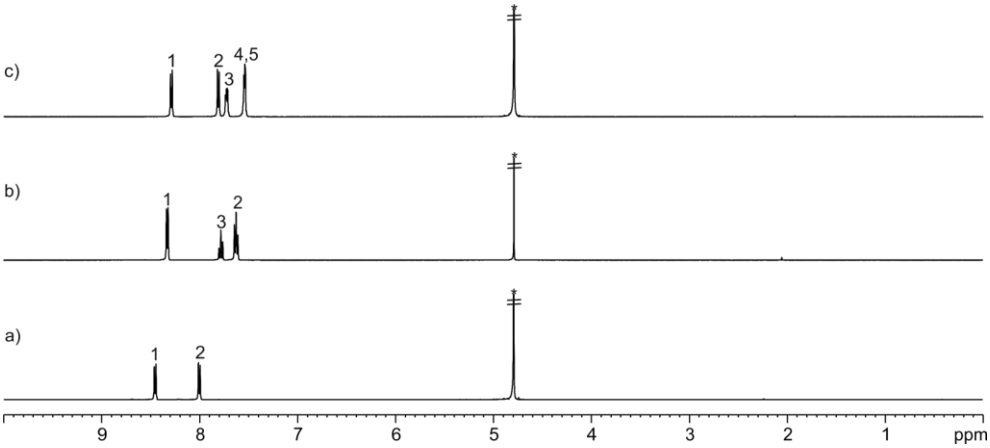

Figure 4.31. ^{1}H NMR (400 MHz, D_2O, 298 K) spectra of: a) **5**; b) **8** and c) **9**. See Figure 4.30 for proton assignments. *Residual solvent peak.

Bis-N-oxide **5**

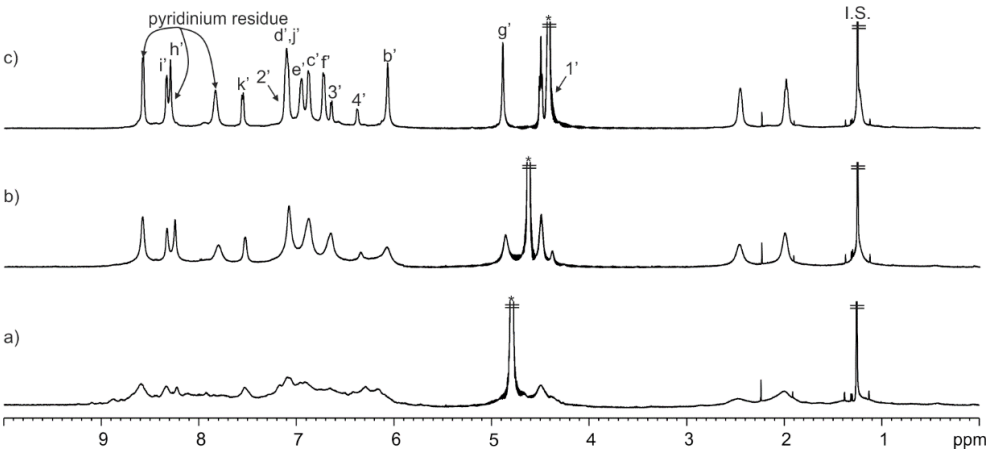

Figure 4.32. VT ^{1}H NMR (500 MHz with cryoprobe, D_2O) spectra of $\mathbf{2}^{4+}$ with *ca.* 1 equiv. of **5**: a) 298; b) 313 and c) 333 K. Primed labels correspond to proton signals of $\mathbf{5}\subset\mathbf{2}^{4+}$. See Scheme 4.1 and Figure 4.30 for proton assignments. *tert*-Butanol (I.S.). *Residual solvent peak.

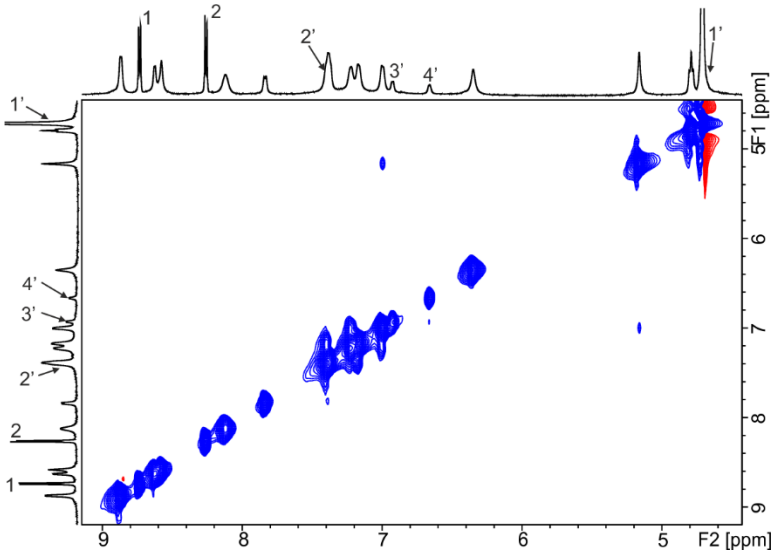

Figure 4.33. Selected region of the ^{1}H-^{1}H EXSY NMR (500 MHz with cryoprobe, D_2O, 333 K, mixing time = 0.3 s) spectrum of **2**$^{4+}$ with *ca.* 2 equiv. of **5**. See Figure 4.30 and Figure 4.37 for proton assignments.

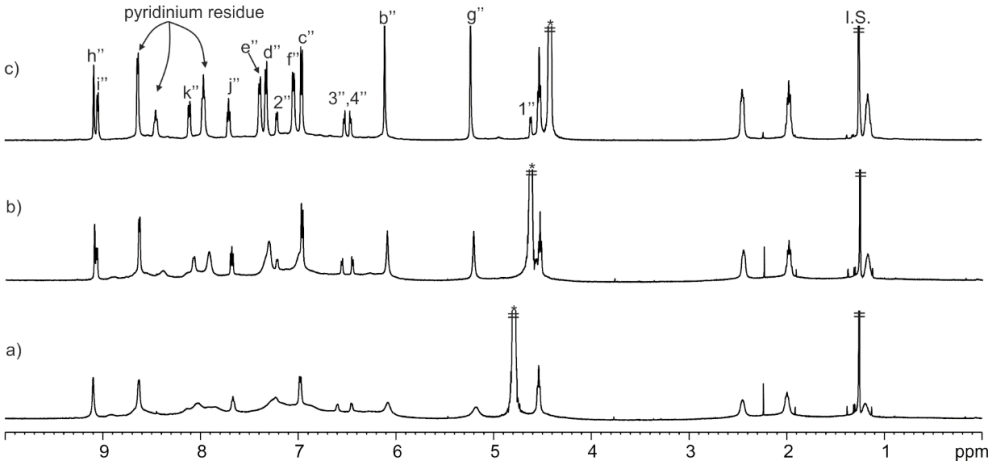

Figure 4.34. VT ^{1}H NMR (500 MHz with cryoprobe, D_2O) spectra of **2**$^{4+}$ with *ca.* 1 equiv. of **5** upon the addition of *ca.* 1 equiv. of Pd(II): a) 298; b) 313 and c) 333 K. Doubly primed labels correspond to proton signals of **5**⊂[**2**•Pd]$^{6+}$. The **5**⊂[**2**•Pd]$^{6+}$ was assembled in an extent larger than 60%. See Scheme 4.1 and Figure 4.37 for proton assignments. *tert*-Butanol (I.S.). *Residual solvent peak.

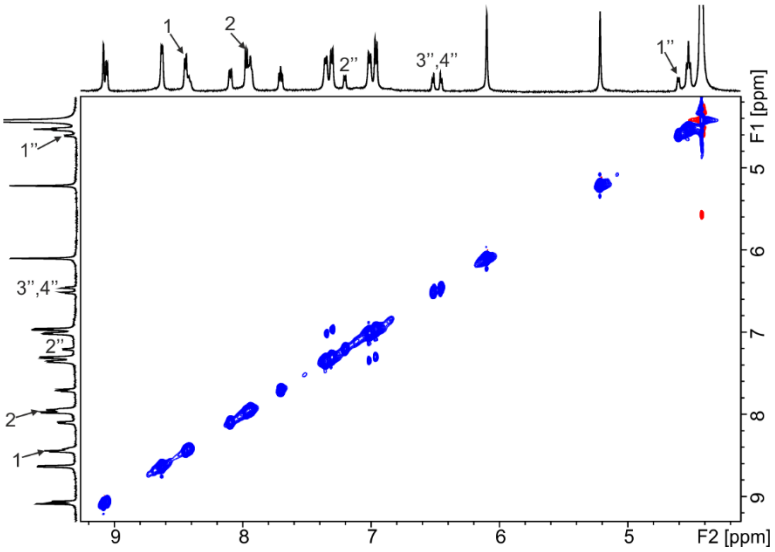

Figure 4.35. Selected region of the ^{1}H-^{1}H EXSY NMR (500 MHz with cryoprobe, D_2O, 333 K, mixing time = 0.3 s) spectrum of [**2**•Pd]$^{6+}$ with *ca.* 2 equiv. of **5**. See Figure 4.30 and Figure 4.37 for proton assignments.

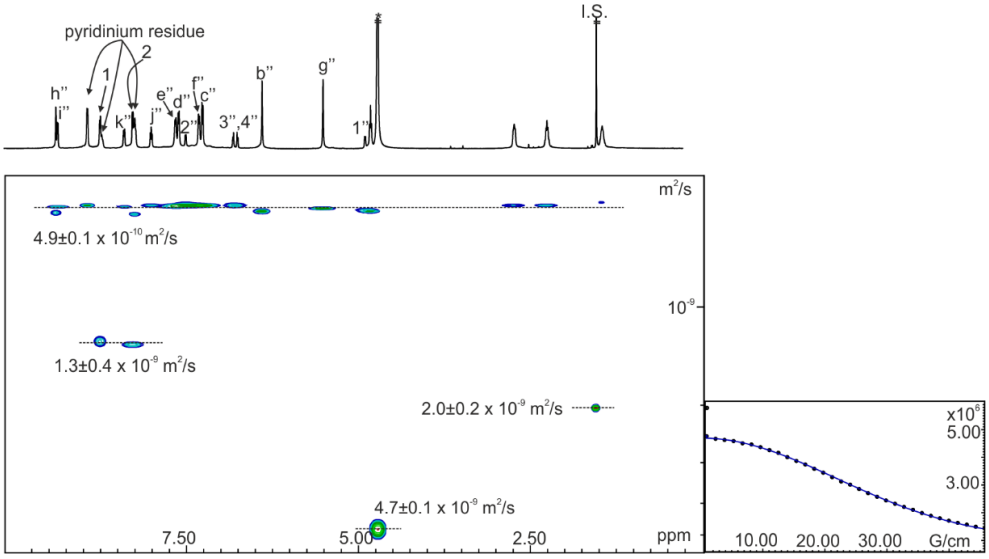

Figure 4.36. left) ^{1}H pseudo 2D DOSY (500 MHz with cryoprobe, D_2O, 333 K, D20 = 0.20 s; P30 = 0.60 ms) of [**2**•Pd]$^{6+}$ with *ca*. 2 equiv. of **5**. right) Fit of the decay of the signal b'' to a mono-exponential function using Dynamics Center from Bruker. Doubly primed labels correspond to proton signals of **5**⊂[**2**•Pd]$^{6+}$. See Scheme 4.1, Figure 4.30 and Figure 4.37 for proton assignments. Errors are indicated as standard deviations. *tert*-Butanol (I.S.). *Residual solvent peak.

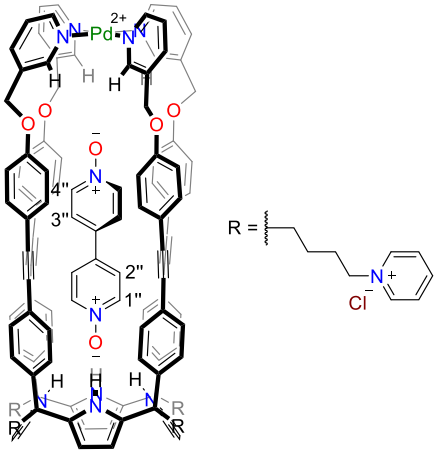

Figure 4.37. Line-drawing structure of the **5**⊂[**2**•Pd]$^{6+}$ cage complex.

Table 4.3. Experimental chemical shifts of free (δ_{free}) and bound (δ_{bound}) *bis*-*N*-oxide **5** and complexation-induced shifts ($\Delta\delta$).

Signal	δ_{free} (ppm)	Signal	δ_{bound} (ppm)	$\Delta\delta$ (ppm)
1	8.45	1''	4.62	-3.83
2	7.97	2''	7.22	-0.75
-	-	3''	6.48	-1.49
-	-	4''	6.48	-1.97

Pyridine *N*-oxide **8**

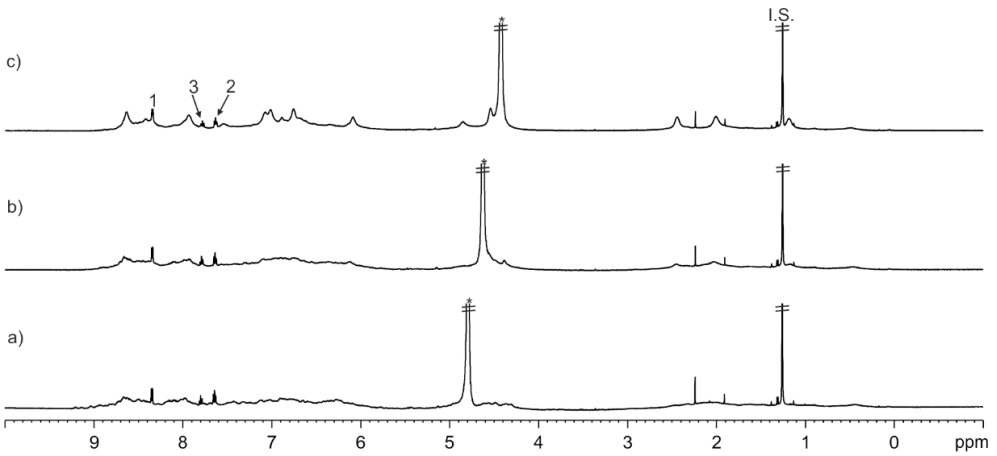

Figure 4.38. VT ^{1}H NMR (500 MHz with cryoprobe, D_2O) spectra of **2**$^{4+}$ with ca. 1 equiv. of **8**: a) 298; b) 313 and c) 333 K. See Figure 4.30 for proton assignment. *tert*-Butanol (I.S.). *Residual solvent peak.

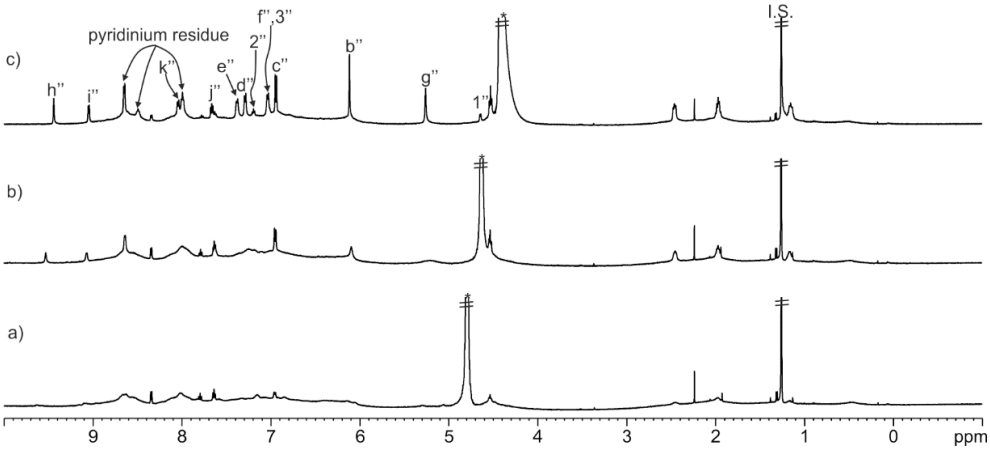

Figure 4.39. VT ^{1}H NMR (500 MHz with cryoprobe, D_2O) spectra of **2**$^{4+}$ with *ca.* 1 equiv. of **8** upon the addition of ca. 1 equiv. of Pd(II): a) 298; b) 313 and c) 333 K. Doubly primed labels correspond to proton signals of **8**⊂[**2**•Pd]$^{6+}$. The **8**⊂[**2**•Pd]$^{6+}$ cage complex was assembled in an extent larger than 30%. See Scheme 4.1 and Figure 4.41 for proton assignments. *tert*-Butanol (I.S.). *Residual solvent peak.

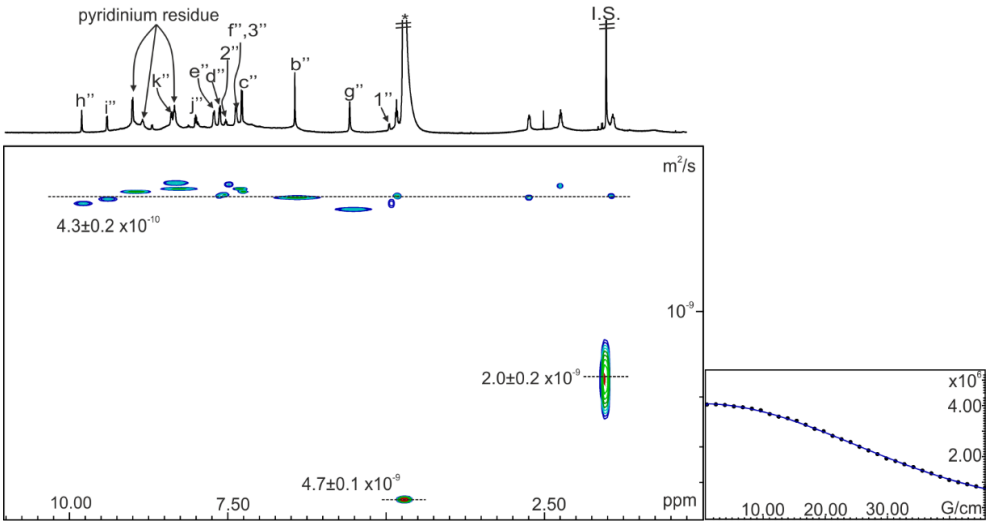

Figure 4.40. left) ^{1}H pseudo 2D DOSY (500 MHz with cryoprobe, D_2O, 333 K, D20 = 0.20 s; P30 = 0.60 ms) of [**2**•Pd]$^{6+}$ with *ca.* 1 equiv. of **8**. right) Fit of the decay of the signal b'' to a mono-exponential function using Dynamics Center from Bruker. Doubly primed labels correspond to proton signals of **8**⊂[**2**•Pd]$^{6+}$. See Scheme 4.1 and Figure 4.41 for proton assignments. Errors are indicated as standard deviations. *tert*-Butanol (I.S.). *Residual solvent peak.

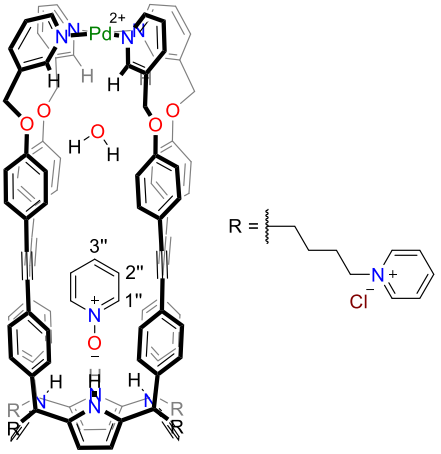

Figure 4.41. Line-drawing structure of the putative [**8**•H_2O]⊂[**2**•Pd]$^{6+}$ cage complex.

Table 4.4. Experimental chemical shifts of free (δ_{free}) and bound (δ_{bound}) pyridine *N*-oxide **8** and complexation-induced shifts ($\Delta\delta$).

Signal	δ_{free} (ppm)	Signal	δ_{bound} (ppm)	$\Delta\delta$ (ppm)
1	8.34	1''	4.61	-3.73
2	7.61	2''	7.17	-0.44
3	7.77	3''	7.04	-0.73

4-Phenylpyridine *N*-oxide **9**

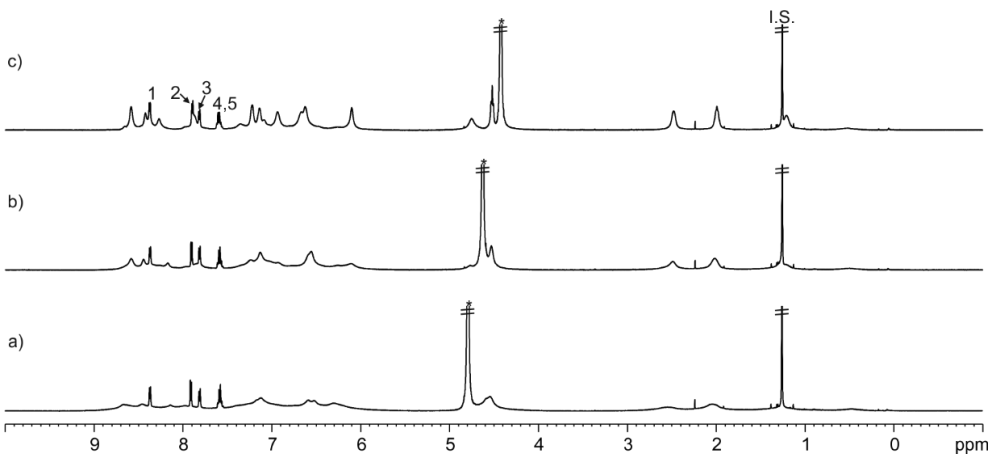

Figure 4.42. VT ^{1}H NMR (500 MHz with cryoprobe, D_2O) spectra of **2**$^{4+}$ with *ca.* 1 equiv. of **9**: a) 298; b) 313 and c) 333 K. See Figure 4.30 for proton assignment. *tert*-Butanol (I.S.). *Residual solvent peak.

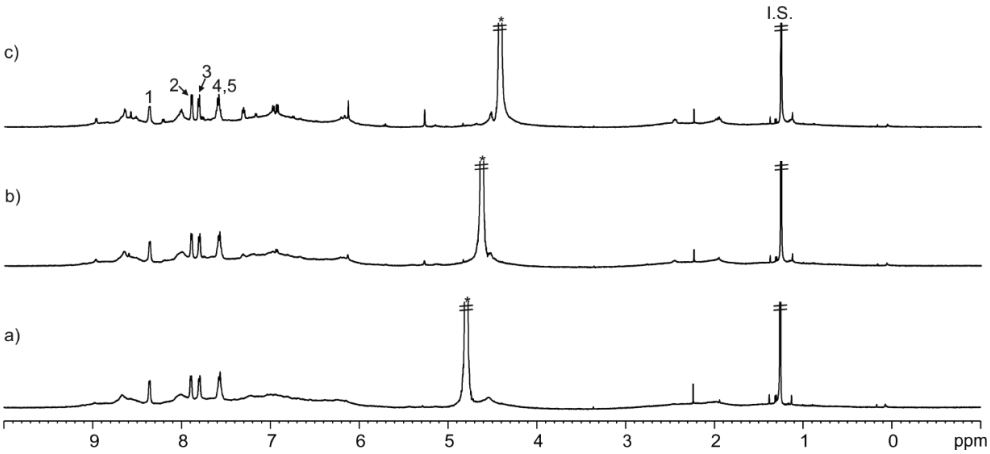

Figure 4.43. VT ^{1}H NMR (500 MHz with cryoprobe, D_2O) spectra of $\mathbf{2}^{4+}$ with *ca.* 1 equiv. of **9** upon the addition of *ca.* 1 equiv. of Pd(II): a) 298; b) 313 and c) 333 K. See Figure 4.30 for proton assignment. *tert*-Butanol (I.S.). *Residual solvent peak.

The addition of *ca.* 1 equiv. of Pd(II) to the equimolar solution of **9** and $\mathbf{2}^{4+}$ provoked the formation of polymeric aggregates to a significant extent.

Self-assembly of the [**2**•Pd]$^{2+}$ with formamides **6**, **7** and **10**

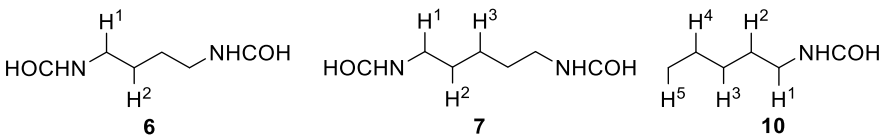

Figure 4.44. Line-drawing structures of **6**, **7** and **10**.

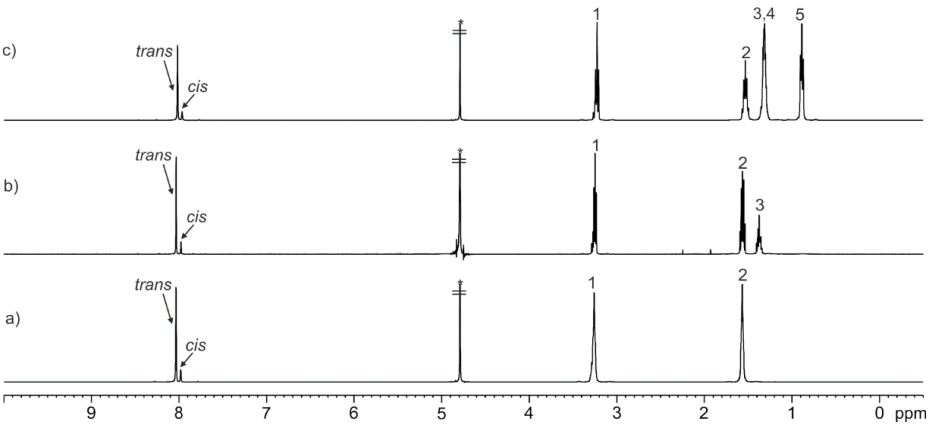

Figure 4.45. ^{1}H NMR (400 MHz, D_2O, 298 K) spectra of: a) **6**; b) **7** and c) **10**. See Figure 4.44 for proton assignments. *Residual solvent peak.

Bis-formamide **6**

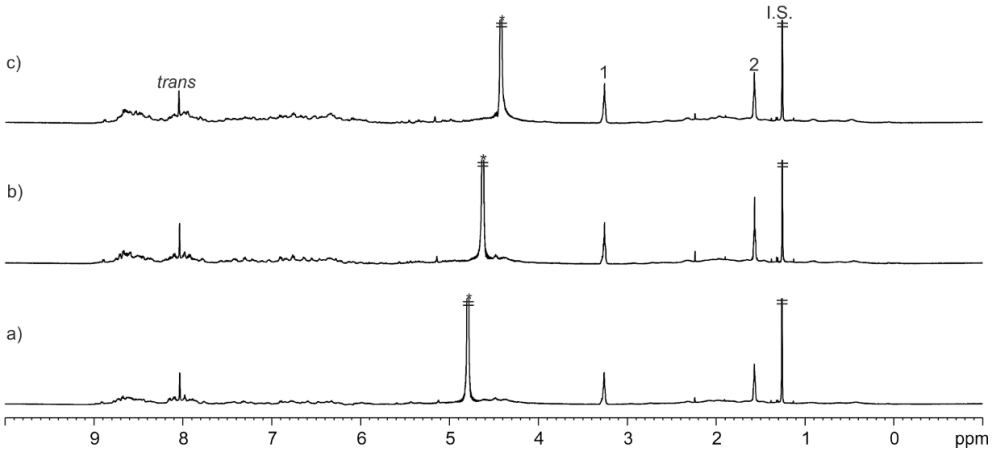

Figure 4.46. VT ^{1}H NMR (500 MHz with cryoprobe, D_2O) spectra of $\mathbf{2}^{4+}$ with *ca.* 1 equiv. of **6**: a) 298; b) 313 and c) 333 K. See Figure 4.44 for proton assignment. *tert*-Butanol (I.S.). *Residual solvent peak.

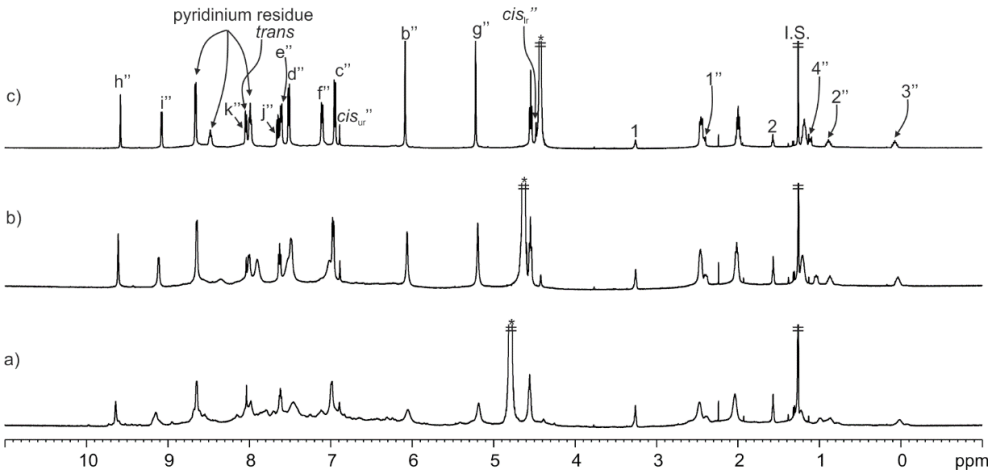

Figure 4.47. VT ^{1}H NMR (500 MHz with cryoprobe, D_2O) spectra of $\mathbf{2}^{4+}$ with *ca.* 1 equiv. of **6** upon the addition of *ca.* 1 equiv. of Pd(II): a) 298; b) 313 and c) 333 K. Doubly primed labels correspond to proton signals of *cis*,*cis*-**6**⊂[**2**•Pd]$^{6+}$. The *cis*,*cis*-**6**⊂[**2**•Pd]$^{6+}$ cage complex was assembled in an extent larger than 60%. See Scheme 4.1 and Figure 4.52 for proton assignments. *tert*-Butanol (I.S.). *Residual solvent peak.

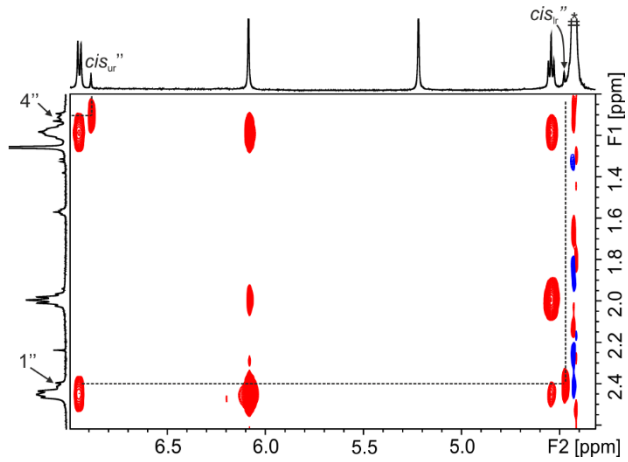

Figure 4.48. Selected region of the ^{1}H-^{1}H ROESY NMR (500 MHz with cryoprobe, D_2O, 333 K, spin lock = 0.3 s) spectrum of [**2**•Pd]$^{6+}$ with *ca.* 1 equiv. of **6**. The ROESY cross-peaks between 1'' and 4'' with the signals at 4.48 and 6.89 ppm, respectively, are highlighted. The observed cross-peaks confirm that the two formamide groups of bound **6** adopt a *cis*-conformation. See Figure 4.52 for proton assignment.

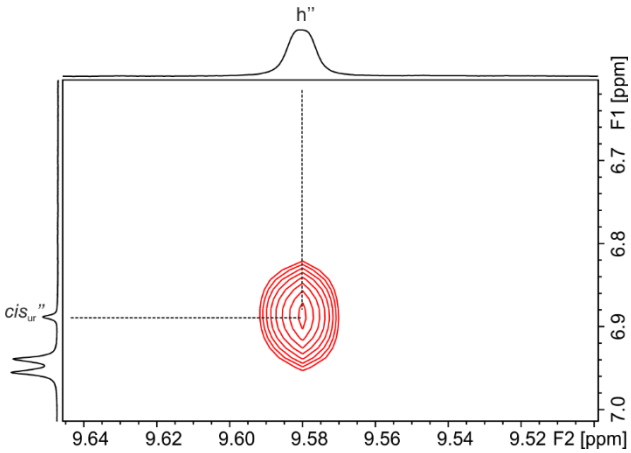

Figure 4.49. Selected region of the ^{1}H-^{1}H ROESY NMR (500 MHz with cryoprobe, D_2O, 333 K, spin lock = 0.3 s) spectrum of [**2**•Pd]$^{6+}$ with *ca*. 1 equiv. of **6**. The ROESY cross-peak between h'' and *cis*$_{ur}$'' is highlighted. The observed cross-peak indicates that one of the formamide groups of bound *cis,cis*-**6** is located in the binding site defined by the inwardly-directed α-pyridyl protons. See Scheme 4.1 and Figure 4.52 for proton assignments.

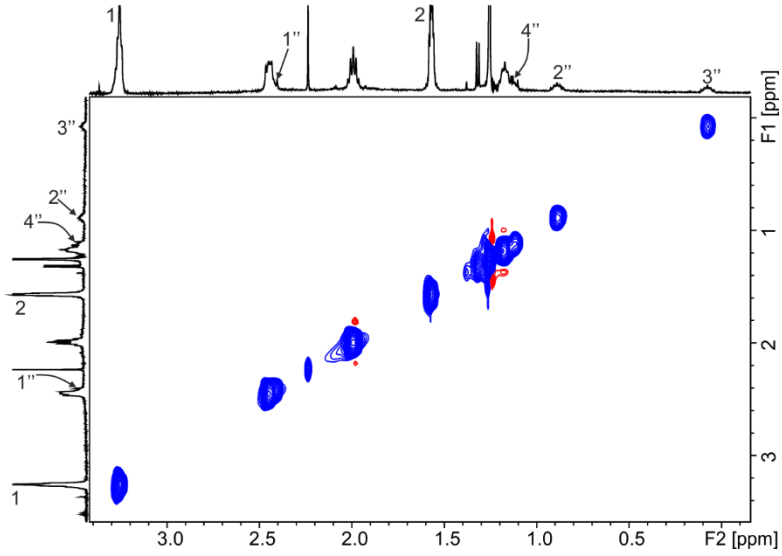

Figure 4.50. Selected region of the ^{1}H-^{1}H EXSY NMR (500 MHz with cryoprobe, D_2O, 333 K, mixing time = 0.3 s) spectrum of [**2**•Pd]$^{6+}$ with *ca.* 2 equiv. of **6**. See Figure 4.44 and Figure 4.52 for proton assignments.

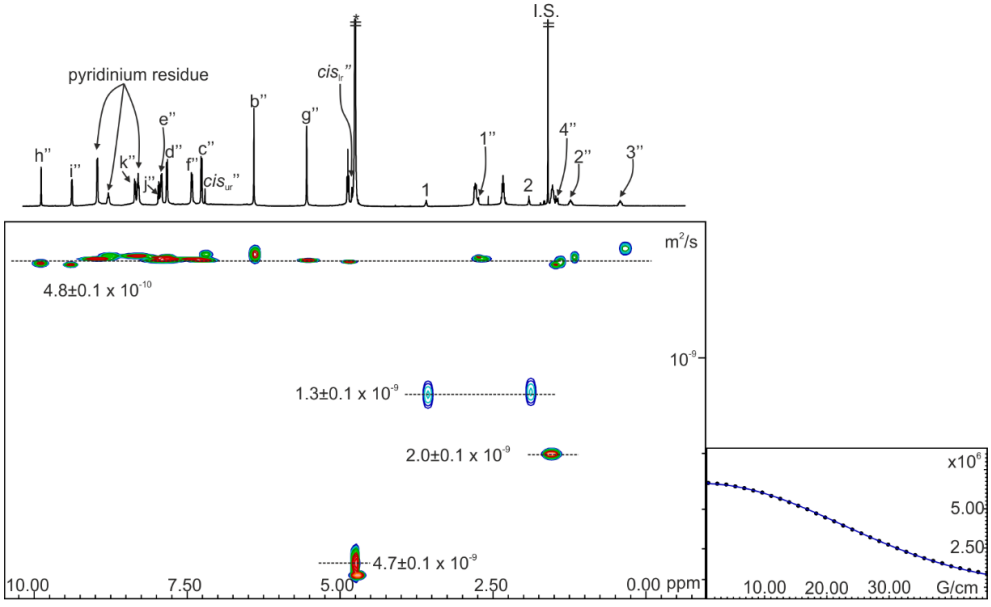

Figure 4.51. left) ^{1}H pseudo 2D DOSY (500 MHz with cryoprobe, D_2O, 333 K, D20 = 0.20 s; P30 = 0.60 ms) of [**2**•Pd]$^{6+}$ with ca. 1 equiv. of **6**. right) Fit of the decay of the signal b'' to a mono-exponential function using Dynamics Center from Bruker. Doubly primed labels correspond to proton signals of *cis,cis*-**6**⊂[**2**•Pd]$^{6+}$. See Scheme 4.1, Figure 4.44 and Figure 4.52 for proton assignments. Errors are indicated as standard deviations. *tert*-Butanol (I.S.). *Residual solvent peak.

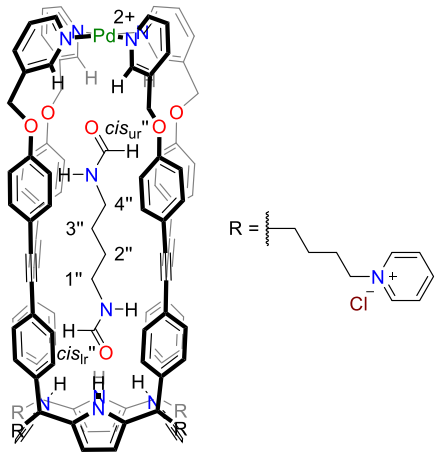

Figure 4.52. Line-drawing structure of the *cis*,*cis*-**6**⊂[**2**•Pd]$^{6+}$ cage complex.

Table 4.5. Experimental chemical shifts of free (δ_{free}) and bound (δ_{bound}) *bis*-formamide **6** and complexation-induced shifts ($\Delta\delta$).

Signal	δ_{free} (ppm)	Signal	δ_{bound} (ppm)	$\Delta\delta$ (ppm)
trans	8.05	-	-	-
cis	8.00	*cis*$_{lr}$''	4.48	-3.52
-	-	*cis*$_{ur}$''	6.89	-1.11
1	3.26	1''	2.41	-0.85
2	1.57	2''	0.89	-0.68
-	-	3''	0.07	-1.50
-	-	4''	1.11	-2.15

Bis-formamide **7**

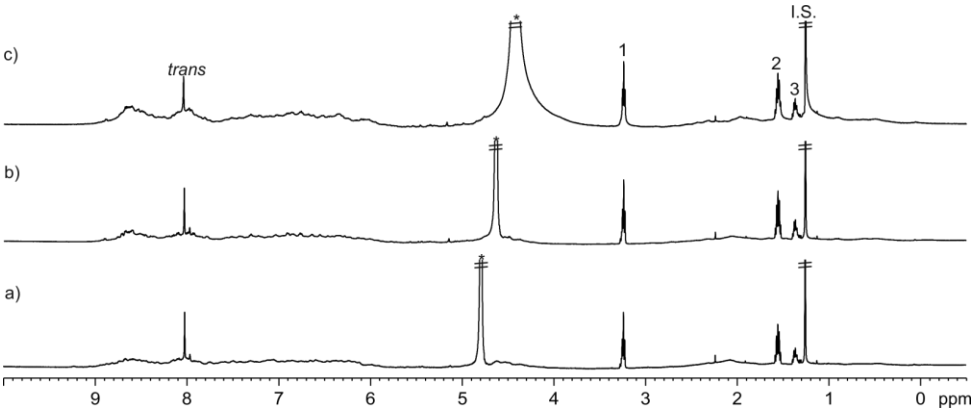

Figure 4.53. VT ^{1}H NMR (500 MHz with cryoprobe, D_2O) spectra of **2**$^{4+}$ with *ca.* 1 equiv. of **7**: a) 298; b) 313 and c) 333 K. See Figure 4.44 for proton assignment. *tert*-Butanol (I.S.). *Residual solvent peak.

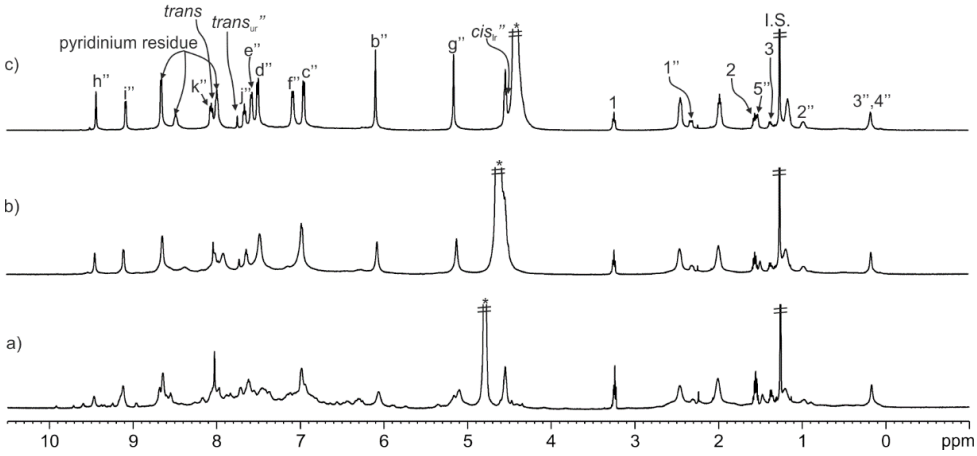

Figure 4.54. VT ^{1}H NMR (500 MHz with cryoprobe, D_2O) spectra of $\mathbf{2}^{4+}$ with *ca*. 1 equiv. of **7** upon the addition of Pd(II): a) 298; b) 313 and c) 333 K. Doubly primed labels correspond to proton signals of *trans*,*cis*-**7**⊂[**2**•Pd]$^{6+}$. The *trans,cis*-**7**⊂[**2**•Pd]$^{6+}$ cage complex was assembled in an extent larger than 60%. See Scheme 4.1 and Figure 4.59 for proton assignments. *tert*-Butanol (I.S.). *Residual solvent peak.

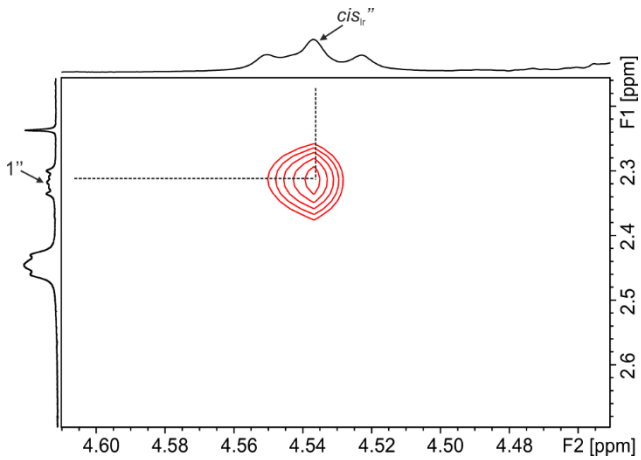

Figure 4.55. Selected region of the ^{1}H-^{1}H ROESY NMR (500 MHz with cryoprobe, D_2O, 333 K, spin lock = 0.3 s) spectrum of [**2**•Pd]$^{6+}$ with *ca.* 1 equiv. of **7**. The ROESY cross-peak between 1'' and the signal at 4.52 ppm is highlighted. The observed cross-peak confirms that one of the formamide groups of bound **7** adopts a *cis*-conformation. See Figure 4.59 for proton assignment.

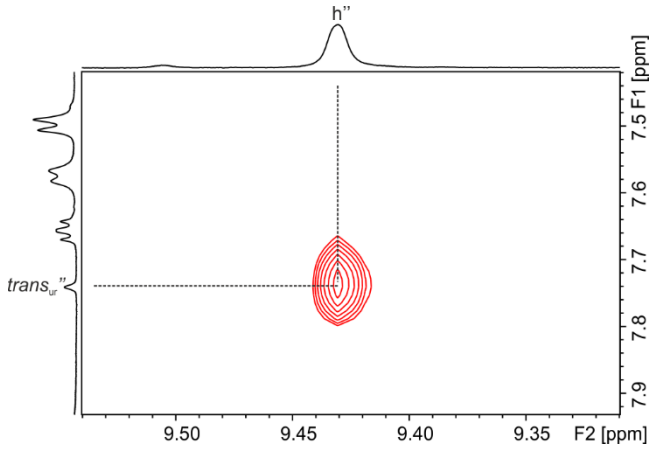

Figure 4.56. Selected region of the ^{1}H-^{1}H ROESY NMR (500 MHz with cryoprobe, D_2O, 333 K, spin lock = 0.3 s) spectrum of [**2**•Pd]$^{6+}$ with *ca.* 1 equiv. of **7**. The ROESY cross-peak between h'' and *trans*$_{ur}$'' is highlighted. The observed cross-peak indicates that one of the formamide groups of bound *trans*,*cis*-**7** is located in the binding site defined by the inwardly-directed *α*-pyridyl protons. See Scheme 4.1 and Figure 4.59 for proton assignments.

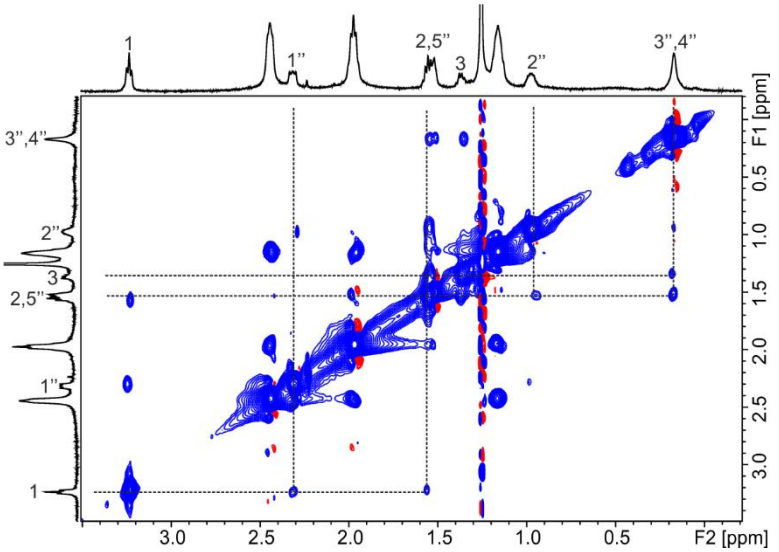

Figure 4.57. Selected region of the ^{1}H-^{1}H EXSY NMR (500 MHz with cryoprobe, D_2O, 333 K, mixing time = 0.3 s) spectrum of [**2**•Pd]$^{6+}$ with *ca.* 1 equiv. of **7**. See Figure 4.44 and Figure 4.59 for proton assignments.

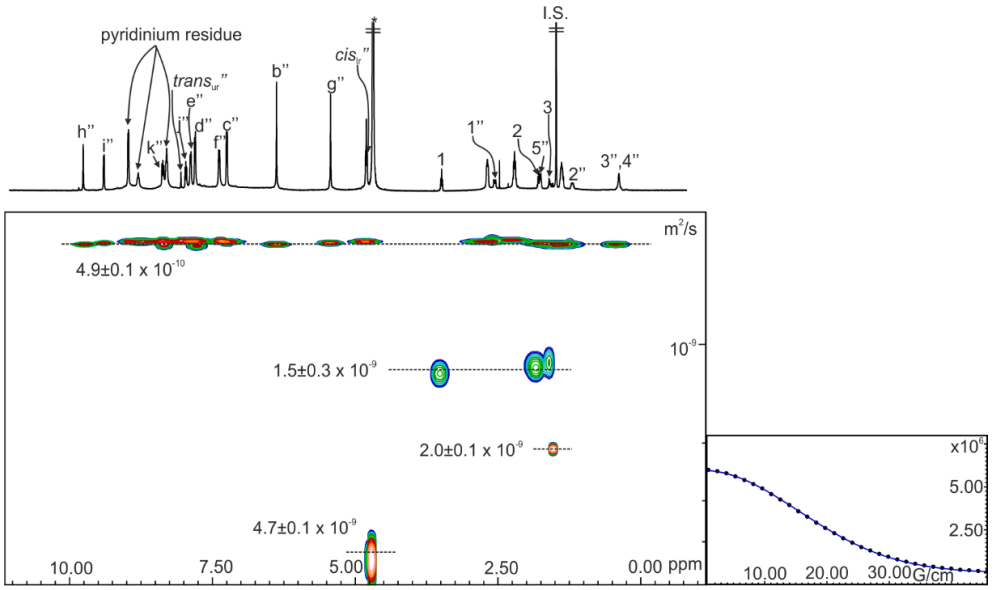

Figure 4.58. left) ^{1}H pseudo 2D DOSY (500 MHz with cryoprobe, D_2O, 333 K, D20 = 0.20 s; P30 = 0.60 ms) of [**2**•Pd]$^{6+}$ with *ca*. 1 equiv. of **7**. right) Fit of the decay of the signal b'' to a mono-exponential function using Dynamics Center from Bruker. Doubly primed labels correspond to proton signals of *trans,cis*-**7**⊂[**2**•Pd]$^{6+}$. See Scheme 4.1, Figure 4.44 and Figure 4.59 for proton assignments. Errors are indicated as standard deviations. *tert*-Butanol (I.S.). *Residual solvent peak.

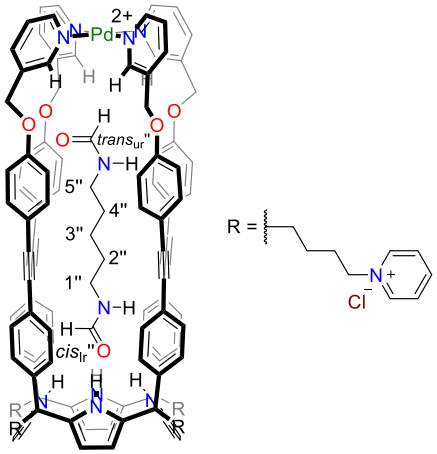

Figure 4.59. Line-drawing structure of the *trans,cis*-**7**⊂[**2**•Pd]$^{6+}$ cage complex.

Table 4.6. Experimental chemical shifts of free (δ_{free}) and bound (δ_{bound}) *bis*-formamide **7** and complexation-induced shifts ($\Delta\delta$).

Signal	δ_{free} (ppm)	Signal	δ_{bound} (ppm)	$\Delta\delta$ (ppm)
trans	8.04	*trans*$_{ur}$''	7.74	-0.30
cis	7.99	*cis*$_{lr}$''	4.52	-3.47
1	3.24	1''	2.31	-0.93
2	1.56	2''	0.98	-0.58
3	1.37	3''	0.17	-1.20
-	-	4''	0.17	-1.39
-	-	5''	1.53	-1.71

Mono-formamide **10**

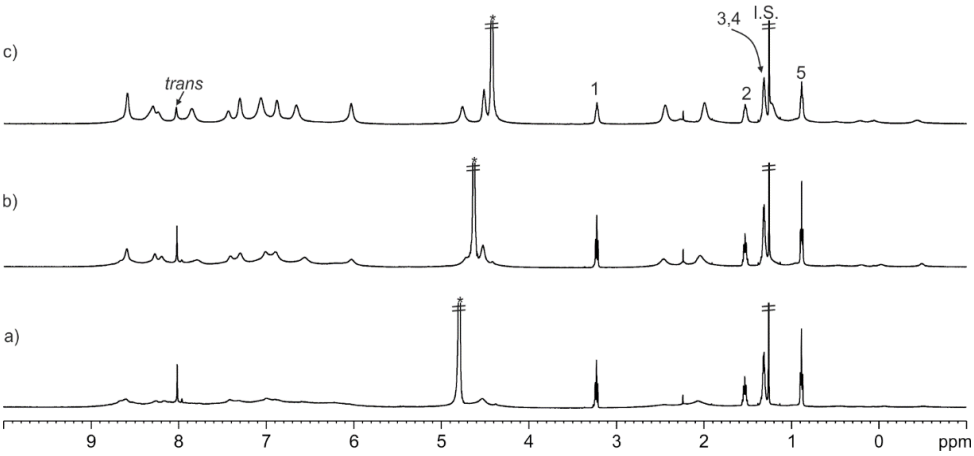

Figure 4.60. VT ^{1}H NMR (500 MHz with cryoprobe, D_2O) spectra of $\mathbf{2}^{4+}$ with *ca.* 1 equiv. of **10**: a) 298; b) 313 and c) 333 K. See Figure 4.44 for proton assignment. *tert*-Butanol (I.S.). *Residual solvent peak.

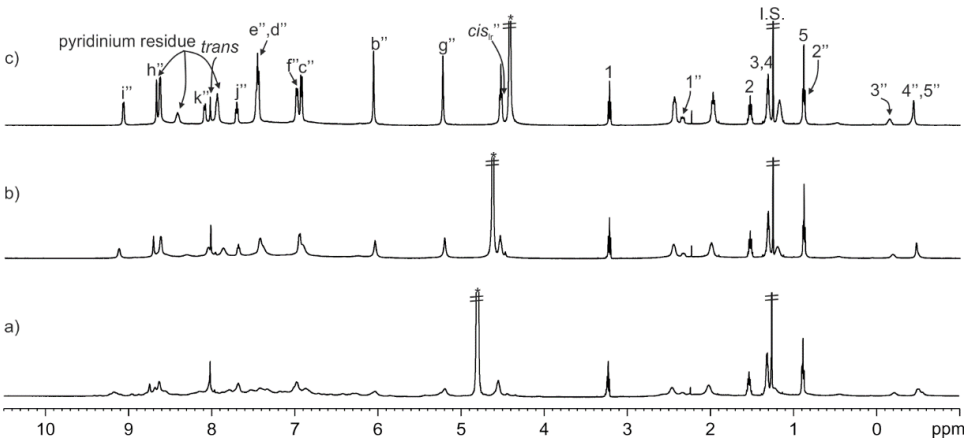

Figure 4.61. VT ^{1}H NMR (500 MHz with cryoprobe, D_2O) spectra of $\mathbf{2}^{4+}$ with *ca.* 1 equiv. of **10** upon the addition of *ca.* 1 equiv. of Pd(II): a) 298; b) 313 and 333 K. Doubly primed labels correspond to proton signals of *cis*-**10**⊂[**2**•Pd]$^{6+}$. The *cis*-**10**⊂[**2**•Pd]$^{6+}$ cage complex was assembled in an extent larger than 60%. See Scheme 4.1 and Figure 4.67 for proton assignments. *tert*-butanol (I.S.). *Residual solvent peak.

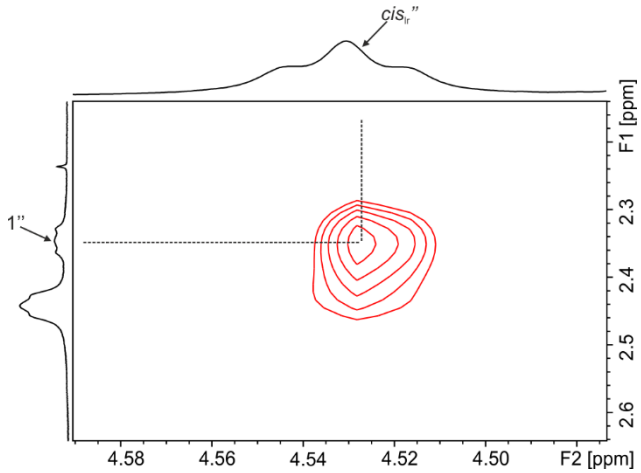

Figure 4.62. Selected region of the ^{1}H-^{1}H ROESY NMR (500 MHz with cryoprobe, D_2O, 333 K, spin lock = 0.3 s) spectrum of [**2**•Pd]$^{6+}$ with *ca.* 1 equiv. of **10**. The ROESY cross-peak between 1'' and the signal at 4.52 ppm is highlighted. The observed cross-peak confirms that the formamide group of bound **10** adopts a *cis*-conformation. See Figure 4.67 for proton assignment.

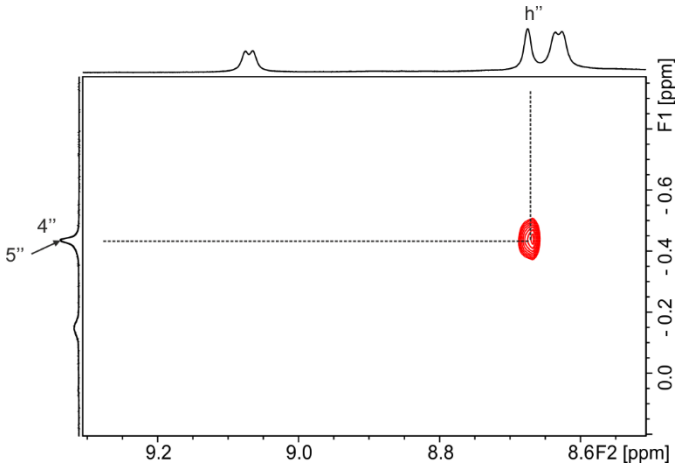

Figure 4.63. Selected region of the ^{1}H-^{1}H ROESY NMR (500 MHz with cryoprobe, D_2O, 333 K, spin lock = 0.3 s) spectrum of [**2**•Pd]$^{6+}$ with *ca.* 1 equiv. of **10**. The ROESY cross-peak between h'' and 5'' is highlighted. The observed cross-peak indicates that the methyl group of bound *cis*-**10** is located in the binding site defined by the inwardly-directed α-pyridyl protons. See Scheme 4.1 and Figure 4.67 for proton assignments.

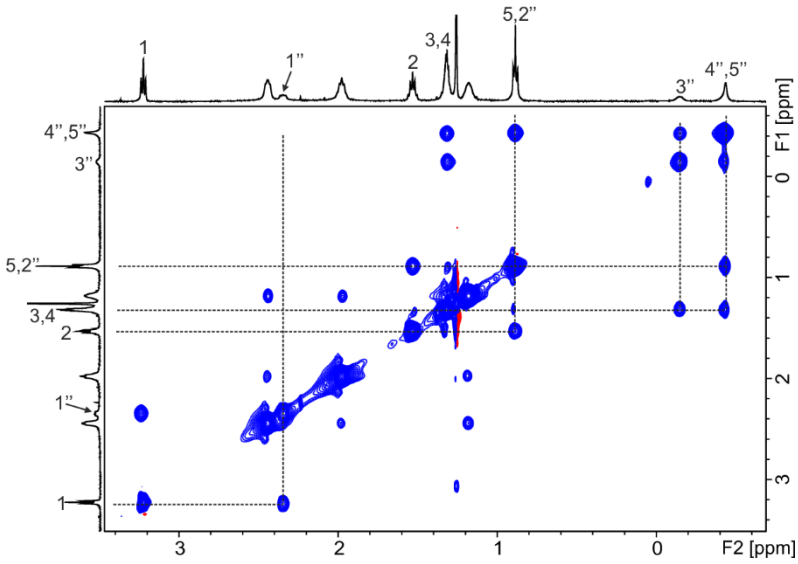

Figure 4.64. Selected region of the ^{1}H-^{1}H EXSY NMR (500 MHz with cryoprobe, D_2O, 333 K, mixing time = 0.3 s) spectrum of [**2**•Pd]$^{6+}$ with *ca.* 1 equiv. of **10**. See Figure 4.67 for proton assignments.

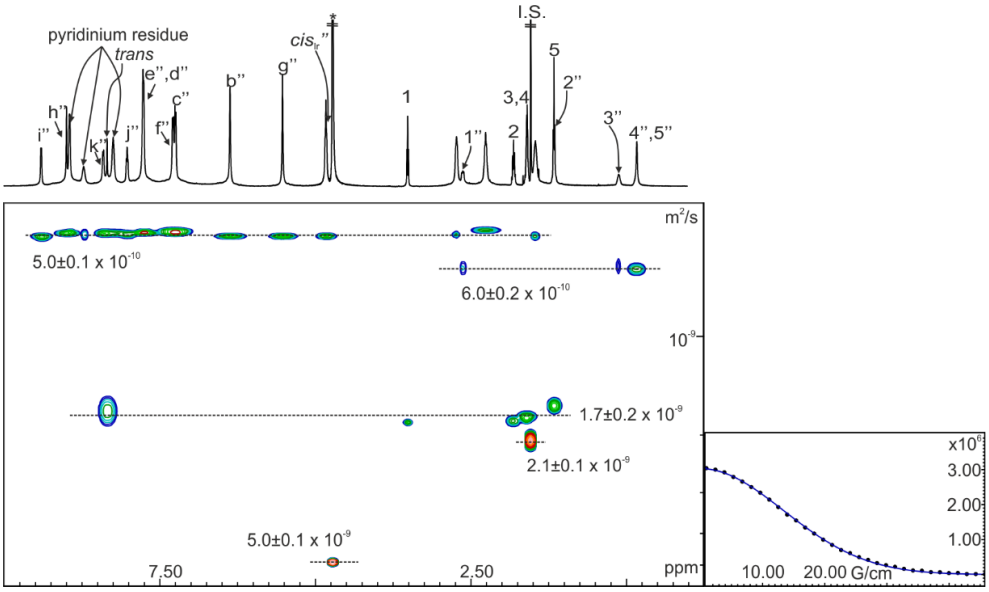

Figure 4.65. left) ^{1}H pseudo 2D DOSY (500 MHz with cryoprobe, D_2O, 333 K, D20 = 0.20 s; P30 = 0.60 ms) of [**2**•Pd]$^{6+}$ with *ca.* 1 equiv. of **10**. right) Fit of the decay of the signal b'' to a mono-exponential function using Dynamics Center from Bruker. Doubly primed labels correspond to proton signals of *cis*-**10**⊂[**2**•Pd]$^{6+}$. See Scheme 4.1, Figure 4.44 and Figure 4.67 for proton assignments. Errors are indicated as standard deviations. *tert*-Butanol (I.S.). *Residual solvent peak.

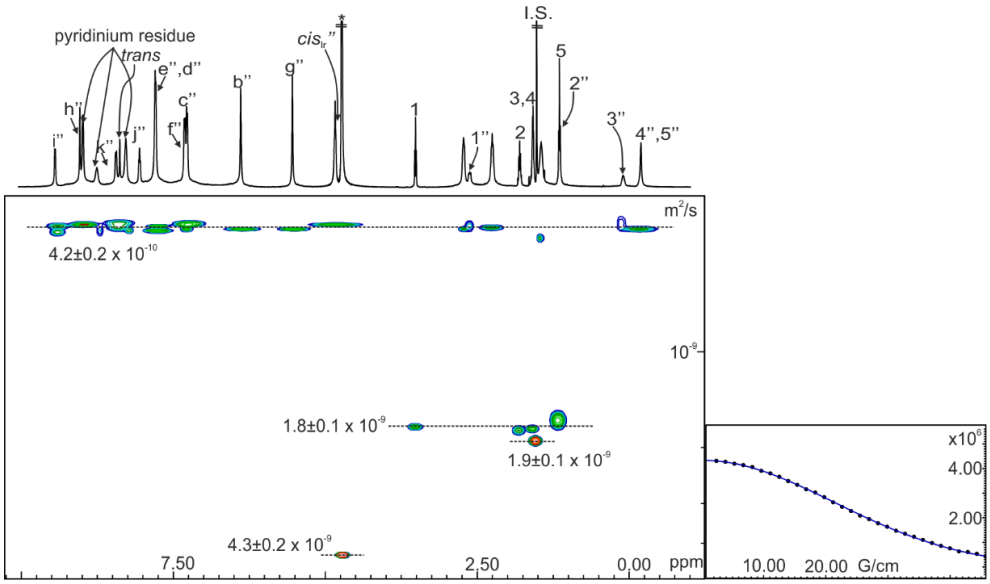

Figure 4.66. left) ^{1}H pseudo 2D DOSY (500 MHz with cryoprobe, D_2O, 333 K, D20 = 0.01 s; P30 = 3.50 ms) of [**2**•Pd]$^{6+}$ with *ca.* 1 equiv. of **10**. right) Fit of the decay of the signal b'' to a mono-exponential function using Dynamics Center from Bruker. Doubly primed labels correspond to proton signals of *cis*-**10**⊂[**2**•Pd]$^{6+}$. See Scheme 4.1, Figure 4.44 and Figure 4.67 for proton assignments. Errors are indicated as standard deviations. *tert*-Butanol (I.S.). *Residual solvent peak.

The diffusion constant value of bound *cis*-**10** differed from those of the [**2**•Pd]$^{6+}$ cage and the free guest **10** in the DOSY experiment with a diffusion time t_d ~ 200 ms (Figure 4.65). On the contrary, the diffusion constant of bound *cis*-**10** coincided with that of the [**2**•Pd]$^{6+}$ cage when the diffusion time was significantly reduced, t_d ~ 10 ms (Figure 4.66). The result obtained with t_d ~ 200 ms indicates that magnetization transfer between bound and free guest molecules occurs during the diffusion time (t_d) in a significant extent.[37]

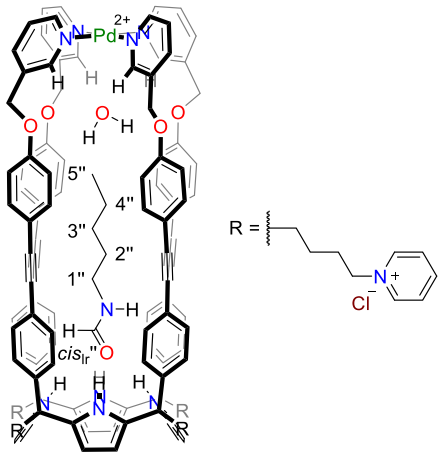

Figure 4.67. Line-drawing structure of the putative [*cis*-**10**•H_2O]⊂[**2**•Pd]$^{6+}$ cage complex.

Table 4.7. Experimental chemical shifts of free (δ_{free}) and bound (δ_{bound}) *mono*-formamide **10** and complexation-induced shifts ($\Delta\delta$).

Signal	δ_{free} (ppm)	Signal	δ_{bound} (ppm)	$\Delta\delta$ (ppm)
trans	8.03	-	-	-
cis	7.98	*cis*$_{Ir}$''	4.52	-3.46
1	3.22	1''	2.35	-0.87
2	1.53	2''	0.88	-0.65
3	1.32	3''	-0.14	-1.46
4	1.32	4''	-0.43	-1.75
5	0.88	5''	-0.43	-1.31

4.4.7 Chemical shifts of the *α*-pyridyl protons in the Pd(II)-cage complexes

Table 4.8. Chemical shifts (*δ*) of the *α*-pyridyl proton signals in the assembled [**2**•Pd]$^{6+}$ cage complexes in D_2O solution at 333 K.

Cage complex	*δ* of signal h'' (ppm)	*δ* of signal i'' (ppm)
5⊂[**2**•Pd]$^{6+}$	9.09	9.05
8⊂[**2**•Pd]$^{6+}$	9.44	9.05
cis,cis-**6**⊂[**2**•Pd]$^{6+}$	9.58	9.07
trans,cis-**7**⊂[**2**•Pd]$^{6+}$	9.43	9.08
cis-**10**⊂[**2**•Pd]$^{6+}$	8.68	9.07

The chemical shifts of the *α*-pyridyl proton signals of tetra-pyridinium SAE-C[4]P tetra-pyridyl ligand **2**$^{4+}$, h'' and i'', upon the addition of *ca.* 1 equiv. of Pd(II) to the equimolar D_2O solution of **2**$^{4+}$ and guest (**5**-**8**,**10**) are in agreement with the formation of pyridyl-Pd(II) coordination bonds.[21]

4.4.8 Displacement of the template in selected cage complexes using the *bis*-*N*-oxide **5** as a competitive binding guest

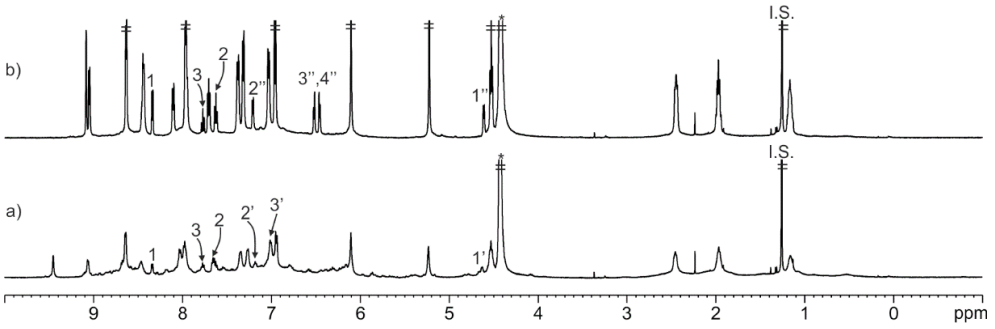

Figure 4.68. ^{1}H NMR (500 MHz with cryoprobe, D_2O, 333 K) spectra of: a) [**2**•Pd]$^{6+}$ with *ca.* 1 equiv. of **8** and b) addition of *ca.* 1 equiv. of **5** to a). Primed labels correspond to proton signals of **8**⊂[**2**•Pd]$^{6+}$. Doubly primed labels correspond to proton signals of **5**⊂[**2**•Pd]$^{6+}$. See Scheme 4.1, Figure 4.41 and Figure 4.37 for proton assignments. *tert*-Butanol (I.S.). *Residual solvent peak.

The **8**⊂[**2**•Pd]$^{6+}$ cage complex was assembled in an extent larger than *ca.* 30%. The addition of *bis*-*N*-oxide **5** to the D_2O solution of **8**⊂[**2**•Pd]$^{6+}$ produced the rapid and quantitative formation of the **5**⊂[**2**•Pd]$^{6+}$ cage complex in an extent larger than *ca.* 60%. Concomitantly, the bound template **8** was released to the bulk solution (Figure 4.68)

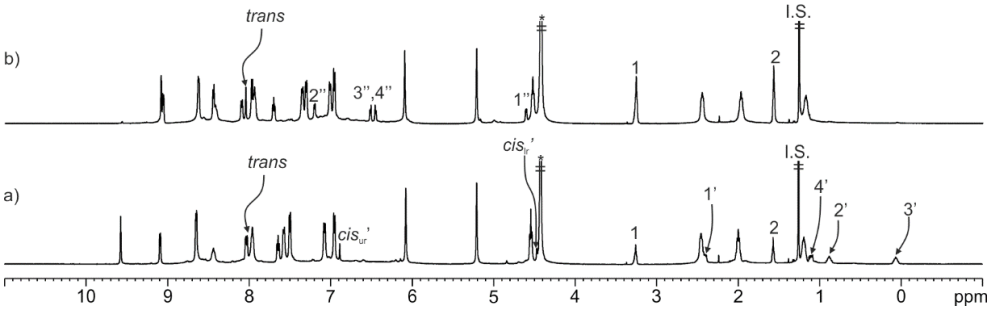

Figure 4.69. ^{1}H NMR (500 MHz with cryoprobe, D_2O, 333 K) spectra of: a) [**2**•Pd]$^{6+}$ with *ca.* 1 equiv. of **6** and b) addition of *ca.* 1 equiv. of **5** to a). Primed labels correspond to proton signals of *cis,cis*-**6**⊂[**2**•Pd]$^{6+}$. Doubly primed labels correspond to proton signals of **5**⊂[**2**•Pd]$^{6+}$. See Scheme 4.1, Figure 4.52 and Figure 4.37 for proton assignments. *tert*-Butanol (I.S.). *Residual solvent peak.

The *cis,cis*-**6**⊂[**2**•Pd]$^{6+}$ cage complex was assembled in an extent larger than *ca.* 60%. The addition of *bis*-*N*-oxide **5** to the D_2O solution of *cis,cis*-**6**⊂[**2**•Pd]$^{6+}$ produced the rapid and quantitative formation of the **5**⊂[**2**•Pd]$^{6+}$ cage complex in an extent larger than *ca*. 60%. Concomitantly, the bound template **6** was released to the bulk solution (Figure 4.69).

4.4.9 Addition of $(CD_3)_2SO$ to the D_2O solutions of ligand **2**$^{4+}$, ligand **2**$^{4+}$ with *bis*-formamide **6** and selected Pd(II)-cage complexes

Tetra-pyridinium SAE-C[4]P tetra-pyridyl ligand **2**$^{4+}$

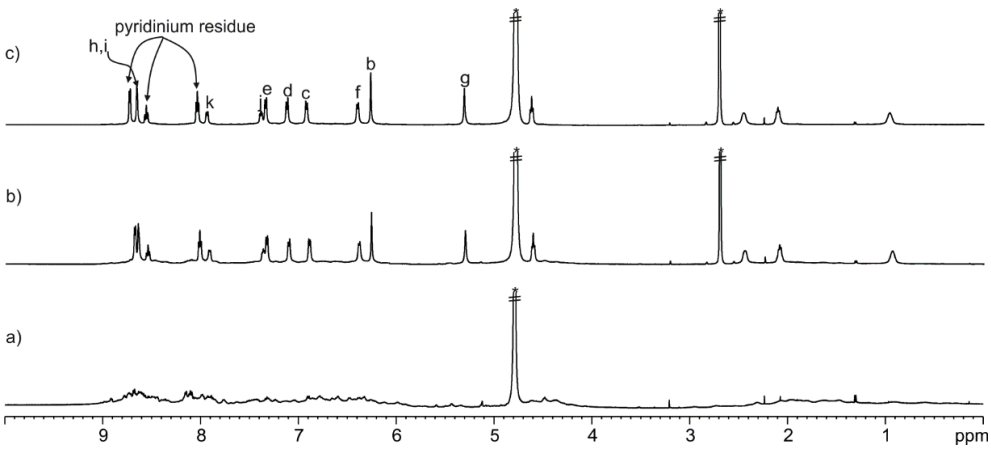

Figure 4.70. ^{1}H NMR (500 MHz with cryoprobe, D_2O, 298 K) spectra of **2**$^{4+}$ upon addition of: a) 0; b) *ca.* 10 and c) *ca*. 20% vol. $(CD_3)_2SO$. See Scheme 4.1 for proton assignment. *Residual solvent peaks.

Tetra-pyridinium SAE-C[4]P tetra-pyridyl ligand **2**$^{4+}$ in 1:9 $(CD_3)_2SO/D_2O$ solution, followed by the addition of Pd(II)

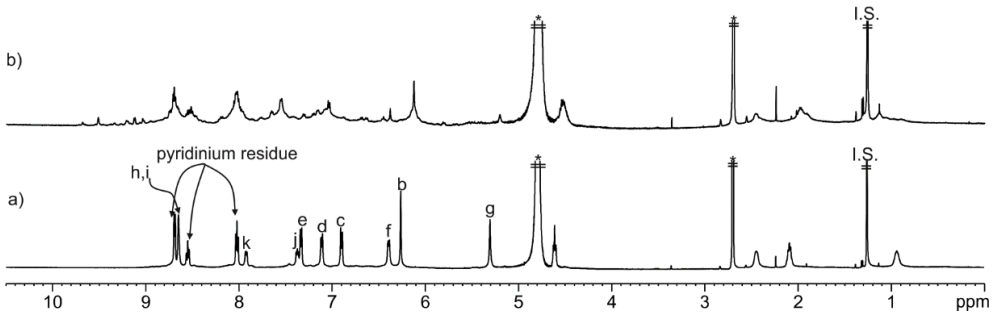

Figure 4.71. ^{1}H NMR (500 MHz with cryoprobe, 1:9 $(CD_3)_2SO/D_2O$, 298 K) spectra of: a) **2**$^{4+}$ and b) **2**$^{4+}$ with *ca*. 1 equiv. of $Pd(NO_3)_2$. See Scheme 4.1 for proton assignment. *tert*-Butanol (I.S.). *Residual solvent peaks.

Tetra-pyridinium SAE-C[4]P tetra-pyridyl ligand **2**$^{4+}$ with *bis*-formamide **6**

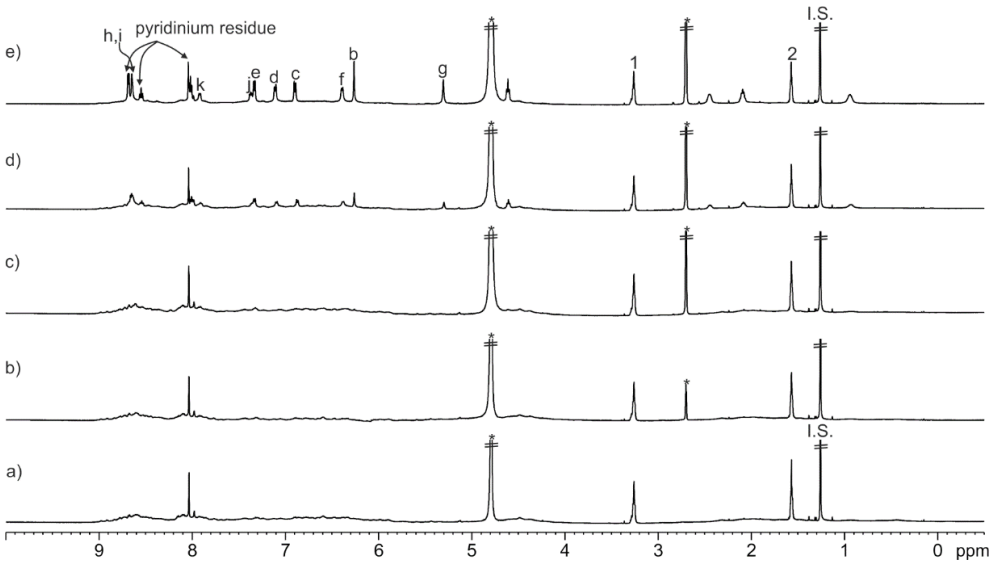

Figure 4.72. ^{1}H NMR (500 MHz with cryoprobe, D_2O, 298 K) spectra of **2**$^{4+}$ with *ca.* 1 equiv. of **6** upon addition of: a) 0; b) *ca.* 1; c) *ca.* 2; d) *ca.* 5 and e) *ca.* 10% vol $(CD_3)_2SO$. See Scheme 4.1 and Figure 4.44 for proton assignments. *tert*-Butanol (I.S.). *Residual solvent peaks.

5⊂[2•Pd]$^{6+}$ cage complex

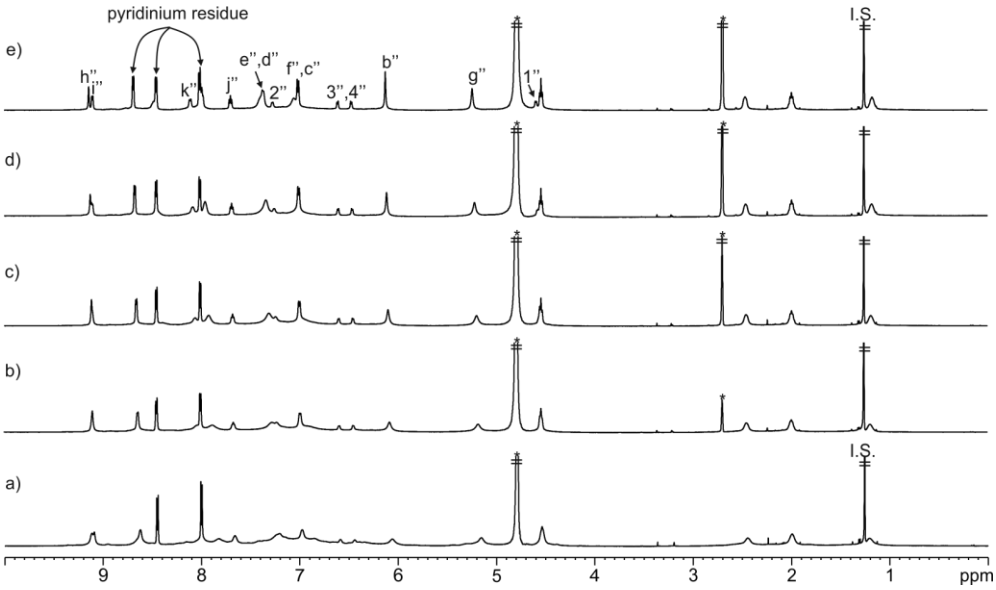

Figure 4.73. ^{1}H NMR (500 MHz with cryoprobe, D_2O, 298 K) spectra of **5**⊂[**2**•Pd]$^{6+}$ upon addition of: a) 0; b) *ca.* 1; c) *ca.* 2; d) *ca.* 5 and e) *ca.* 10% vol. $(CD_3)_2SO$. Doubly primed labels correspond to proton signals of **5**⊂[**2**•Pd]$^{6+}$. See Scheme 4.1 and Figure 4.37 for proton assignments. *tert*-Butanol (I.S.). *Residual solvent peaks.

cis,cis-**6**⊂[**2**•Pd]$^{6+}$ cage complex

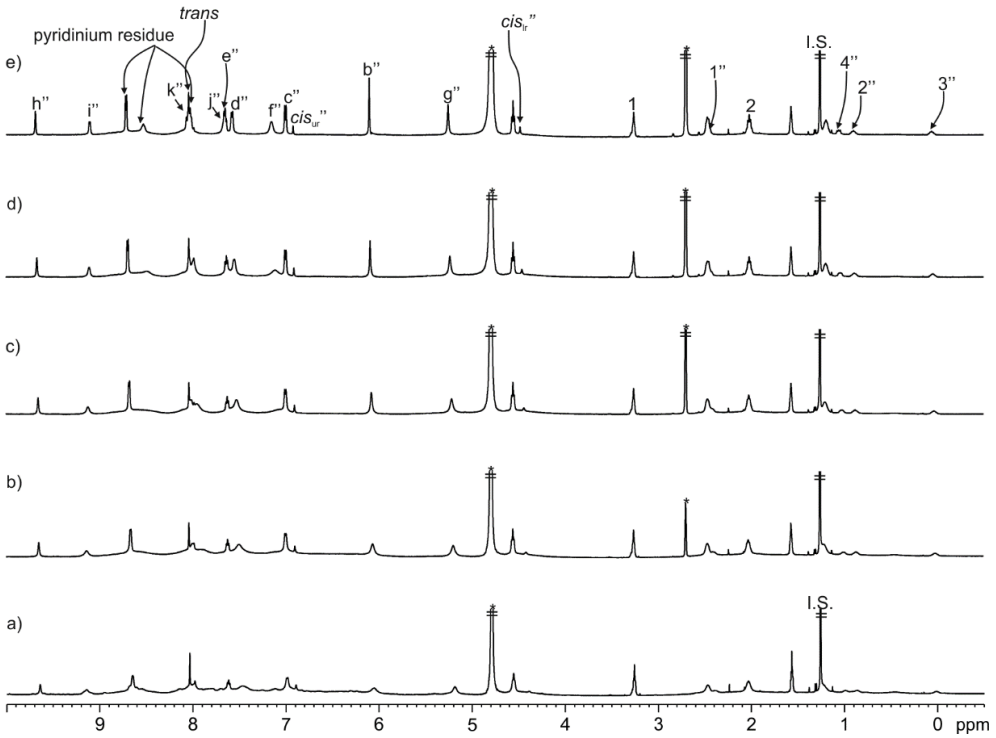

Figure 4.74. ^{1}H NMR (500 MHz with cryoprobe, D_2O, 298 K) spectra of *cis,cis*-**6**⊂[**2**•Pd]$^{6+}$ upon addition of: a) 0; b) *ca*. 1; c) *ca*. 2; d) *ca*. 5 and e) *ca*. 10% vol. $(CD_3)_2SO$. Doubly primed labels correspond to proton signals of *cis,cis*-**6**⊂[**2**•Pd]$^{6+}$. See Scheme 4.1 and Figure 4.52 for proton assignments. *tert*-Butanol (I.S.). *Residual solvent peaks.

cis-**10**⊂[**2**•Pd]$^{6+}$ cage complex

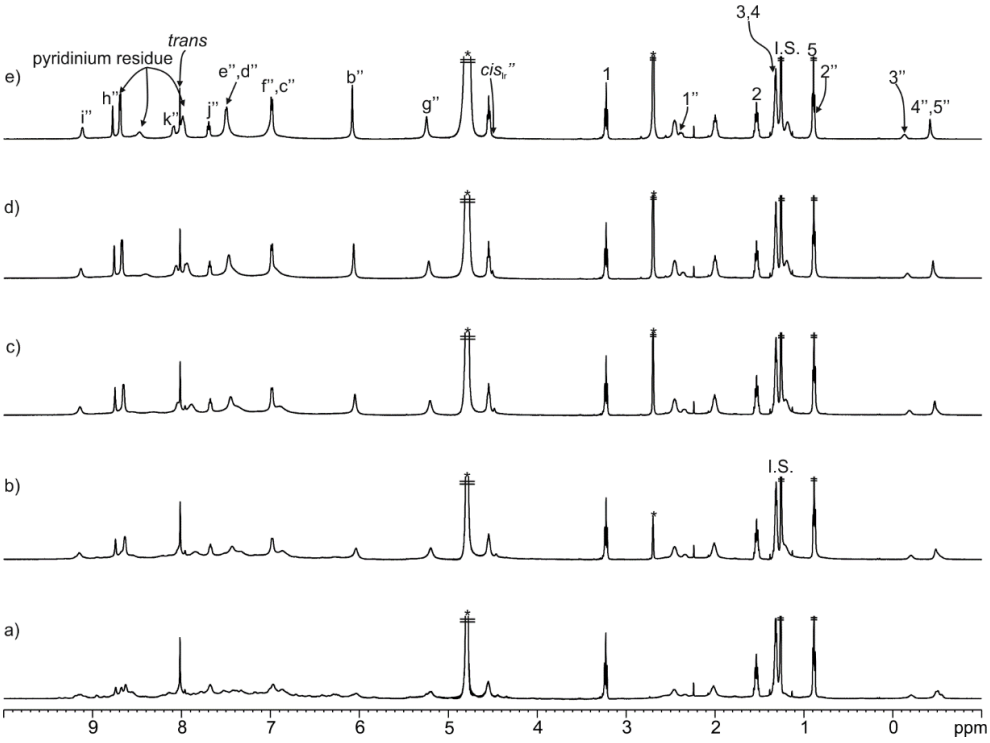

Figure 4.75. ^{1}H NMR (500 MHz with cryoprobe, D_2O, 298 K) spectra of *cis*-**10**⊂[**2**•Pd]$^{6+}$ upon addition of: a) 0; b) *ca.* 1; c) *ca.* 2; d) *ca.* 5 and e) *ca.* 10% vol. $(CD_3)_2SO$. Doubly primed labels correspond to proton signals of *cis*-**10**⊂[**2**•Pd]$^{6+}$. See Scheme 4.1 and Figure 4.67 for proton assignments. *tert*-Butanol (I.S.). *Residual solvent peaks.

The addition of *ca.* 10% of $(CD_3)_2SO$ to the millimolar D_2O solutions of the ligand **2**$^{4+}$ and the Pd(II)-cage complexes, **5**⊂[**2**•Pd]$^{6+}$, *cis*,*cis*-**6**⊂[**2**•Pd]$^{6+}$ and *cis*-**10**⊂[**2**•Pd]$^{6+}$, provoked the sharpening of the proton signals in the NMR spectra at 298 K. These results, together with those obtained using variable-temperature ^{1}H NMR experiments, indicate that the ligand **2**$^{4+}$, as well as the Pd(II)-cage complexes, form ill-defined aggregates in water solution at r.t.

4.4.10 Energy-minimized structures of the Pd(II)-cage complexes

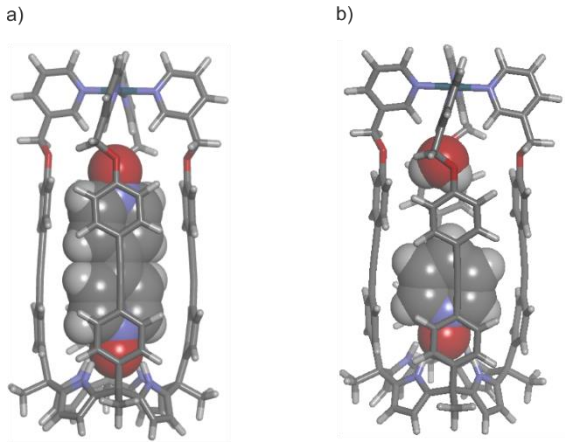

Figure 4.76. Energy minimized structures (MM3) of simplified Pd(II)-cage complexes: a) **5**⊂[**2**•Pd]$^{6+}$ and b) [**8**•H_2O]⊂[**2**•Pd]$^{6+}$. The Pd(II)-cages are depicted in stick representation and the bound guests are shown as CPK models. Water-solubilizing groups were pruned to methyl groups to simplify the calculations.

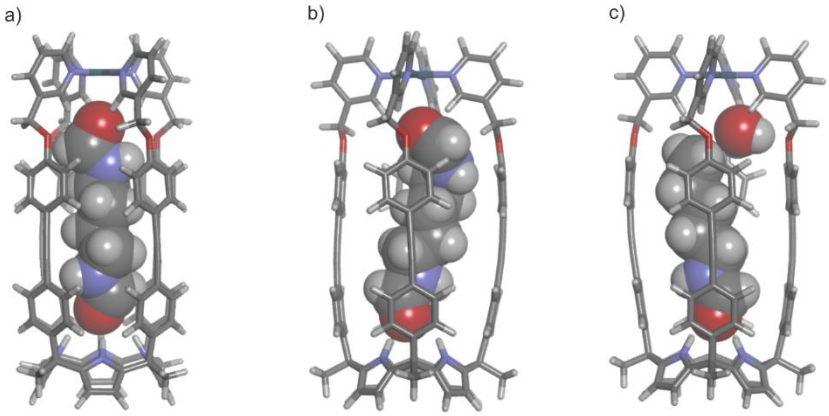

Figure 4.77. Energy minimized structures (MM3) of simplified Pd(II)-cage complexes: a) *cis,cis*-**6**⊂[**2**•Pd]$^{6+}$; b) *trans,cis*-**7**⊂[**2**•Pd]$^{6+}$ and c) [*cis*-**10**•H_2O]⊂[**2**•Pd]$^{6+}$. The Pd(II)-cages are depicted in stick representation and the bound guests are shown as CPK models. Water-solubilizing groups were pruned to methyl groups to simplify the calculations.

4.5 References and Notes

[1] M. Fujita, M. Tominaga, A. Hori and B. Therrien, *Acc. Chem. Res.*, 2005, **38**, 369-378.

[2] R. Chakrabarty, P. S. Mukherjee and P. J. Stang, *Chem. Rev. (Washington, DC, U. S.)*, 2011, **111**, 6810-6918.

[3] E. G. Percástegui, T. K. Ronson and J. R. Nitschke, *Chem. Rev. (Washington, DC, U. S.)*, 2020, **120**, 13480-13544.

[4] A. Galan and P. Ballester, *Chem. Soc. Rev.*, 2016, **45**, 1720-1737.

[5] L. L. K. Taylor, I. A. Riddell and M. M. J. Smulders, *Angew. Chem., Int. Ed.*, 2019, **58**, 1280-1307.

[6] M. Morimoto, S. M. Bierschenk, K. T. Xia, R. G. Bergman, K. N. Raymond and F. D. Toste, *Nat. Catal.*, 2020, **3**, 969-984.

[7] M. Fujita, K. Umemoto, M. Yoshizawa, N. Fujita, T. Kusukawa and K. Biradha, *Chem. Commun. (Cambridge, U. K.)*, 2001, 509-518.

[8] L. Adriaenssens and P. Ballester, *Chem. Soc. Rev.*, 2013, **42**, 3261-3277.

[9] P. M. Bogie, T. F. Miller and R. J. Hooley, *Isr. J. Chem.*, 2019, **59**, 130-139.

[10] M. Tominaga, K. Suzuki, T. Murase and M. Fujita, *J. Am. Chem. Soc.*, 2005, **127**, 11950-11951.

[11] Q.-Q. Wang, S. Gonell, S. H. A. M. Leenders, M. Dürr, I. Ivanović-Burmazović and J. N. H. Reek, *Nat. Chem.*, 2016, **8**, 225-230.

[12] R. Custelcean, J. Bosano, P. V. Bonnesen, V. Kertesz and B. P. Hay, *Angew. Chem., Int. Ed.*, 2009, **48**, 4025-4029.

[13] R. Custelcean, P. V. Bonnesen, N. C. Duncan, X. Zhang, L. A. Watson, G. Van Berkel, W. B. Parson and B. P. Hay, *J. Am. Chem. Soc.*, 2012, **134**, 8525-8534.

[14] S. Yi, V. Brega, B. Captain and A. E. Kaifer, *Chem. Commun. (Cambridge, U. K.)*, 2012, **48**, 10295-10297.

[15] M. C. Young, L. R. Holloway, A. M. Johnson and R. J. Hooley, *Angew. Chem., Int. Ed.*, 2014, **53**, 9832-9836.

[16] L. R. Holloway, P. M. Bogie, Y. Lyon, C. Ngai, T. F. Miller, R. R. Julian and R. J. Hooley, *J. Am. Chem. Soc.*, 2018, **140**, 8078-8081.

[17] C. Ngai, C. M. Sanchez-Marsetti, W. H. Harman and R. J. Hooley, *Angew. Chem., Int. Ed.*, 2020, **59**, 23505-23509.

[18] D. Zhang, T. K. Ronson, J. Mosquera, A. Martinez, L. Guy and J. R. Nitschke, *J. Am. Chem. Soc.*, 2017, **139**, 6574-6577.

[19] D. Zhang, T. K. Ronson, J. Mosquera, A. Martinez and J. R. Nitschke, *Angew. Chem., Int. Ed.*, 2018, **57**, 3717-3721.

[20] D. Yang, L. K. S. von Krbek, L. Yu, T. K. Ronson, J. D. Thoburn, J. P. Carpenter, J. L. Greenfield, D. J. Howe, B. Wu and J. R. Nitschke, *Angew. Chem., Int. Ed.*, 2021, **60**, 4485-4490.

[21] L. Escobar, D. Villarón, E. C. Escudero-Adán and P. Ballester, *Chem. Commun. (Cambridge, U. K.)*, 2019, **55**, 604-607.

[22] S. Peng, Q. He, G. I. Vargas-Zúñiga, L. Qin, I. Hwang, S. K. Kim, N. J. Heo, C.-H. Lee, R. Dutta and J. L. Sessler, *Chem. Soc. Rev.*, 2020, **49**, 865-907.

[23] L. Escobar, E. C. Escudero-Adán and P. Ballester, *Angew. Chem., Int. Ed.*, 2019, **58**, 16105-16109.

[24] L. Escobar and P. Ballester, *Org. Chem. Front.*, 2019, **6**, 1738-1748.

[25] E. A. Meyer, R. K. Castellano and F. Diederich, *Angew. Chem., Int. Ed.*, 2003, **42**, 1210-1250.

[26] D. Dabuleanu, A. Bauza, J. Ortega-Castro, E. C. Escudero-Adan, P. Ballester and A. Frontera, *Molecules*, 2020, **25**, 285.

[27] A. Díaz-Moscoso, D. Hernández-Alonso, L. Escobar, F. A. Arroyave and P. Ballester, *Org. Lett.*, 2017, **19**, 226-229.

[28] The tetra-cationic SAE-C[4]P ligand $\mathbf{2}^{4+}$ was soluble in D_2O at mM concentrations after heating the initial suspension at 50-60 °C for 1 h.

[29] L. Escobar, G. Aragay and P. Ballester, *Chem.--Eur. J.*, 2016, **22**, 13682-13689.

[30] P. Liao, B. W. Langloss, A. M. Johnson, E. R. Knudse, F. S. Tham, R. R. Julian and R. J. Hooley, *Chem. Commun. (Cambridge, U. K.)*, 2010, **46**, 4932-4934.

[31] L. Avram and Y. Cohen, *Chem. Soc. Rev.*, 2015, **44**, 586-602.

[32] Based on the diffusion constant previously reported for [**1a**•Pd]$^{2+}$ in DMSO at 298 K, [*D* (DMSO) × *η* (DMSO)]/298 K ~ [*D* (D_2O) × *η* (D_2O)]/333 K, where *η* is the viscosity. This indicates that [**1a**•Pd]$^{2+}$ and [**2**•Pd]$^{6+}$ feature similar dimensions.

[33] Note that the ^{1}H NMR spectrum of the **5**⊂[**2**•Pd]$^{6+}$ cage complex was acquired at 333 K. The proton signals of this cage complex, and those discussed below, appeared broad at 298 K. However, the addition of *ca.* 10% DMSO to the D_2O solution of selected cage complexes provoked the sharpening of the proton signals and their coincidence with those observed at 333 K. Despite the increase of the overall charge in the assembled species upon the coordination of Pd(II), the cage complexes form water-soluble high-order aggregates at 298 K.

[34] Q. Sun, L. Escobar, P. Ballester, *Angew. Chem., Int. Ed.* **2021**, *60*, 10359-10365.

[35] The ^{1}H NMR spectrum at 333 K of the equimolar D_2O solution of the SAE-C[4]P **2**$^{4+}$ and the *bis*-formamide, **6** or **7**, showed broad proton signals for the receptor. However, we cannot rule out the formation of the 1:1 inclusion complex to a reduced extent (< 10^4 M).

[36] L. Escobar, A. Díaz-Moscoso and P. Ballester, *Chem. Sci.*, 2018, **9**, 7186-7192.

[37] L. Escobar, Y.-S. Li, Y. Cohen, Y. Yu, J. Rebek Jr and P. Ballester, *Chem.--Eur. J.*, 2020, **26**, 8220-8225.

[38] L. Escobar and P. Ballester, *Chem. Rev.*, 2021, **121**, 2445-2514.

[39] The *N*-pentyl formamide **9** is bound to SAE-C[4]P **1b** featuring an apparent binding constant value K_{app} ~ 3 × 10^3 M^{-1} in $CDCl_3$ (298 K) and 7 × 10^2 M^{-1} in 2:1 $CDCl_3$/CD_3CN (233 K).

[40] M. D. Pluth, R. G. Bergman and K. N. Raymond, *J. Org. Chem.*, 2008, **73**, 7132-7136.

[41] H. Takezawa, K. Shitozawa and M. Fujita, *Nat. Chem.*, 2020, **12**, 574-578.

[42] G. R. Fulmer, A. J. M. Miller, N. H. Sherden, H. E. Gottlieb, A. Nudelman, B. M. Stoltz, J. E. Bercaw and K. I. Goldberg, *Organometallics*, 2010, **29**, 2176-2179.

UNIVERSITAT ROVIRA I VIRGILI
ARYL AND SUPER ARYL-EXTENDED CALIX[4]PYRROLES: SYNTHESIS AND APPLICATIONS
Qingqing Sun

Chapter 5

Metallocavitands Derived from an Oxazolo[4,5-*b*]pyrazinyl Substituted Super Aryl-Extended Calix[4]pyrrole

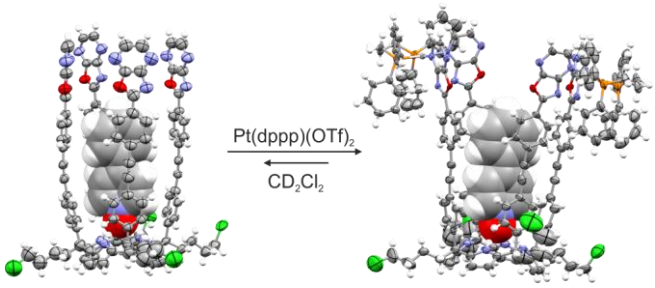

Unpublished results

UNIVERSITAT ROVIRA I VIRGILI
ARYL AND SUPER ARYL-EXTENDED CALIX[4]PYRROLES: SYNTHESIS AND APPLICATIONS
Qingqing Sun

5.1 Introduction

Metal-coordination has emerged as an attractive tool for the construction of diverse self-assembled molecular containers.[1,2,3] One subset of these, metallocavitand complexes, were exploited in the molecular recognition,[4,5] stabilization of reactive species,[6] sensing[7] and catalysis[8,9]. The strategy of metal-ligand self-assembly frequently yields concave and bowl-shaped metallic complexes with deep cavities. The final structure of the assembly will depend on the covalent characteristics of the ligands and the coordination geometry of the metal centers.[10,11] Pt(II)-metallocavitands/cages based on pyridyl ligands are thermodynamically and kinetically more stable than its *N*-Pd(II) counterparts. This is due to the superior strength of the pyridyl *N*-Pt(II) coordination bonds.[12,10,13] The elaboration of the organic ligands through its incorporation in concave scaffolds[14,15,16] represents an efficient strategy for the construction of metal-assemblies capable of guests encapsulation and selective catalysis.

Rebek and co-workers reported resorcin[4]arene cavitand derivatives featuring four quinoxaline walls that were soluble in water solution and organic solvents depending on the characteristics of their feet (lower rim substituents). The coordination of two equivalents of Pd(II) salt to the quinoxaline walls of the cavitands yielded bis-metallo-cavitands with C_{2v} symmetry. The metal coordination step rigidified the receptive vase conformation of the cavitand and enhanced its guest binding properties.[17] The high binding affinity of the water soluble metallocavitand towards primary and secondary alkyl dihalides enforced the almost exclusive formation of the mono-reacted product in the radical reduction reaction mediated by trialkylsilanes.[9,18] Selective guest encapsulation was reported by de Mendoza and co-workers using rhenium coordinated metallocavitands derived from calix[4]arene scaffolds.[19] Typically, the reported metallocavitands lack of polar binding sites in their inner cavities. This characteristic makes them unsuitable for molecular recognition studies with polar substrates.

In this section, we report the template self-assembly of a C_{2v} symmetric metallocavitand starting from a tetra-oxazolo[4,5-*b*]pyrazinyl substituted super aryl-extended calix[4]pyrrole (SAE-C[4]P, **1**) (Scheme 5.1). We use a series of polar guests, *N*-oxides and aliphatic formamide derivatives, as templates for the assembly process. The addition of *ca*. 2 equiv. of a Pt(II) salt precursor to the SAE-C[4]P **1** resulted in the quantitative assembly of a bis-metallocavitand featuring a large polar aromatic cavity. We investigated the displacement of the encapsulated guests in the assembled metallocavitands by means of competitive binding experiments with 4-phenyl pyridine *N*-oxide **4**. Based on the observed kinetics, we proposed the existence of a “French doors” or “constrictive binding” mechanism for the in/out exchange of the bound guests.

5.2 Results and Discussion

The tetra-α isomer of the super aryl-extended calix[4]pyrrole (SAE-C[4]P) **1** was synthesized by quadruple Sonogashira coupling of 2-(4-ethynylphenyl)oxazolo[4,5-

b]pyrazine **2** with tetra-α 4-iodophenyl C[4]P **3**[20]. SAE-C[4]P **1** was isolated in 60% yield after column chromatography purification of the reaction crude. Compound **1** and its synthetic precursors were fully characterized by a complete set of high-resolution spectra (see Experimental Section).

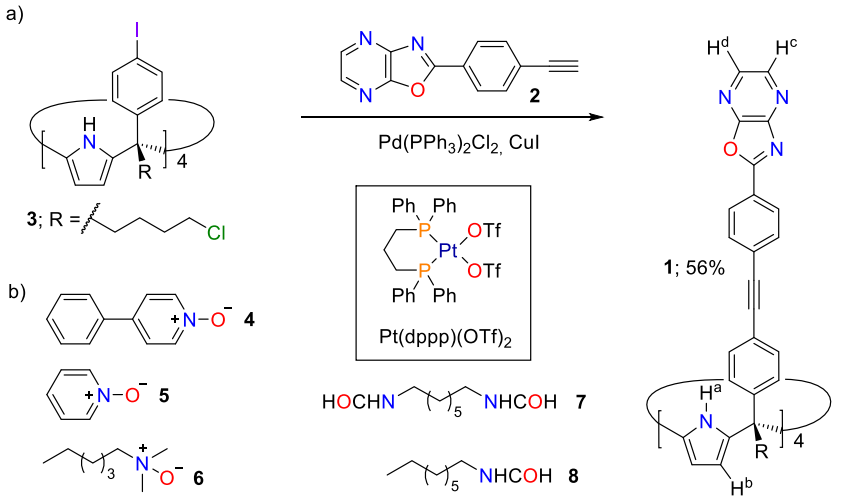

Scheme 5.1. a) Synthesis of tetra-oxazolo[4,5-*b*]pyrazinyl SAE-C[4]P ligand **1**. b) Line-drawing structures of template guests **4**-**8** and Pt(dppp)$(OTf)_2$.

Initially, we studied the coordination of $[Pt(dppp)]^{2+}$ with the SAE-C[4]P ligand **1** in CD_2Cl_2 solution using ^{1}H NMR spectroscopy. The ^{1}H NMR spectrum of a millimolar solution of ligand **1** showed sharp and well-defined proton signals in agreement with C_{4v} symmetry. The incremental addition of $[Pt(dppp)]^{2+}$ to the above solution produced ^{1}H NMR spectra displaying multiple proton signals (Figure 5.12). This observation indicated that ligand **1** and $[Pt(dppp)]^{2+}$ failed to assemble into a metallocavitand $[\mathbf{1}\bullet Pt_n(dppp)_n]^{2n+}$, but rather produced ill-defined polymeric aggregates. Based on this result, we surmised that the polymerization phenomena experienced by ligand **1** was due to its presence in solution mainly in alternate conformations.[21] In CD_2Cl_2 solution, the reduced amount of **1** adopting the cone conformation, if any, prevented the assembly of the metallocavitand. The chelation of the Pt(II) metal centers by the nitrogen atom of adjacent pyrazinyl walls of SAE-C[4]P **1** requires the existence of ligand **1** in cone conformation. We showed previously that Pd(II) coordination cages were assembled in organic solvents[12] only when 1:1 inclusion complexes of a SAE-C[4]P tetra-pyridyl ligand and pyridine *N*-oxides were used as precursors. The 1:1 inclusion complexes locked the SAE-C[4]P in the cone conformation. In this conformation, the four pyridyl residues at the upper rim of the SAE-C[4]P ligand were pre-organized to coordinate with the Pd(II) ion. Because the multitopic coordination step of the metal center involved in the closing of the aromatic cavity of the assembled cage, the encapsulated guest should satisfy the hydrogen

bonding demands of the formed binding site or allow the co-encapsulation of another guest to play this role.

Based on our previous findings, we investigated the use of *N*-oxides **4-6** (see Scheme 5.1 for molecular structures) in the assembly of $[\mathbf{1}\bullet Pt_n(dppp)_n]^{2n+}$ metallocavitands. At 298 K, the ^{1}H NMR spectrum of a 1 mM CD_2Cl_2 solution of **1** containing *ca*.1 equiv. of 4-phenyl-pyridine-*N*-oxide, **4**, displayed sharp proton signals for both binding partners (Figure 5.1b). Specifically, the pyrrole NHs of **1** moved downfield ($\Delta\delta$ = +2.45 ppm) compared to those of the free ligand. This observation indicated their involvement in hydrogen bonding interactions, probably with the oxygen atom of **4**. At the same time, the proton signals of **4** appeared upfield shifted with respect to those of free **4** in solution. The observed upfield shifts located **4** in the aromatic cavity of **1** where they were experiencing the anisotropic shielding caused by the four walls of the SAE-C[4]P. The addition of more than 1 equiv. of **4** produced a separate set of proton signals that corresponded with those of the free guest. Taken together, these results supported the quantitative formation of the 1:1 inclusion complex, **4⊂1**, in the equimolar mixture. The **4⊂1** complex featured slow exchange dynamics with free **4** on the ^{1}H NMR chemical time scale. We estimated that the binding constant of the **4⊂1** complex is larger than 10^4 M^{-1}. Notably, a 2D-EXSY experiment performed on the above solution revealed that the guest's exchange was fast on the EXSY time scale (t_{mix} = 0.3 s) (Figure 5.16).

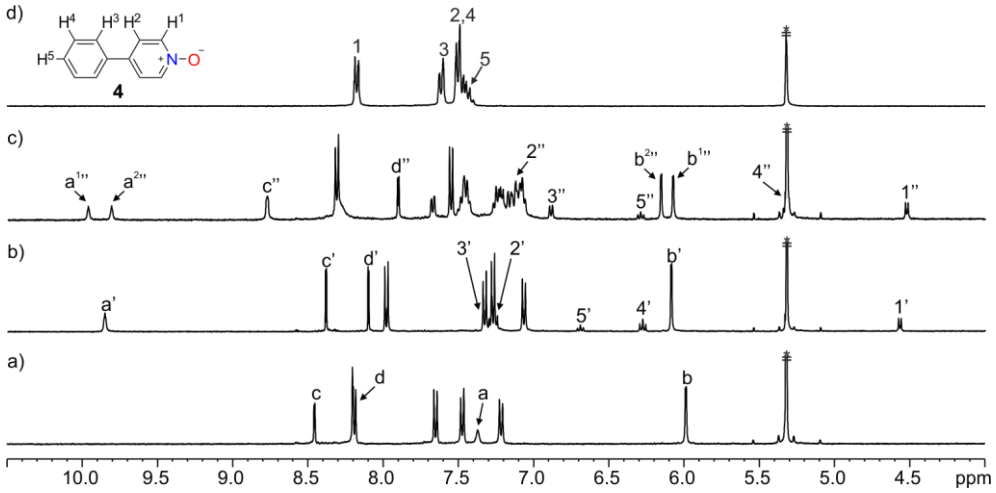

Figure 5.1. Selected region of the ^{1}H NMR (400 MHz, CD_2Cl_2, 298 K) spectra of: a) **1**; b) **4⊂1**; c) **4⊂**$[\mathbf{1}\bullet Pt_2(dppp)_2]^{4+}$ and d) **4**. Primed and doubly primed labels correspond to the proton signals of **4⊂1** and **4⊂**$[\mathbf{1}\bullet Pt_2(dppp)_2]^{4+}$, respectively. See Scheme 5.1 for proton assignment of bound **1**. *Residual solvent peak.

The inclusion **4⊂1** complex was also characterized by X-ray diffraction of a single crystal grown from CH_2Cl_2 solution (Figure 5.2) The solution of the diffracted data revealed that in the solid state the *N*-oxide **4** was deeply included in the aromatic cavity of SAE-C[4]P **1**. In

the **4⊂1** complex, four hydrogen-bonding interactions are established between the pyrrole NHs of **1** and the oxygen atom of the *N*-oxide **4**, $d_{average}$ (N···O) ~ 2.9 Å. Moreover, the aromatic cavity of the upper rim of **1** collapses owing to the establishment of intermolecular CH-π and π-π interactions.

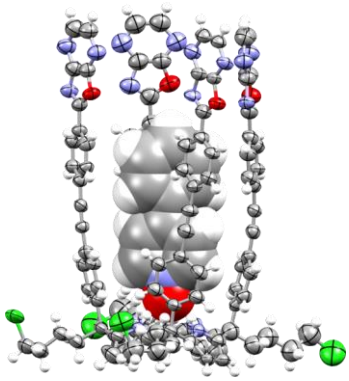

Figure 5.2. X-ray crystal structure of **4⊂1** complex. The receptor is shown in ORTEP view with thermal ellipsoids set at 50% probability. Hydrogen atoms are shown as fixed-size spheres of 0.3 Å radius. The bound guest is shown as CPK model.

Next, the addition of *ca*. 1 equiv. of the Pt(dppp)$(OTf)_2$ to the equimolar solution of ligand **1** and **4** in CD_2Cl_2 produced a ^{1}H NMR spectrum showing multiple sets of proton signals including those of the initial **4⊂1** complex (Figure 5.18). Gratifyingly, the addition of *ca*. 2 equiv. of the $[Pt(dppp)]^{2+}$ simplified the ^{1}H NMR spectrum. The proton signals of the inclusion complex **4⊂1** disappeared and a new set of sharp and well-resolved signals emerged. We assigned the new set of signals to the two bound components in a new inclusion complex (Figure 5.1c). Interestingly, one of the aromatic protons of the pyrazinyl group of the bound ligand **1** moved downfield (H^c, $\Delta\delta$ = +0.39 ppm) and the other upfield (H^d, $\Delta\delta$ = -0.20 ppm), in comparison to those observed in the **4⊂1** complex. The chemical shift change of the H^c proton are consistent with the formation of pyrazinyl *N*-Pt(II) coordination bond, as reported in the literature.[17] The NHs and ß-pyrrole protons H^a and H^b, together with the aromatic protons of the bound ligand **1** in the new complex, experienced reduced chemical shift changes but all of them split into two sets of signals. We also observed that the methylene protons of the bis-phosphine ligand of the metal precursor (dppp) moved downfield and resonated in the 3.79-3.05 ppm region. The protons of the phenyl groups of bis-phosphine ligand overlapped with the aromatic signals of the bound ligand **1** and moved upfiled. Taken in concert, these observations indicated that the calix[4]pyrrole **1** maintains the cone conformation in the new complex. The number of signals observed for the complex is in agreement with C_{2v} symmetry, suggesting the coordination of only two $[Pt(dppp)]^{2+}$ units. In short, two adjacent oxazolo[4,5-*b*]pyrazinyl

panels bind one $[Pt(dppp)]^{2+}$ unit affording the quantitatively assembly of the metallocavitand complex, **4**⊂[**1**•$Pt_2(dppp)_2]^{4+}$.The addition of more than 2 equiv of $[Pt(dppp)]^{2+}$ did not induce chemical shift changes to the protons of the metallocavitand complex, **4**⊂[**1**•$Pt_2(dppp)_2]^{4+}$ (Figure 5.20). The addition of more than 1 equiv. of *N*-oxide **4** to the above solution induced the emergence of the proton signals corresponding to free **4**. Again, no chemical shift changes were observed for the proton signals of the metallocavitand complex. These results indicated that the stoichiometry of the metallocavitand complex **4**⊂[**1**•$Pt_2(dppp)_2]^{4+}$ was not altered by the existence of an excess of the metal or the *N*-oxide guest. It is worth noting here, that the chemical exchange between free and bound *N*-oxide in the **4**⊂[**1**•$Pt_2(dppp)_2]^{4+}$ metallocavitand complex displayed slow dynamics not only on the ^{1}H NMR time scale but also in the EXSY counterpart (t_{mix} = 0.3 s). The quantitative formation of **4**⊂[**1**•$Pt_2(dppp)_2]^{4+}$ metallocavitand complex in an equimolar mixture at 1 mM concentration allowed us to estimate its binding constant as K_a (**4**⊂[**1**•$Pt_2(dppp)_2]^{4+}$) > 10^4 M^{-1}.

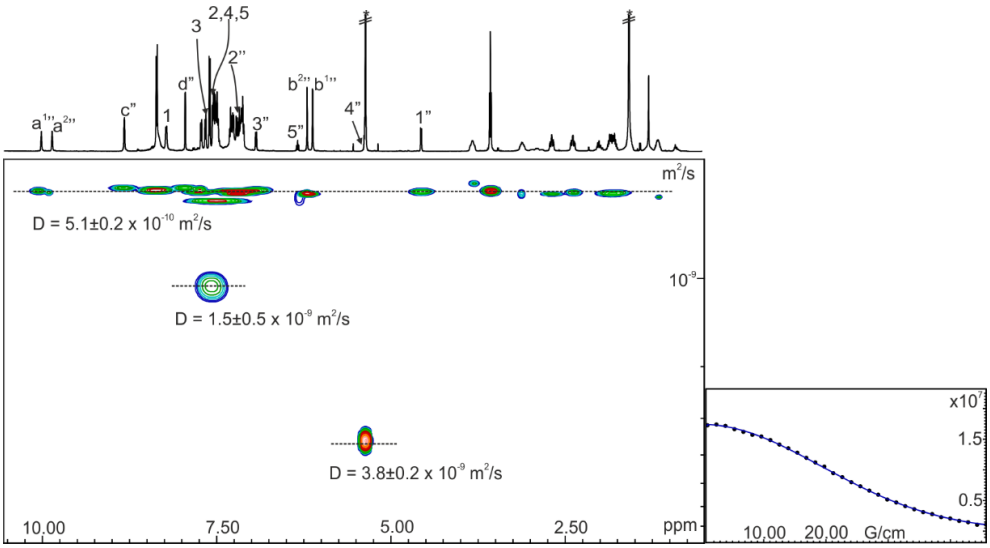

Figure 5.3. (left) ^{1}H pseudo 2D plot of DOSY (500 MHz with cryoprobe, CD_2Cl_2, 298 K, D20 = 0.01 s; P30 = 3.5 ms) of ligand **1** with 4-phenylpyridine *N*-oxide **4** and $Pt(dppp)(OTf)_2$ (*ca.* 1:2:2 ratio). (right) Fit of the decay of the signal $b^{2''}$ to a mono-exponential function using Dynamics Center from Bruker. Double primed labels correspond to proton signals of **4**⊂[**1**•$Pt_2(dppp)_2]^{4+}$. See Scheme 5.1 Errors are indicated as standard deviations. *Residual solvent peaks.

We performed ^{1}H DOSY NMR experiments of the **4**⊂[**1**•$Pt_2(dppp)_2]^{4+}$ metallocavitand complex in CD_2Cl_2 solution (Figure 5.3). The fit of the decay of all proton signals to a mono-exponential function returned identical diffusion constant values for both bound species, **4** and [**1**•$Pt_2(dppp)_2]^{4+}$, -log *D* = 9.29. This indicates that both species are involved in the same complex. Interestingly, we determined a value of -log *D* = 9.21 for the **4**⊂**1** complex

(Figure 5.17). This result is in complete agreement with the similar dimensions of the two diffusive species. The diffusive species of the **4**⊂[**1**•$Pt_2(dppp)_2]^{4+}$ metallocavitand complex (~ 10.4 Å radius and 17 Å height, see Figure 5.4) is larger than the parent **4**⊂**1** complex. In conclusion, the quantitative assembly of the [**1**•$Pt_2(dppp)_2]^{4+}$ metallocavitand in CD_2Cl_2 requires the presence of polar guest capable of binding in its aromatic cavity and locking its cone conformation.

The **4**⊂[**1**•$Pt_2(dppp)_2]^{4+}$ metallocavitand complex was also characterized by ESI+/TOF using an Orbitrap mass spectrometer (Figure 5.23). The mass spectrum showed an intense ion peak at m/z = 3692.75446, which coincided with the exact mass of the mono-charged complex, **4**⊂[**1**•$Pt_2(dppp)_2(OTf)_3]^+$. In addition, the isotopic distribution pattern of the ion peak is in fully agreement with the theoretical one. This result indicated that the **4**⊂[**1**•$Pt_2(dppp)_2]^{4+}$ metallocavitand present in solution can be transferred to the gas phase. It is worth mentioning here that the simulation spectrum of the **4**⊂[**1**•$Pt_2(dppp)_2(OTf)_3]^+$ complex showed different mass patterns depending on the isotope mode: isotopic pattern or profile spectrum. The theoretical profile spectrum provided a superior fit to the experimental one. We learned that for large molecular weights featuring reduced instrumental resolution, the experimental isotopic pattern of the ion-peak shows a superior coincidence with the simulated profile spectrum rather than with the theoretical isotopic pattern.

Luckily, we obtained single crystals of the **4**⊂[**1**•$Pt_2(dppp)_2]^{4+}$ from a CH_2Cl_2/CD_3CN solution mixture that were suitable for X-ray diffraction analysis. (Figure 5.4) In the solid state, the C[4]P unit of **4**⊂[**1**•$Pt_2(dppp)_2]^{4+}$ complex adopts the cone conformation owing to the establishment of four convergent hydrogen bonds between the pyrrole NHs and the oxygen atom of bound **4**, *d* ($N_{pyrrole}\cdots O$) ~ 3.0 Å. At the upper rim, the four oxazolo[4,5-*b*]pyrazinyl units are coordinated to two $[Pt(dppp)]^{2+}$ with an average *d* ($N_{oxazolo[4,5-b]pyrazinyl}\cdots Pt$) ~ 2.1 Å. The results obtained in the solid state are fully consistent with our interpretations of the NMR spectra registered in CD_2Cl_2 solution.

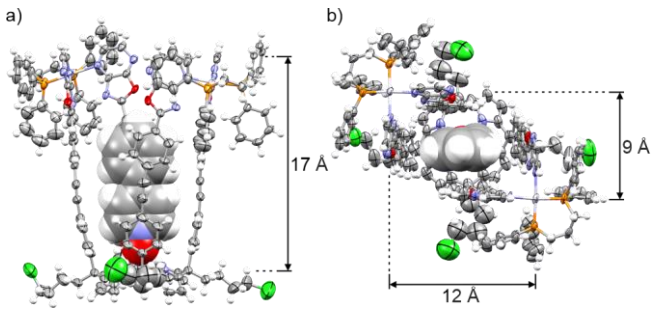

Figure 5.4. X-ray crystal structures of **4**⊂[**1**•$Pt_2(dppp)_2]^{4+}$: a) top and b) side view. The structures are shown in ORTEP view with thermal ellipsoids set at 50% probability for the non-hydrogen atoms. Hydrogen atoms are depicted as fixed-size spheres of 0.3 Å radius. The bound guest **4** is shown as CPK model.

We also studied the assembly of the [**1**•$Pt_2(dppp)_2]^{4+}$ metallocavitand using as starting material the 1:1 inclusion complex of ligand **1** with pyridine *N*-oxide **5** (Figure 5.24). The addition of *ca*. 2 equiv. of Pt(II) salt precursor to the solution of the **5**⊂**1** complex led to the observation of the same diagnostic proton signals corresponding to the **5**⊂[**1**•$Pt_2(dppp)_2]^{4+}$. Moreover, the ^{1}H NMR spectrum displayed broad peaks suggesting the formation of metal mediated polymeric aggregates to a significant extent. The energy minimized structure showed that the pyridine-*N*-oxide **5** is too short to establish similar CH-π and π-π interactions to those found with **4** with the aromatic walls of ligand **1**. The use of the aliphatic *N*-oxide **6** as guest induced the quantitative formation of the 1:1 complex **6**⊂**1**. However, the addition of Pt(II) salt precursor led to the observation of complex and multiple signals in the ^{1}H NMR spectrum of the mixture. This observation indicated that metal-mediated polymers are formed instead of the targeted metallocavitand complex (Figure 5.27). Most likely, the free binding energy of the coordination complex formed with Pt(II) atom and two adjacent oxazolo[4,5-*b*]pyrazinyl walls depends on the included guest. For certain guests, it may become energetically comparable with non-chelated Pt(II) coordination complexes involving different pyrazinyl units of SAE-C[4]P ligand **1**. This latter type of coordination will be responsible for the formation of the observed polymeric aggregates of **1**.

Based on molecular modelling studies (MM3), we selected the aliphatic *bis*-formamide **7**[22] and *mono*-formamide **8**[23] having spacers of seven methylene groups, respectively, as potential templating guests (Figure 5.5). In an extended conformation, both aliphatic formamides are size and shape complementary to the cavity of the [**1**•$Pt_2(dppp)_2]^{4+}$ metallocavitand. The ^{1}H NMR spectrum of an equimolar CD_2Cl_2 solution of *bis*-formamide **7** and SAE-C[4]P ligand **1** showed broad signals for the protons of both compounds. This result suggested that **1** and **7** were involved in the formation of a complex, possibly 1:1 complex, **7**⊂**1**, which displayed intermediate exchange dynamics on the chemical shift time scale with its free components (Figure 5.29). Gratifyingly, the addition of *ca.* 2 equiv. of $[Pt(dppp)]^{2+}$ to the equimolar solution above produced the sharpening of all proton signals. The chemical shift changes experienced by the aromatic protons of the oxazolo[4,5-*b*]pyrazinyl groups of SAE-C[4]P **1**, H^c and H^d, are consistent with its coordination to the Pt(II) metal center. The proton signals of SAE-C[4]P **1** were in agreement with C_{2v} symmetry. We considered these observations as earmarks of the quantitative formation of the metallocavitand [**1**•$Pt_2(dppp)_2]^{4+}$. In addition, all proton signals of the *bis*-formamide **7** were upfield shifted. Specifically, one of its formyl protons resonated at 4.67 ppm ($\Delta\delta$ = -3.32 ppm). Altogether, these observations located *bis*-formamide **7** inside the polar aromatic cavity of the metallocavitand [**1**•$Pt_2(dppp)_2]^{4+}$. One of the terminal formamide groups of **7** was deeply included and hydrogen bonded to the pyrrole NHs. The deep included formamide group adopts the *cis*-conformation (*vide*

infra). In short, *bis*-formamide **7**, is also a good guest to induce the quantitative formation of the **7**⊂[**1**•$Pt_2(dppp)_2]^{4+}$ metallocavitand inclusion complex.

The *cis*-conformation adopted by the deep included formamide group was supported by 2D ROESY experiments of the solution containing the complex. Accordingly, we detected intramolecular NOE cross peaks between the formyl proton of the deep included and hydrogen-bonded formamide group of **7** and the *α*-methylene protons (H^1). In contrast, the analogous cross-peaks for the formyl group at the opposed end of **7** were not observed. (Figure 5.32). These findings supported the selective formation of the *trans,cis*-**7**⊂[**1**•$Pt_2(dppp)_2]^{4+}$ metallocavitand complex.[24] The binding process displayed a slow chemical exchange on the ^{1}H NMR time scale (separate signals for free and bound **7** were observed when 2 equiv. of **7** was added to the metallocavitand's solution). Conversely, the same exchange process was fast on the EXSY time scale (cross-peaks due to chemical exchange between the proton signals of free and bound **7** were detected, t_{mix} = 0.3 s). We use the chemical exchange cross-peaks for the unequivocal assignment of the proton signals of bound *trans*,*cis*-**7**. In addition, the observation of i+2 NOE cross-peaks between the methylene protons of bound **7** supported the extended conformation of its alkyl chain.

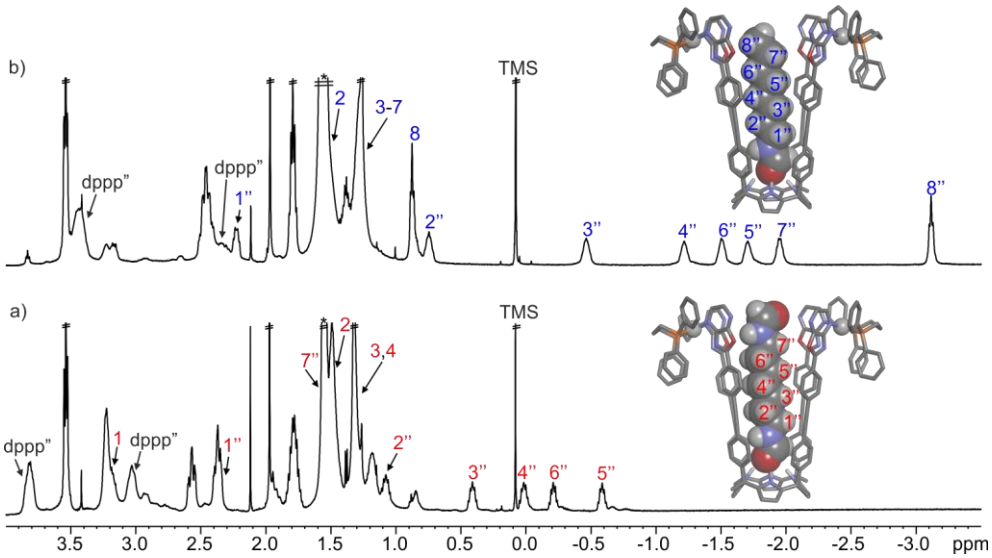

Figure 5.5. Selected region of ^{1}H NMR (500 MHz with cryoprobe, CD_2Cl_2, 298 K) of a) *trans,cis*-**7**⊂[**1**•$Pt_2(dppp)_2]^{4+}$ and b) *cis*-**8**⊂[**1**•$Pt_2(dppp)_2]^{4+}$, together with free guests (*ca*. 1 equiv.). Energy minimized structures (MM3) of simplified *trans,cis*-**7**⊂[**1**•$Pt_2(dppp)_2]^{4+}$ and *cis*-**8**⊂[**1**•$Pt_2(dppp)_2]^{4+}$ metallocaviplexes. The complexes are depicted in stick representation and bound guests are shown as CPK models. Organic-solubilizing groups were pruned to methyl groups to simplify the calculations. Doubly primed labels correspond to the proton signals of the metallocaviplexes. *Residual solvent peaks.

In close analogy to *bis*-formamide **7**, *mono*-formamide **8** also induced the quantitative assembly of the **8**⊂[**1**•$Pt_2(dppp)_2]^{4+}$ metallocavitand complex in CD_2Cl_2 solution (Figure 5.35). The magnitude of the complexation-induced shift (CIS) for the deep included formyl proton of **8** ($\Delta\delta$ = -3.44 ppm), was in complete agreement with that observed for **7**. This result, together with the diagnostic NOE cross peaks in the 2D ROESY NMR spectrum supported that the deep included formamide group of **8** also adopted the *cis*-conformation and was bound to the pyrrole NHs of the C[4]P core in the **8**⊂[**1**•$Pt_2(dppp)_2]^{4+}$ metallocavitand complex. Surprisingly, the **8**⊂[**1**•$Pt_2(dppp)_2]^{4+}$ metallocavitand complex displayed the aromatic proton H^c, *ortho* to the coordinated nitrogen atom of the pyrazinyl residues, noticeably downfield shifted ($\delta(H^c)$ = 9.15 ppm for **8**⊂[**1**•$Pt_2(dppp)_2]^{4+}$ and $\delta(H^c)$ = 8.68 ppm for **7**⊂[**1**•$Pt_2(dppp)_2]^{4+}$). It is worthy to note that the methylene protons of the bound dppp in the **8**⊂[**1**•$Pt_2(dppp)_2]^{4+}$ complex experienced significantly reduced CIS with respect to those observed in the **7**⊂[**1**•$Pt_2(dppp)_2]^{4+}$ and **4**⊂[**1**•$Pt_2(dppp)_2]^{4+}$ metallocaviplexes (Figure 5.5 and Table 5.6). These observations provided initial hints to a possible change in the binding geometry of the bis-phosphine ligand in the two complexes. If this was the case, the same explanation could be used to rationalize the different CIS observed for the methylene protons of the two included guests. Nevertheless, additional experimental and theoretical evidences are required to support this hypothesis. The results of ^{1}H DOSY experiments for the two metallocavitands complexes, **7**⊂[**1**•$Pt_2(dppp)_2]^{4+}$ and **8**⊂[**1**•$Pt_2(dppp)_2]^{4+}$, assigned similar diffusion constant values: -log*D* = 9.28 and 9.31, respectively. These values are almost coincident with that determined for the 4-phenyl pyridine *N*-oxide complex, **4**⊂[**1**•$Pt_2(dppp)_2]^{4+}$, supporting the similar dimensions of the three assemblies (Figure 5.33 and Figure 5.39). The aromatic walls of the metallocavitand are conformationally flexible to adapt the cavity to the size and shape of the included guest. However, this adaptation process does not have a large impact on the overall dimensions of the metallocavitand complexes.

Finally, we studied the kinetics of the displacement reaction of the included guest in the *cis*-**8**⊂[**1**•$Pt_2(dppp)_2]^{4+}$ metallocavitand complex. To this end, we employed 4-phenyl pyridine *N*-oxide **4** as a competitive guest. The exchange process was monitored using ^{1}H NMR spectroscopy (Figure 5.41). The addition of *ca.* 1.2 equiv. of **4** to a 1 mM CD_2Cl_2 solution of the metallocavitand complex *cis*-**8**⊂[**1**•$Pt_2(dppp)_2]^{4+}$ induced a fast and quantitative formation of the **4**⊂[**1**•$Pt_2(dppp)_2]^{4+}$ metallocavitand complex. Concomitantly, the initially bound guest **8** was released to the bulk solution. On the one hand, this result indicated that the **4**⊂[**1**•$Pt_2(dppp)_2]^{4+}$ metallocavitand complex is thermodynamically more stable than the parent counterpart with **4**. On the other hand, the capture and release process of the guests occurred through a low energy barrier as testified by the fast kinetics on the human time scale (< 30s). Consequently, the putative exchange mechanism does not imply the dissociation of coordination bonds that is mandatory for the existence of an exchange mechanism occurring through a conformational change of the C[4]P core. We are in favour of postulating a “French doors” or “constrictive binding” mechanism[25], involving the rotation and flexion of the *meso*-aryl walls. This mechanism should reduce the energy

barrier for the crossing of the passages defined by the *meso*-aryl walls both for the incoming and exiting guests. We consider that the existence of solvent filled metallocavitand intermediates is not likely owing to its high energy (never observed in solution).

5.3 Conclusions

In summary, we reported the synthesis of the unprecedented super aryl-extended calix[4]pyrrole ligand **1**, bearing four oxazolo[4,5-*b*]pyrazinyl substituents at its upper rim. We described the guest induced self-assembly of ligand **1** with $[Pt(dppp)]^{2+}$ in CD_2Cl_2 solution, affording the metallocavitand $[\mathbf{1}\bullet Pt_2(dppp)_2]^{4+}$. The metallocavitand features a large polar aromatic interior in which the *N*-oxides and aliphatic formamide derivatives, **4**-**8**, are encapsulated. A “French doors” or “constrictive binding” mechanism is proposed to explain the fast release and uptake process experienced by the encapsulated guest in the metallocavitand complexes.

5.4 Experimental Section

5.4.1 General information and instruments

Reagents were obtained from commercial suppliers and used without further purification unless otherwise stated. All solvents were commercially obtained and used without further purification except pyrrole which was distilled and freshly used. Dry solvents were taken from a solvent system MB SPS 800. THF, Et_3N, DIPEA and iPr_2NH were dried, distilled and degassed by three freeze-pump-thaw cycles before used in the cross-coupling reactions. Routine ^1H NMR and $^{13}C\{^1H\}$ NMR spectra were recorded on a Bruker Avance 300 (300 MHz for ^1H NMR and 75 MHz for ^{13}C NMR), Bruker Avance 400 (400 MHz for ^1H NMR and 100 MHz for ^{13}C NMR), Bruker Avance 500 (500 MHz for ^1H NMR and 125 MHz for ^{13}C NMR) or Bruker Avance 500 with cryoprobe (500 MHz for ^1H NMR and 125 MHz for ^{13}C NMR). Deuterated solvents used are indicated in the characterization and chemical shifts are given in ppm. Residual solvent peaks were used as reference.[26] All NMR *J* values are given in Hz. COSY, NOESY, ROESY, HMQC and HMBC experiments were recorded to help with the assignment of ^1H and ^{13}C signals. High Resolution Mass Spectra (HRMS) were obtained on a Bruker HPLC-ESI-TOF (MicroTOF Focus), Bruker HPLC-ESI-QqTOF (MaXis Impact) or Thermo Fisher Scientific Q Exactive Orbitrap equipped with a Heated Electrospray Ionization (HESI) probe. IR spectra were recorded on a Bruker Optics FTIR Alpha spectrometer equipped with a DTGS detector, KBr beamsplitter at 4 cm^{-1} resolution using a one bounce ATR accessory with diamond windows. Melting points were measured on a MP70 Melting Point System Mettler Toledo. Crystal structure determinations were carried out using a Rigaku MicroMax-007HF diffractometer equipped with a PILATUS 200K detector and a Bruker Apex II Duo equipped with an APEX II detector. Both using MoKα radiation. Crystal structure solution was achieved using VLD and Patterson methods as implemented in SIR2014 v14.10. Least-squares refinement on F2 using all measured intensities was carried out using the program SHELX-2018/3. In the case of **4**⊂**1**, residual electron density originating from disordered solvent molecules was treated with the OLEX2 program[27] applying a solvent mask. Column chromatography was performed with silica gel technical grade (Sigma-Aldrich), pore size 60 Å, 230-400 mesh particle size, 40-63 μm particle size and Thin Layer Chromatography (TLC) analysis on silica gel 60 F254.

5.4.2 Synthesis and characterization data

Tetra-*α* 4-iodophenyl-4'-chlorobutyl calix[4]pyrrole **3**, *bis*-formamide **7** and *mono*-formamide **8** were synthesized following previously reported procedures in the literature.[28,22,23]

Tetra-α tetra-oxazolo[4,5-*b*]pyrazinyl super aryl-extended calix[4]pyrrole **1**

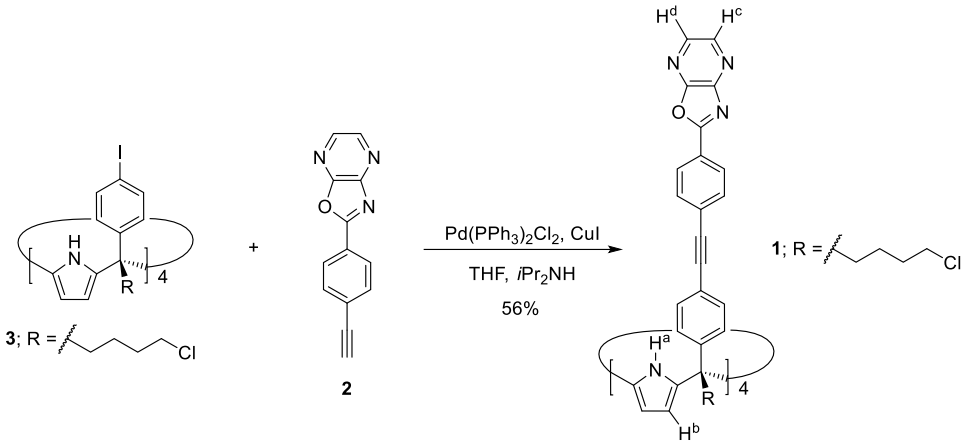

Scheme 5.2. Synthesis of compound **1**.

Compound 1: Tetra-*α* 4-iodophenyl-4'-chlorobutyl calix[4]pyrrole **3** (50 mg, 0.03 mmol, 1 equiv.), 2-(4-ethynylphenyl)oxazolo[4,5-*b*]pyrazine **2** (54.30 mg, 0.25 mmol, 2.1 equiv.), $Pd(PPh_3)_2Cl_2$ (3 mg, 0.004 mmol, 0.03 equiv.) and CuI (1.30 mg, 0.007 mmol, 0.05 equiv.) were kept under Argon atmosphere. Dry and degassed THF (5 mL) and diisopropylamine (5 mL) were added. The reaction was stirred at 45ºC for 8 h. After that, the reaction was stopped and the crude was concentrated. The crude was redissolved in CH_2Cl_2 (15 mL) and washed with 0.5 N HCl (15 mL), brine (15 mL) and water (10 mL). The organic layer was dried (Na_2SO_4), filtered and concentrated. The crude was purified by column chromatography on silica gel (10 g, 4:1 CH_2Cl_2/MTBE) affording the product as a yellow solid (35 mg, 0.02 mmol, 56% yield). Rf = 0.4 (4:1 CH_2Cl_2/MTBE). ^{1}H NMR (500 MHz with cryoprobe, $CDCl_3$, 298 K): *δ* (ppm) = 8.47 (d, *J* = 2.7 Hz, 4H); 8.20 (d, *J* = 2.7 Hz, 4H); 8.17 (m, 8H); 7.62 (m, 8H); 7.42 (m, 8H); 7.22 (br s, 4H); 7.20 (m, 8H); 5.97 (d, *J* = 2.6 Hz, 8H); 3.51 (t, *J* = 6.6 Hz, 8H); 2.32-2.28 (m, 8H); 1.80-1.76 (m, 8H); 1.44-1.39 (m, 8H). ^{13}C{^{1}H} NMR (125 MHz with cryoprobe, $CDCl_3$, 298 K): *δ* (ppm) = 165.8; 153.1; 149.5; 145.1; 142.5; 138.9; 134.9; 132.4; 131.6; 128.4; 128.2; 128.0; 125.1; 121.1; 107.0; 93.3; 89.1; 49.2; 44.9; 39.5; 32.9; 22.7. HRMS (MALDI-TOF) *m/z*: $[M+Na]^+$ Calcd for $C_{112}H_{84}Cl_4N_{16}NaO_4$ 1879.5513; Found: 1879.5511. FTIR *v* (cm^{-1}) = 3421; 2951; 1611; 1506; 1410; 1320; 1260; 1180; 832; 769; 743; 700. M.p. > 260ºC (decompose).

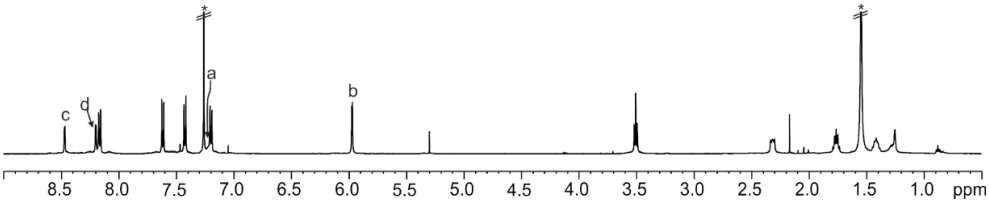

Figure 5.6. ^{1}H NMR (500 MHz with cryoprobe, $CDCl_3$, 298 K) spectrum of **1**. See Scheme 5.1 for proton assignment. *Residual solvent peaks.

2-(4-Ethynylphenyl)oxazolo[4,5-*b*]pyrazine **2**

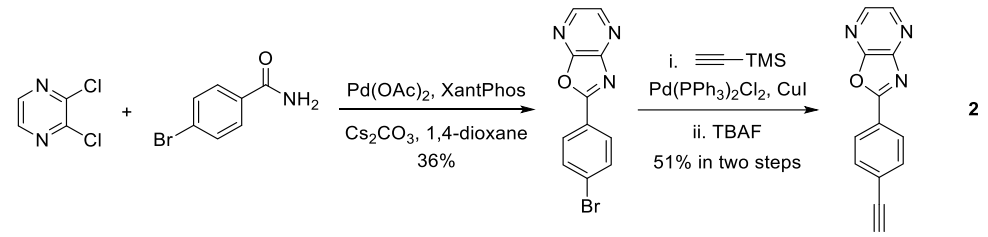

Scheme 5.3. Synthesis of compound **2**.

2-(4-Bromophenyl)oxazolo[4,5-*b*]pyrazine: 4-Bromobenzamide (800 mg, 4 mmol, 1 equiv.), $Pd(OAc)_2$ (50.30 mg, 0.22 mmol, 0.05 equiv.), XantPhos (255 mg, 0.44 mmol, 0.1 equiv.), Cs_2CO_3 (3.10 g, 9.6 mmol, 2.4 equiv.) and 2,3-dichloropyrazine (690 mg, 4.40 mmol, 1.1 equiv.) were placed in an oven-dried flask and purged with Argon. Dry 1,4-dioxane (11 mL) was added and the reaction was stirred overnight under reflux and Argon atmosphere. After that, the reaction was stopped and cooled to r.t. The reaction mixture was diluted with EtOAc (3 mL) and filtered. The precipitate was washed with EtOAc and the combined organic layers were concentrated. The crude was purified by column chromatography on silica gel (80 g, 4:1 Hexane:EtOAc) affording the product as a yellow solid (400 mg, 1.44 mmol, 36% yield). Rf = 0.4 (4:1 Hexane:EtOAc). ^{1}H NMR (400 MHz, $CDCl_3$, 298 K): δ (ppm) = 8.60 (d, J = 3.0 Hz, 1H); 8.33 (d, J = 3.0 Hz, 1H); 8.25-8.22 (m, 2H); 7.76-7.72 (m, 2H). The ^{1}H NMR spectrum ($CDCl_3$) is in agreement with that reported in the literature.[29]

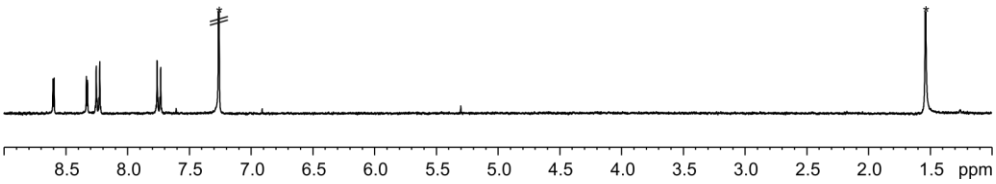

Figure 5.7. ^{1}H NMR (400 MHz, $CDCl_3$, 298 K) spectrum of 2-(4-bromophenyl)oxazolo[4,5-b]pyrazine. *Residual solvent peak.

2-(4-Ethynylphenyl)oxazolo[4,5-*b*]pyrazine: Step i. 2-(4-Bromophenyl)oxazolo[4,5-*b*]pyrazine (60 mg, 0.22 mmol, 1 equiv.), $Pd(PPh_3)_2Cl_2$ (11.40 mg, 0.02 mmol, 0.07 equiv.) and CuI (11.60 mg, 0.06 mmol, 0.28 equiv.) were kept under Argon atmosphere. Dry and degassed THF (0.3 mL) and DIPEA (0.11 mL, 0.65 mmol, 3 equiv.) were added. Ethynyltrimethylsilane (0.09 mL, 0.65 mmol, 3 equiv.) was added. The reaction was stirred at 45ºC for 6 h. After that, the reaction was stopped and the crude was concentrated. The crude was redissolved in CH_2Cl_2 (10 mL) and washed with 1 N HCl (10 mL), brine (10 mL) and water (10 mL). The organic layer was dried (Na_2SO_4), filtered and concentrated. The crude was purified by column chromatography on silica gel (10 g, 4:1 Hexane/EtOAc). The TMS-protected alkyne was isolated as an orange solid (50 mg, 0.17 mmol, 78% yield). Step ii. The TMS-protected alkyne (48 mg, 0.16 mmol, 1 equiv.) was dissolved in dry THF (1.1 mL). TBAF (0.18 mL, 0.18 mmol, 1.1 equiv.) was added dropwise. The reaction was stirred at r.t. under Argon atmosphere for 1 h. After that, the reaction was quenched with aqueous saturated NH_4Cl (1 mL) and the THF was removed under vacuum. The crude was extracted with EtOAc (3×5 mL) and the organic layer was washed with brine (5 mL). The organic layer was dried (Na_2SO_4), filtered and concentrated. The crude was purified by column chromatography on silica gel (5 g, EtOAc) affording the product as a yellow solid (23.60 mg, 0.12 mmol, 65% yield). Rf = 0.5 (EtOAc). ^{1}H NMR (400 MHz, $CDCl_3$, 298 K): δ (ppm) = 8.60 (d, J = 2.7 Hz, 1H); 8.35 (d, J = 2.7 Hz, 1H); 8.33 (m, 2H); 7.69 (m, 2H). 3.32 (s, 1H). ^{13}C{^{1}H} NMR (100 MHz, $CDCl_3$, 298K): δ (ppm) = 165.9; 153.2; 151.2; 142.5; 139.1 (×2); 133.0; 128.5; 127.5; 82.8; 81.3. HRMS (ESI-TOF) m/z: $[M+H]^+$ Calcd for $C_{13}H_8N_3O$ 222.0667; Found 222.0662. FTIR ν (cm^{-1}) = 3207; 3603; 2906; 1514; 1586; 1553; 1488; 1368; 1320; 1254; 1177; 1011; 830; 744. M.p. = 178-180ºC.

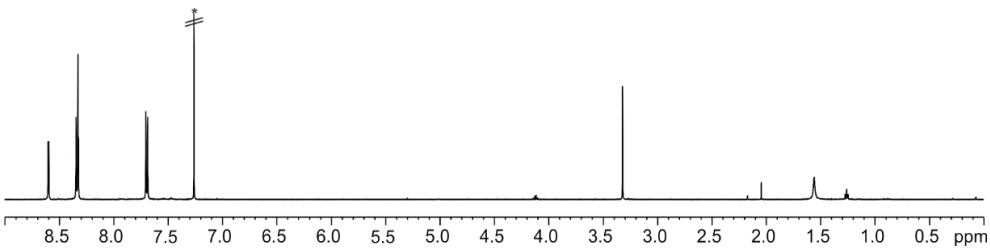

Figure 5.8. ^{1}H NMR (400 MHz, $CDCl_3$, 298 K) spectrum of **2**. *Residual solvent peak.

Pt(dppp)(OTf)$_2$

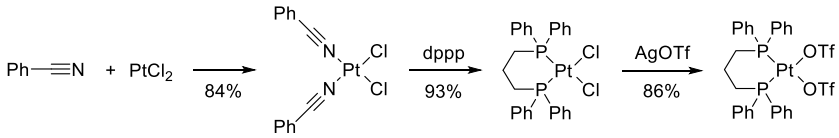

Scheme 5.4. Synthesis of Pt(dppp)(OTf)$_2$.

$Pt(PhCN)_2(Cl)_2$: $PtCl_2$ (0.3 g, 1.13 mmol, 1 equiv.) was added to benzonitrile (3.25 mL) and the resulting solution was stirred at 110°C for 2 h. After that, the reaction mixture was cooled down and hexane (6 mL) was added to induce precipitation. The pale yellow precipitate was filtered, washed with hexane (3×2 mL) and dried under vacuum (0.45 g, 0.95 mmol, 84% yield). ^{1}H NMR (400 MHz, $CDCl_3$, 298 K): δ (ppm) = 7.78 (d, J = 7.8 Hz, 4H); 7.72 (t, J = 7.5 Hz, 2H); 7.59 (t, J = 7.8 Hz, 4H). The ^{1}H NMR spectrum ($CDCl_3$) is in agreement with that reported in the literature.[30]

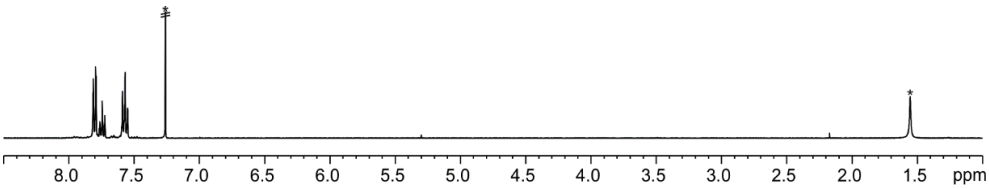

Figure 5.9. ^{1}H NMR (400 MHz, $CDCl_3$, 298 K) spectrum of $Pt(PhCN)_2Cl_2$. *Residual solvent peaks.

$Pt(dppp)(Cl)_2$: $Pt(PhCN)_2(Cl)_2$ (240 mg, 0.51 mmol, 1 equiv.) and *bis*-diphenylphosphinopropane (dppp) (252 mg, 0.61 mmol, 1.2 equiv.) were each dissolved in dry CH_2Cl_2 (19 mL), respectively. The dppp's solution was added to that of $Pt(PhCN)_2Cl_2$. The color of the solution changed from pale yellow to colorless. The reaction mixture was stirred for 2 h at r.t. After that, hexane (40 mL) was added to induce precipitation. The white precipitate was filtered, washed with hexane (3×6 mL) and dried under vacuum (320 mg, 0.47 mmol, 93% yield). ^{1}H NMR (400 MHz, $CDCl_3$, 298 K): δ = 7.77 (m, 8H); 7.42 (m, 12H); 2.51 (m, 4H); 2.05 (m, 2H). The ^{1}H NMR spectrum ($CDCl_3$) is in agreement with that reported in the literature.[30]

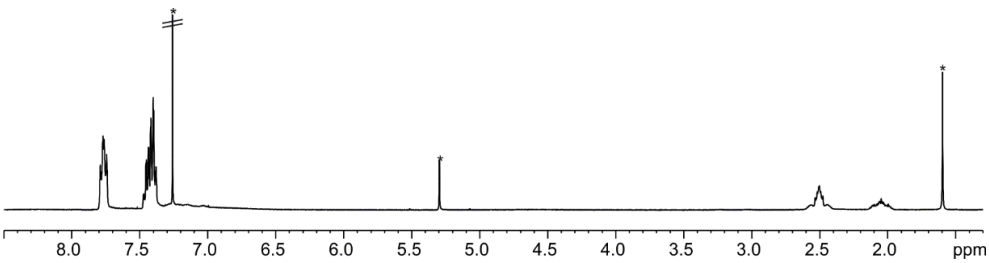

Figure 5.10. ^{1}H NMR (400 MHz, $CDCl_3$, 298 K) spectrum of $Pt(dppp)Cl_2$. *Residual solvent peaks.

$Pt(dppp)(OTf)_2$: $Pt(dppp)(Cl)_2$ (200 mg, 0.29 mmol, 1 equiv.) was dissolved in dry CH_2Cl_2 (60 mL). AgOTf (607 mg, 2.36 mmol, 8 equiv.) was added. The flask was covered with aluminum foil to avoid its exposure to light. The reaction was stirred for 72 h at r.t. After that, the reaction mixture was filtered and concentrated to 10 mL under reduced pressure, followed by the addition of Et_2O (10 mL) to induce precipitation. The white precipitate was filtered, washed with Et_2O and dried under vacuum (230 mg, 0.25 mmol, 86% yield). ^{1}H NMR (400 MHz, CD_2Cl_2, 298 K): δ (ppm) = 7.64-7.57 (m, 12H); 7.51-7.47 (m, 8H); 2.71 (m, 4H); 2.25 (m, 2H). $^{19}F\{^1H\}$ (376 MHz, CD_2Cl_2, 298

K): δ (ppm) = -78.8 (s). $^{31}P\{^{1}H\}$ (162 MHz, CD_2Cl_2, 298 K): δ (ppm) = -7.0 (s with satellites due to ^{195}Pt, J = 3715 Hz).

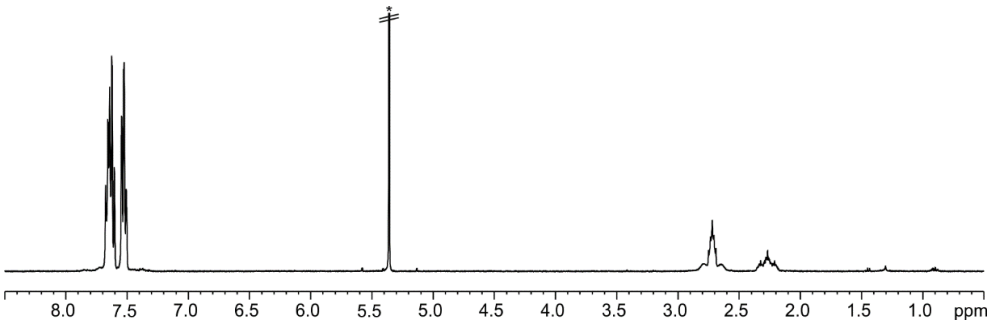

Figure 5.11. ^{1}H NMR (400 MHz, CD_2Cl_2, 298 K) spectrum of Pt(dppp)$(OTf)_2$. *Residual solvent peak.

5.4.3 1D and 2D NMR spectra of the metallocavitand based on SAE-C[4]P **1**

A solution of the host **1** (1 mM) was prepared in CD_2Cl_2. Subsequently, 0.5 mL of the solution were placed in an NMR tube. A solution of the guest (**4**-**8**) was prepared at 20-30-fold higher concentration using the host's solution ([G] = 20-30 mM and [H] = 1 mM). A solution of the Pt(dppp)$(OTf)_2$ was prepared at 10-15-fold higher concentration using the host's solution ([Pt(dppp)$(OTf)_2$] = 10-15 mM and [H] = 1 mM). Immediately, the 0.5 mL of the host's solution was titrated by manually injecting incremental amounts of the guest's solution or the Pt(II) solution using a micro-syringe. A ^{1}H NMR spectrum of the mixture was acquired after each injection and vigorous hand shaking of the NMR tube for few seconds.

Addition of Pt(dppp)$(OTf)_2$ to calix[4]pyrrole ligand **1**

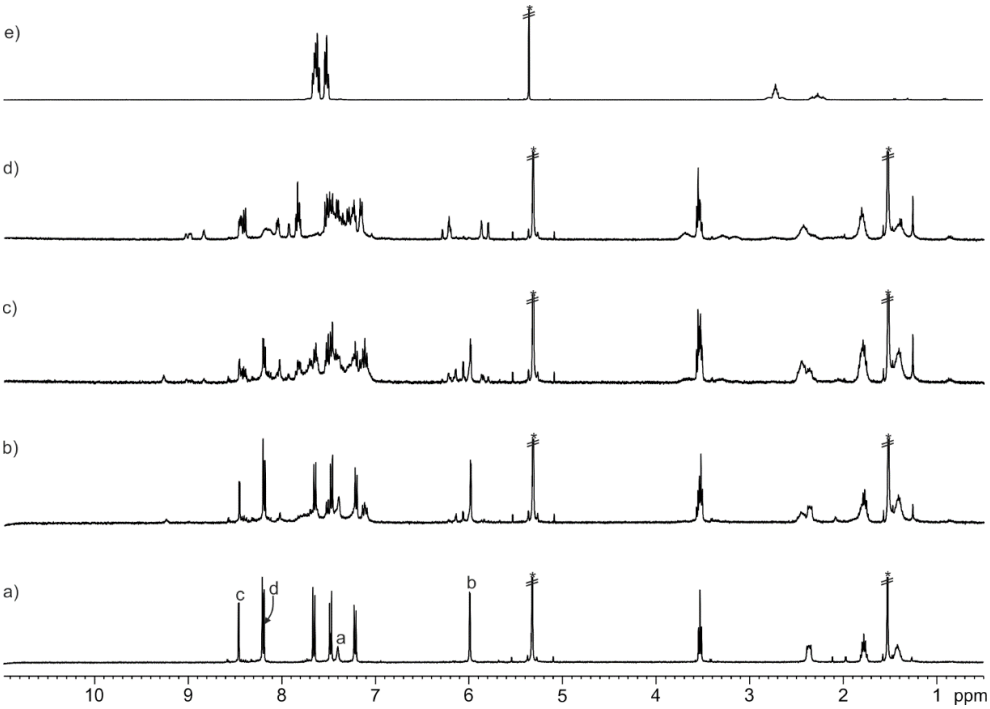

Figure 5.12. ^{1}H NMR (400 MHz, CD_2Cl_2, 298 K) spectra of the titration of ligand **1** with Pt(dppp)$(OTf)_2$: a) 0; b) 0.5; c) 1 and d) 2 equiv.; e) Pt(dppp)$(OTf)_2$. See Scheme 5.1 and Figure 5.11 for proton assignment. *Residual solvent peaks.

The observation of several proton signals in the ^{1}H NMR spectrum of ligand **1** upon the addition of 2 equiv. of Pt(II) suggested the formation of higher-order aggregates of unknown stoichiometry.

Titrations of receptor **1** with *N*-oxides **4**-**6** and addition of Pt(II) to the corresponding 1:1 complexes

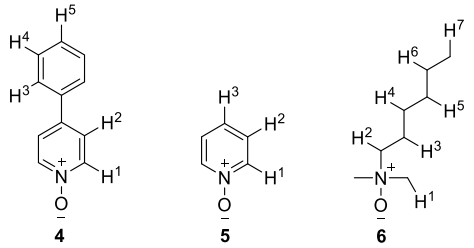

Figure 5.13. Line-drawing structures of *N*-oxides **4**-**6**.

4-Phenylpyridine *N*-oxide **4**

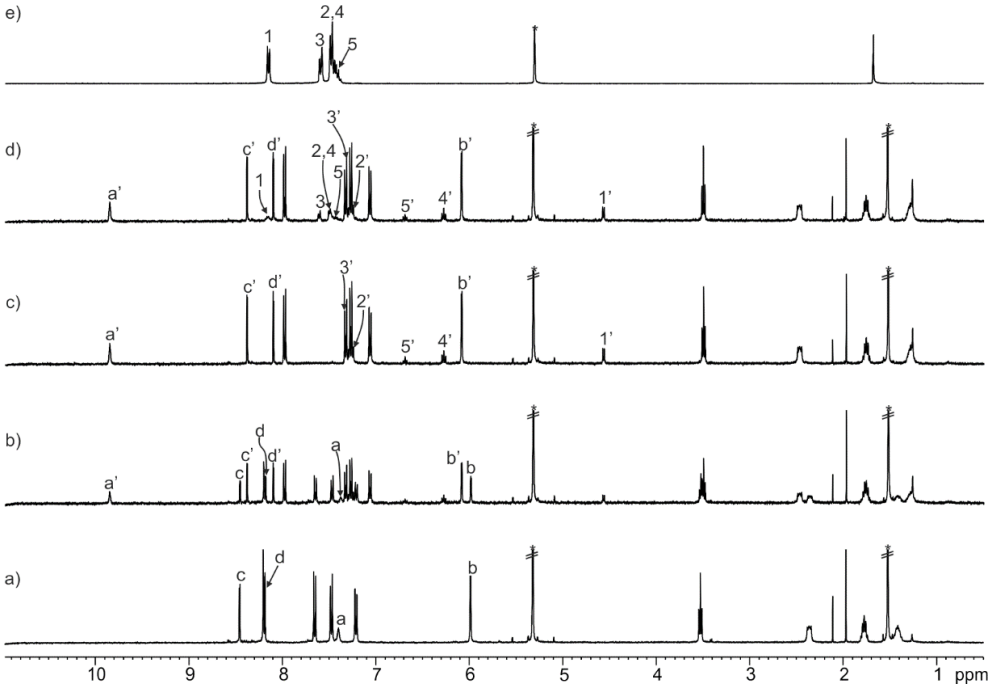

Figure 5.14. ^{1}H NMR (400 MHz, CD_2Cl_2, 298 K) spectra of the titration of receptor **1** with 4-phenylpyridine *N*-oxide **4**: a) 0; b) 0.5; c) 1 and d) 2 equiv.; e) **4**. Primed labels correspond to proton signals of **4⊂1**. See Scheme 5.1 and Figure 5.13 for proton assignments. *Residual solvent peaks.

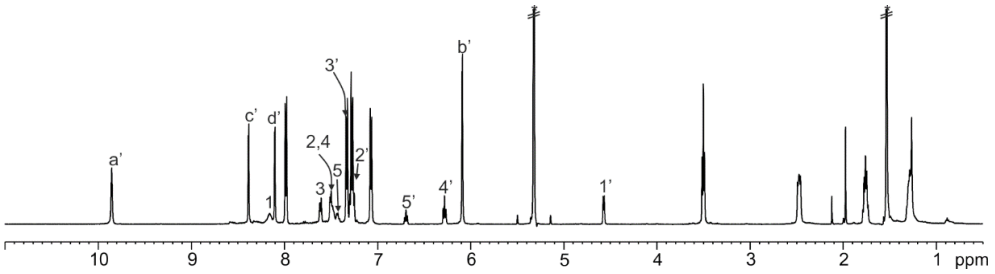

Figure 5.15. ^{1}H NMR (500 MHz with cryoprobe, CD_2Cl_2, 298 K) spectra of receptor **1** with 4-phenylpyridine *N*-oxide **4** (*ca.* 1:2 ratio). Primed labels correspond to proton signals of **4⊂1**. See Scheme 5.1 and Figure 5.13 for proton assignments. *Residual solvent peaks.

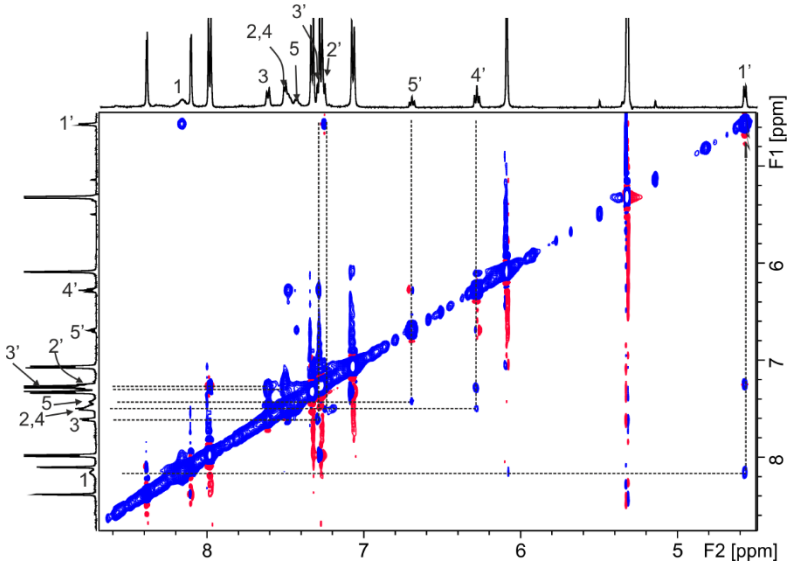

Figure 5.16. Selected region of the ^{1}H-^{1}H EXSY NMR (500 MHz with cryoprobe, CD_2Cl_2, 298 K, mixing time = 0.3 s) spectrum of receptor **1** with 4-phenylpyridine *N*-oxide **4** (*ca*. 1:2 ratio). Primed numbers correspond to proton signals of bound **4**. See Figure 5.13 for proton assignment.

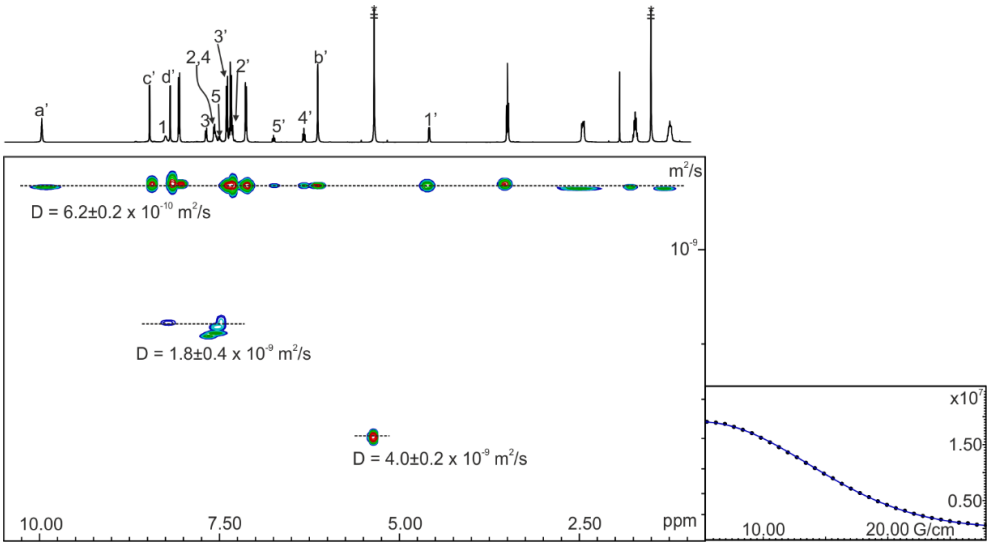

Figure 5.17. (left) ^{1}H pseudo 2D plot of DOSY (500 MHz with cryoprobe, CD_2Cl_2, 298 K, D20 = 0.01 s; P30 = 3.5 ms) of receptor **1** with 4-phenylpyridine *N*-oxide **4** (*ca.* 1:2 ratio). (right) Fit of the decay of the signal b' to a mono-exponential function using Dynamics Center from Bruker. Primed labels correspond to proton signals of **4⊂1**. See Scheme 5.1 and Figure 5.13 for proton assignments. Errors are indicated as standard deviations. *Residual solvent peaks.

Table 5.1. Experimental chemical shifts of free (δ_{free}) and bound (δ_{bound}) **4** in the receptor and complexation-induced shifts ($\Delta\delta$).

Signal	δ_{free} (ppm)	Signal	δ_{bound} (ppm)	$\Delta\delta$ (ppm)
1	8.18	1'	4.57	-3.61
2	7.50	2'	7.25	-0.25
3	7.62	3'	7.32	-0.30
4	7.50	4'	6.28	-1.22
5	7.43	5'	6.69	-0.74

Addition of $Pt(dppp)(OTf)_2$ to the **4⊂1** complex

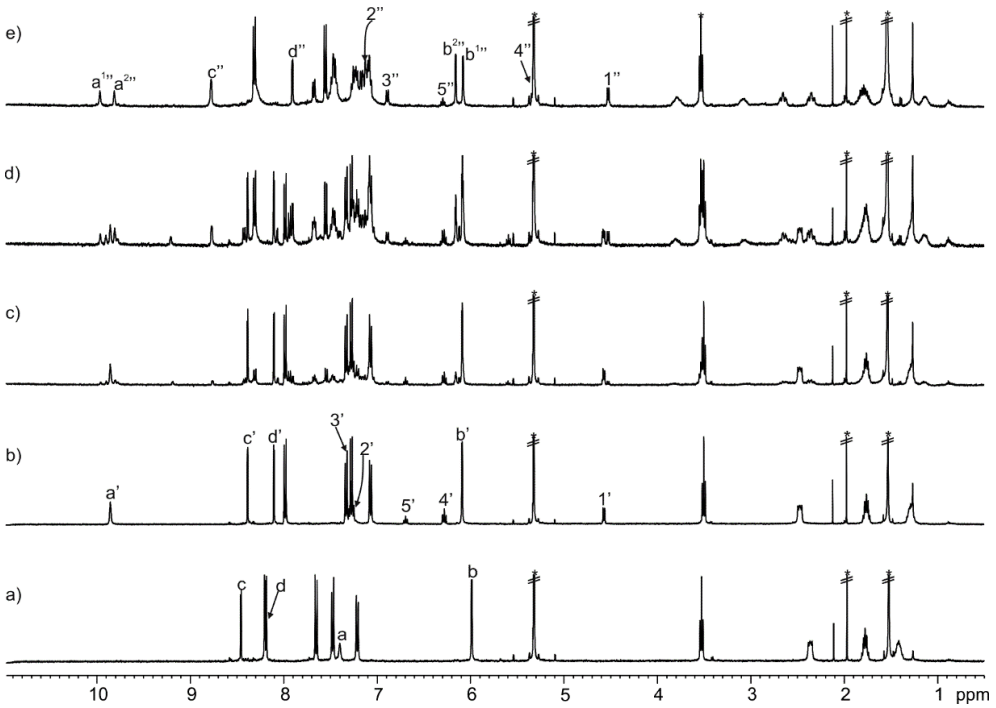

Figure 5.18. ^{1}H NMR (400 MHz, CD_2Cl_2, 298 K) spectra of the titration of ligand **1** with 4-phenylpyridine *N*-oxide **4**: a) 0 and b) 1 equiv.; addition of [Pt(dppp)$(OTf)_2$] to the **4⊂1** complex: c) 0.5; d) 1 and e) 2 equiv. Primed labels correspond to proton signals of **4⊂1**. Double primed labels correspond to proton signals of **4⊂[1•**$Pt_2(dppp)_2]^{4+}$. See Scheme 5.1 and Figure 5.22 for proton assignments. *Residual solvent peaks.

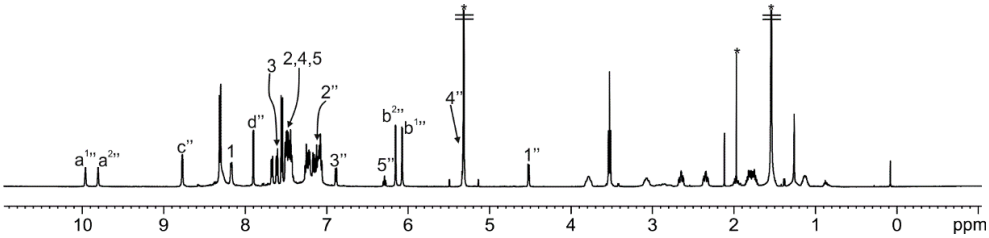

Figure 5.19. ^{1}H NMR (500 MHz with cryoprobe, CD_2Cl_2, 298 K) spectra of ligand **1** with 4-phenylpyridine *N*-oxide **4** and [Pt(dppp)(OTf)$_2$] (*ca.* 1:2:2 ratio). Double primed labels correspond to proton signals of **4**⊂[**1**•Pt$_2$(dppp)$_2$]$^{4+}$. See Scheme 5.1 and Figure 5.22 for proton assignments. *Residual solvent peaks.

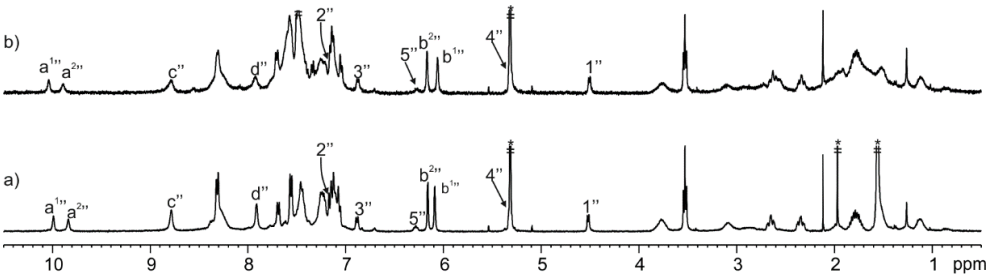

Figure 5.20. ^{1}H NMR (400 MHz, CD_2Cl_2, 298 K) spectra of the titration of the **4**⊂**1** complex with Pt(dppp)(OTf)$_2$: a) 2 and b) 4 equiv. See Scheme 5.1 and Figure 5.22 for proton assignments. *Residual solvent peaks.

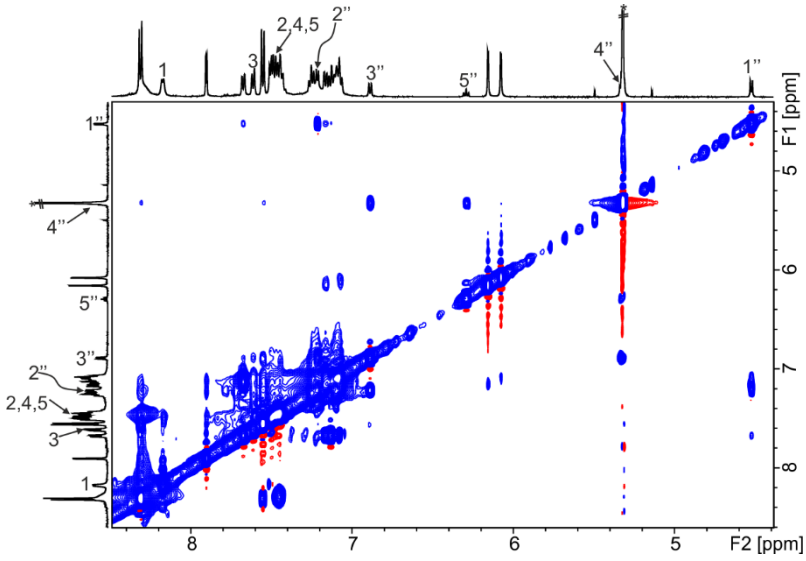

Figure 5.21. Selected region of the ^{1}H-^{1}H EXSY NMR (500 MHz with cryoprobe, CD_2Cl_2, 298 K, mixing time = 0.3 s) spectrum of ligand **1** with 4-phenylpyridine *N*-oxide **4** and Pt(dppp)(OTf)$_2$ (*ca.* 1:2:2 ratio). Double primed labels correspond to proton signals of **4**⊂[**1**•Pt$_2$(dppp)$_2$]$^{4+}$. See Figure 5.22 for proton assignment. *Residual solvent peak.

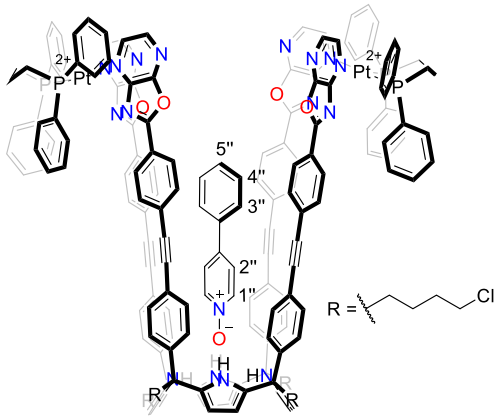

Figure 5.22. Line-drawing structure of the **4**⊂[**1**•$Pt_2(dppp)_2$]$^{4+}$ complex.

Table 5.2. Experimental chemical shifts of free (δ_{free}) and bound (δ_{bound}) **4** in the metallocavitand and complexation-induced shifts ($\Delta\delta$).

Signal	δ_{free} (ppm)	Signal	δ_{bound} (ppm)	$\Delta\delta$ (ppm)
1	8.18	1''	4.53	-3.65
2	7.50	2''	7.17	-0.33
3	7.62	3''	6.89	-0.73
4	7.50	4''	5.33	-2.17
5	7.43	5''	6.29	-1.14

Mass spectrum of [**4**⊂[**1**•$Pt_2(dppp)_2$]$(OTf)_3$]$^+$

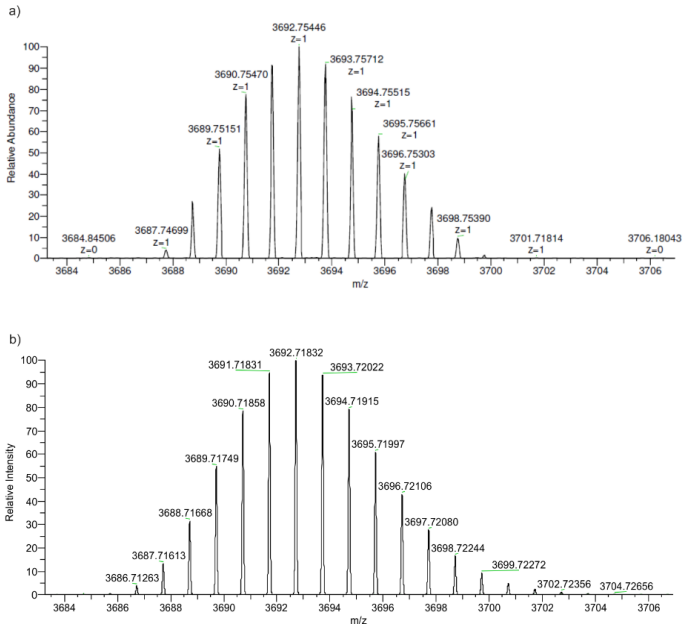

Figure 5.23. a) Experimental and b) theoretical isotopic distributions for [**4**⊂[**1**•$Pt_2(dppp)_2$]$(OTf)_3$]$^+$.

Pyridine *N*-oxide **5**

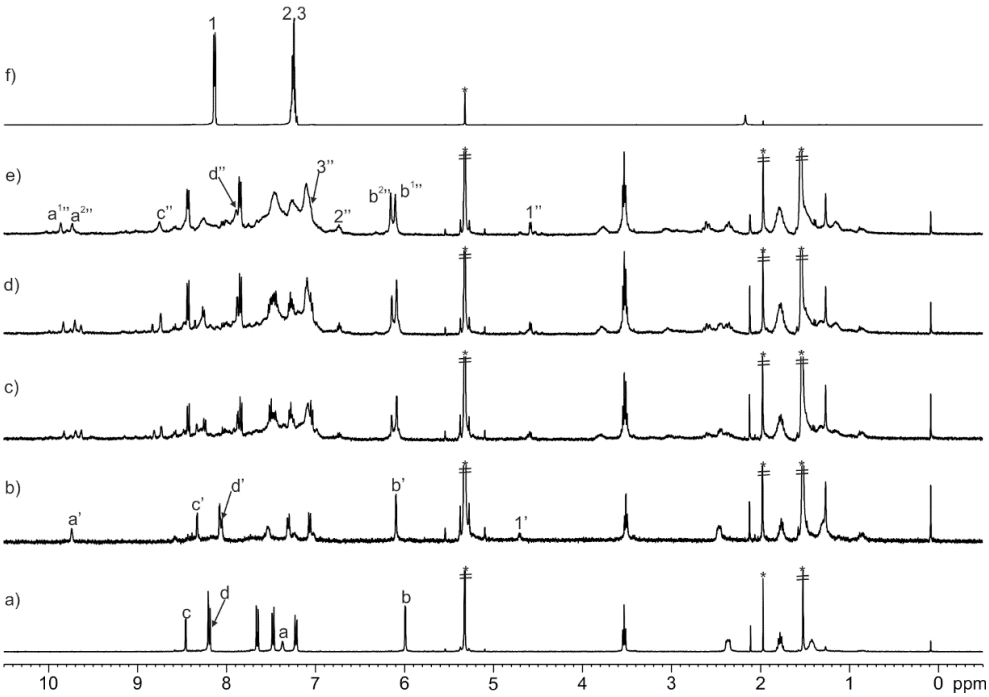

Figure 5.24. ^{1}H NMR (400 MHz, CD_2Cl_2, 298 K) spectra of the titration of ligand **1** with pyridine *N*-oxide **5**: a) 0 and b) 1 equiv.; addition of Pt(dppp)$(OTf)_2$ to the **5⊂1** complex: c) 0.5; d) 1 and e) 2 equiv.; f) **5**. Primed labels correspond to proton signals of **5⊂1**. Double primed labels correspond to proton signals of **5⊂[1•Pt$_2$(dppp)$_2$]$^{4+}$**. See Scheme 5.1 and Figure 5.26 for proton assignments. *Residual solvent peaks.

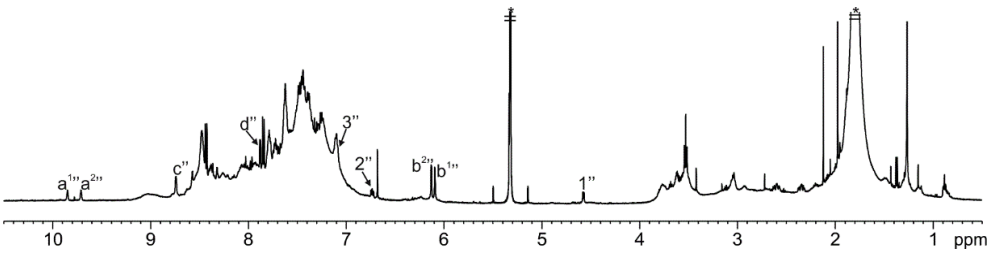

Figure 5.25. ^{1}H NMR (500 MHz with cryoprobe, CD_2Cl_2, 298 K) spectra of ligand **1** with pyridine *N*-oxide **5** and Pt(dppp)$(OTf)_2$ (ca. 1:1:2 ratio). Double primed labels correspond to proton signals of **5⊂[1•Pt$_2$(dppp)$_2$]$^{4+}$**. See Scheme 5.1 and Figure 5.26 for proton assignments. *Residual solvent peaks.

The observation of broad signals in the ^{1}H NMR spectrum of ligand **1** with *N*-oxide **5** and Pt(II) suggested the formation of polymeric aggregates to a significant extent.

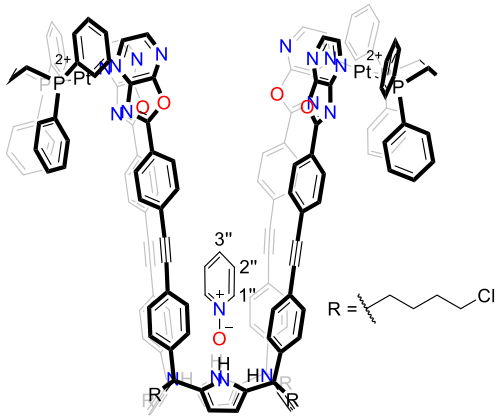

Figure 5.26. Line-drawing structure of the **5**⊂[**1**•$Pt_2(dppp)_2$]$^{4+}$ complex.

Table 5.3. Experimental chemical shifts of free (δ_{free}) and bound (δ_{bound}) **5** in the metallocavitand and complexation-induced shifts ($\Delta\delta$).

Signal	δ_{free} (ppm)	Signal	δ_{bound} (ppm)	$\Delta\delta$ (ppm)
1	8.13	1''	4.57	-3.56
2	7.25	2''	6.73	-0.52
3	7.25	3''	7.09	-0.16

N,*N*-dimethylhexylamine *N*-oxide **6**

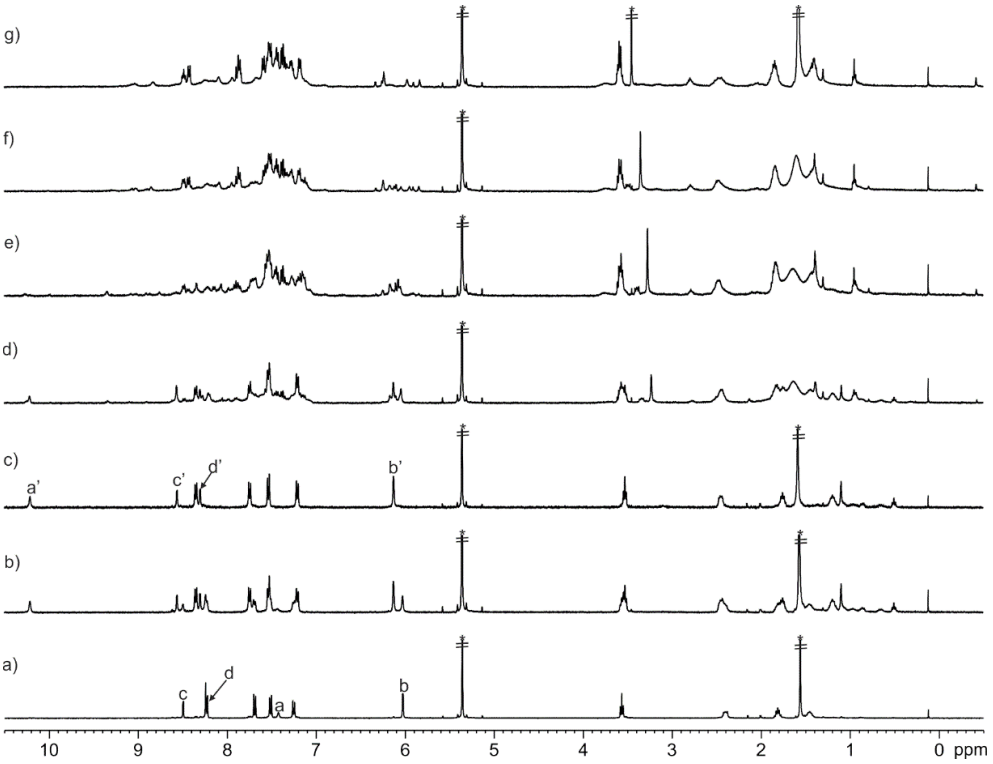

Figure 5.27. ^{1}H NMR (400 MHz, CD_2Cl_2, 298 K) spectra of the titration of ligand **1** with *N*-oxide **6**: a) 0; b) 0.5 and c) 1 equiv.; addition of Pt(dppp)$(OTf)_2$ to the **6⊂1** complex: d) 0.5; e) 1; f) 2 and g) 3 equiv. Primed labels correspond to proton signals of **6⊂1**. See Scheme 5.1 for proton assignments. *Residual solvent peaks.

The observation of several proton signals in the ^{1}H NMR spectrum of ligand **1** with *N*-oxide **6** and Pt(II) suggested the formation of higher-order aggregates of unknown stoichiometry.

Titrations of receptor **1** with formamides **7**, **8** and addition of Pt(II) to the corresponding 1:1 complexes

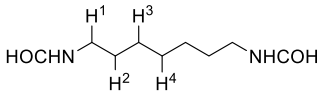

7

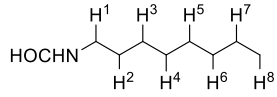

8

Figure 5.28. Line-drawing structures of formamides **7** and **8**.

Bis-formamide **7**

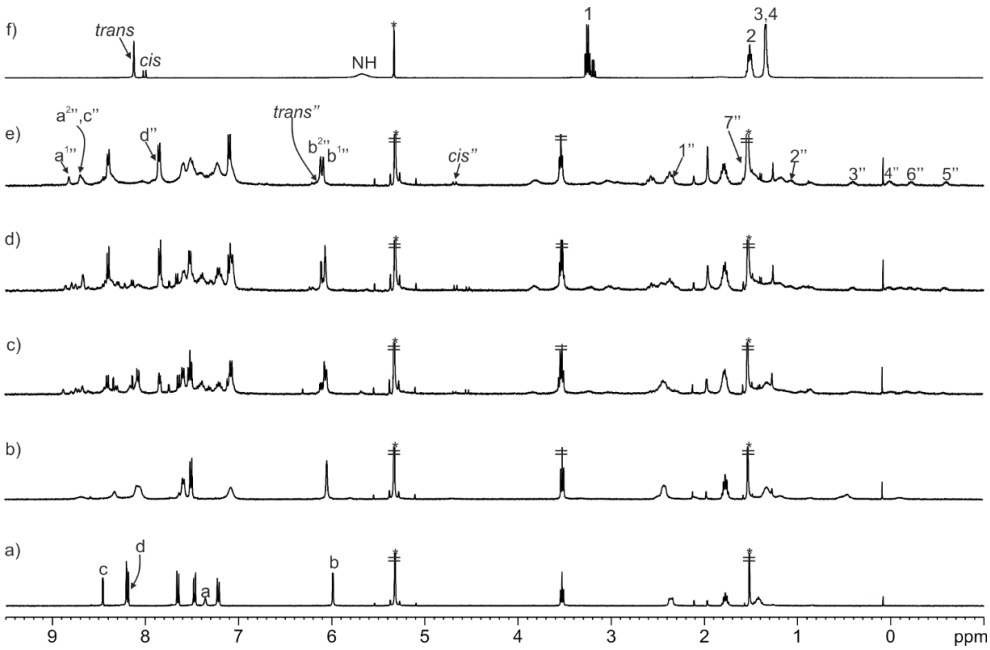

Figure 5.29. ^{1}H NMR (400 MHz, CD_2Cl_2, 298 K) spectra of the titration of ligand **1** with *bis*-formamide **7**: a) 0 and b) 1 equiv.; addition of Pt(dppp)$(OTf)_2$ to **7⊂1** complex: c) 0.5; d) 1 and e) 2 equiv.; f) **7**. Double primed labels correspond to proton signals of *trans,cis*-**7**⊂[**1**•$Pt_2(dppp)_2]^{4+}$. See Scheme 5.1 and Figure 5.34 for proton assignments. *Residual solvent peaks.

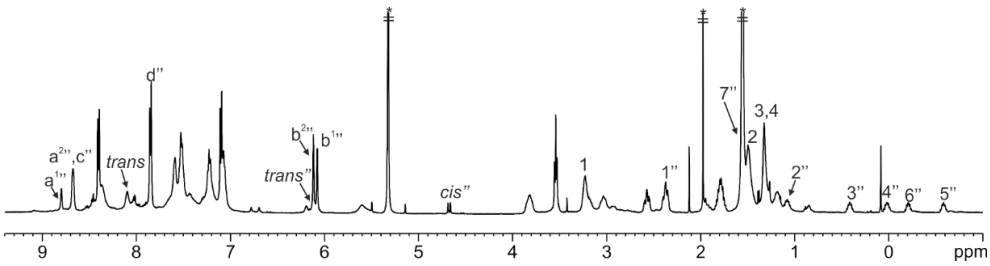

Figure 5.30. ^{1}H NMR (500 MHz with cryoprobe, CD_2Cl_2, 298 K) spectrum of ligand **1** with *bis*-formamide **7** and Pt(dppp)$(OTf)_2$ (*ca.* 1:2:2 ratio). Double primed labels correspond to proton signals of *trans,cis*-**7**⊂[**1**•$Pt_2(dppp)_2]^{4+}$. See Scheme 5.1 and Figure 5.34 for proton assignments. *Residual solvent peaks.

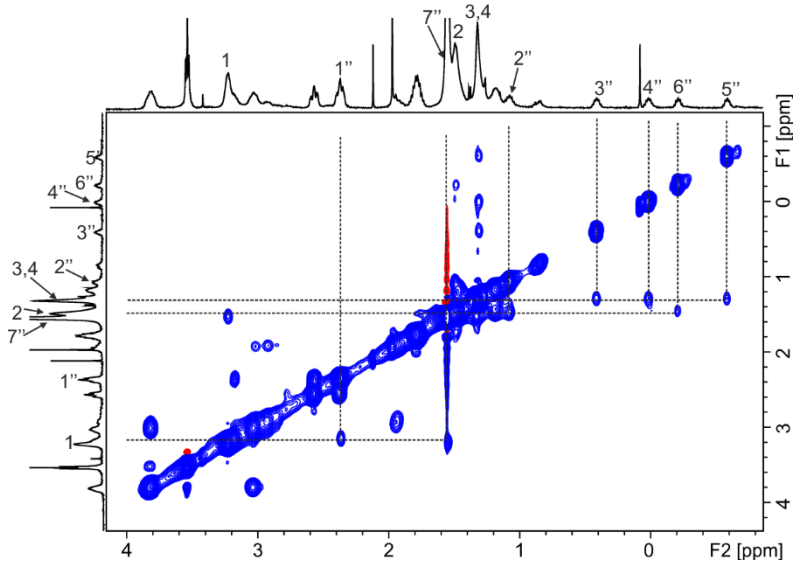

Figure 5.31. Selected region of the ^{1}H-^{1}H EXSY NMR (500 MHz with cryoprobe, CD_2Cl_2, 298 K, mixing time = 0.3 s) spectrum of ligand **1** with *bis*-formamide **7** and Pt(dppp)(OTf)$_2$ (*ca.* 1:2:2 ratio). Double primed labels correspond to proton signals of *trans,cis*-**7**⊂[**1**•Pt$_2$(dppp)$_2$]$^{4+}$. See Figure 5.34 for proton assignment.

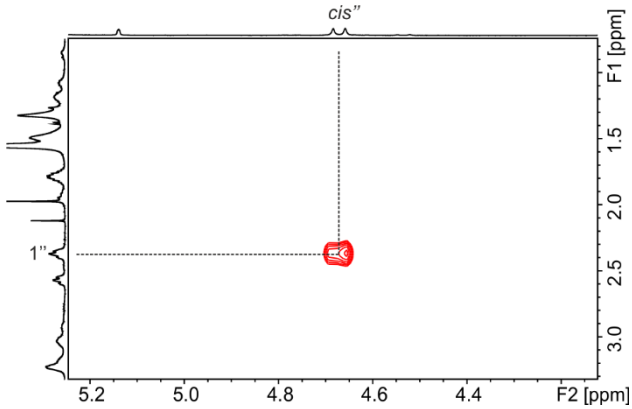

Figure 5.32. Selected region of the ^{1}H-^{1}H ROESY NMR (500 MHz with cryoprobe, CD_2Cl_2, 298 K, spin lock = 0.3 s) spectrum of ligand **1** with *bis*-formamide **7** and Pt(dppp)(OTf)$_2$ (*ca.* 1:2:2 ratio). The ROESY cross-peak between 1'' and the signal at 4.67 is highlighted. The observed cross-peak confirmed that one of the formamide groups of bound **7** adopts a *cis*-conformation. See Figure 5.34 for proton assignment.

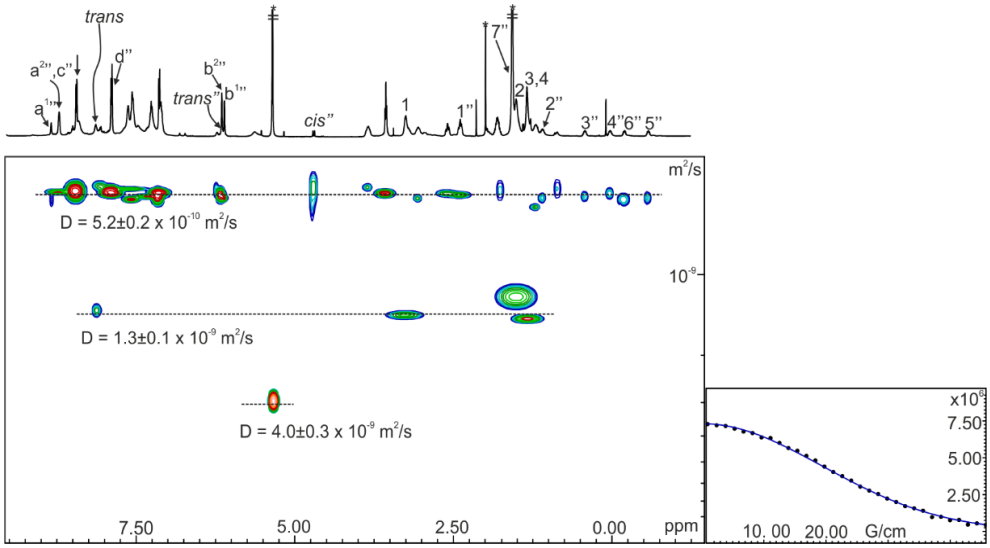

Figure 5.33. (left) ^{1}H pseudo 2D plot of DOSY (500 MHz with cryoprobe, CD_2Cl_2, 298 K, D20 = 0.01 s; P30 = 3.5 ms) of ligand **1** with *bis*-formamide **7** and Pt(dppp)(OTf)$_2$ (*ca.* 1:2:2 ratio). (right) Fit of the decay of the signal b^{2}'' to a mono-exponential function using Dynamics Center from Bruker. Double primed labels correspond to proton signals of *trans,cis*-**7**⊂[**1**•Pt$_2$(dppp)$_2$]$^{4+}$. See Scheme 5.1 and Figure 5.34 for proton assignments. Errors are indicated as standard deviations. *Residual solvent peak.

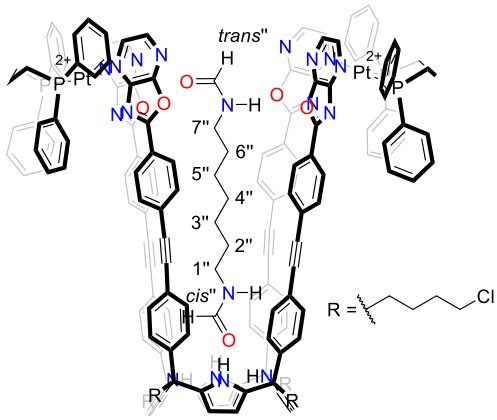

Figure 5.34. Line-drawing structure of the *trans,cis*-**7**⊂[**1**•Pt$_2$(dppp)$_2$]$^{4+}$ complex.

Table 5.4. Experimental chemical shifts of free (δ_{free}) and bound (δ_{bound}) **7** and complexation-induced shifts ($\Delta\delta$).

Signal	δ_{free} (ppm)	Signal	δ_{bound} (ppm)	$\Delta\delta$ (ppm)
trans	8.11	*trans''*	6.13	-1.98
cis	7.99	*cis''*	4.67	-3.32
1	3.24	1''	2.37	-0.87
2	1.50	2''	1.08	-0.42
3	1.33	3''	0.41	-0.92
4	1.33	4''	0.02	-1.31
-		5''	-0.59	-1.92
-		6''	-0.21	-1.71
		7''	1.55	-1.69

Mono-formamide **8**

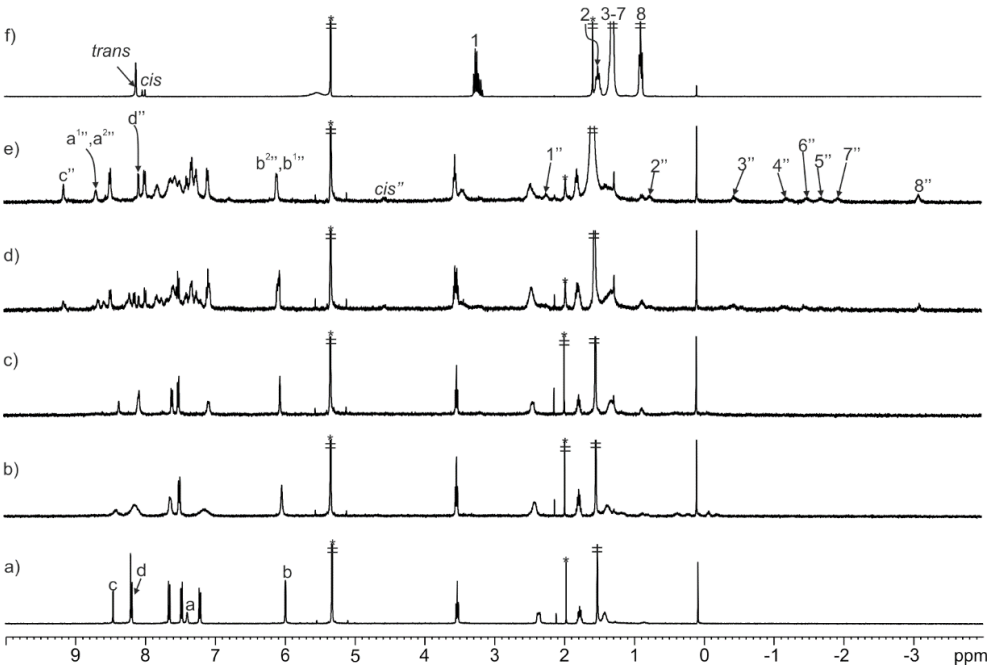

Figure 5.35. ^{1}H NMR (400 MHz, CD_2Cl_2, 298 K) spectra of the titration of ligand **1** with *mono*-formamide **8**: a) 0; b) 0.5 and c) 1 equiv.; addition of $Pt(dppp)(OTf)_2$ to **8⊂1** complex: d) 1 and e) 2 equiv.; f) **8**. Double primed labels correspond to proton signals of *cis*-**8**⊂[**1**•$Pt_2(dppp)_2$]$^{4+}$. See Scheme 5.1 and Figure 5.40 for proton assignments. *Residual solvent peaks.

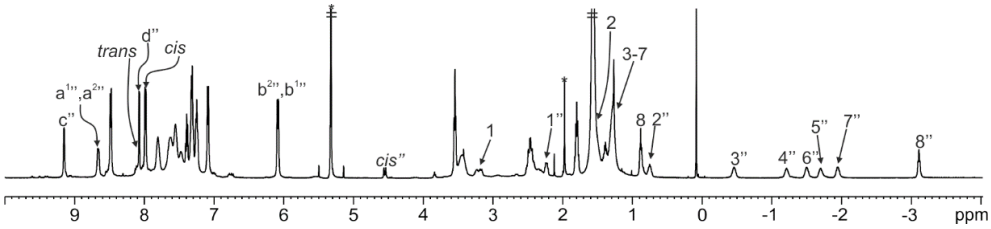

Figure 5.36. ^{1}H NMR (500 MHz with cryoprobe, CD_2Cl_2, 298 K) spectrum of ligand **1** with *mono*-formamide **8** and Pt(dppp)$(OTf)_2$ (*ca.* 1:2:2 ratio). Double primed labels correspond to proton signals of *cis*-**8**⊂[**1**•$Pt_2(dppp)_2]^{4+}$. See Scheme 5.1 and Figure 5.40 for proton assignments. *Residual solvent peaks.

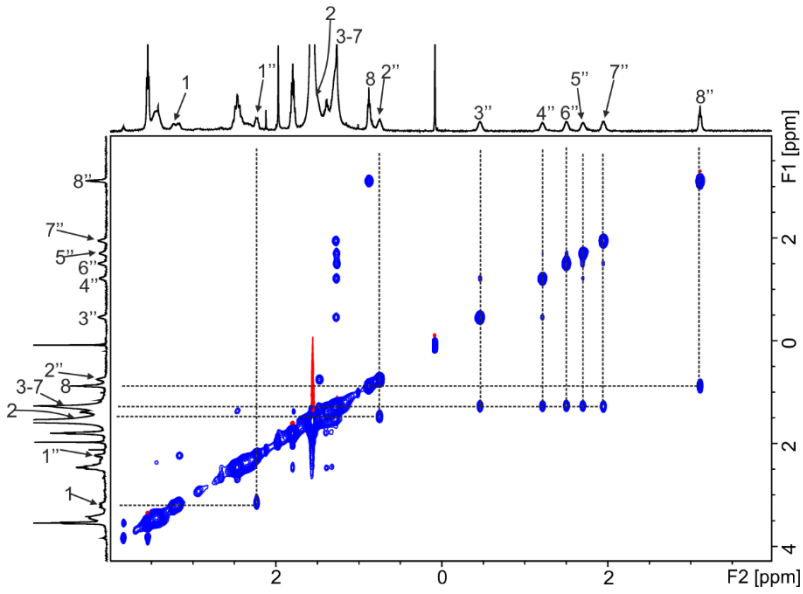

Figure 5.37. Selected region of the ^{1}H-^{1}H EXSY NMR (500 MHz with cryoprobe, CD_2Cl_2, 298 K, mixing time = 0.3 s) spectrum of ligand **1** with *mono*-formamide **8** and Pt(dppp)$(OTf)_2$ (*ca.* 1:2:2 ratio). Double primed labels correspond to proton signals of *cis*-**8**⊂[**1**•$Pt_2(dppp)_2]^{4+}$. See Figure 5.40 for proton assignment.

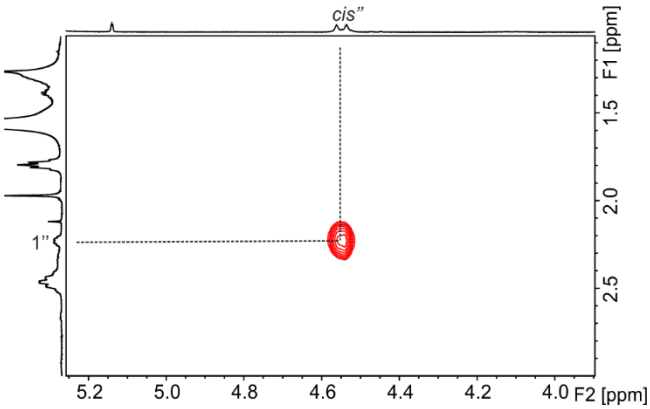

Figure 5.38. Selected region of the ^{1}H-^{1}H ROESY NMR (500 MHz with cryoprobe, CD_2Cl_2, 298 K, spin lock = 0.3 s) spectrum of ligand **1** with *mono*-formamide **8** and [Pt(dppp)(OTf)$_2$] (*ca*. 1:2:2 ratio). The ROESY cross-peak between 1'' and the signal at 4.55 is highlighted. The observed cross-peak confirmed that the formamide group of bound **8** adopts a *cis*-conformation. See Figure 5.40 for proton assignment.

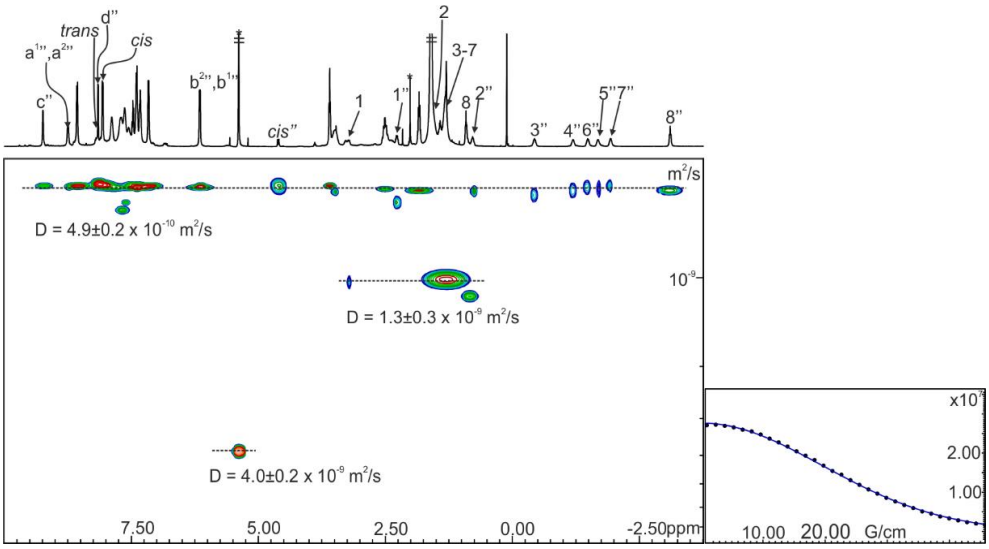

Figure 5.39. (left) ^{1}H pseudo 2D plot of DOSY (500 MHz with cryoprobe, CD_2Cl_2, 298 K, D20 = 0.01 s; P30 = 3.5 ms) of ligand **1** with *mono*-formamide **8** and Pt(dppp)(OTf)$_2$ (*ca*. 1:2:2 ratio). (right) Fit of the decay of the signal b^{2}'' to a mono-exponential function using Dynamics Center from Bruker. Double primed labels correspond to proton signals of *cis*-**8**⊂[**1**•Pt$_2$(dppp)$_2$]$^{4+}$. See Scheme 5.1 and Figure 5.40 for proton assignments. Errors are indicated as standard deviations. *Residual solvent peaks.

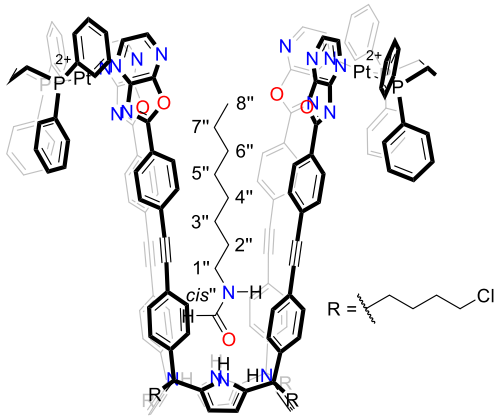

Figure 5.40. Line-drawing structure of the *cis*-**8**⊂[**1**•$Pt_2(dppp)_2]^{4+}$ complex.

Table 5.5. Experimental chemical shifts of free (δ_{free}) and bound (δ_{bound}) **8** and complexation-induced shifts ($\Delta\delta$).

Signal	δ_{free} (ppm)	Signal	δ_{bound} (ppm)	$\Delta\delta$ (ppm)
trans	8.11	-	-	-
cis	7.99	*cis*''	4.55	-3.44
1	3.23	1''	2.23	-1.00
2	1.50	2''	0.75	-0.75
3	1.29	3''	-0.46	-1.75
4	1.29	4''	-1.21	-2.50
5	1.29	5''	-1.70	-2.99
6	1.29	6''	-1.51	-2.80
7	1.29	7''	-1.95	-3.24
8	0.88	8''	-3.11	-3.99

Table 5.6. Comparison of complexation-induced shifts ($\Delta\delta$) of **7**, **8** and $Pt(dppp)(OTf)_2$ in the *trans*,*cis*-**7**⊂[**1**•$Pt_2(dppp)_2]^{4+}$ and *cis*-**8**⊂[**1**•$Pt_2(dppp)_2]^{4+}$ metallocaviplexes.

trans,*cis*-**7**⊂[**1**•$Pt_2(dppp)_2]^{4+}$		*cis*-**8**⊂[**1**•$Pt_2(dppp)_2]^{4+}$	
Signal	**$\Delta\delta$ (ppm)**	**Signal**	**$\Delta\delta$ (ppm)**
cis''	-3.32	*cis*''	-3.44
1''	-0.87	1''	-1.00
2''	-0.42	2''	-0.75
3''	-0.92	3''	-1.75
4''	-1.31	4''	-2.50
5''	-1.92	5''	-2.99
6''	-1.71	6''	-2.80
7''	-1.69	7''	-3.24
-	-	8''	-3.99
dppp''	1.59	dppp''	0.76
dppp''	0.35	dppp''	0.11

5.4.4 Competitive displacement of the bound template in selected metallocaviplexes

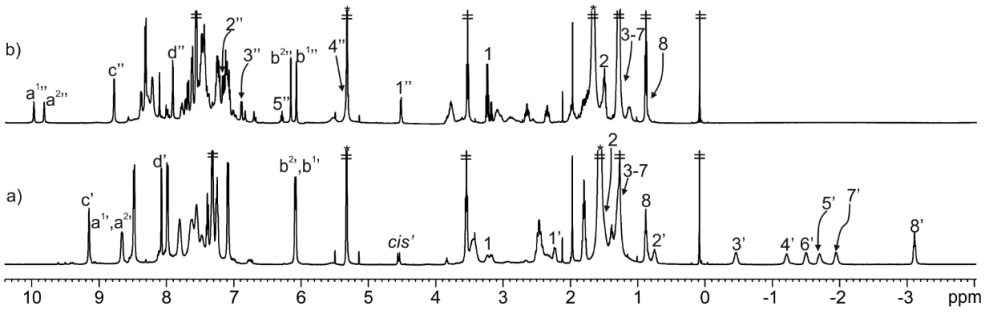

Figure 5.41. ^{1}H NMR (500 MHz with cryoprobe, CD_2Cl_2, 298 K) spectra of: a) [**1**•$Pt_2(dppp)_2]^{4+}$ with *ca.* 1.2 equiv. of **8** and b) addition of *ca.* 1.5 equiv. of **4** to a). Primed labels correspond to proton signals of *cis*-**8**⊂[**1**•$Pt_2(dppp)_2]^{4+}$. Double primed labels correspond to proton signals of **4**⊂[**1**•$Pt_2(dppp)_2]^{4+}$. See Scheme 5.1 and Figure 5.40 and Figure 5.22 for proton assignments. *Residual solvent peaks.

The addition of 4-phenylpyridine *N*-oxide **4** to a solution containing the metallocaviplex *cis*-**8**⊂[**1**•$Pt_2(dppp)_2]^{4+}$ and free **8** produced the rapid and quantitative formation of the **4**⊂[**1**•$Pt_2(dppp)_2]^{4+}$ counterpart. Concomitantly, the bound guest **8** was released to the bulk solution.

5.4.5 Calculated chemical shifts of the oxazolopyrazinyl substituent

The chemical structure was optimized at the DFT level of theory (B3LYP/6-31G*) in the gas phase using Spartan version 7.2.6. Chemical shifts were computed using the same software.

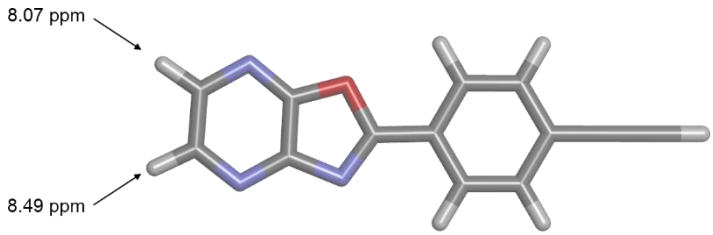

Figure 5.42. Energy minimized structure (B3LYP/6-31G*) of an oxazolopyrazinyl structure. Calculated chemical shifts are indicated.

5.5 References and Notes

[1] A. J. McConnell, C. S. Wood, P. P. Neelakandan and J. R. Nitschke, *Chem. Rev.*, 2015, **115**, 7729-7793.

[2] T. R. Cook and P. J. Stang, *Chem. Rev*., 2015, **115**, 7001-7045.

[3] E. G. Percástegui, T. K. Ronson and J. R. Nitschke, *Chem. Rev.*, 2020, **120**, 13480-13544.

[4] P. D. Frischmann and M. J. MacLachlan, *Chem. Soc. Rev.*, 2013, **42**, 871-890.

[5] D. Zhang, T. K. Ronson, J. Mosquera, A. Martinez, L. Guy and J. R. Nitschke, *J. Am. Chem. Soc.*, 2017, **139**, 6574-6577.

[6] A. Galan and P. Ballester, *Chem. Soc. Rev.*, 2016, **45**, 1720-1737.

[7] L. You, J. S. Berman and E. V. Anslyn, *Nat. Chem.*, 2011, **3**, 943-948.

[8] S. Korom and P. Ballester, *J. Am. Chem. Soc.*, 2017, **139**, 12109-12112.

[9] M. Petroselli, V. Angamuthu, F.-U. Rahman, X. Zhao, Y. Yu and J. Rebek, *J. Am. Chem. Soc.*, 2020, **142**, 2396-2403.

[10] L. Escobar, E. C. Escudero-Adán and P. Ballester, *Angew. Chem., Int. Ed.*, 2019, **58**, 16105-16109.

[11] M. L. Saha, X. Yan and P. J. Stang, *Acc. Chem. Res.*, 2016, **49**, 2527-2539.

[12] L. Escobar, D. Villarón, E. C. Escudero-Adán and P. Ballester, *Chem. Commun. (Cambridge, U. K.)*, 2019, **55**, 604-607.

[13] M. Fujita, M. Tominaga, A. Hori and B. Therrien, *Acc. Chem. Res.*, 2005, **38**, 369-378.

[14] L. Poorters, D. Armspach, D. Matt, L. Toupet and P. G. Jones, *Angew. Chem., Int. Ed.*, 2007, **46**, 2663-2665.

[15] L. Escobar and P. Ballester, *Chem. Rev.*, 2021, **121**, 2445-2514.

[16] J. Aguilera-Sigalat, C. Sáenz de Pipaón, D. Hernández-Alonso, E. C. Escudero-Adán, J. R. Galan-Mascarós and P. Ballester, *Cryst. Growth Des.*, 2017, **17**, 1328-1338.

[17] F. U. Rahman, Y. S. Li, I. D. Petsalakis, G. Theodorakopoulos, J. Rebek and Y. Yu, *Proc. Natl. Acad. Sci. U. S. A.*, 2019, **116**, 17648-17653.

[18] Y. Yu, M. Petroselli and J. Rebek, *Chem.--Eur. J.*, 2020, **27**, 3284.

[19] E. Botana, E. Da Silva, J. Benet-Buchholz, P. Ballester and J. de Mendoza, *Angew. Chem., Int. Ed.*, 2007, **46**, 198-201.

[20] A. Díaz-Moscoso, D. Hernández-Alonso, L. Escobar, F. A. Arroyave and P. Ballester, *Org. Lett.*, 2017, **19**, 226-229.

[21] A. Galán, E. C. Escudero-Adán and P. Ballester, *Chem. Sci*, 2017, **8**, 7746-7750.

[22] Q. Sun, L. Escobar and P. Ballester, *Angew. Chem., Int. Ed.*, 2021, **60**,10359-10365.

[23] Y.-S. Li, L. Escobar, Y.-J. Zhu, Y. Cohen, P. Ballester, J. Rebek and Y. Yu, *Proc. Natl. Acad. Sci. U. S. A.*, 2019, **116**, 19815.

[24] The amount of *cis*,*cis*-**7**⊂[**1**•$Pt_2(dppp)_2$]$^{4+}$ complex is beyond the limit to be detected due to its low abundance (~2%).

[25] M. D. Pluth and K. N. Raymond, *Chem. Soc. Rev.*, 2007, **36**, 161-171.

[26] G. R. Fulmer, A. J. M. Miller, N. H. Sherden, H. E. Gottlieb, A. Nudelman, B. M. Stoltz, J. E. Bercaw and K. I. Goldberg, *Organometallics*, 2010, **29**, 2176-2179.

[27] O. V. Dolomanov, L. J. Bourhis, R. J. Gildea, J. A. K. Howard and H. Puschmann, *J. Appl. Crystallogr.*, 2009, **42**, 339-341.

[28] L. Escobar and P. Ballester, *Org. Chem. Front.*, 2019, **6**, 1738-1748.

[29] C. S. Demmer, J. C. Hansen, J. Kehler and L. Bunch, *Adv. Synth. Catal.*, 2014, **356**, 1047-1055.

[30] S. S. Roy, K. M. Appleby, E. J. Fear and S. B. Duckett, *J. Phys. Chem. Lett.*, 2018, **9**, 1112-1117.

UNIVERSITAT ROVIRA I VIRGILI
ARYL AND SUPER ARYL-EXTENDED CALIX[4]PYRROLES: SYNTHESIS AND APPLICATIONS
Qingqing Sun

General Conclusions

In this Thesis, we successfully prepared a series of unprecedented aryl-extended (AE-C[4]Ps) and super aryl-extended calix[4]pyrroles (SAE-C[4]Ps) bearing alkyl chains and ionizable groups at either the upper or lower rims, and in both of them. We studied the molecular recognition properties of the reported synthetic receptors with tetraalkylammonium chloride salts and neutral polar guests in organic solvents and in water. We investigated the applications of the synthesized receptors in chemistry research areas that span from the use of supramolecular protecting groups to the study of self-assembly processes of metallocages and metallocavitands. We also investigated the possible mechanisms operating in the in/out exchange of the included guests in mono-metallic coordination cages by determining the kinetics of the competitive binding experiments.

The following conclusions are derived from the experimental work:

1) The mono gold(I)-phosphine substituted organometallic AE-C[4]P and its parent “two-wall” calix[4]pyrrole bis-alkynyl α,α-isomer bind tetraalkylammonium chloride salts and operate as heteroditopic or homotopic receptors in dichloromethane (DCM) and acetone solution, respectively. Both receptors bind stronger MTOACl compared to TBACl.

2) The organometallic gold(I)-phosphine AE-C[4]P complexes of tetraalkylammonium chloride salts are energetically less stable than their non-organometallic counterparts. Most likely, this is due to the stronger repulsive chloride-π interactions in the former.

3) Water-soluble SAE-C[4]P form 1:1 stable complexes with a series of difunctional guests: *bis*-isonitriles, *bis*-formamides and formamide-isonitriles.

4) Water-soluble SAE-C[4]P can serve as a supramolecular protecting group in the acid-catalyzed hydrolysis of symmetric aliphatic α,ω-*bis*-isonitriles. It modifies the selectivity towards mono-hydrolysed products as well as the reaction rate compared to the same reaction occuring in bulk solution.

5) Water soluble tetra-pyridyl tetra-pyridinium SAE-C[4]P self-assembles into a coordination Pd(II)-cage featuring two endohedral polar binding sites in the presence of ditopic guests that satisfy the hydrogen-bonding demands of the two distal binding sites of the cage and adequately filled its cavity.

6) The use of monotopic guests in the formation of SAE-C[4]P-Pd(II) cage requires the co-inclusion of a water molecule to fulfill the demands of the other polar binding site and the cavity filling.

7) The endohedrally functionalized water-soluble SAE-C[4]P-Pd(II) cage featured conformational selectivity for the encapsulation of aliphatic *bis*-formamides. The guest displacement most likely occurs through a “French doors” mechanism.

8) Tetra-oxazolo[4,5-*b*]pyrazinyl SAE-C[4]P self-assembles into a *bis*-metallocavitand in solution in the presence of suitable platinum salts as metal precursors and adequate guests.

9) The tetra-oxazolo[4,5-*b*]pyrazinyl SAE-C[4]P chelates only two Pt(II) metals between its adjacent substituents affording metallocavitand complexes displaying C_{2v} symmetry.

10) The guest encapsulated in metallocavitand complexes experiences a rapid release/uptake process most likely due to a “French doors” or “constrictive binding” mechanism.

We foresee that the large polar characteristics of the aromatic cavities present in the metallic assemblies will find potential applications in the development of supramolecular chemosensors, the encapsulation of reactive species and the modulation of the reactivity of the bound substrates.

List of Abbreviations

MTOACl	–	Methyl-tri-octyl ammonium chloride
TBACl	–	Tetra-butyl ammonium chloride
ITC	–	Isothermal Titration Calorimetry
DFT	–	Density Functional Theory
PTA	–	1,3,5-triaza-7-phosphaadamantane
UV	–	UltraViolet
Vis	–	Visible
ESP	–	Electrostatic Surface Potential
CPK	–	Corey-Pauling-Koltun model
TMACl	–	Tetramethylammonium chloride
TEACl	–	Tetraethylammonium chloride
FTIR	–	Fourier-Transform InfraRed spectroscopy
COSY	–	COrrelated SpectroscopY
AE	–	Aryl-Extended
SAE	–	Super Aryl-Extended
C[4]P	–	Calix[4]pyrrole
CIS	–	Complexation Induced Shift
EXSY	–	EXchange SpectroscopY
NOE	–	Nuclear Overhauser Effect
HMBC	–	Heteronuclear Multiple Bond Correlation
HMQC	–	Heteronuclear Multiple-Quantum Correlation
ROESY	–	Rotating-frame Overhauser Enhancement SpectroscopY

ESI	–	ElectroSpray Ionization
FTIR	–	Fourier-Transform InfraRed spectroscopy
HRMS	–	High-Resolution Mass Spectrometry
IR	–	InfraRed
MALDI	–	Matrix-Assisted Laser Desorption Ionization
TMS	–	TetraMethylSilane
CC	–	Coordination Cage
DOSY	–	Diffusion Ordered SpectroscopY
ATR	–	Attenuated Total Reflectance
ROE	–	Rotating-frame Overhauser Effect
DMSO	–	Di-Methyl Sulfoxide
Equiv.	–	Equivalent
HPLC	–	High-Performance Liquid Chromatography
MM	–	Molecular Mechanics force field
NMR	–	Nuclear Magnetic Resonance
ORTEP	–	Oak Ridge Thermal Ellipsoid Plot
MS	–	Mass Spectrometry
°C	–	Celsius
PC	–	Packing Coefficient
kcal	–	Kilocalorie
K	–	Kelvin
THF	–	TetraHydroFuran
TLC	–	Thin Layer Chromatography

DIPEA	–	*N*,*N*-Diisopropylethylamine
r.t.	–	Room Temperature
iPr_2NH	–	diisopropylamine
SIR	–	Selective Inversion Recovery
SPS	–	Solvent Purification System
L-Pro	–	L-proline
ΔC_p	–	Heat Capacity
GC	–	Gas Chromatography

UNIVERSITAT ROVIRA I VIRGILI
ARYL AND SUPER ARYL-EXTENDED CALIX[4]PYRROLES: SYNTHESIS AND APPLICATIONS
Qingqing Sun

UNIVERSITAT ROVIRA I VIRGILI
ARYL AND SUPER ARYL-EXTENDED CALIX[4]PYRROLES: SYNTHESIS AND APPLICATIONS
Qingqing Sun

UNIVERSITAT ROVIRA I VIRGILI
ARYL AND SUPER ARYL-EXTENDED CALIX[4]PYRROLES: SYNTHESIS AND APPLICATIONS
Qingqing Sun

UNIVERSITAT ROVIRA I VIRGILI
ARYL AND SUPER ARYL-EXTENDED CALIX[4]PYRROLES: SYNTHESIS AND APPLICATIONS
Qingqing Sun

UNIVERSITAT
ROVIRA i VIRGILI

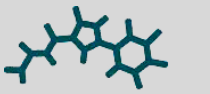

ICIQ

Institut
Català
d'Investigació
Química